Dielectric and Viscoelastic Investigation of Global Dynamics of Cis-Polyisoprene

Yumi Matsumiya

2002

Dielectric and Viscoelastic Investigation of Global Dynamics of Cis-Polyisoprene

Yumi Matsumiya

2002

Contents

CHAPTER 1

Introduction

1-1. General 1
1-2. Attempts of Molecular Explanation 3
1-3. Scope of This Thesis 6
References 8

CHAPTER 2

Materials and Measurements

2-1. Introduction 11
2-2. Preparation and Characterization of Samples 11
2-2-1. Preparation 11
2-2-2. Characterization 12
2-3. Viscoelastic Measurements 12
2-3-1. Principle 12
2-3-2. Viscoelastic mode distribution and relaxation time. 16
2-3-3. Method 18
2-4 Dielectric Measurements 18
2-4-1. Principle 18
2-4-2. Dielectric mode distribution and relaxation time 19
2-4-3. Method 20
References 24

CHAPTER 3

Theory: Molecular Expression of Dynamic Properties

3-1. Introduction 25
3-2. Coarse-Grained Chain 25
3-3. Expression of Linear Viscoelastic Properties 27
3-3-1. Relaxation modulus 27
3-3-2. Insensitivity of $G(t)$ expression to degree of coarse-graining 28
3-4. Expression of Dielectric Properties 30
3-4-1. Dielectric relaxation function. 30
3-4-1-1. Linear chains 30
3-4-1-2. Star chains 32
3-4-2. Insensitivity of $\Phi(t)$ expression to degree of coarse-graining. 33
3-5. Difference between Viscoelastic and Dielectric Properties3,13) 33
References 34

CHAPTER 4

Molecular Models of Chain Dynamics

4-1. Introduction 35

4-2. Bead-Spring Models 35
4-2-1. Rouse model 35
4-2-1-1. Viscoelastic properties 35
4-2-1-2. Dielectric properties 36
4-2-2. Ham model 37
4-2-2-1. Viscoelastic properties 37
4-2-2-2. Dielectric properties 38
4-3. Doi-Edwards Model 39
4-3-1. Viscoelastic properties 40
4-3-2. Dielectric properties 41
4-3-3. Comment for the reptation and Rouse dynamics 41
4-4. Thermal Constraint Release Model 42
4-4-1. Linear chains 42
4-4-2. Star chains 43
4-5. DTD Model for Linear Chains 44
4-5-1. Marrucci model 44
4-5-1-1. Viscoelastic properties of monodisperse systems 44
4-5-1-2. Viscoelastic properties of blends 46
4-5-2. Supplement to Marrucci model (a model developed in this study) 46
4-5-2-1. Dielectric properties of monodisperse systems 47
4-5-2-2. Dielectric properties of binary blends 48
4-6. DTD Model for Monodisperse Star Chains 49
4-6-1. Ball-McLeish model 49
4-6-1-1. Arm retraction in dilated tube 50
4-6-1-2. Viscoelastic properties 51
4-6-2. Milner-McLeish model 52
4-6-3. Supplement to BM and MM models (a model developed in this study) 53
4-6-3-1. Arm motion in the dilated tube 53
4-6-3-2. DTD relationship between Φ and μ of star chains 55
4-6-3-3. Reformulation of BM and MM models for Φ 56
4-6-3-4. Modified DTD relationship accounting tube-edge effect 57
References 60

CHAPTER 5

Effects of Constraint Release on Eigenmodes of Dilute Probe in Blends

5-1. Introduction 61
5-2. Experimental 63
5-2-1. Materials 63
5-2-2. Measurements 63
5-3. Results 64
5-3-1. Dielectric behavior of regular PI chains in B263 64
5-3-2. Overview of dielectric behavior of dipole-inverted PI chains 66
5-3-3. Estimation of CR contribution 68
5-3-4. Evaluation of f_p and $\tau_{\varepsilon,p}$ 69
5-4. Discussion 74

5-4-1. CR effects on eigenmodes 74
5-4-2. Comparison of ΔF_p and $\tau_{\varepsilon,p}$ data with models 75
5-5. Concluding Remarks 77
Appendix 5A. Characteristic Relationships for the Eigenfunctions 77
References and Notes 79

CHAPTER 6

Effects of Constraint Release on the Coherence of the Submolecule Motion in Linear Chain

6-1. Intruduction 81
6-2. Theoretical 82
6-2-1. General 82
6-2-2. Expression of ε'' 82
6-2-3. Expression of G^* 83
6-3. Experimental 84
6-4. Results 85
6-4-1. Overview of viscoelastic behavior of I-I 49-0/PB blends 85
6-4-2. Evaluation of G_I^* for I-I 49-0 in PB matrices 87
6-4-2-1. G_I^* in B9 matrix 87
6-4-2-2. G_I^* in B263 matrix 87
6-5. Discussion 89
6-5-1. Entanglement spacing for I-I 49-0 in PB matrices 89
6-5-2. Calculation of $G_{r,coh}^*$ and $G_{r,incoh}^*$ 90
6-5-3. CR effects on coherence of submolecule motion 91
6-5-4. Comparison with tube model 94
6-6. Concluding Remarks 94
References and Notes 94

CHAPTER 7

Test of Tube Dilation Molecular Picture for Linear Chains

7-1. Introduction 97
7-2. Theoretical Background 97
7-2-1. Monodisperse systems 97
7-2-2. Blends 98
7-3. Experimental 98
7-4. Results and Discussion 99
7-4-1. Monodisperse systems 99
7-4-2. Dilute PI probe in blends 101
7-5. Concluding Remarks 104
Appendix 7A. Iteration Method for Evaluation of Dielectric Spectrum 104
7A-1. Iteration Method 104
7A-2. meaning of the use of dielectric spectrum in the test of DTD picture 105
References 106

CHAPTER 8

Tube Dilation Process in Star-Branched *cis*-Polyisoprenes

8-1. Introduction 107
8-2. Theory 107
8-3. Experimental 108
8-3-1. Materials 108
8-3-2. Measurements 108
8-4. Results and Discussion 108
8-4-1. Overview of dielectric data 108
8-4-2. Test of DTD relationship in absence of tube-edge effect 111
8-4-3. Effect of branching-point fluctuation in dilated tube 112
8-4-3-1. Test of DTD relationship for star chains with various q 112
8-4-3-2. DTD criteria in absence of tube-edge effect 116
8-4-3-3. Estimation of f and t_w 117
8-4-3-4. Origin of failure/validity of DTD picture 118
8-4-4. Comparison of data with DTD model in absence of tube-edge effect 119
8-4-5. Comparison of data with DTD model in presence of tube-edge effect 123
8-4-6. Effect of terminal CR relaxation 124
8-4-6-1. Estimation of z^{**} and t_w 124
8-4-6-2. CR-relaxation process 126
8-4-6-3. Effective friction for terminal CR relaxation 128
8-4-6-4. Comparison of DTD-CR model with experiments 129
8-5. Concluding Remarks 131
Appendix 8A. Viscoelastic and Dielectric Features of BM and MM Models 132
References and Notes 134

CHAPTER 9

Summary 137

List of Publications

I. Publications Included in This Thesis 139
II. Other Publications 140

Acknowledgements 141

CHAPTER 1
Introduction

1-1. General

Polymeric materials consisting of flexible chains have been extensively utilized over past several decades. The processing, providing a desired shape to these materials, is intimately related to dynamics of polymer chains therein. In addition, the dynamics of flexible polymer chains is one of the most important subjects in the field of polymer physics. Thus, the chain dynamics has been extensively investigated from both scientific as well as industrial points of view.

At equilibrium, the flexible chains behave as random coils because of a huge freedom in the spatial arrangements of their constituent units (monomers).[1] Corresponding to this huge freedom, the chains exhibit various types of motion according to the time and spatial scales of observation. In general, the fast dynamics corresponds to the chain motion in small spatial scales, while the slow dynamics reflects the motion over large spatial scales. The very local, rapid motion in the scales of chemical bonds (e.g., the bond vibration) is not significantly different from that in low molecular weight (M) materials and is essentially determined by the chemical structure of the chains. However, at larger scales, the polymer chains exhibit unique dynamic features not found for the low-M materials. These features, corresponding to the motion in the spatial scales well above the monomer size and strongly influenced by the chain connectivity, are very similar for the polymer chains of various chemical structures[2]. This universality (independence from the chemical structure) is indicative of the existence of the global dynamics common for various kinds of polymer chains.

The motion of polymer chains is reflected in many kinds of dynamic properties, e.g., viscoelastic (rheological) and dielectric properties. Among these properties, the viscoelastic properties have been most extensively studied (partly because of their intimate relationship with practical processing). A comprehensive summary of results of early studies is given in Ferry's textbook[2] and Graessley's review.[3] Those studies revealed some important dynamic features of polymer chains to establish the corresponding molecular concepts (including the universality explained above).

Probably, the firstly noted basic features were the *viscoelastic* memory effect of polymeric liquids and the dependence of some viscoelastic quantities on the chain molecular weight M. Examples of this M dependence for monodisperse linear chains are shown in Fig. 1-1 (for the dynamic storage and loss moduli, G' and G'', of linear polystyrenes (PS))[4] and in Fig. 1-2 (for the zero-shear viscosity η_0 of these linear PS chains): As noted in Fig. 1-1, the behavior of high-M polymers is similar to that of cross-linked rubbers at high frequencies ω where G' (an elastic component of the modulus) is insensitive to ω and G''(a dissipative component) is much smaller than G'. Thus, at such high ω (at short time scales), the high-M polymers behave as elastic

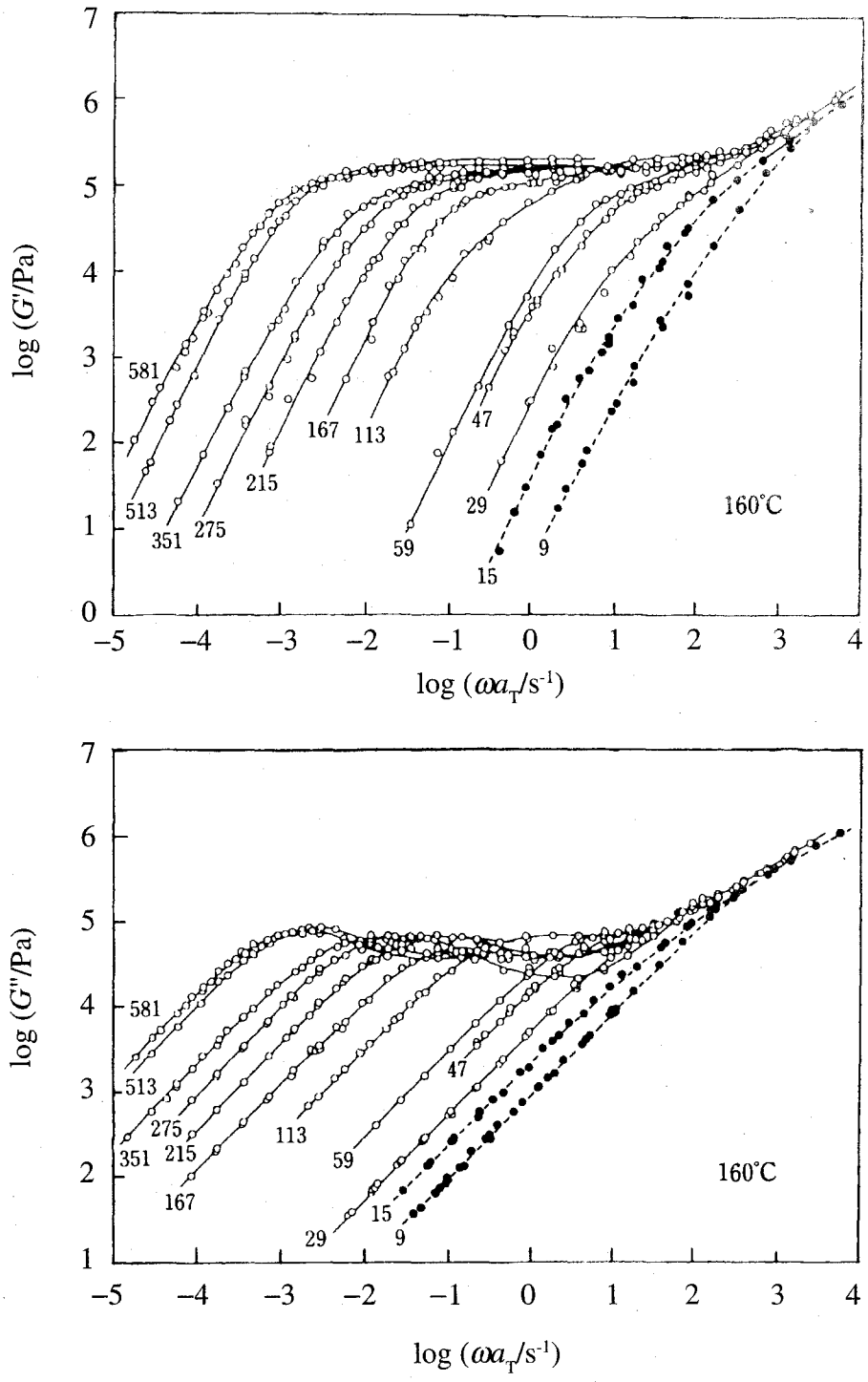

Fig. 1-1 Frequency dependence of storage and loss moduli of monodisperse, linear polystyrene (PS) samples of various molecular weights M reported by Onogi et al[4] The numbers indicate M in unit of 1000. For the two lowest M samples ($M = 9\times10^3$ and 15×10^3), the free volume correction[2] was made to compare the data at an iso-frictional state.

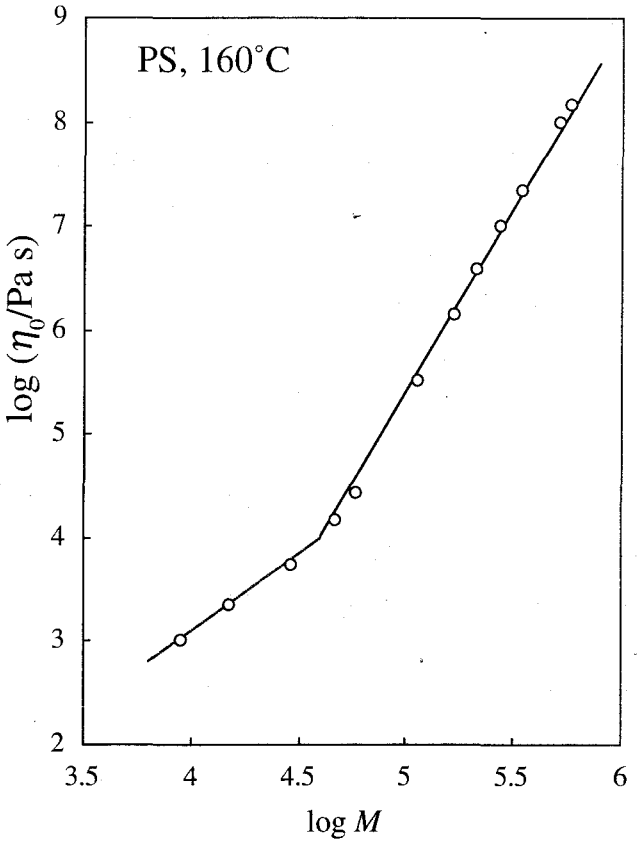

Fig. 1-2 Molecular weight dependence of zero-shear viscosity η_0 of monodisperse, linear polystyrene samples at 160°C.[4] The free volume correction[2] was made for the η_0 data for $M = 9 \times 10^3$ and 15×10^3 to compare the data at an iso-frictional state.

solids. However, both G' and G'' decreases with decreasing ω and the mechanical response is dominated by G'' ($>> G'$) at low ω, meaning that the polymers behave as viscous fluids in long time scales. This change in the response most clearly represents the viscoelastic relaxation of high-M polymer chains. Since a characteristic time of this relaxation increases with M, the frequency for crossover from the elastic behavior to viscous behavior (the relaxation frequency) decreases with M (cf. Fig. 1-1) and the viscosity η_0 increases with M accordingly (cf. Fig. 1-2).

Under the recognition that the mechanical stress of polymeric liquids is related to the anisotropy in the chain conformation induced by the applied strain/flow, the viscoelastic relaxation (such as seen in Fig. 1-1) is related to the chain motion that reduces this anisotropy and allows the stress to relax. This stress-conformation relationship, known as the stress-optical rule,[2,5] enabled investigation of the chain motion through viscoelastic quantities and contributed significantly to the development of molecular concepts of the polymer dynamics.

1-2. Attempts of Molecular Explanation

Molecular concepts of the polymer dynamics have been developed to explain the experimentally observed viscoelastic features such as those seen in Figs. 1-1 and 1-2. In this development, the universality of the slow viscoelastic relaxation enabled the use of coarse-grained

models that account for no chemical details of the chain but preserve the essential structural character, the chain connectivity.

For description of the viscoelastic behavior, the Rouse model[6] was firstly developed. In this model, the chain is divided into coarse-grained submolecules. The submolecules are further replaced by beads that have a M-independent friction coefficient ζ and are connected by springs of strength κ. The Rouse model was originally formulated for an isolated chain in dilute solutions. However, because of the lack of hydrodynamic interaction in the model, this model cannot describe the behavior of dilute solutions. Nevertheless, this model was found to describe the viscoelastic behavior of *short*, linear chains in *concentrated* systems very well[1,2]; Prediction of this model is in close agreement with the zero-shear viscosity data ($\eta_0 \propto \zeta M$; Fig. 1-2) and the ω dependence of the G' and G'' data (Fig. 1-1) for low-M polymer chains.

In concentrated systems, long chains exhibit viscoelastic features quite different from those of short chains. For such high-M linear chains, η_0 increases in proportion to $M^{3.5}$ (Fig. 1-2) and G' exhibits a plateau region (having M-independent height) that extends to lower ω with increasing M (Fig. 1-1). This kind of strong M-dependence is attributed to a dynamic interaction between long chains referred as '*entanglement*'.[2,3] This entanglement effect originates from uncrossability of mutually interpenetrating long chains.

An attempt was made to modify the Rouse model to describe this entanglement behavior.[2,3] In order to explain the slow dynamics of long chains, a modified version of the Rouse model considered two types of beads: some of them have a friction coefficient proportional to $M^{1.5}$, and others have M-independent friction coefficient. This model can explain the η_0 data ($\propto M^{3.5}$) in high-M region. However, the viscoelastic relaxation mode distribution reflected in the ω dependence of G' and G'' cannot be described by the modified Rouse model.

Breakthrough of this situation was brought by de Gennes[7] who proposed a totally different molecular picture for the dynamics of entangled chains. For a linear chain trapped in a cross-linked network , he considered that the large scale of motion of the chain is limited in a direction of the chain backbone because the network disturbs the lateral chain motion over distances larger than network mesh size. The resulting curvilinear diffusion along the chain backbone is referred to as '*reptation*'.[7]

Doi and Edwards[8-11] extended this reptation picture to polymer melts/solutions and developed a model that enables consistent calculation of various dynamic properties of entangled linear chains. The chains in the entangled melts/solutions form a dynamical mesh to mutually constrain their large scale motion. For a given chain (probe) in this mesh, the Doi-Edwards (DE) model assumes that the large scale probe motion is constrained in a *tube-like* region surrounding the probe backbone and this constraint survives (i.e., the tube is fixed in space) in a time scale of the probe relaxation. For this motion at equilibrium, the DE model introduces a further approximation that the probe contour length measured along the tube axis does not fluctuate with time. For this case, reptation is the only possible large scale motion of the probe; this motion is described in terms of a few, well defined molecular parameters and all kinds of dynamic quantities corresponding to this motion, i.e., those in the linear response regime, are

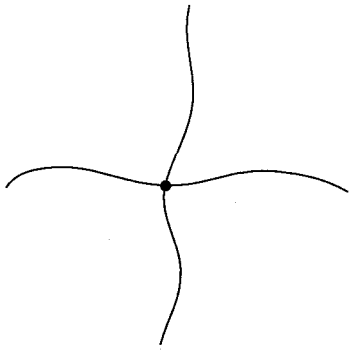

Fig. 1-3 Schematic illustration of star-branched chain.

readily calculated.

The tube concept was applied also to entangled star-branched polymers[12-14] (Fig. 1-3). In the bead-spring model for star chains (developed in a way similar to that for the Rouse model), the branching point for the star arms affects the degeneracy of the motional modes (eigenmodes) of the chain but raises no essential difference in the chain dynamics.[15] Thus the proportionality between η_0 and M is commonly predicted from the bead-spring models for the star[15] and linear[6] chains. In contrast, in the tube model for entangled star chains,[12-14] the branching point significantly changes the chain dynamics: The branching point is assumed to be fixed in space thereby prohibiting the reptation of the star-arms. Consequently, the model considers that the arm motion in the tube is associated with changes in its contour length (arm retraction). Since the arm retraction results in a decrease of conformational entropy, the predicted viscoelastic features of the star chains corresponding to this retraction are quite different from these of the reptating linear chains; for example, η_0 of the star is predicted to increase exponentially with the arm molecular weight M_a,[13,14] and this M_a dependence is much stronger than that for the linear chains. This prediction of the tube model is in qualitative agreement with experiments.[16]

The above, early versions of the tube models stimulated, either explicitly or implicitly, extensive experimental studies of various dynamic properties of entangled chains. Some properties such as the nonlinear damping function under large step strains[17-21] were found to be well described by tube model. For the star chains, the Pearson-Helfand (PH) model[14] considering the arm retraction in the fixed tube was found to quantitatively describe the linear viscoelastic moduli, G' and G''. However, nontrivial differences were also observed for a wide variety of properties: For example, the observed η_0 of linear chains is proportional to $M^{3.5\pm0.2}$ (cf. Fig.1-2) while the DE model[9] predicts $\eta_0 \propto M^3$. For blends of long and short linear chains of widely separated molecular weights, the DE model cannot explain the observed acceleration of the relaxation of the long chains with decreasing long chain content.[16,22-24] Furthermore, for the star chain, a parameter value in the PH model[14] giving the excellent description of the G' and G'' data was considerably different from the value intrinsically deduced from the model. (In other words, the excellent agreement with the data was obtained after an adjustment of this parameter.)

Considering these discrepancies between experiments and predictions of the early versions of the tube models, theoretical efforts have been made to generalize the tube model by incorporating extra mechanisms of large scale chain motion not considered in the earlier models. These mechanisms include the *contour length fluctuation* (CLF) of the chain trapped in the tube and the *tube motion* that allows large scale lateral motion of the chain therein.

The CLF concept[25-27] was naturally incorporated in the DE model that originally considered a flexible probe chain (Rouse chain) constrained in the tube. The latter concept of tube motion[27-31] was also naturally introduced for the chains in entangled melts/solutions because the chains entangling with a given probe chain can exhibit the motion equivalent to the probe motion; for example, if a linear probe chain in monodisperse systems reptates in its tube, the surrounding (tube-forming) chains equivalent to the probe should also reptate in their own tubes to induce, in principle, the motion of the tube for the probe.

The tube motion has two important effects on the probe dynamics. The tube motion allows large scale motion of the probe in a direction lateral to its backbone to induce the probe relaxation.[27-31] This type of probe relaxation is referred to as the *constraint release* (CR) relaxation. The tube motion also increases an effective tube diameter (effective entanglement mesh size) for the probe in a coarse-grained time scale, i.e., on an increase of an unit time of observation (below which the probe motion is averaged). This concept[32,33] is referred to as *dynamic tube dilation* (DTD). In particular, recent models[34-38] incorporate the DTD mechanism as an important mechanism for relaxation. These models describe the viscoelastic data of linear and star chains considerably well.

1-3. Scope of This Thesis

Despite the significant effort in the development of the recent, modified tube models considering the reptation, arm retraction, contour length fluctuation, constraint release (CR), and dynamic tube dilation (DTD) mechanisms, a fundamental problem still remains in the molecular description of the chain dynamics. These models have been tested for viscoelastic data, and good agreement with those data is obtained.

However, the viscoelastic relaxation detects only a limited aspect of the stochastic chain motion, i.e., decay of orientational anisotropy with time, and the success of the modified tube models does not guarantee that the chains actually move in a way considered in the models. Thus, the chain motion itself needs to be experimentally examined to critically test the models.

This experimental examination can be most efficiently conducted through comparison of different types of dynamic properties that differently average the stochastic chain motion. Following this strategy, this study focuses on dielectric and viscoelastic properties of *cis*-polyisoprene (PI). The PI chains have so-called type-A dipoles[39] parallel along the chain contour, and the global chain motion results in not only viscoelastic but also dielectric relaxation.[40-42] The viscoelastic relaxation reflects decay of orientational anisotropy due to the chain motion (the behavior summarized as the stress-optical rule[2,5]), while the dielectric relaxation detects decay of a memory of initial chain configuration.[42-45] Thus, the viscoelastic and dielectric properties

differently average the same stochastic chain motion, and comparison of these properties can reveal detailed features of the chain motion (that cannot be resolved from any single property).

This thesis presents results of the study on the basis of this idea.

The thesis is composed of nine chapters including this introductory chapter.

Chapter 2 summarizes methods of preparation and characterization of the samples, linear and star-branched *cis*-polyisoprene (PI) chains. The principle and methods of physical measurements are also explained in this chapter.

Chapter 3 explains molecular expressions of viscoelastic and dielectric properties of type-A chains. These expressions serve as a rigid basis for analyzing/discussing these properties.

Chapter 4 gives a summary of molecular models for entangled chains relevant to this study.[8,9,27,32,33,35] A summary is given also for models developed in this study. These models are utilized for discussing the viscoelastically and dielectrically detected chain dynamics.

Chapter 5 investigates dielectric behavior for a series of linear PI chains in three different environments having different constraint release (CR) contribution to the chain dynamics. These PI chains have almost identical molecular weight but differently once-inverted type-A dipoles.[43-45] Thus, the global motion is the same but the dielectric response is different (due to the difference of the inversion point) for the series of PI chains. This dielectric difference is utilize to experimentally determine eigenfunctions for the chain motion in the three environment. These eigenfunctions and the associating relaxation times are compared with those of molecular models and discussed in relation to the CR contribution from the three environments.

Chapter 6 utilizes the eigenfunctions and relaxation times f_p and τ_p determined in Chapter 5 to examine detailed features of the chain dynamics. Specifically, viscoelastic moduli are calculated from f_p and τ_p for two specific cases, one case for perfectly correlated (coherent) motion of different submolecules in the chain and the other case for uncorrelated (incoherent) submolecule motion. From comparison of these calculated moduli and the viscoelastic data, the degree of coherence in the submolecular motion is experimentally specified. Furthermore, effects of the CR mechanism on this coherence of submolecule motion is discussed in relation to the molecular models explained in Chapter 4.

Chapter 7 is devoted for an experimental test of the dynamic tube dilation (DTD) mechanism for linear chains. Specifically, a DTD relationship between viscoelastic and dielectric relaxation functions (Φ and μ) of linear type-A chains, derived in Chapter 4, is tested for linear PI chains (without dipole inversion) in monodisperse systems and blends. The results are utilized to discuss the criteria for the validity of the DTD mechanism.

Chapter 8 examines the DTD mechanism for star branched PI chains. For this purpose, a DTD relationship between Φ and μ of these chains, formulated in Chapter 4, is tested experimentally. In addition, the viscoelastic and dielectric data of the star chains are compared with the predictions of recent tube models and the limitation of these models is specified. The results are discussed in relation to the DTD criteria, with an emphasis being placed on the similarity/difference between the star and linear chains.

Finally, Chapter 9 presents a summary of this thesis.

References

1. H. Yamakawa, *Modern Theory of Polymer Solutions*, Harper & Row, New York (1971).
2. J. D. Ferry, *Viscoelastic Properties of Polymers (3rd ed)*, Wiley, New York (1980).
3. W. W. Graessley, *Adv. Polym. Sci.* **16**, 1 (1974).
4. S. Onogi, T. Masuda, and K. Kitagawa, *Macromolecules* **3**,109 (1970).
5. H. Janeschitz-Kriegl, *Polymer Melt Rheology and Flow Birefringence*, Springer, Berlin (1983).
6. P. E. Rouse, *J. Chem. Phys.* **21**,1272 (1953).
7. P. G. de Gennes, *J. Chem. Phys.*, **55**, 572 (1971).
8. M. Doi and S. F. Edwards, *J. Chem. Soc. Faraday Trans. 2* **74**,1789 (1978).
9. M. Doi and S. F. Edwards, *J. Chem. Soc. Faraday Trans. 2* **74**,1802 (1978).
10. M. Doi and S. F. Edwards, *J. Chem. Soc. Faraday Trans. 2* **74**,1818 (1978).
11. M. Doi and S. F. Edwards, *J. Chem. Soc. Faraday Trans. 2* **75**, 38 (1979).
12. P. G. de Gennes, *J. Phys. (Paris)* **36**, 1199 (1975).
13. M. Doi and N. Kuzuu, *J. Polym. Sci. Polym. Lett. Ed* **18**,775 (1980).
14. D. S. Pearson and E. Helfand, *Macromolecules* **17**, 888 (1984).
15. J. S. Ham, *J. Chem. Phys.* **26**, 625 (1957).
16. H. Watanabe, *Prog. Polym. Sci.,* **24**, 1253 (1999).
17. K. Osaki, S. Kimura, and M. Kurata, *J. Polym. Sci., Polym. Phys. Ed.* **19**, 517 (1981).
18. K. Osaki, S. Kimura, M. Kimura, and M. Kurata, *J. Rheol.* **25**, 549 (1981).
19. K. Osaki, S. Kimura, K. Nishizawa, and M. Kurata, *Macromolecules* **14**, 455 (1981).
20. K. Osaki, K. Nishizawa, and M. Kurata, *Macromolecules* **15**, 1068 (1982).
21. K. Osaki, E. Takatori, M. Kurata, H. Watanabe, H. Yoshida, and T. Kotaka, *Macromolecules* **23**, 4392 (1990).
22. H. Watanabe, T. Sakamoto, and T. Kotaka, *Macromolecules* **18**,1008 (1985).
23. H. Watanabe, T. Sakamoto, and T. Kotaka, *Macromolecules* **18**,1436 (1985).
24. H. Watanabe and T. Kotaka, *Macromolecules* **19**, 2520 (1986).
25. M. Doi, *J. Polym. Sci., Polym. Lett. Ed.* **19**, 265 (1981).
26. M. Doi, *J. Polym. Sci., Polym. Phys. Ed.* **21**, 667 (1983).
27. W. W. Graessley, *Adv. Polym. Sci.* **47**, 68 (1982).
28. J. Klein, *Macromolecules* **11**, 852 (1978).
29. M. Daoud and P. G. de Gennes, *J. Polym. Sci., Polym. Phys. Ed.* **17**,1971 (1979).
30. J. Klein, *Macromolecules* **19**,105 (1986).
31. M. Rubinstein and R. H. Colby, *J. Chem. Phys.,* **89**, 5291 (1988).
32. G. Marrucci, *J. Polym. Sci., Polym. Phys. Ed.* **23**,159 (1985).
33. R. C. Ball and T. C. B. McLeish, *Macromolecules* **22**,1911 (1989).
34. S. T. Milner, *J. Rheol.* **40**, 303 (1996).
35. S. T. Milner and T. C. B. McLeish, *Phys. Rev. Lett.* **81**, 725 (1998).
36. S. T. Milner and T. C. B. McLeish, *Macromolecules* **30**, 2159 (1997).

37. S. T. Milner and T. C. B. McLeish, *Macromolecules* **31**, 7479 (1998).
38. S. T. Milner, T. C. B. McLeish, R. N. Young, A. Hakiki, and J. M. Johnson, *Macromolecules* **31**, 9345 (1998).
39. W. H. Stockmayer, *Pure Appl. Chem.* **15**, 539 (1967).
40. K. Adachi and T. Kotaka, *Macromolecules* **17**, 120 (1984).
41. K. Adachi and T. Kotaka, *Prog. Polym. Sci.* **18**, 585 (1993).
42. H. Watanabe, *Macromol. Rapid Commun.*, **22**, 127 (2001).
43. H. Watanabe, O. Urakawa, and T. Kotaka, *Macromolecules* **26**, 5073 (1993).
44. H. Watanabe, O. Urakawa, and T. Kotaka, *Macromolecules* **27**, 3525 (1994).
45. H. Watanabe, M.-L. Yao, and K. Osaki, *Macromolecules* **29**, 97 (1996).

CHAPTER 2
Materials and Measurements

2-1. Introduction

In this thesis, all polymeric samples were synthesized via anionic polymerization and characterized with gel permeation chromatography (GPC). These samples were subject to rheological and dielectric measurements. This chapter explains the methods of the sample preparation / characterization as well as the methods and principle of the measurements.

2-2. Preparation and Characterization of Samples

2-2-1. Preparation

Linear polyisoprene (PI) and polybutadiene (PB) chains and star-branched PI chains were synthesized via anionic polymerization. The PI and PB chains were polymerized at room temperature in heptane and benzene, respectively, and *sec*-butyllithium was utilized as the initiator for both cases. The PI and PB chains obtained under these conditions have the microstructures, *cis*: *trans*: *vinyl* ≅ 75: 25: 5 (for PI) and 40: 50:10 (for PB).[1-3] The PI sample with this microstructure have the type-A dipoles parallel to the chain backbone.

In addition to these PI and PB samples prepared in this study, some PI and PB samples synthesized previously (under similar conditions)[3-5] were also utilized. These previous samples were sealed in Ar atmosphere and stored in a deep freezer (under presence of antioxidant, butyl hydroxytoluene (BHT)) until use in this study. For these samples, GPC measurements confirmed lack of degradation.

The anionic synthesis in this study was conducted with high vacuum technique[1,2] utilizing glass flasks and breakable seals. The linear PI and PB chains were obtained via a standard polymerization/termination (with methanol) procedure[1,2] under conditions explained above. The star PI chains were obtained by the anionic coupling method[1,2] described below.

A series of star PI samples having the same arm molecular weight M_a (= 35.5×10^3) but different arm numbers q (= 4, 6, 9, and 15) were synthesized from the same batch of living arm anions. After completion of polymerization of linear PI anions (arm anions), an aliquot, terminated with methanol, was recovered for characterization of the arm. The remaining arm anions were divided into three reaction flasks (in vacuum) to separately synthesize the star PI samples with q = 4, 6, 9, and 15. The 4- and 6-arm star chains were prepared *via* coupling of the arm anions with tetra- and hexa-functional couplers, bis(dichlorosilyl)ethane and bis(trichlorosilyl)ethane, respectively. The coupler concentration was adjusted to be ~90% equimolar of the arm anions in the reaction vessel to ensure full coupling (no contamination of insufficiently coupled star chains). The coupling reaction at 40°C was completed in a week. After this reaction, the crude product was repeatedly fractionated from benzene/methanol mixed solvent to remove the excess (unreacted) arm anions and recover the monodisperse, 4- and 6-arm

star samples.

The star samples with the arm numbers q = 9 and 15 were prepared via end-modification of the living arm anions with an equimolar of divinyl benzene (dianionic end-crosslinker) and successive coupling with bis(trichloromethyl silyl)ethane (~90% equimolar to the anions). The crude product had bimodal molecular weight distribution (detected by GPC) with rather sharp peaks corresponding to the stars with q = 9 and 15. This product was thoroughly fractionated from benzene/methanol mixtures to recover these star samples. GPC traces of these star samples are shown later in Fig. 2-1.

A series of 6-arm star PI samples having various M_a were also synthesized via coupling with bis(trichlorosilyl)ethane. The synthetic procedure was similar to that utilized for the first series of star PI (except that the anion-dividing step was omitted).

2-2-2. Characterization

The PI and PB samples synthesized in this study (including the linear precursor PI (arm) for the star PI samples) were characterized with GPC (CO-8020 and DP-8020, Tosoh) combined with a low-angle laser-light scattering (LALS) photometer (LS-8000, Tosoh). The eluent was THF, and the monodisperse linear PI and PB samples synthesized in previous studies[3-5] were utilized as the elution standards.

The molecular weights of the linear samples were determined from the elution calibration for the refractive index (RI) increment signal. In contrast, the molecular weights of the star PI samples were determined from the RI and LALS signal intensities A_{RI} and A_{LALS} (obtained for dilute solutions):[6] $M_w = K A_{LALS}/A_{RI}$ with K being the instrumental constant determined for standard PI samples.

As an example of the GPC results, Fig. 2-1 shows RI and LALS signals for the first series of star samples having the same M_a but different q (= 4, 6, 9, and 15). For comparison, the signals are shown also for their precursor (arm). For all samples, the signals are shown with the same sensitivity so that the sample molecular weights ($\propto A_{LALS}/A_{RI}$) can be easily compared. The elution volume decreases and the LALS signal increases on an increase of the arm number q, as well known for the star chains.[1,2,7,8] (Note also that the fractionation was successfully conducted to obtain the stars with very small polydispersity.)

Characteristics of all the samples utilized in this study (including the previously synthesized samples) are summarized in Tables 2.1.-2.4.

2-3. Viscoelastic Measurements

2-3-1. Principle

When a material is subjected to a step shear strain γ at a time t = 0, the shear stress $\sigma(t)$ arises at t = 0 and decays with time. In the linear response regime for $\gamma << 1$, this $\sigma(t)$ is written as[9]

$$\sigma(t) = G(t)\gamma \qquad (2.1)$$

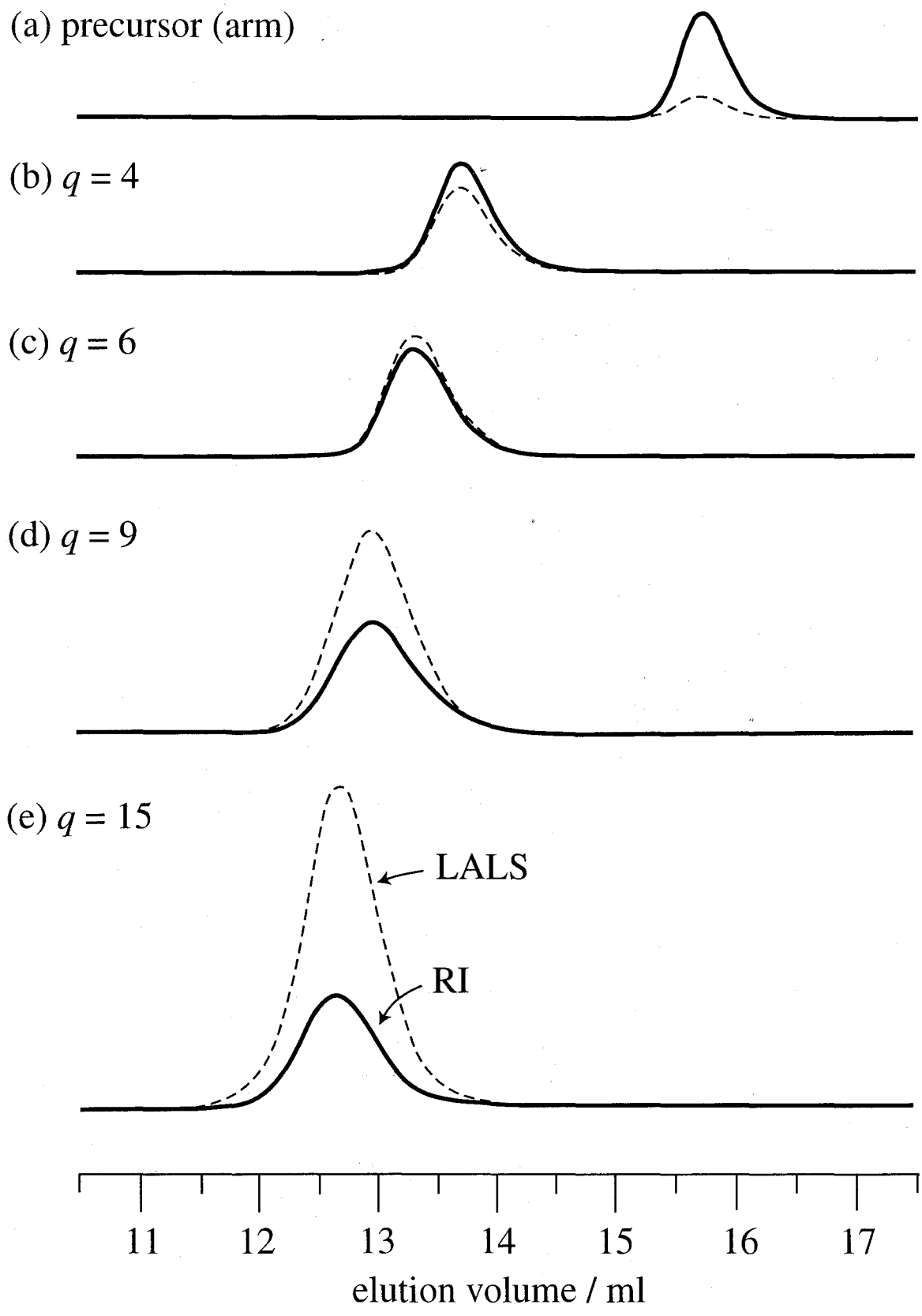

Fig. 2-1 GPC traces of star PI chains with various arm numbers q and their precursor.
(a) linear precursor (arm) with molecular weight $M_w = 35.5\times10^3$ (b) star chain with q=4 (c) star chain with q=6 (d) star chain with q=9 (e) star chain with q=15. The thick solid and thin dashed curves indicate the RI and LALS signals, respectively. For all samples, the signals are shown with the same sensitivity so that their molecular weights ($\propto A_{LALS}/A_{RI}$) can be easily compared.

Table 2.1. Characteristics of Linear PI and PB Samples Used in Chapters 5 and 6

code	$10^{-3}M_w$	M_w/M_n	n^*/N^a
Series of Dipole-Inverted Polyisoprenes[b]			
I-I 49-0[c]	48.8	1.05	0
I-I 50-6	55.4	1.06	0.109
I-I 35-9	44.4	1.05	0.213
I-I 35-14	47.6	1.07	0.283
I-I 28-18	47.4	1.06	0.396
I-I 24-24[d]	47.7	1.06	0.5
Regular Polyisoprenes (without dipole inversion)			
I14	13.7[e]	1.05[e]	
I19	19.0[e]	1.05[e]	
Polybutadienes			
B263	263[e]	1.05[e]	
B9[b]	9.24	1.07	

[a] Normalized location of the dipole inversion point.

[b] Synthesized/characterized in previous studies[3,4] and stored under Ar in a deep freezer until use in this study.

[c] I-I 49-0, without dipole inversion, is included in this series as an extreme case of the inversion at the chain end.

[d] With symmetrically inverted dipoles.

[e] Determined from elution calibration of GPC. (LALS-GPC analysis gave M_w/M_n values smaller than those shown here.)

Table 2.2. Characteristics of Linear PI Samples Used in Chapter 7

$10^{-3}M_w$	M_w/M_n	N^a
9.49[b]	1.07	1.9
20.7[b]	1.05	4.1
48.8[b]	1.05	9.8
94.0[c]	1.05[c]	19
180[c]	1.06[c]	36
308[c]	1.08[c]	62

[a] Number of entanglements per chain, $N=M_w/M_e$ (M_e: entanglement spacing of PI;M_e = 5000 in monodisperse bulk state).

[b] Synthesized in previous study[3] and stored under Ar in a deep freezer until use in this study.

[c] Determined from elution calibration of GPC. (LALS-GPC analysis gave M_w/M_n values smaller than those shown here.)

Table 2.3. Characteristics of 6-arm Star PI Samples Used in Chapter 8

$10^{-3}M_w$[a]	$10^{-3}M_a$[b]	N_a[c]	M_w/M_n[d]
54.2[e]	9.49	1.9	1.05
117[e]	20.7	4.1	1.06
182	30.6	6.1	1.04
249	40.7	8.1	1.03
354	59.0	12	1.05
459	80.1	16	1.06

[a] Determined from LALS combined with GPC.

[b] arm molecular weight determined from elution calibration of GPC.

[c] Number of entanglements per arm, $N_a=M_a/M_e$ (M_e: entanglement spacing of PI; M_e = 5000 in monodisperse bulk state).

[d] Determined from elution calibration of GPC. (LALS-GPC analysis gave M_w/M_n values smaller than those shown here.)

[e] Synthesized and characterized in previous study[5] and stored under Ar in a deep freezer until use in this study.

Table 2.4. Characteristics of Star PI Samples with Different Arm Number q Used in Chapter 8[a]

q[b]	$10^{-3}M_w$[c]	M_w/M_n[d]
4	145	1.02
6	208	1.02
9	313	1.03
15	524	1.05

[a] All samples were prepared from the same batch of living arm anion and had the same M_a (=35.5 × 10^3).

[b] The number of arms q was evaluated as M_w/M_a. The rounded q values shown here are very close to the M_w/M_a ratios of respective star PI.

[c] Determined from LALS combined with GPC.

[d] Determined from elution calibration of GPC. (LALS-GPC analysis gave M_w/M_n values smaller than those shown here.)

Here, $G(t)$ is the shear relaxation modulus that specifies *all* linear viscoelastic features of the material. For example, the zero-shear viscosity (defined under slow steady shear) is given by an integral of $G(t)$ with respect to t (= 0 - ∞).

In the linear regime, Boltzmann's superposition principle[9] is valid. Thus, for a shear strain of arbitrary history $\gamma(t)$, the shear stress $\sigma(t)$ is given by[9]

$$\sigma(t) = \int_{-\infty}^{t} G(t-t') \frac{d\gamma(t')}{dt'} dt' \qquad (2.2)$$

On the basis of this superposition, linear viscoelastic measurements are typically conducted under sinusoidal shear strain that oscillates with time at an angular frequency ω and amplitude γ_0 (<< 1),

$$\gamma(t) = \gamma_0 \sin \omega t \qquad (2.3)$$

As noted from eq 2.2, the resulting stress $\sigma(t)$ in a stationary state oscillates at the same ω but with a phase difference from $\gamma(t)$. This $\sigma(t)$ is conveniently expressed as[9]

$$\sigma(t) = \gamma_0 [G'(\omega)\sin \omega t + G''(\omega)\cos \omega t] \qquad (2.4)$$

The storage and loss moduli, G' and G'', characterize the elastic and viscous components of the stress that are in-phase and out-phase with respect to the sinusoidal strain. These moduli are related to the relaxation modulus $G(t)$ through Fourier transformation,

$$G'(\omega) = \omega \int_0^{\infty} G(t) \sin \omega t \, dt, \quad G''(\omega) = \omega \int_0^{\infty} G(t) \cos \omega t \, dt \qquad (2.5)$$

Thus, G' and G'' are equivalent to $G(t)$ and specify all linear viscoelastic features. These G' and G'' are frequently expressed as a complex modulus, $G^* = G' + iG''$ with $i = \sqrt{-1}$.

2-3-2. Viscoelastic mode distribution and relaxation time.

For flexible polymers such as polyisoprene examined in this thesis, $G(t)$ reflects the orientational relaxation (as explained in details in Chapter 3). These chains have a huge freedom in their conformation and thus exhibit a distribution of the orientational relaxation modes.[10] This distribution leads to a viscoelastic mode distribution of $G(t)$ that is conveniently represented as[9,10]

$$G(t) = \sum_p h_p \exp[-t/\tau_{Gp}] = \int_{-\infty}^{\infty} H(\tau) \exp[-t/\tau] \, d\ln \tau \qquad (2.6)$$

Here, h_p and $\tau_{G,p}$ are the intensity and characteristic time for the p-th viscoelastic mode. (The first subscript "G" for τ indicates that $\tau_{G,p}$ is the viscoelastic time.) The relaxation modes are numbered with a decreasing order of their characteristic times ($\tau_{G,1} > \tau_{G,2} > \tau_{G,3}$ ...). The quantity H(τ) in eq. 2.6, referred to as the viscoelastic relaxation spectrum,[9] gives an continuous expression of the mode intensity distribution. In all viscoelastic expressions explained below, H(τ) can be used instead of h_p after the replacement $\tau_{G,p} \to \tau$ and $\sum_p \to \int_{-\infty}^{\infty} .. \, d\ln \tau$.

Corresponding to the above feature of $G(t)$, the storage and loss moduli $G'(\omega)$ and $G''(\omega)$ also exhibit the mode distribution. This distribution is expressed in terms of g_p and $\tau_{G,p}$ (cf. eqs 2.5 and 2.6),

$$G'(\omega) = \omega^2 \sum_p h_p \frac{[\tau_{G,p}]^2}{1 + \omega^2 [\tau_{G,p}]^2}, \quad G''(\omega) = \omega \sum_p h_p \frac{\tau_{G,p}}{1 + \omega^2 [\tau_{G,p}]^2} \tag{2.7}$$

Since the mode intensity h_p is magnified by $[\tau_{G,p}]^2$ for G' and by $\tau_{G,p}$ for G'', weak but slow modes (having large $\tau_{G,p}$) are more sensitively reflected in G' than in G'', while intensive and fast modes are more clearly detected in G''.

As noted from eq 2.7, G' and G'' exhibit the terminal behavior, $G' \propto \omega^2$ and $G'' \propto \omega$ at ω well below $[\tau_{G,1}]^{-1}$. The zero-shear viscosity η_0 (= $[G''/\omega]_{\omega \to 0}$) and the steady state compliance J_e (=$[G'/(G'')^2]_{\omega \to 0}$), characterizing this terminal behavior, are expressed in terms of h_p and $\tau_{G,p}$,

$$\eta_0 = \sum_p \tau_{G,p} h_p, \quad J_e = \frac{\sum_p [\tau_{G,p}]^2 h_p}{\left[\sum_p \tau_{G,p} h_p\right]^2} \tag{2.8}$$

As noted from this expression, J_e is very sensitive to slow relaxation modes.

From eq 2.8, two types of average relaxation times are defined:[10,11]

$$\langle \tau_G \rangle_w \equiv J_e \eta_0 = \frac{\sum_p [\tau_{G,p}]^2 h_p}{\sum_p \tau_{G,p} h_p}, \quad \langle \tau_G \rangle_n \equiv \eta_0 / G_N = \frac{\sum_p \tau_{G,p} h_p}{\sum_p h_p} \tag{2.9}$$

Here, G_N (= $G'(\infty)$) is the high-ω plateau modulus; for entangled polymers, the rubbery plateau modulus[9] is used as G_N. The second-moment relaxation time $\langle \tau_G \rangle_w$ is an average of $\tau_{G,p}$ with a weighing factor $\tau_{G,p} h_p$. This factor enhances the contribution of slow modes to $\langle \tau_G \rangle_w$ and thus $\langle \tau_G \rangle_w$ is usually close to the longest relaxation time $\tau_{G,1}$. On the other hand, the first-moment

relaxation time $<\tau_G>_n$ has the weighing factor h_p and is shorter than $<\tau_G>_w$. A product of J_e and G_N, that coincides with a $<\tau_G>_w/<\tau_G>_n$ ratio, gives a measure of a width of the relaxation mode distribution,

$$J_e G_N = \frac{\left[\sum_p h_p\right]\left[\sum_p [\tau_{G,p}]^2 h_p\right]}{\left[\sum_p \tau_{G,p} h_p\right]^2} \tag{2.10}$$

(The product $J_e G_N$ increases as the mode distribution broadens.)

2-3-3. Method

Linear viscoelastic measurements were conducted with strain-controlled laboratory rheometers, RMS605 and ARES (both from Rheometrics), in a coaxial parallel-plate geometry with the plate diameter of 2.5 cm. In the measurements, one of the plates was sinusoidally displaced around the axis to impose the strain to the material sandwiched between the plates. The strain amplitude was kept small (< 0.1) so as to ensure the linearity of the viscoelastic response. The stress of the material was detected by a transducer attached to the other plate and converted into the storage and loss moduli according to eq 2.4. (This conversion was made with the rheometer program.)

2-4 Dielectric Measurements

2-4-1. Principle

On application of a constant electric field E to a dielectric material (placed in a dielectric cell), an electrical displacement evolves with time. In the linear response regime, the electrical displacement density D (= displacement normalized per unit area of the electrode) is written as[12)]

$$D(t) = [\varepsilon_0 - \Delta\varepsilon\Phi(t)]E\varepsilon_{vac} \quad \text{with } \Delta\varepsilon = \varepsilon_0 - \varepsilon_\infty \tag{2.11}$$

Here, $\Phi(t)$ is the normalized dielectric relaxation function[12,13)] ($\Phi(0) = 1$ and $\Phi(\infty) = 0$), ε_0 is the static dielectric constant, ε_∞ is the unrelaxed (high frequency) dielectric constant, $\Delta\varepsilon$ is the dielectric relaxation intensity, and ε_{vac} is the dielectric constant of vacuum. (ε_0, ε_∞, and $\Delta\varepsilon$ are defined as the quantities relative to vacuum.) Normalized dielectric features of the material are represented by $\Phi(t)$.

In the linear response regime, Boltzmann's superposition principle is valid. Then, $D(t)$ for a field of arbitrary history $E(t)$ is written as

$$D(t) = \varepsilon_{vac}\left(\varepsilon_0 E(t) - \Delta\varepsilon\int_{-\infty}^{t} \Phi(t-t')\frac{dE(t')}{dt'}\,dt'\right) \tag{2.12}$$

On the basis of this superposition, the dielectric measurements are frequently carried out by subjecting the material to a sinusoidal electric field,

$$E(t) = E_0 \sin \omega t \tag{2.13}$$

The resulting electrical displacement density in the stationary state is given by (cf. eq 2.12)

$$D(t) = \varepsilon_{vac} E_0 [\varepsilon'(\omega)\sin \omega t - \varepsilon''(\omega)\cos \omega t] \tag{2.14}$$

The (relative) dynamic dielectric constant $\varepsilon'(\omega)$ and dielectric loss $\varepsilon''(\omega)$ appearing in eq 2.14 specify the storage and loss of electrostatic energy. As noted from eq 2.12 (after integration by parts), ε' and ε'' are given by the Fourier transformation of the dielectric relaxation function $\Phi(t)$,[12,13]

$$\varepsilon'(\omega) = \varepsilon_\infty - \Delta\varepsilon \int_0^\infty \frac{d\Phi(t)}{dt} \cos \omega t \, dt, \quad \varepsilon''(\omega) = -\Delta\varepsilon \int_0^\infty \frac{d\Phi(t)}{dt} \sin \omega t \, dt \tag{2.15}$$

Thus, ε' and ε'' are equivalent to $\Phi(t)$ and specify all dielectric features.

2-4-2. Dielectric mode distribution and relaxation time

For the type-A polyisoprene chains examined in this study, $\Phi(t)$ reflects the decay of orientational correlation (as explained in details in Chapter 3). Because of the flexibility of these chains, $\Phi(t)$ exhibits the dielectric mode distribution. As similar to the treatment for the viscoelastic $G(t)$, the mode distribution of $\Phi(t)$ is conveniently expressed as[13]

$$\Phi(t) = \sum_p g_p \exp[-t/\tau_{\varepsilon,p}] \quad \text{with } \Phi(0) = \sum_p g_p = 1 \tag{2.16}$$

where g_p and $\tau_{\varepsilon,p}$ ($\tau_{\varepsilon,1} > \tau_{\varepsilon,2} > \tau_{\varepsilon,3}$ ...) are the normalized intensity and characteristic time for the p-th dielectric mode. The subscript "ε" is added to the dielectric $\tau_{\varepsilon,p}$ to avoid confusion with the viscoelastic $\tau_{G,p}$ defined in eq 2.6.

From eqs 2.15 and 2.16, $\varepsilon'(\omega)$ and $\varepsilon''(\omega)$ are expressed in terms of g_p and $\tau_{\varepsilon,p}$,

$$\frac{\varepsilon_0 - \varepsilon'(\omega)}{\Delta\varepsilon} = \omega^2 \sum_p g_p \frac{\tau_{\varepsilon,p}^2}{1+\omega^2 \tau_{\varepsilon,p}^2}, \quad \frac{\varepsilon''(\omega)}{\Delta\varepsilon} = \omega \sum_p g_p \frac{\tau_{\varepsilon,p}}{1+\omega^2 \tau_{\varepsilon,p}^2} \tag{2.17}$$

As noted from this expression, the dielectric terminal behavior specified by the power-law dependencies, $\varepsilon_0 - \varepsilon' \propto \omega^2$ and $\varepsilon'' \propto \omega$, is observed at ω well below $[\tau_{\varepsilon,1}]^{-1}$.

Since the above expression for $\varepsilon_0 - \varepsilon'$ and ε'' are formally identical to that for G' and G'' (eq. 2.7), some quantities characterizing the terminal dielectric relaxation can be defined in a

way similar to that for the viscoelastic relaxation. For example, two types of average relaxation times (analogous to $<\tau_G>_w$ and $<\tau_G>_n$ given by eq 2.9) are defined as[13]

$$<\tau_\varepsilon>_w \equiv \frac{\left[\{\varepsilon_0 - \varepsilon'(\omega)\}/\omega^2\right]_{\omega\to 0}}{\left[\varepsilon''(\omega)/\omega\right]_{\omega\to 0}} = \frac{\sum_p \tau_{\varepsilon,p}^2 g_p}{\sum_p \tau_{\varepsilon,p} g_p} \tag{2.18}$$

and

$$<\tau_\varepsilon>_n \equiv \frac{\left[\varepsilon''(\omega)/\omega\right]_{\omega\to 0}}{\Delta\varepsilon} = \frac{\sum_p \tau_{\varepsilon,p} g_p}{\sum_p g_p} \tag{2.19}$$

The $<\tau_\varepsilon>_w/<\tau_\varepsilon>_n$ ratio quantifies the dielectric mode distribution; this ratio increases as the mode distribution broadens. ($<\tau_\varepsilon>_w/<\tau_\varepsilon>_n = 1$ for the single relaxation process.)

As noted from eqs 2.7 and 2.17, the dielectric and viscoelastic relaxation processes are described within a formally identical phenomenological framework. However, from a molecular point of view, an important difference exists between these processes. The viscoelastic relaxation corresponds to the decay of orientational anisotropy while the dielectric relaxation detects decay of the orientational correlation, as explained in Chapter 3. Thus, the two relaxation processes reflect the same dynamic process (thermal motion of the chain) in different ways.

2-4-3. Method

Dielectric measurements were conducted with the transformer bridge (TB) method at rather short times (high frequencies) where the direct current (dc) conductance due to ionic impurities was negligible compared to a relaxational current due to the chain motion. The adsorption current (AdC) method was utilized at long times where this dc conductance was not negligible.

TB method: In the TB method, the material charged in a guarded parallel plate cell (with a vacant capacity $C_0 = 120$ pF) was subjected to an oscillating electric field (of amplitude $E_0 < 10$ V/mm) at various angular frequencies $\omega/s^{-1} = 6 \times 10^2$ - 1×10^6. The resulting sinusoidal current was compensated with a transformer bridge (1620A, QuadTech) by tuning the capacitance C and conductance G of this bridge. The dynamic dielectric constant ε' and dielectric loss ε'' of the material were obtained from these C and G values as

$$\varepsilon'(\omega) = C(\omega)/C_0, \quad \varepsilon''(\omega) = G(\omega)/C_0\omega \tag{2.20}$$

AdC method: In the AdC method, the material charged in the same dielectric cell was subjected

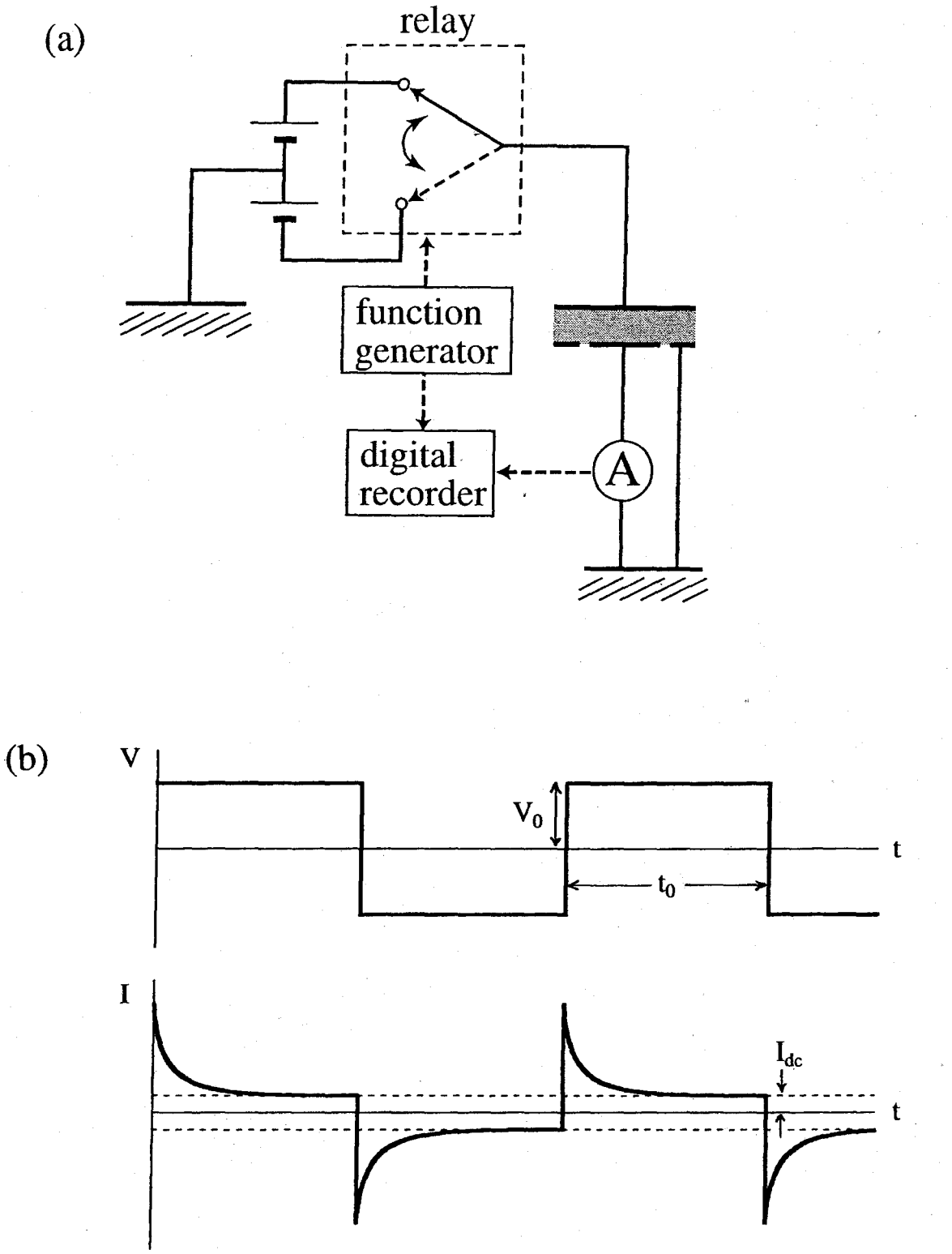

Fig. 2-2 Schematic explanation of the adsorption current method. (a) block diagram of the circuit. (b) Applied voltage (V) and resulting current (I).

to an oscillatory rectangular voltage $V(t)$ (of amplitude V_0 = 18 and/or 27 V) with a homemade circuit schematically shown in Fig. 2-2a. The polarity of the voltage was periodically switched with a function generator (WF1944, NF Corporation), and the resulting current $I(t)$ was measured with an electrometer (TR8411, Advantest) and stored in a digital recorder (DL708G, Yokogawa).

The stationary changes of $V(t)$ and $I(t)$ with time t are schematically shown in Fig. 2-2b. This $V(t)$, composed of Fourier components, is written as

$$V(t) = V_0 \sum_{p=\text{odd}} \frac{4}{p\pi} \sin \omega_p t \quad \text{with} \quad \omega_p = \frac{p\pi}{t_0} \tag{2.21}$$

where ω_p is a frequency of the p-th Fourier component determined by the half-period t_0 of $V(t)$. The corresponding current, $I(t) = A\{dD(t)/dt\}$ (A = the electrode area) is contributed from the current $I_{\text{relax}}(t)$ due to the dielectric relaxation (reflecting the chain motion in the material) and the dc current $I_{\text{dc}}(t)$ due to ionic impurities,

$$I(t) = I_{\text{dc}}(t) + I_{\text{relax}}(t) \quad \text{with} \quad I_{\text{dc}}(t) = AG_{\text{ion}}V(t) \tag{2.22}$$

Here, G_{ion} is the dc conductance of the impurities.

As noted from eq 2.12, the relaxation current $I_{\text{relax}}(t)$ is related to the dielectric relaxation function $\Phi(t)$ as

$$I_{\text{relax}}(t) = \frac{A}{L}\varepsilon_{\text{vac}}\left(\{\varepsilon_0 - \Delta\varepsilon\}\frac{dV(t)}{dt} - \Delta\varepsilon\int_{-\infty}^{t} \frac{\partial\Phi(t-t')}{\partial t}\frac{dV(t')}{dt'}\,dt'\right)$$

$$= \frac{4V_0C_0}{t_0}\left(\varepsilon_\infty \sum_{p=\text{odd}} \cos \omega_p t - \Delta\varepsilon\int_0^\infty \frac{d\Phi(t'')}{dt''} \sum_{p=\text{odd}} \cos \omega_p(t-t'')\,dt''\right) \tag{2.23}$$

Here, L is the gap between the electrodes (= sample thickness) utilized for converting V into the (macroscopically defined) electric field $E = V/L$, and the vacant capacity of the cell C_0 is given by $C_0 = A\varepsilon_{\text{vac}}/L$. As noted from eqs 2.15 and 2.23, ε' and ε'' are obtained by integration of $I_{\text{relax}}(t) = I(t) - I_{\text{dc}}(t)$,

$$\varepsilon'(\omega_p) = \frac{1}{2V_0C_0}\int_0^{t_0} I_{\text{relax}}(t) \cos \omega_p t\,dt \tag{2.24}$$

$$\varepsilon''(\omega_p) = \frac{1}{2V_0C_0}\int_0^{t_0} I_{\text{relax}}(t) \sin \omega_p t\,dt \tag{2.25}$$

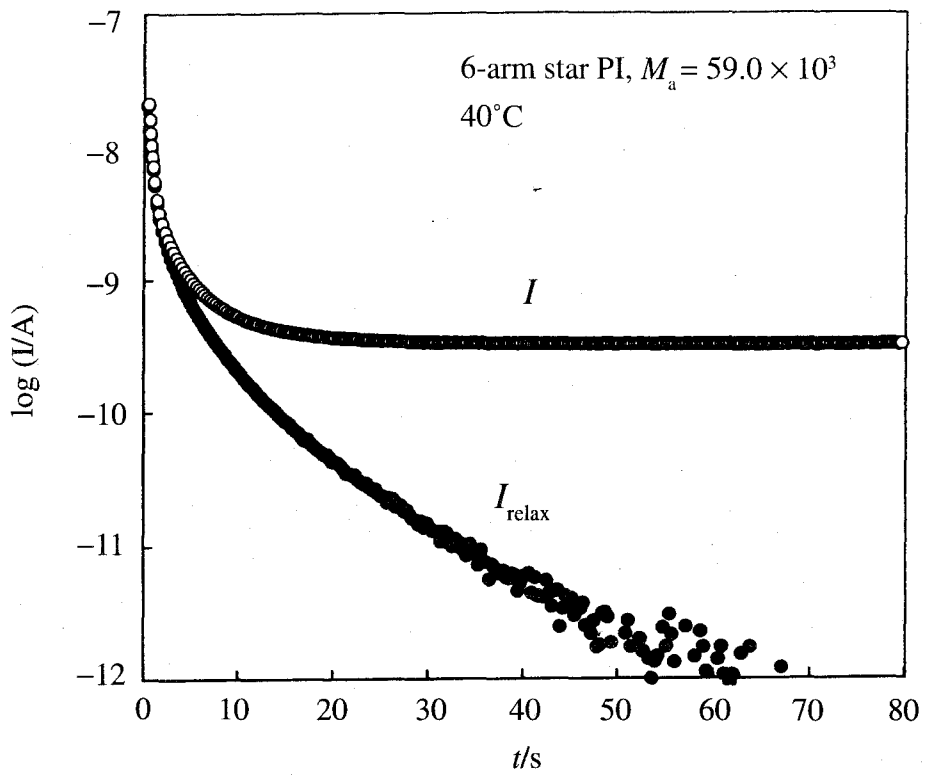

Fig. 2-3 Adsorption current (unfilled circles) measured for a 6-arm star PI with M_a=59.0 × 10^3 at 40°C. Filled circles indicate the relaxation current $I_{relax}(t)$ obtained by subtracting dc contribution from $I(t)$.

In actual measurements, the $I(t)$ signal was averaged over 32 periods to reduce the electrical noise. The half-period t_0 was chosen to be 6 - 10 times longer than the terminal viscoelastic relaxation time $<\tau_G>_w$ (eq 2.9) so that the chain relaxation in the material was completed within the time t_0. With this choice, the I_{dc} was clearly observed and accurately evaluated as a flat (time-independent) part of $I(t)$ at long time side in each period. An example of such $I(t)$, measured for a 6-arm star PI sample at 40°C, is shown in Fig. 2-3 (unfilled circles). The $I_{relax}(t)$ obtained by subtracting this I_{dc} from $I(t)$ was integrated according to eqs 2.24 and 2.25 to obtain ε' and ε''.

This integration was limited to $t > 0.1$ s where the response of the circuit (Fig. 2-2a) accurately followed the dielectric change in the material. (For $t < 0.1$, a delay in the circuit itself was not negligible). Consequently, the ε' obtained by this integration did not include the instantaneous response (characterized by ε_∞) and thus corresponded to $\varepsilon' - \varepsilon_\infty$. Since the dielectric loss is not contributed from the instantaneous response, the limitation of the integration range (to $t >$ 0.1 s) did not introduce any significant uncertainty in the ε'' obtained with eq 2.25.

With the above choice of t_0 ($\cong 6<\tau_G>_w$ - $10<\tau_G>_w$), the $I_{relax}(t)$ practically coincides with $2\Delta\varepsilon V_0 C_0\{-d\Phi(t)/dt\}$(cf. eqs. 2.15 and 2.25). Thus, $I_{relax}(t)$ was expressed in terms of the dielectric relaxation times $\tau_{\varepsilon,p}$ and intensities g_p (cf. eq 2.16),

$$I_{\text{relax}}(t) = 2V_0C_0\Delta\varepsilon\sum_p \frac{g_p}{\tau_{\varepsilon,p}}\exp[-t/\tau_{\varepsilon,p}]$$

$$= Q_{\text{relax}}\sum_p \frac{g_p}{\tau_{\varepsilon,p}}\exp[-t/\tau_{\varepsilon,p}] \quad \text{with } Q_{\text{relax}} = \int_0^{t_0} I_{\text{relax}}(t)\,dt \qquad (2.26)$$

In derivation of eq 2.26, Q_{relax} is regarded to coincide with an integral $\int_0^\infty I_{\text{relax}}(t)\,dt$ (because the $\exp[-t/\tau_{\varepsilon,p}]$ terms (almost) fully decay to zero at $t = t_0 \geq 6<\tau_G>_w$). On the basis of eq 2.26, the measured $I_{\text{relax}}(t)/Q_{\text{relax}}$ ratio was decomposed into exponentially decaying modes to evaluate $\tau_{\varepsilon,p}$ and g_p for small p (≤ 8). At low ω, the ε' and ε'' calculated from these $\tau_{\varepsilon,p}$ and g_p (cf. 2.17) agreed well with those obtained from the integration (eqs 2.24 and 2.25). Thus, the ε' and ε'' obtained from the mode decomposition of the $I_{\text{relax}}(t)/Q_{\text{relax}}$ ratio were utilized together with those obtained from eqs 2.24 and 2.25.

References

1. M. Morton and L. J. Fetters, *Rubber Chem. Technol.*, **48**, 359 (1975).
2. T. Fujimoto and M. Nagasawa, *Advanced Techniques for Polymer Synthesis*, Kagaku-Dojin, Kyoto (1972).
3. H. Watanabe, O. Urakawa, and T. Kotaka, *Macromolecules*, **26**, 5073 (1993).
4. H. Watanabe, H. Yamazaki, H. Yoshida, K. Adachi and T. Kotaka, *Macromolecules*, **24**, 5363 (1991).
5. H. Yoshida, K. Adachi, H. Watanabe, and T. Kotaka, *Polym. J.*, **21**, 863 (1989).
6. T. Takeuchi, and S. Mori, *Gel Permeation Chromatgraphy*, Maruzen, Tokyo (1976).
7. J. Roovers and S. Bywater, *Macromolecules*, **7**, 443 (1974).
8. N. Hadjichristidis and J. Roovers, *J. Polym. Sci., Polm. Phys. Ed.*, **12**, 2521 (1974).
9. J. D. Ferry, *Viscoelastic Properties of Polymers, 3rd ed.*, Wiley, New York (1980).
10. H. Watanabe, *Prog. Polym. Sci.*, **24**, 1253 (1999).
11. W. W. Graessley, *Adv. Polym. Sci.*, **16**, 1 (1974).
12. E. Riande and E. Saiz, *Dipole Moments and Birefringence of Polymers,* Prentice Hall, New Jersey (1992).
13. H. Watanabe, *Macromol. Rapid Commun.*, **22**, 127 (2001).

CHAPTER 3
Theory: Molecular Expression of Dynamic Properties

3-1. Introduction

In this thesis, viscoelastic and dielectric properties are examined for polyisoprene (PI) chains having the type-A dipoles. These properties are utilize to discuss detailed features of the chain motion. This chapter presents the molecular expressions of the viscoelastic and dielectric properties that serve as a rigid basis of this discussion.

3-2. Coarse-Grained Chain

Slow dynamic properties of flexible polymer chains are insensitive to chemical structure of the chains and governed only by the chain connectivity; see Chapter 1. This fact enables a use of coarse-grained chains[1)] to express a relationship between those properties and time evolution of the chain conformation. Some features of this coarse-grained chain are explained in this section.

Firstly, a concentrated, monodisperse system of linear chains (each composed of m monomers) is considered as the simplest system. The excluded volume effect is negligibly small in the concentrated system,[1)] and the chain has the Gaussian conformation[1,2)] in large spatial scales. A coarse-grained chain is obtained by dividing the real chain into N submolecules each containing g (= m /N) monomers; see Fig. 3-1a. The number g is chosen to be sufficiently small so that the coarse-grained chain has a large freedom in its conformation. At the same time, g is chosen to be sufficiently large so that the coarse-grained chain preserves the Gaussian nature,[1,3)]

$$\langle \mathbf{u}(n,t)\mathbf{u}(n',t)\rangle = \frac{a^2}{3}\delta_{nn'}\,\mathbf{I} \quad \textit{at equilibrium} \tag{3.1}$$

Here, $\mathbf{u}(n,t)$ is the bond-vector (end-to-end vector) of the n-th submolecule at time t (cf. Fig. 3-1a), $\delta_{nn'}$ is the Kronecker delta, and $\mathbf{I}$ is a unit tensor (having the components δ_{ij}). The dyadic $\langle \mathbf{u}(n,t)\mathbf{u}(n',t)\rangle$ measures the isochronal orientational correlation of two submolecules. The average size of the submolecule a , appearing in eq 3.1, is related to the effective step length of the monomer, b, as[1,2)]

$$a^2 = gb^2 \tag{3.2}$$

The coarse-grained star chain is similarly defined as a bundle of coarse-grained arms each composed of N_a submolecules ($N_a = m_a/g$ with m_a being the monomer number per each arm); cf. Fig. 3-2. The bond vector of the n-th segment in α-th arm at time t is denoted by $\mathbf{u}_\alpha(n,t)$. This $\mathbf{u}_\alpha$ satisfies the Gaussian relationship,

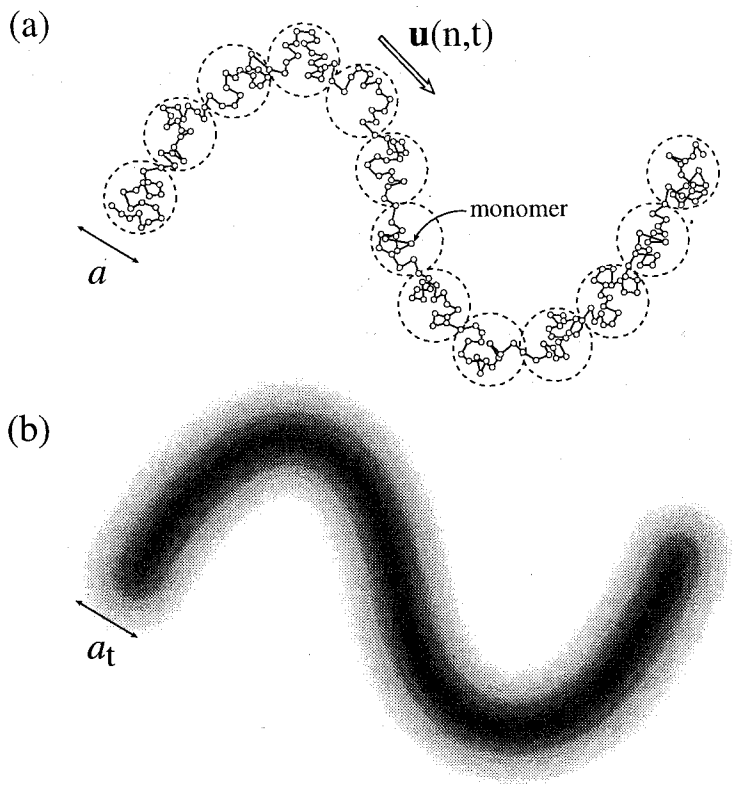

Fig. 3-1 Schematic illustration of the real chain and coarse-grained chain. In part a, the small beads connected by rods indicate monomeric segments, and the dotted circles represent the submolecules of the coarse-grained chain. Part b shows a hypothetical photograph of the real chain taken with a certain exposure time.

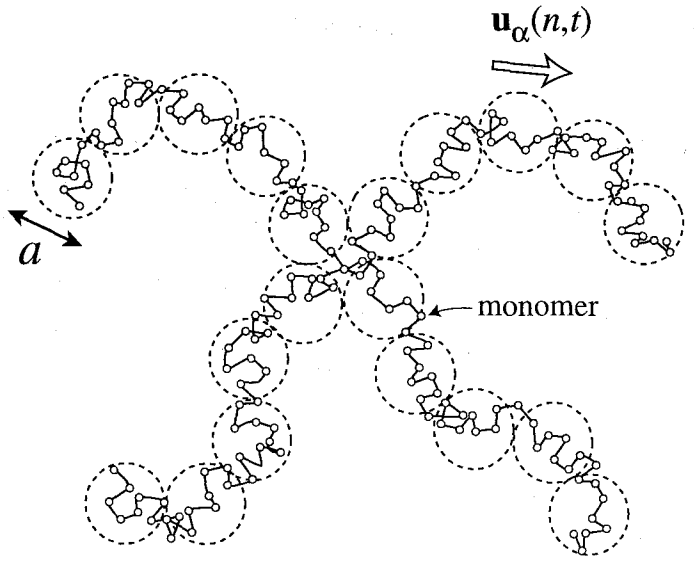

Fig. 3-2 Schematic illustration of the coarse-grained star-branched chain. Notation is the same as that in Fig. 3-1.

$$\langle \mathbf{u}_\alpha(n,t)\mathbf{u}_{\alpha'}(n',t)\rangle = \frac{a^2}{3}\delta_{nn'}\delta_{\alpha\alpha'}\mathbf{I} \quad \textit{at equilibrium} \tag{3.3}$$

It should be emphasized that the spatial and time scales are synchronously coarse-grained when the real chain is represented as a sequence of N submolecules. This fact can be noted from a hypothetical experiment of taking a photograph of the real chain with an exposure time t_{ex}.[3] An example of this photograph (for a linear chain) is shown in Fig. 3-1b. For large t_{ex}, the chain looks like a fuzzy thread with a width $a_t >> b$ because of the chain motion over the time t_{ex}. This motion and the local conformation in the spatial scale $< a_t$ are averaged in the photograph, and the successively taken photographs (with the exposure time t_{ex} for each) represent the chain motion in the spatial and time scales larger than a_t and t_{ex}, respectively.

The coarse-grained chain (Fig. 3-1a) is a discretized representation of this fuzzy thread.[3] In each submolecule, the monomer positions (local conformations) are equilibrated within a certain characteristic time, τ^*. This τ^* and the submolecule size a correspond to t_{ex} and a_t of the fuzzy thread, and the static and dynamic properties of the coarse-grained chain coincide with those of the real chain in the spatial scale $> a$ and time scale $> \tau^*$. Thus, any coarse-grained chain can be utilized to examine the dynamic features of the real chain as long as its submolecular equilibration time τ^* is longer than the unit time of the observation, t_{ob}. (In fact, the chains of different degree of coarse-graining exhibit the same properties as long as their τ^* is smaller than t_{ob}. This point is demonstrated later in sections 3-3-2 and 3-4-2.)

The coarse-grained chain, utilized throughout this thesis, is hereafter referred to as the "chain" unless its coarse-grained nature is to be emphasized. The viscoelastic and dielectric properties in long time scales are expressed in terms of $\mathbf{u}(n,t)$ of the coarse-grained chains. These expressions are summarized below.

3-3. Expression of Linear Viscoelastic Properties

3-3-1. Relaxation modulus

Since Boltzmann's superposition holds in the linear regime (for small strains), all linear viscoelastic features are described by the relaxation modulus $G(t)$ defined against the step shear;[4] see Chapter 2. Thus, all viscoelastic data obtained in this study are discussed/analyzed on the basis of an expression of $G(t)$ in terms of the bond vectors $\mathbf{u}(n,t)$ of the coarse-grained chain.

The proportionality between the mechanical stress and optical anisotropy, known as the stress-optical rule,[1,4,5] is well established from extensive experiments for concentrated, homogeneous polymeric liquids. The optical anisotropy detects non-isotropic orientation of chemical bonds in the real chain and thus corresponds to the orientational anisotropy of the submolecules in the (coarse-grained) chain.

For the linear chains subjected to the step shear γ, this anisotropy is quantitatively represented by an *orientation function*,[1,3]

$$S(n,t) = \frac{1}{a^2} \langle u_x(n,t) u_y(n,t) \rangle \quad \text{for linear chains} \tag{3.4}$$

Here, the shear and shear gradient directions are chosen as x and y directions, and $u_x(n,t)$ and $u_y(n,t)$ are the x and y components of $\mathbf{u}(n,t)$. The ensemble average $\langle \cdots \rangle$ is taken for all chains in the system. Similarly, for the star chains, the orientational anisotropy in the α-th arm is represented by

$$S_\alpha(n,t) = \frac{1}{a^2} \langle u_{\alpha,x}(n,t) u_{\alpha,y}(n,t) \rangle \quad \text{for star chains} \tag{3.5}$$

The shear stress $\sigma(t)$ is proportional to a summation of the orientational anisotropy of all submolecules in unit volume. Thus, the shear relaxation modulus $G(t)$ $(= \sigma(t)/\gamma)$ is represented in terms of the orientation function,[1,3]

$$G(t) = \frac{3\nu k_B T}{\gamma} \sum_{n=1}^{N} S(n,t) \quad \text{for linear chains} \tag{3.6}$$

$$G(t) = \frac{3\nu k_B T}{\gamma} \sum_{\alpha=1}^{q} \sum_{n=1}^{N_a} S_\alpha(n,t) \quad \text{for } q\text{-arm star chains} \tag{3.7}$$

Here, k_B is the Boltzmann constant, T is the absolute temperature, ν is the chain number density, N and N_a are the number of submolecules per each linear chain and star arm, respectively, and q is the number of arms per star chain. All linear viscoelastic quantities are readily calculated from these $G(t)$; see Chapter 2.

The relationship between $S(n,t)$ and $G(t)$ (eqs 3.6 and 3.7) does not change with the type of chain dynamics. Thus, this relationship provides a rigid basis for examining the chain motion (inducing decay of $S(n,t)$) through the viscoelastic properties.

At the same time, it should be emphasized that the n and t dependencies of $S(n,t)$ and the t dependence of $G(t)$ change with the type of chain dynamics. (Some examples are found for the molecular models explained in Chapter 4.) Specifically, the distribution of the orientational decay modes of $S(n,t)$, determining the viscoelastic relaxation modes through eqs 3.6 and 3.7, changes with the type of chain dynamics. This point becomes a key in detailed discussion in Chapters 5 and 6.

3-3-2. Insensitivity of $G(t)$ expression to degree of coarse-graining

The expression of the relaxation modulus (eqs 3.6 and 3.7) is *formally* dependent on the choice of the submolecule (choice of N and/or N_a), and one might consider this dependence as a

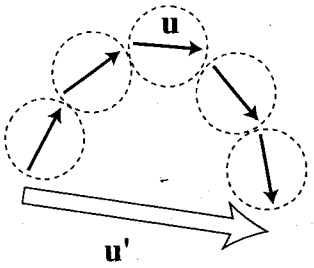

Fig. 3-3 Schematic illustration indicating combination of successive submolecules into a larger submolecule.

deficiency (non-definiteness) of the use of the coarse-grained chain. However, this formal dependence is related to magnitudes of the coarse-graining: There is no real difference of $G(t)$ calculated for submolecules of different sizes.[3)]

To demonstrate this point, one can calculate the modulus sustained by successive β submolecules in a chain; cf. Fig. 3-3. The equilibration time for the monomers in each submolecule, τ^*, is shorter than the unit time of observation, t_{ob}.

Now, the bond-vectors of the β submolecules, $\mathbf{u}(n,t)$ (n = 1, 2,.., β), are allowed to equilibrate under a constraint that their sum is kept at $\mathbf{u}'$. *If* a characteristic time τ^{**} of this equilibration is smaller than t_{ob}, $\mathbf{u}(n,t_{ob})$ can be generally written as[3)]

$$\mathbf{u}(n,t_{ob}) = \frac{1}{\beta}\mathbf{u}' + \mathbf{v}(n) \tag{3.8}$$

where $\mathbf{v}$ is an *isotropically* distributed vector (having $\langle v_x v_y \rangle = 0$) that is uncorrelated with $\mathbf{u}'$. Then, the modulus sustained by the ensemble of the β submolecules is expressed as (cf. eqs 3.5-3.7)

$$G_\beta = \frac{3k_BT}{\gamma}\sum_{n=1}^{\beta}\frac{1}{a^2}\langle u_x(n,t_{ob})u_y(n,t_{ob})\rangle = \frac{3k_BT}{\gamma}\frac{1}{\beta a^2}\langle u'_x u'_y\rangle \tag{3.9}$$

This modulus is identical to the modulus calculated for an enlarged submolecule being composed of β submolecules and having an average size $\beta^{1/2}a$. Namely, the mutually equilibrated β submolecules behave as an enlarged, modulus-sustaining unit as a whole.

The above result demonstrates that the calculation of the modulus is not affected by the choice of the submolecule *if* the chosen submolecule is internally equilibrated within t_{ob}. In other words, all coarse-grained chains composed of submolecules having $\tau^* \le t_{ob}$ exhibit the same modulus at $t \ge t_{ob}$, meaning that the modulus expression for these chains (eqs 3.6 and 3.7) gives the same, correct $G(t)$ value.

At the same time, it should be emphasized that eqs 3.6 and 3.7 cannot be applied to the coarse-grained chains if their submolecules are not internally equilibrated within t_{ob}. If the β submolecules preserve their initial orientational anisotropy S_0, the modulus sustained by these submolecules is given by $G\beta = 3\beta k_B T S_0/\gamma$ (cf. eq 3.6), not by $G_{\beta,eq} = 3k_B T S_0/\gamma$ calculated for the equilibrated β submolecules. In other words, the equilibration over β submolecules reduces the modulus by a factor $1/\beta$. This fact becomes a key in the test of the dynamic tube dilation mechanism[6-9] described later in Chapters 7 and 8.

3-4. Expression of Dielectric Properties

3-4-1. Dielectric relaxation function.

Since Boltzmann's superposition holds in the linear regime, all dielectric features are described by the relaxation function $\Phi(t)$ defined against a constant electric field; see Chapter 2. Thus, the analysis of the dielectric ε' and ε'' data presented in this thesis just requires an expression of $\Phi(t)$ in terms of the bond vectors $\mathbf{u}(n,t)$ of the coarse-grained chains.

At equilibrium (where the ε' and ε'' data were obtained), $\Phi(t)$ is given by an auto-correlation of the polarization $\mathbf{P}(t)$,[10,11]

$$\Phi(t) = \frac{\langle \mathbf{P}(t) \cdot \mathbf{P}(0) \rangle}{\langle \mathbf{P}^2 \rangle} \tag{3.10}$$

The relationship between $\mathbf{P}(t)$ and $\mathbf{u}(n,t)$ changes with the relative arrangement of the type-A dipoles with respect to the chain backbone.[12,13] For the linear and star chains, this relationship is separately summarized below.

3-4-1-1. Linear chains

This study utilizes linear polyisoprene (PI) chains having once-inverted type-A dipoles.[14-16] For these chains each composed of N submolecules, the polarization $\mathbf{P}(t)$ is written in terms of $\mathbf{u}(n,t)$ of the submolecules as

$$\mathbf{P}(t) = \nu m_d \sum_{n=1}^{N} \vartheta(n)\mathbf{u}(n,t) \tag{3.11}$$

Here, ν is the chain number density, and m_d is a magnitude of the type-A dipoles reduced to unit length of $\mathbf{u}$. (Equation 3.11 assumes that all chains have the same arrangement of the monomeric type-A dipoles and that the dipoles in each submolecules are aligned in the same direction along the chain backbone. These assumptions are satisfied for the monodisperse PI chains utilized in this study.)

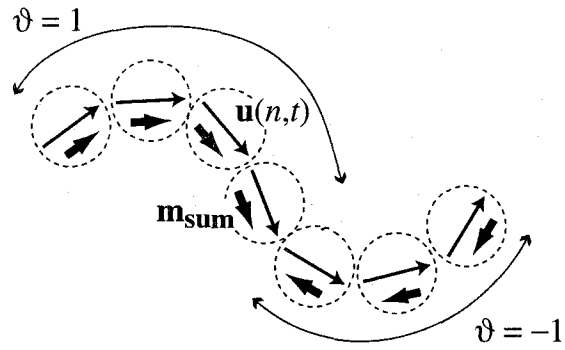

Fig. 3-4 Schematic illustration of a linear, dipole-inverted type-A chain. Thin long arrows indicate the bond vectors of submolecules, and the thick short arrows denote the sum of the type-A dipoles in each submolecule.

A vectorial sum $\mathbf{m}_{\mathbf{sum}}$ of these type-A dipoles in each submolecule is either parallel or anti-parallel to $\mathbf{u}$. The parameter $\vartheta(n)$ in eq 3.11 specifies this direction of $\mathbf{m}_{\mathbf{sum}}$: $\vartheta(n) = 1$ (or -1) if $\mathbf{m}_{\mathbf{sum}}$ is parallel (or anti-parallel) to $\mathbf{u}$ for the *n-th* submolecule; see Fig. 3-4.

In principle, $\Phi(t)$ includes cross-correlation terms for different chains, $\langle \mathbf{u}_\alpha(n,t) \bullet \mathbf{u}_{\alpha'}(n',0) \rangle$ with α and $\alpha'(\neq \alpha)$ being the chain index (cf. eqs 3.10 and 3.11). However, for non-polar chains like PI having only weak dipoles, this cross-correlation can be safely neglected for the following reason. Since the dipole-dipole interaction energy of these chains is negligibly small (compared to the thermal energy k_BT), the n'-th submolecule of the α'-th chain take two opposite configurations, $\mathbf{u}_{\alpha'}(n',0)$ and $-\mathbf{u}_{\alpha'}(n',0)$, with the same probabilities for a given configuration of the n-th submolecule of α-th chain, $\mathbf{u}_\alpha(n,t)$.[13] Thus, the cross-correlation terms vanish when summed over all chains, i.e., $\sum_{\alpha'(\neq\alpha)} \langle \mathbf{u}_\alpha(n,t) \bullet \mathbf{u}_{\alpha'}(n',0) \rangle = 0$.

From the above argument, $\Phi(t)$ is written in terms of the auto-correlation of respective chains,

$$\Phi(t) = \frac{1}{N} \sum_{n=1}^{N} \sum_{n'=1}^{N} \vartheta(n)\vartheta(n')\, C(n,t;n') \quad (\Phi(0) = 1) \tag{3.12}$$

with

$$C(n,t;n') = \frac{1}{a^2} \langle \mathbf{u}(n,t) \bullet \mathbf{u}(n',0) \rangle \tag{3.13}$$

Here, $\langle \cdots \rangle$ indicates an ensemble average at equilibrium. (The normalization constant, $1/N$ appearing in eq 3.12, reflects the Gaussian nature of the submolecules.[13])

The quantity $C(n,t;n')$, referred to as a *local correlation function*,[13] specifies the orientational correlation of two submolecules in the same chain at times t and 0. The global chain motion results in decay of the orientational memory to decrease the C value. This leads to the dielectric relaxation (decay of Φ; cf. eq. 3.12).

It should be emphasized that the functional form of $C(n,t;n')$ and the corresponding t

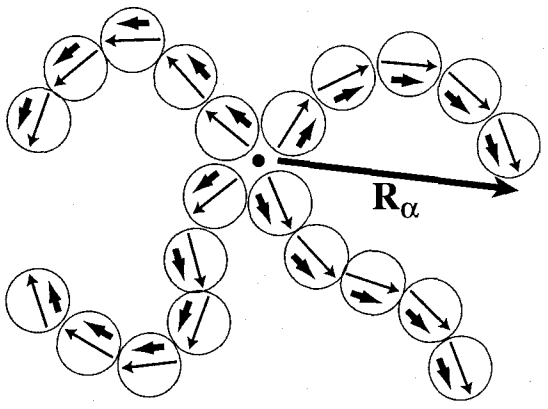

Fig. 3-5 Schematic illustration of star chain being synthesized by anionic coupling. This chain has the type-A dipoles aligned in each arm. Thin arrows indicate bond vectors of the submolecules of the arm chain, and thick short arrows denote the sum of the type-A dipoles in each submolecule.

dependence of $\Phi(t)$ change with the type of chain dynamics (as noted, for example, from the behavior of the models summarized in Chapter 4). Specifically, distribution of the memory decay modes of C, affecting the dielectric relaxation modes through eq 3.12, changes with the types of chain dynamics. This point becomes a key in detailed discussion in Chapters 5 and 6.

3-4-1-2. Star chains

For the star PI chains prepared by the anionic coupling method (cf. Chapter 2), the type-A dipoles are aligned in the same direction in each arm but are inverted at the branching point; see Fig. 3-5. For such star chains, the polarization $\mathbf{P}_\alpha(t)$ of the α-th arm is proportional to a vector $\mathbf{R}_\alpha(t)$ that connects the branching point and the free arm end. Thus, the dielectric relaxation function of those star chains is expressed as[13,17]

$$\Phi(t) = \frac{1}{qN_a a^2} \sum_{\alpha,\,\alpha'=1}^{q} \langle \mathbf{R}_\alpha(t)\cdot\mathbf{R}_{\alpha'}(0)\rangle \quad \text{for } q\text{-arm stars} \tag{3.14}$$

where N_a is the number of submolecules per each arm.

It should be emphasized that this $\Phi(t)$ includes a cross-correlation of different arms, $\langle \mathbf{R}_\alpha(t)\cdot\mathbf{R}_{\alpha'}(0)\rangle$ with $\alpha \neq \alpha'$. *If* the branching point is fixed in space in the time scale of terminal dielectric relaxation (as assumed in the tube model[7-9,18,19]), this cross-correlation vanishes and eq 3.14 is simplified to[13]

$$\Phi(t) = \frac{1}{N_a a^2} \langle \mathbf{R}_\alpha(t)\cdot\mathbf{R}_\alpha(0)\rangle \quad \text{for fixed branching point} \tag{3.15}$$

(Here, the arm index α stands for a representative arm.) However, the branching point is not

fixed and the cross-correlation emerges when the constraint release motion occurs,[20,21] as explained in Chapter 4. This cross-correlation becomes a key in the discussion of the terminal dielectric behavior of the star chains presented in Chapter 8.

3-4-2. Insensitivity of $\Phi(t)$ expression to degree of coarse-graining.

The expression of the dielectric $\Phi(t)$ (eqs 3.12 and 3.14) is *formally* dependent on the choice of the submolecular size (choice of N and/or N_a). However, this formal dependence is related to a magnitude of the coarse-graining, and no real difference exists for the $\Phi(t)$ values calculated for submolecules of different sizes.[13]

This point is easily demonstrated by calculating the polarization $\mathbf{P}_\beta(t)$ of successive β submolecules in a chain; see Fig. 3-3. If the type A dipoles are parallel to $\mathbf{u}(n,t)$ of these submolecules, this polarization is given by

$$\mathbf{P}_\beta(t) = m_d \sum_{n=1}^{\beta} \mathbf{u}(n,t) = m_d \mathbf{u}'(t) \tag{3.16}$$

Thus, the polarization is always equal to that defined for the enlarged bond vector, $\mathbf{u}'(t) = \sum_{n=1}^{\beta} \mathbf{u}(n,t)$. This result means that the $\Phi(t)$ value calculated for such enlarged bond vectors (for enlarged submolecules) coincides with that calculated for the smaller submolecules. In other words, the calculated $\Phi(t)$ value is insensitive to the choice of the submolecular size.

It should be noted that this insensitivity is derived irrespective of the equilibration over β segments. Namely, the equilibration does nor change the $\Phi(t)$ value (unless the enlarged $\mathbf{u}'$ fluctuates). This feature of $\Phi(t)$ is different from the feature of $G(t)$; the equilibration always leads to the decay of G (cf. section 3-3-2).

3-5. Difference between Viscoelastic and Dielectric Properties[3,13]

The viscoelastic and dielectric relaxation processes reflect the same, stochastic motion of the chain. However, the expressions of $G(t)$ (eqs 3.6 and 3.7) and $\Phi(t)$ (eqs 3.12 and 3.14) demonstrate two important differences of these processes.

The first difference concerns the *time* included in $G(t)$ and $\Phi(t)$. The viscoelastic relaxation reflects the decay of the *isochronal* orientational anisotropy, and the correlation at *two separate times* (t and 0) is not included in $G(t)$; see eqs 3.6 and 3.7. In contrast, the dielectric relaxation detects this correlation (because the electric current emerges only when the polarization changes in a interval of time between 0 and t), and $\Phi(t)$ includes this correlation; see eqs 3.12 and 3.14.

The second difference is for the correlation of different submolecules. $G(t)$ reflects the orientational anisotropy of *individual* submolecules (eqs 3.6 and 3.7), while $\Phi(t)$ detects the

cross-correlation of different submolecules in addition to the auto-correlation of respective submolecules (eqs 3.12 - 3.14).

These differences of $G(t)$ and $\Phi(t)$, intrinsically related to the nature of mechanical and electrical phenomena, in turn indicate an interesting possibility that detailed features of the chain motion (differently averaged in G and Φ) can be experimentally tested *via* comparison of the viscoelastic and dielectric properties. This test is successfully made in this study, as demonstrated in Chapters 5-8.

References

1. M. Doi and S. F. Edwards, *The Theory of Polymer Dynamics,* Clarendon, Oxford (1986).
2. H. Yamakawa, *Modern Theory of Polymer Solutions*, Harper & Row, New York (1971).
3. H. Watanabe, *Prog. Polym. Sci.* **24**, 1253 (1999).
4. J. D. Ferry, *Viscoelastic Properties of Polymers (3rd ed)*, Wiley, New York (1980).
5. H. Janeschitz-Kriegl, *Polymer Melt Rheology and Flow Birefringence*, Springer, Berlin (1983).
6. G. Marrucci, *J. Polym. Sci., Polym. Phys. Ed.* **23**, 159 (1985).
7. R. C. Ball and T. C. B. McLeish, *Macromolecules* **22**, 1911 (1989).
8. S. T. Milner and T. C. B. McLeish, *Macromolecules* **30**, 2159 (1997).
9. S. T. Milner and T. C. B. McLeish, *Macromolecules* **31**, 7479 (1998).
10. R. H. Cole, *J. Chem. Phys.* **42**, 637 (1965).
11. E. Riande and E. Saiz, *Dipole Moments and Birefringence of Polymers*, Prentice Hall, Englewood Clifts, New Jersey (1992).
12. W. H. Stockmayer, *Pure Appl. Chem.* **15**, 539 (1967).
13. H. Watanabe, *Macromol. Rapid Commum*, 22, 127 (2001).
14. H. Watanabe, O. Urakawa, and T. Kotaka, *Macromolecules* **26**, 5073 (1993).
15. Y. Matsumiya, H. Watanabe, K. Osaki, and M.-L. Yao, *Macromolecules* **31**, 7528 (1998).
16. H. Watanabe, Y. Matsumiya, K. Osaki, and M.-L. Yao, *Macromolecules* **31**, 7538 (1998).
17. H. Watanabe, Y. Matsumiya, and K. Osaki, *J. Polym. Sci., Polym. Phys.* **38**, 1024 (2000).
18. M. Doi and N. Kuzuu, *J. Polym. Sci. Polym. Lett. Ed* **18**, 775 (1980).
19. D. S. Pearson and E. Helfand, *Macromolecules* **17**, 888 (1984).
20. J. Klein, *Macromolecules* **11**, 852 (1978).
21. W. W. Graessley, *Adv. Polym. Sci.* **47**, 68 (1982).

CHAPTER 4
Molecular Models of Chain Dynamics

4-1. Introduction

In this study, the global motion of type-A chains (polyisoprene; PI) is discussed through their viscoelastic and dielectric properties on a basis of the molecular expressions of these properties explained in Chapter 3. Some molecular models are utilized for convenience of this discussion. This chapter summarizes dynamic features of these models relevant to this study. Models developed in this study are also explained.

4-2. Bead-Spring Models[1-4)]

4-2-1. Rouse model[1,3)]

The Rouse model is formulated for a *linear* chain composed of N Gaussian submolecules and placed in a uniform, frictional medium. Each submolecule, composed of g monomers, is further modeled as a bead having a friction coefficient $\zeta = g\zeta_0$ (ζ_0 = monomeric friction), and neighboring beads are connected by a Gaussian spring with a spring constant $\kappa = 3k_BT/a^2$ ($a^2 = \langle \mathbf{u}^2 \rangle_{equilibrium}$); see Fig. 4-1.

The Rouse model is a model for an isolated, non-entangled chain. However, the tube model for entangled chains is formulated on the basis of the Rouse dynamics, and the constraint release model considers that the tube moves according to this dynamics. Because of this importance of the Rouse model, its features are summarized below.

4-2-1-1. Viscoelastic properties

The time evolution of the bond vectors **u** is described by the Rouse equation of motion that considers a balance of the elastic and frictional forces as well as the Brownian force acting on respective beads.[3,4)] The orientation function $S(n,t)$ (eq 3.4) is calculated by solving this equation against a step shear strain γ. In a continuous limit (for $N >> 1$), the result is cast in a compact form,[3,4)]

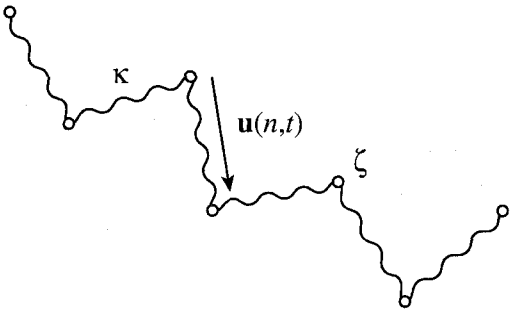

Fig.4-1 Schematic illustration of bead-spring chain.

$$S(n,t) = \frac{2\gamma}{3N}\sum_{p=1}^{N}\sin^2\left(\frac{p\pi n}{N}\right)\exp\left(-\frac{tp^2}{\tau_{R,G}}\right) \tag{4.1}$$

Here, the longest viscoelastic relaxation time of the Rouse chain, $\tau_{R,G}$, is given by

$$\tau_{R,G} = \frac{\zeta a^2 N^2}{6\pi^2 k_B T} \tag{4.2}$$

For a monodisperse system of Rouse chains with the number density ν, the relaxation modulus is calculated by inserting eq 4.1 into eq 3.6 (with a replacement $\Sigma_n \rightarrow \int_0^N \ldots dn$ in the continuous limit). The result is

$$G(t) = \nu k_B T\sum_{p=1}^{N}\exp\left(-\frac{tp^2}{\tau_{R,G}}\right) \tag{4.3}$$

From eq 4.3, the viscoelastic relaxation time $\tau_{G,p}$ and intensity h_p of p-th viscoelastic mode appearing in eqs 2.6 and 2.7 are obtained as

$$\tau_{G,p} = \tau_{R,G}/p^2,\ h_p = \nu k_B T \tag{4.4}$$

From these $\tau_{G,p}$ and h_p, the storage and loss moduli are readily calculated (cf. eq 2.7).

4-2-1-2. Dielectric properties

The local correlation function (eq 3.13), calculated from the Rouse equation motion at equilibrium, is cast in a compact form (in the continuous limit),[4,5]

$$C(n,t;n') = \frac{2}{N}\sum_{p=1}^{N}\sin\left(\frac{p\pi n}{N}\right)\sin\left(\frac{p\pi n'}{N}\right)\exp\left(-\frac{tp^2}{\tau_{R,\varepsilon}}\right) \tag{4.5}$$

with

$$\tau_{R,\varepsilon} = \frac{\zeta a^2 N^2}{3\pi^2 k_B T} \tag{4.6}$$

The longest relaxation time of this C, $\tau_{R,\varepsilon}$, is twice of the viscoelastic $\tau_{R,G}$ (eq 4.2).

For a given arrangement of the type-A dipoles represented by $\vartheta(n)$ in eq 3.11, all dielectric properties are calculated from the above $C(n,t;n')$ through eq 3.12 and eqs 2.15-2.17. Specifically, the dielectric relaxation time and intensity appearing in eqs 2.16 and 2.17, $\tau_{\varepsilon,p}$ and g_p, are

given by

$$\tau_{\varepsilon,p} = \tau_{\mathrm{R},\varepsilon}/p^2, \quad g_p = \frac{2}{N^2}\left[\int_0^N \vartheta(n)\sin\left(\frac{p\pi n}{N}\right)\mathrm{d}n\right]^2 \tag{4.7}$$

(This g_p is obtained from eqs 4.5 and 3.12 with a replacement $\Sigma_n \rightarrow \int_0^N \ldots \mathrm{d}n$ in eq 3.12.)

4-2-2. Ham model [2)]

The Ham-model for unentangled, q-arm star chains is formulated for a star-branched bead-spring chain with each arm being composed of N_a beads; see Fig. 4-2a. The Ham equation of motion is formulated by considering a balance of the elastic, frictional, and Brownian forces acting on respective beads.

The motional modes calculated from this equation is similar to those derived from the Rouse equation, except that the od*d* modes inducing no motion of the branching point (BP) is degenerated by a factor of $q-1$ (because each odd mode corresponds to antisymmetric motion of a *pair* of the arms) while the *even* mode inducing the BP motion activates synchronized symmetric motion of *all* arms and is not degenerated;[2,4)] cf. Fig. 4-2b. The viscoelastic and dielectric properties, calculated from these motional modes, are summarized below.

4-2-2-1. Viscoelastic properties[2,4)]

The orientation function $S_\alpha(n,t)$ of α-th arm of the q-arm Ham chain (cf. eq 3.5) is contributed from the degenerated odd modes and the undegenerated even modes. The corresponding $G(t)$, calculated from eq 3.7 (with a replacement $\Sigma_n \rightarrow \int_0^N \ldots \mathrm{d}n$), is given by

$$G(t) = \nu k_\mathrm{B}T\sum_{p=1}^{N_\mathrm{a}} d_p \exp\left(-\frac{tp^2}{\tau_{\mathrm{H},G}}\right) \tag{4.8}$$

with

$$d_p = q-1 \text{ (for } p = \text{odd)}, \ 1 \text{ (for } p = \text{even)} \tag{4.9}$$

and

$$\tau_{\mathrm{H},G} = \frac{2\zeta a^2 N_\mathrm{a}^2}{3\pi^2 k_\mathrm{B}T} \tag{4.10}$$

Here, ν is the chain number density, and d_p represents the mode degeneracy. From eqs 4.8 and 4.9, the relaxation time $\tau_{G,p}$ and intensity h_p of p-th viscoelastic mode are obtained as

$$\tau_{G,p} = \tau_{\mathrm{H},G}/p^2, \ h_p = \nu k_\mathrm{B}T d_p \tag{4.11}$$

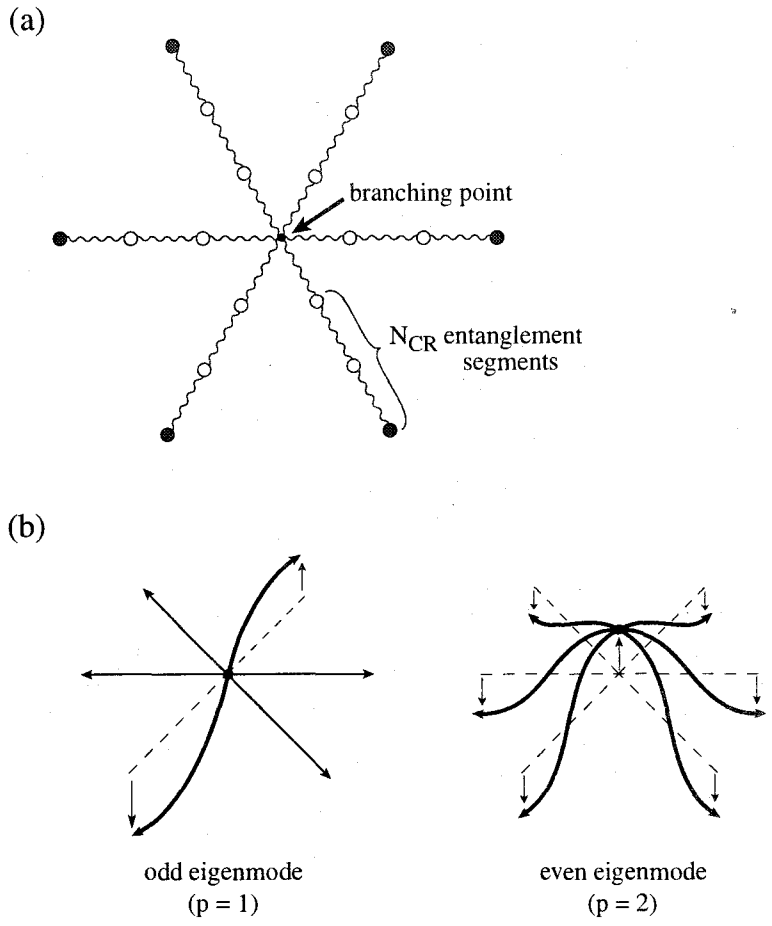

Fig.4-2 (a) Schematic illustration of star-branched bead-spring chain (Ham chain). (b) Schematic illustration of odd and even modes of this chain. For the star chains having the dipoles (thick arrows) inverted at the branching point, all odd eigenmodes and a subset of even eigenmodes (having the mode indices = twice of even integers) are dielectrically inert.

The above viscoelastic behavior of the Ham chain is similar to that of the linear Rouse chain composed of $2N_a$ submolecules, except that the mode distribution specified by h_p (eqs 4.4 and 4.11) is a little narrower for the former.

4-2-2-2. Dielectric properties[5,6]

The star polyisoprene chains utilized in this study have symmetrical inversion of the type-A dipoles at the branching point. The odd modes of the Ham chain activate antisymmetric motion of two arms (cf. Fig. 4-2b) and induce no change of the polarization of the dipole-inverted star chains. These odd modes are dielectrically inert. Thus, the dielectric $\Phi(t)$ (eq 3.14) of those star chains is contributed only from the even modes.[6]

In a continuous limit (for $N_a >> 1$), this $\Phi(t)$ is written as[6]

$$\Phi(t) = \sum_{p=\text{odd}} \frac{8}{p^2\pi^2} \exp\left(-\frac{4p^2t}{\tau_{H,\varepsilon}}\right) \qquad \text{for dipole-inverted stars} \qquad (4.12)$$

with

$$\tau_{H,\varepsilon} = \frac{4\zeta a^2 N_a{}^2}{3\pi^2 k_B T} \qquad (4.13)$$

The *dielectrically observed* terminal relaxation time, $\tau_{H,\varepsilon}/4$ (cf. eq 4.12), is half of the viscoelastic $\tau_{H,G}$ (eq 4.10) because the slowest motional mode (odd mode with p=1), contributing to $G(t)$, is erased in the dielectric response of the dipole-inverted star chains.

4-3. Doi-Edwards Model [3,7,8]

For entangled chains, the entanglement mesh size is conveniently chosen as the submolecular size a. The corresponding submolecular molecular weight M_e, often referred to as the entanglement spacing, is evaluated from the entanglement plateau modulus G_N,[9]

$$M_e = \frac{cRT}{G_N} \qquad (4.14)$$

Here, c is the chain concentration in mass/volume unit, and R is the gas constant. Thus, the entangled linear chain of the molecular weight M is coarse-grained into a chain composed of $N = M/M_e$ submolecules. This particular submolecule is referred to as the *entanglement segment.*

Entangled chains are deeply interpenetrating with each other. In the molecular picture of Doi and Edwards (DE), a given linear chain (probe chain) in the system moves anisotropically with respect to its backbone:[3,7,8] The lateral motion is restricted by the surrounding chains (matrix chains) within a small distance a, while the motion along the backbone is not constrained by the matrix and occurs freely over large distances. In other words, the DE model considers that the probe motion is limited in a tube-like region of the diameter a; cf. Fig. 4-3.

The DE model further introduces simplifying assumptions that the probe length measured along the tube does not fluctuate with time and that the tube is fixed in space during the course of

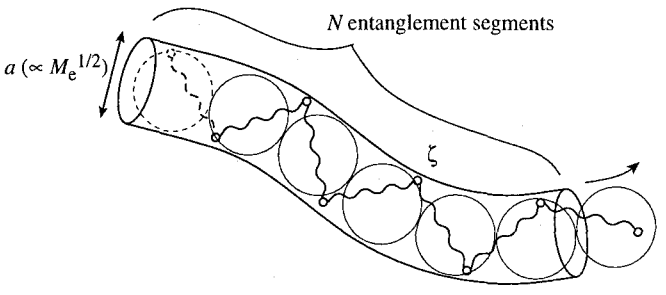

Fig.4-3 Schematic illustration of reptating chain.

the probe relaxation.[7,8] Under these assumptions, the global motion of the probe occurs only through *reptation*, the curvilinear diffusion along the probe contour; this diffusion is characterized with the number N and friction coefficient ζ of the entanglement segments. The linear viscoelastic and dielectric properties of the DE model derived from this reptation picture are summarized below.

4-3-1. Viscoelastic properties

The time evolution of the orientation function $S(n,t)$ of the reptating chain is described by a diffusion equation (with the curvilinear diffusivity $k_BT/N\zeta$). This equation is solved against a step strain γ to give[3,7,8]

$$S(n,t) = S_0 \sum_{p=\text{odd}} \frac{4}{p\pi} \sin\left(\frac{p\pi n}{N}\right) \exp\left(-\frac{tp^2}{\tau_{\text{rep}}}\right) \tag{4.15}$$

with

$$S_0 = 4\gamma/15 \text{ (DE initial condition)} \tag{4.16}$$

and

$$\tau_{\text{rep}} = \frac{\zeta N^3 a^2}{\pi^2 k_B T} \tag{4.17}$$

Here, τ_{rep} is the reptation time required for the chain to escape from the tube.

Equations 4.15-4.17 and eq 3.6 (with a replacement $\Sigma_n \rightarrow \int_0^N \ldots dn$) are utilized to calculate the relaxation modulus $G(t)$ of the reptating chains ,

$$G(t) = G_N \mu_{\text{rep}}(t) \tag{4.18}$$

with

$$\mu_{\text{rep}}(t) = \sum_{p=\text{odd}} \frac{8}{p^2\pi^2} \exp\left(-\frac{tp^2}{\tau_{\text{rep}}}\right) \tag{4.19}$$

Here, G_N is the entanglement plateau modulus, and $\mu_{\text{rep}}(t)$ is the normalized relaxation modulus for the reptation process. From this $G(t)$, viscoelastic relaxation times and mode intensities appearing in eqs 2.6 and 2.7 are obtained as

$$\tau_{G,p} = \tau_{\text{rep}}/p^2, \quad h_p = 8G_N/p^2\pi^2 \text{ (for } p = \text{odd}), \quad h_p = 0 \text{ (for } p = \text{even}) \tag{4.20}$$

A comment needs to be added for the above expression of $G(t)$. From the DE initial condition for S (eq 4.16), the molecular weight of the entanglement segment is calculated to be $M_e = 4cRT/5G_N$.[3,8] This M_e is 4/5 times smaller than that defined by eq 4.14. However, effects of this difference of M_e on the viscoelastic properties are adsorbed in the G_N factor in eq 4.18. In other words, the difference of M_e rises no difference of the $G(t)$ expression as long as the G_N value is experimentally determined. This situation is common for all dynamic properties calculated from various versions of the tube model described in this chapter.

4-3-2. Dielectric properties

For the reptation process, the time evolution of the local correlation function $C(n,t;n')$ is again described by a diffusion equation.[4,5] A solution of this equation (at equilibrium) gives[4,5]

$$C(n,t;n') = \frac{2}{N}\sum_{p\geq 1} \sin\left(\frac{p\pi n}{N}\right)\sin\left(\frac{p\pi n'}{N}\right)\exp\left(-\frac{tp^2}{\tau_{rep}}\right) \tag{4.21}$$

Here, τ_{rep} is the reptation time given by eq 4.17. From eqs 4.21 and eq 3.12 (with a replacement $\Sigma_n \rightarrow \int_0^N \ldots dn$), the relaxation time and intensity of the p-th dielectric mode, $\tau_{\varepsilon,p}$ and g_p, are obtained as

$$\tau_{\varepsilon,p} = \tau_{rep}/p^2, \quad g_p = \frac{2}{N^2}\left[\int_0^N \vartheta(n)\sin\left(\frac{p\pi n}{N}\right)dn\right]^2 \tag{4.22}$$

Here $\vartheta(n)$ is a parameter specifying the arrangement of the type-A dipoles (cf. eq 3.12).

4-3-3. Comment for the reptation and Rouse dynamics

As noted from eqs 4.20 and 4.22, the dielectric $\tau_{\varepsilon,p}$ of the reptating chain is identical to the viscoelastic $\tau_{G,p}$. In addition, for the chain without the dipole inversion ($\vartheta(n) = 1$ for $n = 0$ - N), the dielectric mode intensities given by eq 4.22 are identical to the normalized viscoelastic mode intensities, h_p/G_N (eq 4.20). Thus, the normalized viscoelastic and dielectric relaxation functions μ_{rep} and Φ_{rep} are exactly the same for the reptating type-A chain having no dipole inversion.

In contrast, the Rouse model predicts a significant difference between these mode distributions; see eq 4.4 and eq 4.7 (with $\vartheta(n) = 1$ for $n = 0$ - N). Furthermore, the Rouse and reptation predictions are the same for the dielectric mode distribution (cf. eqs 4.7 and 4.22) but different for the viscoelastic mode distribution (cf. eqs 4.4 and 4.20).

These results serve as a good example demonstrating the important difference between the dielectric and viscoelastic properties (cf. section 3-5): The dielectric properties detect the orientational correlation at two separate times while the viscoelastic properties reflect the orientational anisotropy at respective times. Thus, the same stochastic chain motion is differently averaged in

these properties, thereby giving the above difference between the Rouse and reptation predictions for the mode distribution.

4-4. Thermal Constraint Release Model [4,10-13]

The tube introduced in the DE model represents the topological constraint for a given chain (probe) from the surrounding chains (matrix). Thus, the tube moves according to the motion of the matrix chains. This tube motion is important in particular for polydisperse chains (e.g., blends) and/or star chains.

The tube motion affects the probe dynamics through two different but related mechanisms. [4] The tube motion allows a large-scale *lateral* motion of the probe (with respect to its backbone).[10-13] This mechanism is referred to as the *constraint release* (CR). The tube motion can also increase an effective tube diameter for the probe in a coarse-grained time scale.[4,14,15] This mechanism is referred to as the *dynamic tube dilation* (DTD).

This section explains models for *thermal* CR induced by *equilibrium* matrix motion. The models incorporating the DTD mechanism is explained later in sections 4.5 and 4.6.

4-4-1. Linear chains

Fig. 4-4a shows a conventional molecular picture for the CR motion of the probe (filled thread) induced by diffusion of the tube-forming (entangling) matrix chains.[10-13] When a matrix chain (unfilled thread) diffuses away, an entanglement segment of the probe acquires a freedom to locally jump. After this jump, either the same or different matrix chain approaches the probe to reform the constraint for this segment. Accumulation of this type of local jumps leads to the global CR motion of the probe.

Graessley[12] evaluated a mean waiting time t_w for the local jump due to pure reptation of linear matrix chains (with no contour length fluctuation). The result is given by

$$t_w = \Lambda \tau_{mat} \quad \text{with} \quad \Lambda = \frac{1}{z_g}\left(\frac{\pi^2}{12}\right)^{z_g} \tag{4.23}$$

Here, τ_{mat} is the matrix relaxation time that is assumed, in the Graessley model, to be given by the reptation time of the matrix chain composed of N_1 entanglement segments; $\tau_{mat} = \tau_{rep}(N_1)$ (cf. eq 4.17). The z_g is an average number of constraints per each entanglement point. The t_w given by eq 4.23 is regarded as a lifetime of one entanglement point.

Graessley assumed that the local jump occurs immediately after the local constraint is removed and that the probe contour length is *preserved* during this jump.[12] Under these assumptions, the thermal CR motion of the probe is described by a local bond-flip model[16] for freely jointed rods each having the constant length a and being constrained by the slip-link of the finite lifetime t_w; see Fig. 4-4b. Irrespective of details of the bond-flip stochastics, slow dynamic properties of this model coincide with those of the Rouse model.[3]

Thus, for the linear probe chain composed of N_2 entanglement segments, the longest vis-

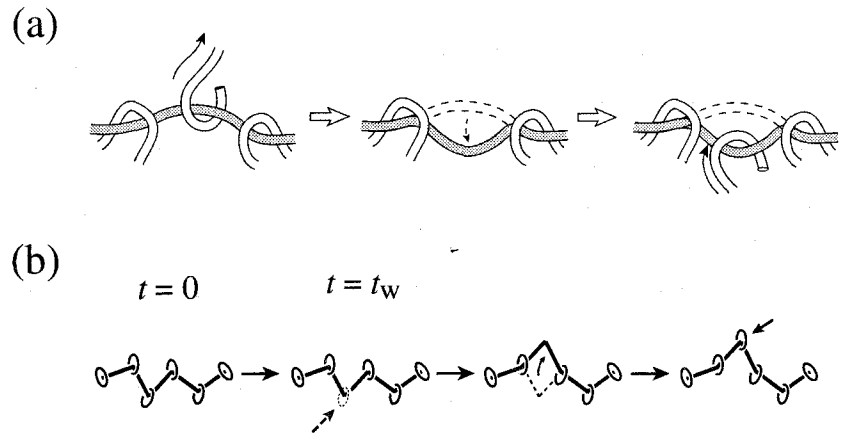

Fig.4-4 Schematic illustration of consraint release (CR) process.

coelastic and dielectric relaxation times $\tau_{CR,G}$ and $\tau_{CR,\varepsilon}$ obtained from the Graessley model are written as[12)]

$$\tau_{CR,G} = \frac{1}{2}\tau_{CR,\varepsilon} = \frac{2t_w}{\pi^2} N_2^2 = \frac{2\zeta\Lambda a^2}{\pi^4 k_B T} N_1^3 N_2^2 \qquad (4.24)$$

The viscoelastic and dielectric properties for the Rouse-CR process are described by eqs 4.3, 4.4, and 4.7 after replacing the $\tau_{R,G}$ and $\tau_{R,\varepsilon}$ therein by $\tau_{CR,G}$ and $\tau_{CR,\varepsilon}$ (eq 4.24). This replacement corresponds to a replacement of ζ for the Rouse chain by an effective friction coefficient for a tube segment, $\zeta_{tube} = 12k_BTt_w/a^2$. Equation 4.24 (with the Λ factor different from that given by eq 4.23) is obtained also from the CR models of Klein[10)] and of Daoud and de Gennes.[11)]

Real matrix chains have fluctuating contour length and do not exhibit the purely reptative motion.[3,4)] Thus, the N_1 dependence of t_w ($\propto N_1^3$; cf. eqs 4.17 and 4.23) changes accordingly. However, in a refined CR molecular picture considering multiple contribution[13)] of several matrix chains to a given entanglement point of the probe, the dependence of t_w on the matrix relaxation time τ_{mat} also changes from that shown in eq 4.23.[4)] These two changes almost cancel each other, resulting in the N_1 dependence of $\tau_{CR,G}$ and $\tau_{CR,\varepsilon}$ almost indistinguishable from that shown in eq 4.24.[4)]

4-4-2. Star chains

The CR model for a q-arm star probe chain can be formulated on the basis of the Ham dynamics described in section 4-2-2. For this star probe having N_a entanglement segments in each arm, the viscoelastic and dielectric properties are described by eqs 4.8-4.13 with the $\tau_{H,G}$ and $\tau_{H,\varepsilon}$ therein being replaced by $\tau_{CR,G}$ and $\tau_{CR,\varepsilon}$ given below.[4)]

$$\tau_{CR,G} = \frac{1}{2}\tau_{CR,\varepsilon} = \frac{2\zeta_{tube}a^2N_a^2}{3\pi^2k_BT} \quad \text{with} \quad \zeta_{tube} = 12k_BTt_w/a^2 \qquad (4.25)$$

For monodisperse *star* chains, the entanglement lifetime t_w is not given by eq 4.23 (formulated for linear matrix chains) but can be self-consistently calculated from the arm motion. Details of this calculation is described in Chapter 8.

4-5. DTD Model for Linear Chains

4-5-1. Marrucci model

Marrucci[14] developed a concept of dynamic tube dilation (DTD) and calculated $G(t)$ on the basis of this concept. Although he did not specify the condition required for the DTD process to occur, his model includes all basic ideas utilized in more elaborated DTD models.[15,17-20] Considering this importance of the Marrucci model, its features are summarized below.

For a probe chain composed of N entanglement segments (of size a), the enlarged (dynamically dilated) tube is defined at respective t. This tube is composed $N'(t)$ enlarged segments of the size $a'(t)$ ($> a$), and each enlarged segment includes $\beta(t)$ entanglement segments, where $N'(t) = Na^2/[a'(t)]^2$ and $\beta(t) = [a'(t)]^2/a^2$. The central quantity in the Marrucci model is a fraction of the enlarged segments that *survive* at the time t, $\varphi'(t)$.

The meaning of this $\varphi'(t)$ is schematically explained in Fig. 4-5.[4] The filled (gray) and unfilled circles indicate the entanglement segments of the chain at times 0 and t, respectively. The enlarged tube at the time t has the diameter $a' = \beta^{1/2}a$. As a reference for this tube, every β entanglement segments *at the time 0* are combined into an enlarged segment to define the *initial,* enlarged tube of the diameter a'. At the time t, the hatched portion of this initial, enlarged tube still constrains the chain. The $\varphi'(t)$ is defined as a ratio, n_{suv}/N, where n_{suv} is the number of entanglement segments at time t that remain in this portion of the enlarged tube.

If the tube is fixed, this $\varphi'(t)$ is identical to the surviving fraction $\varphi(t)$ of the non-dilated tube of the diameter a. However, when the tube dynamically dilates, $\varphi'(t)$ is not identical to $\varphi(t)$, because of the mutual equilibration of β entanglement segments in each enlarged tube segment.

4-5-1-1. Viscoelastic properties of monodisperse systems

For a monodisperse system of entangled linear chains each composed of N entanglement segments, the normalized relaxation modulus $\mu(t) = G(t)/G_N$ deduced from the Marrucci model is written as[14]

$$\mu(t) = \frac{N'(t)}{N}\varphi'(t) \tag{4.26}$$

Here, $N'(t)$ is the number of the enlarged segments per chain at the time t, and $\varphi'(t)$ is the surviving fraction of these segments explained in Fig. 4-5.

In polymer solutions in usual solvents, the entanglement mesh size a_{sol} scales with the polymer volume fraction υ as $a_{sol} = a\upsilon^{-\alpha/2}$ (α = 1-1.3).[9] Marrucci assumed that the fully

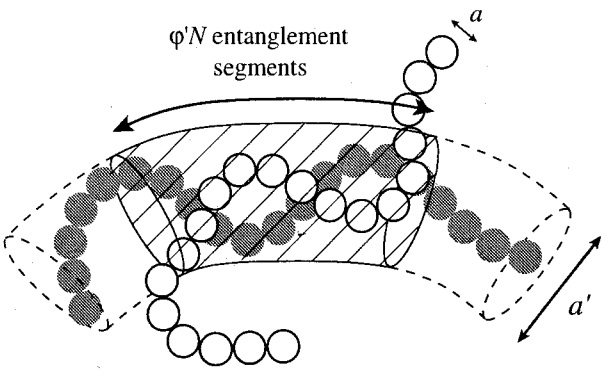

Fig.4-5 Schematic illustration of an initial, enlarged tube for a linear chain in a dynamically dilated tube. The hatching indicates the surviving portion of this initial tube having the fraction $\varphi'(t)$, and the filled (gray) and unfilled circles indicate the entanglement segments of the chain at times 0 and t.

relaxed portion of the chain (the portion out of the initial, enlarged tube) behaves as the solvent.[14] Then, $a'(t)$ is replaced by $a[\varphi'(t)]^{-\alpha/2}$. The corresponding expressions for $N'(t)$ and the number $\beta(t)$ of the entanglement segments in an enlarged tube segment are given by

$$N'(t) = N[\varphi'(t)]^{\alpha}, \quad \beta(t) = [\varphi'(t)]^{-\alpha} \tag{4.27}$$

From eq 4.27, eq 4.26 is rewritten as

$$\mu(t) = [\varphi'(t)]^{1+\alpha} \quad (\alpha = 1 - 1.3) \tag{4.28}$$

Some comments need to be added for this $\mu(t)$ expression. Among the N entanglement segments, only $N\varphi'(t)$ segments staying in the initial, enlarged tube (hatched portion in Fig. 4-5) contribute to $\mu(t)$. In the Marrucci model, these $N\varphi'(t)$ segments are (implicitly) assumed to have *partially relaxed* in a way that successive $\beta(t)$ segments are instantaneously equilibrated at any t under a constraint of preserving a vectorial sum of their bond vectors.[4] In other words, the $\beta(t)$ segments are assumed to be instantaneously coarse-grained into a larger modulus-sustaining unit (cf. section 3-3-2). Thus, the fractional memory of the initial chain orientation is given by $\varphi'(t)/\beta(t) = [\varphi'(t)]^{1+\alpha}$ (cf. eq 4.27). This fractional memory, being equivalent to an average of the orientation function $S(n,t)$ defined for the entanglement segments,[4] agrees with the $\mu(t)$ deduced from the Marrucci model (eq 4.28). This agreement means that the Marrucci model satisfies the stress optical rule (under the assumption of the instantaneous equilibration of the $\beta(t)$ entanglement segments).[4]

However, these $\beta(t)$ segments should have finite equilibration times determined by the entanglement lifetime t_w:[4] A time $\tau^{**} \sim t_w[\beta(t)]^2$ is required for their mutual equilibration (*via* the constraint release dynamics) in the dilated tube segment. A longer time $\tau^{***} \sim t_w N^2$ is necessary for complete equilibration of the chain contour length measured along the dilated tube. Thus the Marrucci expression of $\mu(t)$ (eq 4.28) is valid only in time scales $> \tau^{**}$, and the reptation in the dilated tube (assumed in the Marrucci model) would occur only at times $> \tau^{***}$.

For explicit calculation of the t dependence of $\mu(t)$, Marrucci considered decay of the orientational anisotropy *via* reptative diffusion and convection, the latter due to shortening of the tube during the DTD process.[14] The resulting $\mu(t)$ is written as

$$\mu(t) \cong [1 - t/\tau_{rep}(N)]^2 \quad \text{for } \alpha = 1 \tag{4.29}$$

where $\tau_{rep}(N)$ is the pure reptation time given by eq 4.17. In a range of $t \leq 0.4\tau_{rep}(N)$, this $\mu(t)$ is not significantly different from a single-exponential decay function, $\exp(-2.5t/\tau_{rep})$.[14] This result means that the DTD mechanism formulated in Marrucci's way accelerates the relaxation of monodisperse chain by a factor of 2.5 compared to the no dilation case (pure reptation case). This acceleration is in accord to experiments.[4]

4-5-1-2. Viscoelastic properties of blends

For blends of linear chains, Marrucci[14] considered reptation of the component chains in respective dilated tubes. The surviving fraction of the dilated tube for the *i*-th chain component at the time *t*, defined in the way explained in Fig. 4-5, is denoted by $\varphi_i'(t)$. Then, an average survival fraction is given by

$$\varphi'(t) = \sum_i v_i \varphi_i'(t) \tag{4.30}$$

where v_i is the volume fraction of the *i*-th component. The corresponding $\mu(t)$ is calculated with an argument similar to that for the monodisperse system. For the case of the dilation exponent $\alpha = 1$, the result is[14]

$$\mu(t) = \left[\sum_i v_i \varphi_i'(t)\right]^2 = [\varphi'(t)]^2 \tag{4.31}$$

Thus, the blending can affect the *t* dependence of $\varphi'(t)$ but does not change the relationship between $\mu(t)$ and $\varphi'(t)$ (cf. eqs 4.28 and 4.31).

For the above case of $\alpha = 1$, Marrucci again considered reptative diffusion and convection to calculate (in an approximate way) the *t* dependence of $\mu(t)$ of binary blends. The resulting $\mu(t)$ exhibits two-step relaxation processes;[14] the fast process corresponds to the relaxation of both short and long chain components, and the slow process reflects the relaxation of the long chain component. The relaxation intensity of the slow process scales as square of the volume fraction v_2 of the long chain component, while the terminal relaxation time scales as v_2. These features are close to those observed for actual binary blends.[4]

4-5-2. Supplement to Marrucci model (a model developed in this study[21])

The DTD molecular picture introduced in the Marrucci model can be easily applied to the

dielectric behavior of linear chains having *non-inverted* type-A dipoles, although Marrucci did not examine this behavior by himself. Thus, the dielectric relaxation function for the DTD process was formulated in this study.[21] The results obtained for monodisperse systems and blends are summarized below.

4-5-2-1. Dielectric properties of monodisperse systems

From eqs 3.12 and 3.13 with $\vartheta = 1$ for $n = 1\text{-}N$, the dielectric relaxation function $\Phi(t)$ of the type-A chain composed of N entanglement segments is written as

$$\Phi(t) = \frac{1}{Na^2} \sum_{n=1}^{N} \sum_{n'=1}^{N} \langle \mathbf{u}(n,t) \cdot \mathbf{u}(n',0) \rangle \tag{4.32}$$

Now, every successive β segments are combined into an enlarged segment having the bond vector $\mathbf{u}'$,

$$\mathbf{u}'(i,t) = \sum_{n=1+(i-1)\beta}^{i\beta} \mathbf{u}(n,t), \quad i = 1, 2, ..., N' \ (= N/\beta) \tag{4.33}$$

Because of an identity $\Sigma_{n=1}^{N} = \Sigma_{i=1}^{N'} \Sigma_{n=1+(i-\beta)}^{i\beta}$, the $\Phi(t)$ given by eq 4.32 is rewritten, *in any time scale,* in terms of this $\mathbf{u}'$ as

$$\Phi(t) = \frac{1}{N' \{a'\}^2} \sum_{i=1}^{N'} \sum_{j=1}^{N'} \langle \mathbf{u}'(i,t) \cdot \mathbf{u}'(j,0) \rangle \text{ with } \{a'\}^2 = \beta a^2 = \langle \mathbf{u}'^2 \rangle \tag{4.34}$$

This result indicates that the $\Phi(t)$ value does not change even if the β segments are mutually equilibrated in each enlarged segment under the constraint of preserving $\mathbf{u}'$. This feature of $\Phi(t)$ is different from the feature of $G(t)$; the mutual equilibration reduces the $G(t)$ value by the factor $1/\beta$; cf. section 3-3-2.

The above dielectric feature is utilized to calculate $\Phi(t)$ of the chain in the dilated tube. Under the situation depicted in Fig. 4-5, the size of the enlarged segment utilized in eq 4.34 can be chosen to be identical to the dilated tube diameter. These segments preserve their initial memory when they are in the surviving portion of the dilated tube (hatched portion). Thus, the averages in eq 4.34 are given by $\langle \mathbf{u}'(i,t) \cdot \mathbf{u}'(j,0) \rangle = (a')^2$ if the i-th and j-th enlarged segments at times t and 0 are located at the same position in this surviving portion. For the other cases, $\langle \mathbf{u}'(i,t) \cdot \mathbf{u}'(j,0) \rangle = 0$. From these arguments, $\Phi(t)$ is expressed as[21]

$$\Phi(t) = \frac{1}{N'} \sum_{i}^{'} \sum_{j}^{'} \delta_{ij'} = \varphi'(t) \tag{4.35}$$

where the summation Σ' is taken for the enlarged segments in the surviving portion of the dilated tube.

This result leads to an interesting relationship between the dielectric $\Phi(t)$ and viscoelastic $\mu(t)$ of the chain in the dilating tube (cf. eqs 4.28 and 4.35),

$$\mu(t) = [\Phi(t)]^{1+\alpha} \cong [\Phi(t)]^2 \tag{4.36}$$

This relationship, deduced from the general arguments for the expressions of $\Phi(t)$ and $G(t)$, is valid for the dominant part of relaxation at $t < \tau_1$ (terminal relaxation time) for $N >> 1$ irrespective of details of the chain motion in the dilating tube.[4,21] In other words, eq 4.36 holds not only for the Marrucci model[14] but also for the other models considering the chain in the dilated tube, e.g., the model of Viovy et al.[22] The DTD relationship, eq 4.36, is experimentally tested later in Chapter 7.

4-5-2-2. Dielectric properties of binary blends[21]

In the binary blends considered here, the probe and matrix chains (referred to as the components 2 and 1) may be chemically different but are uniformly mixed and entangled with each other. The number fractions of the entanglement segments of the probe and matrix are denoted by υ'_2 and υ'_1, respectively. (These υ'_i are reduced to the volume fractions if the probe and matrix are chemically identical.[21]) Either the probe or matrix chains, or both, have the non-inverted type-A dipoles. The survival fractions of the dilated tubes for the probe and matrix, $\varphi_2'(t)$ and $\varphi_1'(t)$, are defined in the way explained for the Marrucci model, and the average survival fraction is given by $\varphi'(t) = \upsilon'_1\varphi_1'(t) + \upsilon'_2\varphi_2'(t)$.

For both probe and matrix chains, the mutual equilibration of successive entanglement segments (DTD process itself) does not lead to decay of the dielectric memory. (This situation is similar to that explained for the monodisperse system.) Thus, the dielectric $\Phi(t)$ of the blend as a whole can be written as[21]

$$\Phi(t) = \tilde{\upsilon}'_1\Phi_1(t) + \tilde{\upsilon}'_2\Phi_2(t) \text{ with } \Phi_i(t) = \varphi_i'(t) \tag{4.37}$$

Here, $\Phi_i(t)$ and $\tilde{\upsilon}'_i$ are the dielectric relaxation function and intensity coefficient of the component i, the latter being defined by

$$\tilde{\upsilon}'_i = \frac{\upsilon'_i\delta_i}{\upsilon'_1\delta_1 + \upsilon'_2\delta_2} \quad (i = 1, 2) \tag{4.38}$$

In eq 4.38, δ_i represents the squared magnitude of type-A dipoles per entanglement segment of

the component i ($\delta_i = 0$ if this component has no type-A dipoles). The $\tilde{v}'_i$ is reduced to the volume fraction of the component i if the probe and matrix are chemically identical.

For the DTD process (with the dilation exponent $\alpha = 1$), eqs 4.31 and 4.37 specify the relationship between the viscoelastic and dielectric properties of the blend. Hereafter, a focus is placed on a special class of blends in which the probe is dilute and entangled only with the matrix chains and only the probe has the type-A dipoles ($\delta_1 = 0$ in eq 4.38).

The dilute probes do not affect the behavior of the matrix chains. Then, the average tube survival fraction $\varphi'(t)$ in the blend should coincide with the fraction $\varphi_{1,m}'(t)$ in the monodisperse system of the matrix. This $\varphi_{1,m}'(t)$ can be expressed in terms of the normalized relaxation modulus $\mu_{1,m}(t)$ of this system if the DTD picture is valid; $\varphi_{1,m}'(t) \cong [\mu_{1,m}(t)]^{1/2}$ (cf. eq 4.28 with $\alpha = 1$). Thus, if the DTD pre-requisite (immediate CR equilibration of entanglement segments on removal of topological constraints)[4] is valid for the dilute type-A probe in the blend, eqs 4.31 and 4.37 are combined to give a relationship between $\mu_2(t)$ and $\Phi_2(t)$ of this probe,[21]

$$\mu_2(t) = \varphi'(t)\varphi_2'(t) \cong [\mu_{1,m}(t)]^{1/2}\,\Phi_2(t) \qquad (4.39)$$

This DTD relationship is tested experimentally in Chapter 7.

4-6. DTD Model for Monodisperse Star Chains

4-6-1. Ball-McLeish model[15]

Within the context of the tube model, the branching point of a star chain is assumed to be fixed in space (in the time scale of full relaxation), and the star arm is considered to relax by retracting along the tube.[3]

The early models proposed by Doi and Kuzuu (DK)[23] and by Pearson and Helfand (PH)[24] assumed the arm retraction in a *fixed* tube. This retraction over a curvilinear distance z measured along the arm contour (with $z = 0$ corresponding to the free arm end; see Fig. 4-6) is associated with an entropic potential $U_{DK}(z)$,[23,24]

$$U_{DK}(z) = \nu_G k_B T N_a \frac{z^2}{\{L_{eq}\}^2} \quad \text{with } L_{eq} = aN_a \text{ (equilibrium arm length)} \qquad (4.40)$$

Here N_a is the number of entanglement segments in each arm. For the Gaussian arms, the coefficient ν_G has a well-defined value, 15/8.[3,15]

The DK and PH models predict that the terminal viscoelastic relaxation time τ_{arm} ($\propto \exp[U_{DK}(L_{eq})/k_BT]$) increases exponentially with N_a.[23,24] The predicted τ_{arm} value as well as the calculated viscoelastic mode distribution quantitatively agree with experiments *if* the coefficient ν_G in the models is *adjusted* to $\cong 0.6$.[24] However, for long arm stars, this adjustment corresponds an adjustment of τ_{arm} by orders of magnitude;[15] for example, for $N_a = 20$, the τ_{arm} value for $\nu_G = 15/8$ (correct Gaussian coefficient) is 10^{11} times longer than the τ_{arm} value for the

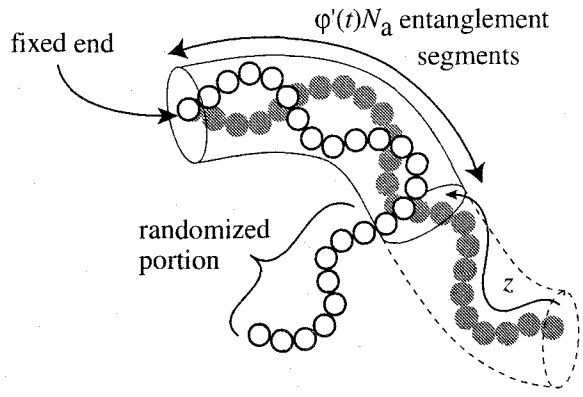

Fig.4-6 Schematic illustration of dynamically dilated tube for star arm with the fixed end.

adjusted $\nu_G \cong 0.6$. This tremendous difference suggests that the assumption of the fixed tube made in the DK and PH models is not valid for monodisperse star chains. Focusing on this problem, Ball and McLeish (BM)[15] applied the dynamic tube dilation (DTD) concept to the arm retraction process. Features of the BM model are summarized below.

4-6-1-1. Arm retraction in dilated tube

If the arm *once* retracts over the curvilinear distance z (cf. Fig. 4-6), the entanglement segments near the arm end are randomized to fully relax when the arm stretches to the original, equilibrium length L_{eq}. The number of the randomized segments is given by $N_a z/L_{eq}$. The BM model considers that these segments behave as a solvent and the tube dilates accordingly.[15] This dilation leads to enlargement of the modulus-sustaining segment (in the sense explained for the Marrucci model; cf. section 4-5-1). Consequently, the number of the enlarged segments N_a' decreases as the tube dilates.

For a given retraction distance z, the BM model introduces a conditional survival fraction of the dilated tube $\tilde{\varphi}'(z) = 1 - z/L_{eq}$ to express N_a' as[15]

$$N_a' = \tilde{\varphi}' N_a \tag{4.41}$$

This expression corresponds to the dynamic dilation with the exponent $\alpha = 1$; cf. eq 4.27. The arm retraction over an infinitesimal distance dz from z to $z+dz$ is assumed to be associated with an entropic potential $dU_{BM}(z)$ determined by this N_a'. Specifically, utilizing the functional form of the DK potential (eq 4.40) but replacing the N_a factor therein by N_a', the BM model expresses the potential as[15]

$$dU_{BM} = \frac{2\nu_G k_B T}{\{L_{eq}\}^2}[N_a \tilde{\varphi}']\, z\, dz = \frac{2\nu_G N_a k_B T}{\{L_{eq}\}^2}\left(1 - \frac{z}{L_{eq}}\right) z\, dz \tag{4.42}$$

With this activation potential, the relaxation time $\tau_{BM}(z+dz)$ for the segment located at the curvi-

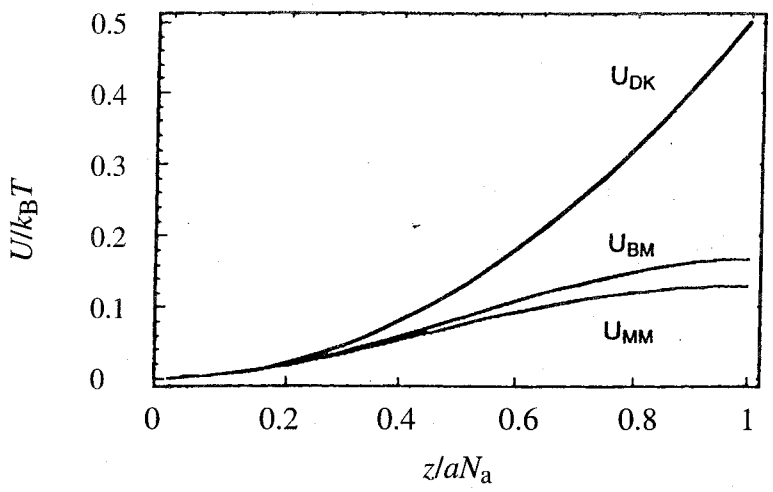

Fig.4-7 Comparison of the activation barriers for the star arm retraction, U_{DK}, U_{BM}, and U_{MM}, utilized in the Doi-Kuzuu and Pearson-Helfand models, the Ball-McLeish model, and the Milner-McLeish model, respectively.

linear distance z+dz is related to the relaxation time $\tau_{BM}(z)$ at z,

$$\tau_{BM}(z+dz) = \tau_{BM}(z) \exp\left[\frac{dU_{BM}(z)}{k_BT}\right] \tag{4.43}$$

Integration of eq 4.43 gives the BM prediction for the relaxation time,[15]

$$\tau_{BM}(z) = \tau^* \exp\left[\frac{U_{BM}(z)}{k_BT}\right] \text{ with } U_{BM}(z) = \nu_G N_a k_B T\left[\frac{z^2}{L_{eq}^2} - \frac{2z^3}{3L_{eq}^3}\right] \tag{4.44}$$

Here, τ^* is the Rouse relaxation time within one entanglement segment.

From eq 4.44, the longest relaxation time is found to be

$$\tau_{arm} = \tau_{BM}(L_{eq}) = \tau^* \exp\left[\frac{\nu_G N_a}{3}\right] \tag{4.45}$$

This τ_{arm} is much shorter than that predicted from the fixed tube model, $\tau_{arm} \cong \tau^* \exp[U_{DK}(L_{eq})/k_BT] = \tau^* \exp[\nu_G N_a]$. In fact, the BM model effectively reduces the ν_G factor in the fixed tube model by a factor of 1/3 (cf. eq 4.45), thereby explaining the measured τ_{arm} values with considerable accuracy. This result is related to a reduction of the activation potential by the DTD mechanism:[15] This reduction, made through the $-2z^3/3L_{eq}^3$ term in U_{BM} (eq 4.44), is more significant for deeper arm retraction. Fig. 4-7 compares this U_{BM} potential with U_{DK} utilized in the fixed tube model.

4-6-1-2. Viscoelastic properties

In the BM model, the modulus sustained by the segments at the curvilinear distances between z and z+dz is given by $dG = d|\{(\tilde{\varphi})^2 G_N\}| = 2G_N\{1 - (z/L_{eq})\}dz/L_{eq}$.[4,15] The model

considers that these segments have a well-defined relaxation time $\tau_{BM}(z)$ (eq 4.44) and this dG relaxes at a rate $1/\tau_{BM}(z)$. Thus, the relaxation modulus deduced from the BM model is given by[15]

$$G(t) = G_N \frac{2}{L_{eq}} \int_0^{L_{eq}} \left[1 - \frac{z}{L_{eq}}\right] \exp\left(-\frac{t}{\tau_{BM}(z)}\right) dz \tag{4.46}$$

(This expression of $G(t)$ is consistent with the stress-optical rule because of the internal equilibration assumed for the chain in the dilated tube,[4] as discussed for the Marrucci model.)

4-6-2. Milner-McLeish model [17,18]

Milner and McLeish (MM) refined the BM model by considering (1) the thermal fluctuation of the arm contour length, (2) a solution of the first passage problem that gives a more accurate expression of $\tau(z)$ than eq 4.44, and (3) the dilation exponent $\alpha = 4/3$ suggested by Colby and Rubinstein[25] (instead of $\alpha = 1$ utilized in the BM model).

For the point (1), Milner and McLeish focused on the arm retraction over a small curvilinear distance $z << L_{eq}$ (= aN_a). This *shallow retraction* occurs *via* the Rouse fluctuation[3,17] free from the activation potential ($U(z) << k_BT$). Considering that the branching point of the arm does not influence the shallow retraction and thus the time $\tau_{sh}(z)$ for this retraction is independent of N_a, they evaluated $\tau_{sh}(z)$ as[17]

$$\tau_{sh}(z) = \frac{225\pi^3 \tau^* N_a^4}{256}\left(\frac{z}{L_{eq}}\right)^4 = \frac{225\pi^3 \tau^*}{256 a^4} z^4 \tag{4.47}$$

with τ^* being the Rouse equilibration time within one entanglement segment.

For large z (*deep retraction*), the arm feels the potential. Considering the above point (3), Milner and McLeish expressed the potential as[17,18]

$$U_{MM}(z) = \frac{2\nu_G N_a k_B T}{(\alpha+1)(\alpha+2)}\left[1 - \left(1 - \frac{z}{L_{eq}}\right)^{\alpha+1}\left(1 + \frac{(\alpha+1)z}{L_{eq}}\right)\right] \tag{4.48}$$

with $\alpha = 4/3$ and $\nu_G = 15/8$. This U_{MM} is shallower than U_{BM}, as shown in Fig. 4-7. Solving the first passage problem for the arm end motion under the potential U_{MM} (the point (2)), they evaluated the time $\tau_{dp}(z)$ required for the deep retraction over the curvilinear distance z.[17,18] The result is

$$\tau_{dp}(z) \cong \frac{\tau^* N_a^{3/2} \pi^{5/2} \exp\left(\frac{U_{MM}(z)}{k_B T}\right)}{30^{1/2}\left(\frac{z}{L_{eq}}\right)\left[\left\{1 - \frac{z}{L_{eq}}\right\}^{2\alpha} + \Gamma\left(\frac{1}{\alpha+1}\right)^{-2}\left(\frac{4+4\alpha}{15N_a}\right)^{2\alpha/(\alpha+1)}\right]^{1/2}} \tag{4.49}$$

Milner and McLeish further combined this $\tau_{dp}(z)$ with $\tau_{sh}(z)$ (eq 4.47) to obtain an (approximate) expression of the relaxation time in the entire range of z,[17,18]

$$\tau_{MM}(z) \cong \frac{\tau_{sh}(z)\exp\left(\frac{U_{MM}(z)}{k_BT}\right)}{1 + \frac{\tau_{sh}(z)}{\tau_{dp}(z)}\exp\left(\frac{U_{MM}(z)}{k_BT}\right)} \qquad (4.50)$$

The crossover from the shallow retraction (eq 4.47) to the deep retraction (eq 4.49) occurs at $z \cong N_a^{1/2}a$ ($\cong$ thermal fluctuation length of the arm).

In the MM model, the modulus sustained by the segments at the curvilinear distances between z and z+dz is given by $dG = d|\{(\tilde{\varphi})^{1+\alpha}G_N\}| = (\alpha+1)G_N\{1-(z/L_{eq})\}^{\alpha}dz/L_{eq}$. (Here, $\tilde{\varphi}(z) = 1 - z/L_{eq}$ is the conditional survival fraction of the dilated tube for a given z.) These segments have a well-defined relaxation time $\tau_{MM}(z)$. Thus, the relaxation modulus deduced from the MM model is written as[17,18]

$$G(t) = G_N\frac{(\alpha+1)}{L_{eq}}\int_0^{L_{eq}}\left[1-\frac{z}{L_{eq}}\right]^{\alpha}\exp\left(-\frac{t}{\tau_{MM}(z)}\right)dz \quad \text{with } \alpha = 4/3 \qquad (4.51)$$

4-6-3. Supplement to BM and MM models (a model developed in this study[26,27])

The DTD molecular picture considered in the BM and MM models can be applied to the dielectric behavior of the type-A star chains, although Ball, Milner, and McLeish did not examine this behavior by themselves. Thus, the dielectric relaxation function for the DTD process of those star chains was formulated in this study.[26,27] The results are summarized below.

4-6-3-1. Arm motion in the dilated tube

Fig. 4-8 depicts the arm motion in the dilated tube of the diameter a'. The filled and unfilled circles indicate the entanglement segments at times 0 and t, respectively. In Fig. 4-8, the branching point is not fixed in space but allowed to displace in the dilated tube by $\mathbf{D}_b(t)$ (thick dotted arrow). The tube survival fraction $\varphi_\alpha'(t)$ for the α-th arm is defined as a ratio n_α/N_a, where n_α is the number of the entanglement segments of this arm remaining somewhere in the entire surviving portion of the dilated tube, i.e., in the cross-hatched zone shown in Fig. 4-8a. The average survival fraction of the dilated tube is given by[26]

$$\varphi'(t) = \frac{1}{q}\sum_{\alpha=1}^{q}\varphi_\alpha'(t) \qquad (4.52)$$

The total number of entanglement segments in the surviving portion is $q\varphi'(t)N_a$.

In consideration of the motion of the α-th arm, it is convenient to subdivide the contour of

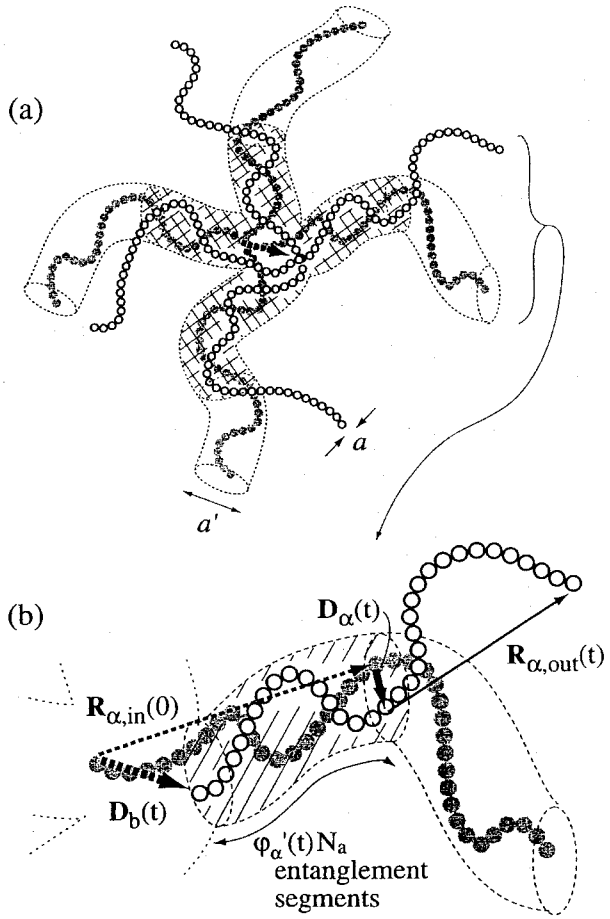

Fig.4-8 (a) Schematic illustration of motion of the star chain in a dilating tube of diameter $a'(t)$; (b) magnified view for motion of a particular (α-th) arm. In both parts (a) and (b), filled and unfilled circles indicate the entanglement segments at time 0 and t. The dotted tube indicates an initial thick tube defined at the time 0, and the cross-hatched portion in part (a) represents the portion of this initial thick tube surviving at time t.

this arm at the time t in two portions, the outer portion that has escaped from the dilated tube (*via* any type of motion) and the inner portion remaining in this tube. The outer portion has an end-to-end vector $\mathbf{R}_{\alpha,out}(t)$ (thin solid arrow in Fig. 4-8b) that is uncorrelated with the initial chain configuration characterized with the vectors connecting the branching point and arm ends, $\mathbf{R}_{\alpha'}(0)$ with $\alpha' = 1 - q$. This portion has no contribution to $\varphi_\alpha'(t)$. In contrast, the inner portion preserves its initial memory to some extent and contributes to $\varphi_\alpha'(t)$.

At the time t, the end-to-end vector of this inner portion can be expressed as[26]

$$\mathbf{R}_{\alpha,in}(t) = \mathbf{R}_{\alpha,in}(0) + \mathbf{D}_\alpha(t) - \mathbf{D}_b(t) \tag{4.53}$$

Here, $\mathbf{D}_b(t)$ is a displacement of the branching point, and $\mathbf{D}_\alpha(t)$ denotes a displacement of the entanglement segment of the α-th arm at the outer edge of the surviving portion of the dilated tube; cf. Fig. 4-8b. This ed*ge-segment* at the time t is not necessarily the same as that at the time 0 because of the branching point displacement: $\mathbf{D}_\alpha(t)$ is defined as the vector connecting the edge-segments at these two times (thick solid arrow in Fig. 4-8b). Finally, $\mathbf{R}_{\alpha,in}(0)$ is a vector

connecting the branching point and the edge-segment, both at the time 0 (thin dotted arrow).

Some general features of the arm motion can be specified without detailed knowledge about the arm dynamics. The dilated tube diameter $a'(t)$ represents a length scale over which the lateral motion of the arm can occur in a given time scale t. Thus, the displacement $\mathbf{D}_b(t)$ should be uncorrelated with the initial configuration, as-long as its magnitude $|\mathbf{D}_b(t)|$ is smaller than a'. This argument suggests a relationship,[26]

$$<\mathbf{D}_b(t)\cdot\mathbf{R}_{\alpha'}(0)> = 0 \quad (\alpha' = 1 - q) \tag{4.54}$$

A comment needs to be made for eq 4.54. For $|\mathbf{D}_b(t)| > a'$, the branching point penetrates into a tube for a particular (α'-th) arm to raise correlation between $\mathbf{D}_b(t)$ and $\mathbf{R}_{\alpha'}(0)$ and violate eq 4.54; see Fig. 4-8b. For this case, the other arms are sucked into this particular tube. However, this sucked-in motion, similar to that of pom-pom chains in the no*nlinear* regime,[28] is an unlikely motion for the star chains in the *linear regime*. Thus, eq 4.54 can be safely assumed at equilibrium (where the dielectric relaxation is detected).

The coincidence of the dilated tube diameter and the scale of lateral motion also means that the displacement $\mathbf{D}_\alpha(t)$ of the edge-segment has a magnitude $|\mathbf{D}_\alpha(t)| < a'$. Thus, $\mathbf{D}_\alpha(t)$ would not be correlated with the initial arm configuration *if* the time scale considered is well below a time $\tau_{eq,in}$ required for equilibration of the configuration of the inner portion, i.e., equilibration of both length $R_{\alpha,in} = |\mathbf{R}_{\alpha,in}|$ and orientation $\mathbf{R}_{\alpha,in}/R_{\alpha,in}$. This argument suggests a relationship,

$$<\mathbf{D}_\alpha(t)\cdot\mathbf{R}_{\alpha'}(0)> = 0 \text{ for } t < \tau_{eq,in} \quad (\alpha' = 1 - q) \tag{4.55}$$

A comment needs to be made also for eq 4.55. The complete orientational equilibration occurs only when the arm escapes from the dilated tube, and $\tau_{eq,in}$ is close to the longest relaxation time τ_{arm}. Nevertheless, some degree of equilibration may occur even at $t < \tau_{eq,in}$ and eq 4.55 may have to be modified accordingly. However, discussion of this modification is postponed to section 4-6-3-4 and, in the next section, the expression of the dielectric relaxation function $\Phi(t)$ is derived in the simplest way by utilizing eq 4.55 (without the modification) together with eq 4.54.

4-6-3-2. DTD relationship between Φ and μ of star chains

The dielectric $\Phi(t)$ of the q-arm star chains (eq 3.14) is contributed from the auto-correlation and cross-correlation of the end-to-end vectors of the arms, $<\mathbf{R}_\alpha(t)\cdot\mathbf{R}_{\alpha'}(0)>$ with $\alpha, \alpha' = 1 - q$. The outer portion of the arm having escaped from the dilated tube at time t is uncorrelated with $\mathbf{R}_{\alpha'}(0)$, as explained in the previous section. From eqs 4.53-4.55, the surviving correlation terms $<\mathbf{R}_{\alpha,in}(t)\cdot\mathbf{R}_{\alpha'}(0)>$ are replaced by $<\mathbf{R}_{\alpha,in}(0)\cdot\mathbf{R}_{\alpha'}(0)>$. Thus, $\Phi(t)$ is rewritten as[26]

$$\Phi(t) = \frac{1}{q N_a a^2} \sum_{\alpha,\, \alpha' = 1}^{q} <\mathbf{R}_{\alpha,in}(0)\cdot\mathbf{R}_{\alpha'}(0)> \tag{4.56}$$

At equilibrium, the $<\mathbf{R}_{\alpha,in}(0)\bullet\mathbf{R}_{\alpha'}(0)>$ terms included in eq 4.56 satisfy the Gaussian relationships,[26]

$$<\mathbf{R}_{\alpha,in}(0)\bullet\mathbf{R}_{\alpha'}(0)> = <\{\mathbf{R}_{\alpha,in}(0)\}^2>\delta_{\alpha\alpha'} \tag{4.57}$$

and

$$\sum_{\alpha=1}^{q} <\{\mathbf{R}_{\alpha,in}(0)\}^2> = \sum_{\alpha=1}^{q} <\{\mathbf{R}_{\alpha,in}(t)\}^2> = q\varphi'(t)N_a a^2 \tag{4.58}$$

In eq 4.58, the *entire* portion of the surviving dilated tube (cross-hatched portion in Fig. 4-8a) is considered to contain the same number of entanglement segments at the times 0 and t. This number is given by $q\varphi'(t)N_a$, where $\varphi'(t)$ is the average survival fraction of the dilated tube defined by eq 4.52.

Substitution of eqs 4.57 and 4.58 into eq 4.56 gives the expression of $\Phi(t)$,

$$\Phi(t) = \varphi'(t) \text{ for the star chains} \tag{4.59}$$

As similar to the situation for linear chains, the normalized relaxation modulus $\mu(t)$ of the star chains is given by $[\varphi'(t)]^{1+\alpha}$ with α (= 1-1.3) being the dilation exponent; cf. eq 4.28. Thus, $\Phi(t)$ and $\mu(t)$ of the monodisperse star chains satisfy a DTD relationship[26]

$$\mu(t) = [\Phi(t)]^{1+\alpha} \tag{4.60}$$

This relationship for the stars, obtained with the aid of eq 4.55 and thus valid in a time scale where eq 4.55 holds, is formally identical to the DTD relationship derived for the monodisperse linear chains (eq 4.36), although the t dependence of $\Phi(t)$ is quite different for the star and linear chains. In addition, the BM and MM models can be reformulated for $\Phi(t)$ to obtain the same relationship in the dominant part of relaxation, as demonstrated in the next section.

Thus, the above DTD relationship has a rather wide applicability and holds whenever eq 4.55 holds and the tube dilates in a way considered in Fig. 4-8. This relationship is experimentally tested for the star polyisoprene chains later in Chapter 8.

4-6-3-3. Reformulation of BM and MM models for Φ

In the BM and MM models,[15,17,18] the dielectric memory $\tilde{\Phi}(z)$ for a given arm retraction distance z is given by $1-z/L_{eq}$. (For this z, the memory is preserved for the entanglement segments located at curvilinear distances $z' > z$ but vanishes for those at $z' < z$; cf. Fig. 4-6.) Thus, the dielectric memory sustained by the segments at the curvilinear distances between z and z+dz is given by $d|\tilde{\Phi}| = dz/L_{eq}$. Within the context of the BM and MM models, this memory decays

with the well-defined relaxation time of these segments, $\tau_{BM}(z)$ and/or $\tau_{MM}(z)$ (eqs 4.44 and 4.50). Thus, the dielectric relaxation functions of the stars deduced from the BM and MM models are commonly written as[26)]

$$\Phi(t) = \frac{1}{L_{eq}} \int_0^{L_{eq}} \exp\left(-\frac{t}{\tau(z)}\right) dz \quad \text{with } \tau(z) = \tau_{BM}(z) \text{ and/or } \tau_{MM}(z) \qquad (4.61)$$

For long arms ($N_a >> 1$), both $\tau_{BM}(z)$ and $\tau_{MM}(z)$ increase exponentially on an increase of z (> thermal fluctuation length ~ $N_a^{1/2}a$). For this case, the exponentially decaying term appearing in eq 4.61 can be approximated as $\exp\{-t/\tau(z)\} \cong 1$ for $z > z^*$ and $\exp\{-t/\tau(z)\} \cong 0$ for $z < z^*$,[15)] where $z^*(t)$ is an average retraction distance at the time t determined from an equation, $\tau_{BM}(z^*(t)) = t$ and/or $\tau_{MM}(z^*(t)) = t$. (Equations 4.44 and 4.50 need to be numerically inverted to evaluate this z^*.) This approximation, valid for the dominant part of the relaxation (at t well below the arm relaxation time τ_{arm}), means that the arm segments at $z > z^*(t)$ have hardly relaxed while those at $z < z^*(t)$ have fully relaxed at t.

With the above approximation, the integral (eq 4.61) leads to an expression of $\Phi(t)$,[26)]

$$\Phi(t) \cong 1 - \frac{z^*(t)}{L_{eq}} \qquad (4.62)$$

Here, the factor $1 - z^*(t)/L_{eq}$ is equivalent to the average survival fraction of the dilated tube. With the same approximation, the normalized relaxation modulus $\mu(t) = G(t)/G_N$, originally obtained in the BM and MM models (eqs 4.46 and 4.51), becomes[26)]

$$\mu(t) \cong \left[1 - \frac{z^*(t)}{L_{eq}}\right]^{1+\alpha} \quad (\alpha = 1 \text{ and } 4/3 \text{ for the BM and MM models}) \qquad (4.63)$$

As noted from eqs 4.62 and 4.63, the BM and MM models also lead to the DTD relationship (eq 4.60) for the dominant part of the relaxation of the long arm stars.

4-6-3-4. Modified DTD relationship accounting tube-edge effect[27)]

Equation 4.55, utilized in derivation of the DTD relationship (eq 4.60), should be valid at a time scale t well below the time $\tau_{eq,in}$ required for equilibration of both length and orientation of the inner portion of the arm remaining in the dilated tube. However, as t approaches $\tau_{eq,in}$, this equilibration may gradually proceed and eq 4.60 may fail accordingly. For this case, the DTD relationship needs to be modified. In this section, this modification is made for a special case that the branching point is fixed in space and the star arms move independently (as assumed in the BM and MM models).

For this case, the end-to-end vector of the inner portion $\mathbf{R}_{\alpha,in}(t)$ (eq 4.53 with $\mathbf{D}_b(t) = \mathbf{0}$) and its squared average are given by

$$\mathbf{R}_{\alpha,\mathrm{in}}(t) = \mathbf{R}_{\alpha,\mathrm{in}}(0) + \mathbf{D}_\alpha(t) \tag{4.64}$$

$$\langle\{\mathbf{R}_{\alpha,\mathrm{in}}(t)\}^2\rangle = \langle\{\mathbf{R}_{\alpha,\mathrm{in}}(0)\}^2\rangle + 2\langle\mathbf{D}_\alpha(t)\cdot\mathbf{R}_{\alpha,\mathrm{in}}(0)\rangle + \langle\{\mathbf{D}_\alpha(t)\}^2\rangle \tag{4.65}$$

For the case of the fixed branching point, the surviving portion of the dilated tube for each arm should contain the same number of the entanglement segments in *fully equilibrated* states at the times 0 and t.[27] Then, as noted from eq 4.65, $\langle\{\mathbf{R}_{\alpha,\mathrm{in}}(t)\}^2\rangle$ coincides with $\langle\{\mathbf{R}_{\alpha,\mathrm{in}}(0)\}^2\rangle$ to raise a correlation between $\mathbf{D}_\alpha(t)$ and $\mathbf{R}_{\alpha,\mathrm{in}}(0)$,[27]

$$\langle\mathbf{D}_\alpha(t)\cdot\mathbf{R}_{\alpha,\mathrm{in}}(0)\rangle = -\frac{1}{2}\langle\{\mathbf{D}_\alpha(t)\}^2\rangle \tag{4.66}$$

Under an assumption that the edge segment at times 0 and t is located at an arbitrary position in the edge of the dilated tube shown in Fig. 4-8b (designated as ξ-η plane), the mean-square displacement of this segment in the interval of time between 0 and t is calculated as[27]

$$\langle\mathbf{D}_\alpha^2(t)\rangle = \frac{1}{\pi^2\,(a'/2)^4}\int\left\{(\xi-\xi_0)^2 + (\eta-\eta_0)^2\right\}d\xi\,d\xi_0\,d\eta\,d\eta_0 = \left(\frac{a'-a}{2}\right)^2 \tag{4.67}$$

Here, (ξ, η) and (ξ_0, η_0) represents the coordinates of the edge segment at times t and 0, respectively, and the integral is conducted in a circular region of diameter $a'-a$ specified by an inequality, $\xi^2+\eta^2 < (a'-a)^2/4$), i.e., in the region available for the center of mass of the segment. (The displacement is set to be zero when the tube is not dilated.)

From eqs 4.64 - 4.67 together with eq 3.15 (definition of $\Phi(t)$ for the case of fixed branching point), an expression of $\Phi(t)$ can be obtained as[27]

$$\begin{aligned}\Phi(t) &= \frac{1}{N_a a^2}\langle\mathbf{R}_{\alpha,\mathrm{in}}(t)\cdot\mathbf{R}_{\alpha,\mathrm{in}}(0)\rangle \\ &= \frac{1}{N_a a^2}\left(\langle\mathbf{R}_{\alpha,\mathrm{in}}(0)\cdot\mathbf{R}_{\alpha,\mathrm{in}}(0)\rangle - \frac{1}{2}\langle\{\mathbf{D}_\alpha(t)\}^2\rangle\right) \\ &= \varphi'(t) - \frac{1}{8N_a}\left[\{\varphi'(t)\}^{-\alpha/2} - 1\right]^2 \quad (\alpha = 1\text{-}1.3)\end{aligned} \tag{4.68}$$

Here, $\varphi'(t) = \langle\mathbf{R}_{\alpha,\mathrm{in}}(0)\cdot\mathbf{R}_{\alpha,\mathrm{in}}(0)\rangle/N_a a^2$ is the survival fraction of the dilated tube (for the case of the fixed branching point), and the expression for the dilated tube diameter $a' = a\{\varphi'(t)\}^{-\alpha/2}$ was applied to $\langle\{\mathbf{D}_\alpha(t)\}^2\rangle = (a'-a)^2/4$.

At $t < \tau_{\mathrm{arm}}$, eq 4.68 overestimates the effect of the displacement of the edge segment (*tube-edge effect*) on the dielectric relaxation because the complete equilibration (assumed for eq 4.66) requires a time ~ τ_{arm}. Thus, the above expression of $\Phi(t)$ is to be considered as an ex-

treme expression for the case of the maximum tube-edge effect. This expression is different from the expression without the tube-edge effect (eq 4.59) by a factor $-[\{\varphi'(t)\}^{-\alpha/2}-1]^2/8N_a$. This factor, representing the (maximum) tube-edge effect, becomes important at long t where $\varphi'(t)$ decays to the order of $N_a^{-1/(1+\alpha)}$ and the factors φ' and $\{\varphi'\}^{-\alpha}/N_a$ become comparable in magnitudes.

The above tube-edge effect does not introduce significant changes in the expression of the normalized relaxation modulus, $\mu(t) = \{\varphi'(t)\}^{1+\alpha}$ (for the dominant part of the arm relaxation). Thus, the DTD relationship between $\mu(t)$ and $\Phi(t)$ of the star chains, being modified for this effect (eq 4.68), can be written as[27]

$$\Phi(t) = \{\mu(t)\}^{1/(1+\alpha)} - \frac{1}{8N_a}\left[\{\mu(t)\}^{-\alpha/2(1+\alpha)} - 1\right]^2 \tag{4.69}$$

Again, the difference between this expression and the expression given by eq 4.60 (without the tube-edge effect) becomes important at long t where $\varphi'(t) \sim O(N_a^{-1/(1+\alpha)})$ and $\mu(t) \sim O(1/N_a)$. Experiments[4] indicate that the steady state compliance J_e of well-entangled star chains is close to the Rouse-Ham value, $J_{RH} = 2(15q-14)M/5(3q-2)^2cRT \cong 2N_a/3G_N$ (for the arm number $q \geq 6$). Thus, the normalized terminal relaxation intensity $\mu(\tau_{arm})$ scales as $1/G_N J_e \sim 1/G_N J_{RH} = 3/2N_a$, suggesting that the tube-edge effect becomes important at long $t \sim O(\tau_{arm})$ where $\mu(t)$ decays to $O(1/N_a)$. [27]

The tube-edge effect can be also incorporated in the BM and MM models reformulated for $\Phi(t)$ (section 4-6-3-3). With this effect, the dielectric memory $\tilde{\Phi}(z)$ for a given arm retraction distance z is evaluated as the Φ given by eq 4.68 with φ' being replaced by $1-z/L_{eq}$. Then, the dielectric memory sustained by the entanglement segments at the curvilinear distances between z and $z+dz$ can be expressed as

$$d\left|\tilde{\Phi}\right| = \left[1 + \frac{\alpha}{8N_a}\left(1-\frac{z}{L_{eq}}\right)^{-(\alpha+1)} - \frac{\alpha}{8N_a}\left(1-\frac{z}{L_{eq}}\right)^{-(1+\alpha/2)}\right]\frac{dz}{L_{eq}} \tag{4.70}$$

Within the context of the BM and MM models, this memory decays with a well-defined relaxation time, $\tau(z) = \tau_{BM}(z)$ and/or $\tau_{MM}(z)$ (eqs 4.44 and 4.50). Thus, $\Phi(t)$ deduced from the BM and MM models in presence of the (maximum) tube-edge effect can be written as[27]

$$\Phi(t) = \frac{1}{K_n L_{eq}}\int_0^{z_c}\left[1 + \frac{\alpha}{8N_a}\left\{\left(1-\frac{z}{L_{eq}}\right)^{-(\alpha+1)} - \left(1-\frac{z}{L_{eq}}\right)^{-(1+\alpha/2)}\right\}\right]\exp\left(-\frac{t}{\tau(z)}\right)dz$$

$$\text{with } z_c = L_{eq} - a \text{ and } K_n = \frac{z_c}{L_{eq}} + \frac{1}{8N_a}\left[1-\left(1-\frac{z_c}{L_{eq}}\right)^{-\alpha/2}\right]^2 \tag{4.71}$$

In eq 4.71, the upper bound of the integral z_c is introduced to avoid divergence of the integral.

(This upper bound value was chosen according to a fact that the entanglement segment closest to the branching point fully relaxes when the arm end retracts by a distance $L_{eq} - a$.) The K_n is a normalization factor ensuring $\Phi(0) = 1$.

References

1. P. E. Rouse, *J. Chem. Phys.* **21**, 1272 (1953).
2. J. S. Ham, *J. Chem. Phys.* **26**, 625 (1957).
3. M. Doi and S. F. Edwards, *The Theory of Polymer Dynamics,* Clarendon, Oxford (1986).
4. H. Watanabe, *Prog. Polym. Sci.*, **24**, 1253 (1999).
5. H. Watanabe, *Macromol. Rapid Commun.*, **22**, 127 (2001).
6. H. Watanabe, H. Yoshida, and T. Kotaka, *Polym. J.* **22**, 153 (1990).
7. M. Doi and S. F. Edwards, *J. Chem. Soc. Faraday Trans. 2* **74**,1789 (1978).
8. M. Doi and S. F. Edwards, *J. Chem. Soc. Faraday Trans. 2* **74**,1802 (1978).
9. J. D. Ferry, *Viscoelastic Properties of Polymers (3rd ed)*, Wiley, New York (1980).
10. J. Klein, *Macromolecules* **11**, 852 (1978).
11. M. Daoud and P. G. de Gennes, *J. Polym. Sci., Polym. Phys. Ed.* **17**, 1971 (1979).
12. W. W. Graessley, *Adv. Polym. Sci.* **47**, 68 (1982).
13. J. Klein, *Macromolecules* **19**, 105 (1986).
14. G. Marrucci, *J. Polym. Sci., Polym. Phys. Ed.* **23**, 159 (1985).
15. R. C. Ball and T. C. B. McLeish, *Macromolecules* **22**, 1911 (1989).
16. R. A. Orwoll and W. H. Stockmayer, *Adv. Chem. Phys.* **15**, 305 (1969).
17. S. T. Milner and T. C. B. McLeish, *Macromolecules* **30**, 2159 (1997).
18. S. T. Milner and T. C. B. McLeish, *Macromolecules* **31**, 7479 (1998).
19. S. T. Milner, T. C. B. McLeish, R. N. Young, A. Hakiki, and J. M. Johnson, *Macromolecules* **31**, 9345 (1998).
20. S. T. Milner and T. C. B. McLeish, *Phys. Rev. Lett.* **81**, 725-728 (1998).
21. Y. Matsumiya, H. Watanabe, and K. Osaki, *Macromolecules* **33**, 499 (2000).
22. J. L. Viovy, M. Rubinstein, and R. H. Colby, *Macromolecules* **24**, 3587 (1991).
23. M. Doi and N. Kuzuu, *J. Polym. Sci. Polym. Lett. Ed* **18**, 775 (1980).
24. D. S. Pearson and E. Helfand, *Macromolecules* **17**, 888 (1984).
25. R. H. Colby and M. Rubinstein, *Macromolecules* **23**, 2753 (1990).
26. H. Watanabe, Y. Matsumiya, and K. Osaki, *J. Polym. Sci., Part B, Polym. Phys.* **38**, 1024 (2000).
27. H. Watanabe, Y. Matsumiya, and T. Inoue, submitted to *Macromolecules.*
28. T. C. B. McLeish and R. G. Larson, *J. Rheol.* **42**, 81 (1998).

CHAPTER 5

Effects of Constraint Release on Eigenmodes of Dilute Probe in Blends.

5-1. Introduction

Cis-polyisoprene (PI) chains have dipoles parallel along their backbone,[1] and their global motion induces molecular weight (M) dependent dielectric relaxation at long time scales. Utilizing this feature, extensive dielectric studies have been carried out for PI chains in various environments such as the bulk state,[1-6] solutions,[4,7-11] and blends.[4,12-16]

The fundamental aspect of the slow dielectric relaxation of linear PI chains is described by a local correlation function $C(n,t;n')$ (eq 3.13).[6] The global motion of individual PI chains, being reflected in $C(n,t;n')$, depends on the dynamic nature of the surrounding environment.

Most of the dielectric studies so far carried out have been for linear, *regular* PI chains with no inversion of the dipoles.[1,2,4,5,7-9,12,16] For the regular PI chain composed of N segments, the polarization $\mathbf{P}$ is proportional to the end-to-end vector $\mathbf{R}$ and the dielectric relaxation function $\Phi(t)$ (eq 3.10) is related to $C(n,t;n')$ as (cf. 3.12 with a replacement $\Sigma_n \rightarrow \int_0^N \ldots dn$ and $\vartheta(n) = 1$ for $n = 0 - N$)[6]

$$\Phi(t) = \frac{\langle \mathbf{R}(t)\cdot\mathbf{R}(0)\rangle}{\langle \mathbf{R}^2\rangle} = \frac{1}{N}\int_0^N dn \int_0^N dn'\, C(n,t;n') \qquad (5.1)$$

The n and n' dependence of $C(n,t;n')$ is averaged in $\Phi(t)$. Thus, details of the chain dynamics reflected in this dependence were not well elucidated in the studies of the regular PI chains.

These details can be dielectrically examined for a series of specially designed PI chains that have identical M but differently once-inverted dipoles.[6] The structure of these chains is shown schematically in Fig. 5-1. For a PI chain having its dipole inversion at the n^*-th segment, the polarization is proportional to the difference vector $\Delta\mathbf{R} = \mathbf{R}_1 - \mathbf{R}_2$, with $\mathbf{R}_1$ and $\mathbf{R}_2$ being two end-to-center vectors (see Fig. 5-1). Thus, in a continuous limit, the dielectric relaxation func-

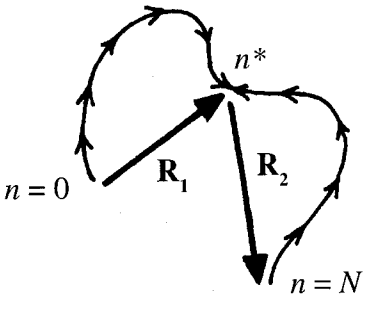

Fig.5-1 Schematic illustration of a dipole-inverted linear type-A chain.

tion $\Phi(t)$ is related to $C(n,t;n')$ as (cf. eq 3.12 with $\vartheta(n) = 1$ for $n = 0 - n^*$ and $\vartheta(n) = -1$ for $n = n^* - N$)[6]

$$\Phi(t;n^*) = \frac{1}{N}\left[\int_0^{n^*} dn - \int_{n^*}^{N} dn\right]\left[\int_0^{n^*} dn' - \int_{n^*}^{N} dn'\right] C(n,t;n') \qquad (5.2)$$

The above series of dipole-inverted PI chains having the same M (or N) are dynamically identical to each other and thus have the same $C(n,t;n')$. However, $\Phi(t;n^*)$ of these chains are different because of the difference in n^*. The dielectric data from these chains can be used to experimentally determine the eigenfunctions $f_p(n)$ and relaxation times $\tau_{\varepsilon,p}$ defined for $C(n,t;n')$,[6]

$$C(n,t;n') = \frac{2}{N}\sum_{p=1}^{N} f_p(n) f_p(n') \exp[-t/\tau_{\varepsilon p}] \qquad (5.3)$$

(This symmetric form of the eigenmode expansion of C reflects the symmetry of the orientational correlation, $\langle \mathbf{u}(n,t)\bullet\mathbf{u}(n',0)\rangle = \langle \mathbf{u}(n',t)\bullet\mathbf{u}(n,0)\rangle$.[6]) The $f_p(n)$ and $\tau_{\varepsilon,p}$ separately determine the n and t dependence of $C(n,t;n')$ and contain detailed information regarding the chain dynamics.

Watanabe et al. examined the dielectric behavior of such a series of dipole-inverted PI chains and determined $f_p(n)$ and $\tau_{\varepsilon,p}$ for the lowest three eigenmodes (p = 1-3) in the bulk state,[6] solutions,[10,11] and blends.[15] Of particular importance to this study is the behavior of dilute, dipole-inverted PI probe chains in a matrix of much shorter, entangling polybutadiene (PB) chains.[15] These probe chains relaxed with the constraint release (CR) mechanism due to motion (diffusion) of the matrix PB chains (see section 4-4-1).[19-21]

The CR relaxation of the probe has been considered to proceed *via* retarded Rouse-like dynamics (cf. section 4-4-1).[19-21] However, for the dipole-inverted PI probes in the short PB matrix, $f_p(n)$ is non-sinusoidal with respect to n and not explained by the Rouse-type CR model (despite a success of this model for describing the CR relaxation time).[15] On the basis of this result, the dynamics of the dipole-inverted PI chains in a high-M PB matrix (where the CR mechanism makes a negligible contribution to the PI relaxation) is investigated in this and next chapters to elucidate further details of the CR effect on the eigenmode.

In this chapter, $f_p(n)$ and $\tau_{\varepsilon,p}$ (p= 1-3) are dielectrically determined for the dipole-inverted PI chains dilutely blended in the high-M PB matrix. The CR effect on the eigenmodes of the PI chains is examined by comparing $f_p(n)$ and $\tau_{\varepsilon,p}$ for the same PI chains in the high-M and low-M entangling PB matrices as well as in the monodisperse bulk state of the PI chains. (The CR contribution to the PI relaxation is different in these environments.)

The next chapter[31] addresses the relationship between dielectric and viscoelastic quantities. Specifically, the $f_p(n)$ and $\tau_{\varepsilon,p}$ data obtained in this chapter are utilized to calculate vis-

coelastic moduli. Short-time coherence of the PI motion is examined in a purely experimental way through comparison of the calculated moduli and the viscoelastic data.

5-2. Experimental

5-2-1. Materials

Table 2.1 summarizes molecular characteristics of the dipole-inverted PI, regular PI (without dipole inversion), and PB samples used in this chapter. The dipole-inverted PI chains are composed of two PI blocks connected in a head-to-head fashion, and the dipoles are aligned in the same direction in each block but inverted at the block junction.[6] The sample code for those PI chains indicates the molecular weights of the two blocks in units of 1000; for example, I-I 35-14 is the dipole-inverted PI composed of two blocks of molecular weights 35×10^3 and 14×10^3. As shown in Table 2.1, the dipole-inverted PI chains have nearly the same M but differently inverted dipoles that are specified by the reduced location of the inversion point, n^*/N (cf. Fig. 5-1).

The systems subjected to dielectric measurements were homogeneous blends of the dipole-inverted PI chains in the B263 matrix (having $M_{PB} >> M_{PI}$). The blends were prepared by dissolving prescribed amounts of the PI and B263 samples in benzene and then allowing benzene to completely evaporate. The PI volume fraction in the blends was kept small ($\phi_{PI} = 0.05$) so that the PI chains ($M \cong 50 \times 10^3$) were not entangled among themselves and homogeneously mixed in the B263 matrix.

Blends of the regular PI chains (I14 and I19) in the B263 matrix ($\phi_{PI} = 0.05$) were also prepared with the method explained above. These blends were utilized to evaluate the longest relaxation time of the dipole-inverted PI chains in this matrix.

5-2-2. Measurements

For the homogeneous blends of the dipole-inverted PI chains in the B263 matrix ($\phi_{PI} = 0.05$), dielectric measurements were carried out with a high precision transformer bridge (Model 1620A, QuadTech). Details of the measurement were explained in section 2-4-3. The dielectric loss ε'' was measured at various temperatures between 0°C and 130°C. Time-temperature superposition worked well and the ε'' data were reduced to a previously used reference temperature,[6,15] $T_r = 40$°C. The B263 matrix chains had no type-A dipoles and exhibited negligibly small ε'' at the angular frequency ω examined. Thus the dielectric dispersion seen for the blends was exclusively attributed to the global motion of the PI chains.

For the dipole-inverted PI chains, the slowest eigenmode does not always have the largest dielectric intensity.[6,10,15] Specifically, the slowest eigenmode is dielectrically inert in the case of symmetrical dipole inversion ($n^* = N/2$); cf. eq 5.3 and eq 3.12 with $\vartheta(n) = 1$ for $n = 0$ - $N/2$ and $\vartheta(n) = -1$ for $n = N/2$ - N).[6,10,15] Thus, for those chains, the relaxation time $\tau_{\varepsilon,1}$ of the slowest eigenmode was not easily determined from their ε'' data in particular when n^* was close to $N/2$. To evaluate $\tau_{\varepsilon,1}$ for the dipole-inverted chains, dielectric measurements were also carried out for blends of the regular PI chains (I14, I19, and I-I 49-0) in the B263 matrix ($\phi_{PI} = 0.05$). The

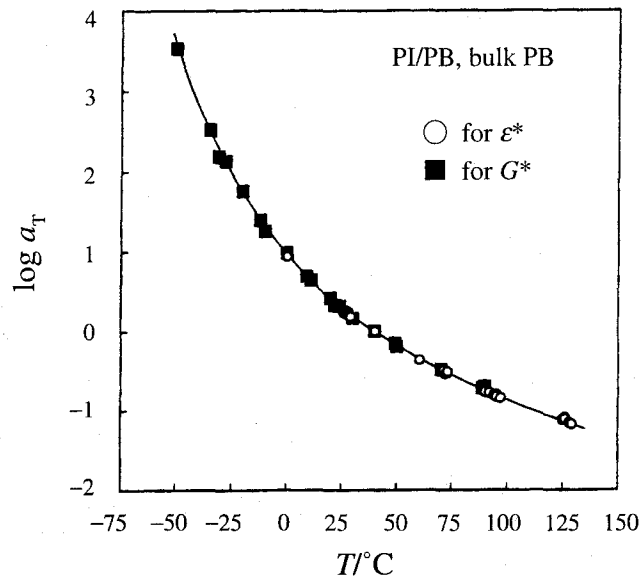

Fig.5-2 Temperature dependence of the shift factors for the dielectric data of dilute PI chains (with and without dipole inversion) entangled with PB matrices (unfilled circles). For comparison, the shift factors for viscoelastic moduli of I-I 49-0/B263 blend (ϕ_{PI} = 0.05) and bulk B263 are also shown (filled squares).

ε'' data for these regular chains were reduced to 40°C, and their $\tau_{\varepsilon,1}$ data were interpolated/ extrapolated to determine $\tau_{\varepsilon,1}$ for the dipole-inverted chains.

The shift factors $a_{T,\varepsilon}$ used in the above time-temperature superposition were the same for the dipole-inverted and regular PI chains in the B263 matrix. These $a_{T,\varepsilon}$, data are shown in Fig. 5-2. For comparison, Fig. 5-2 also shows the shift factor $a_{T,G}$ for viscoelastic moduli G^* of the PI/263 blends and bulk B263 matrix (cf. Chapter 6).[31] Excellent agreement is noted for the $a_{T,\varepsilon}$ (unfilled circle) and $a_{T,G}$ (filled square). The $a_{T,\varepsilon}$ represents the acceleration of the motion of the dilute PI chains in the B263 matrix with temperature, while $a_{T,G}$ essentially reflects the acceleration of the motion of the B263 chains.[13] Thus the coincidence of $a_{T,\varepsilon}$ and $a_{T,G}$ indicates that the PI and B263 chains are uniformly mixed and the segmental motion of the dilute PI chains is activated by that of the surrounding B263 chains, as also noted in a previous study.[13]

5-3. Results

5-3-1. Dielectric behavior of regular PI chains in B263

In the dielectrically inert B263 matrix, each of I14, I19, and I-I 49-0 chains (ϕ_{PI} = 0.05) exhibited a sharp ε'' peak immediately followed by a terminal tail ($\varepsilon'' \propto \omega$) on lower-$\omega$ side of the peak. Since these chains have no dipole inversion, the terminal dielectric mode characterized by this peak corresponds to the slowest eigenmode.[6,10,15] Thus, the relaxation time $\tau_{\varepsilon,1}$ for this eigenmode was evaluated from the angular frequency ω_{peak} at the ε'' peak,

$$\tau_{\varepsilon,1} = 1/\omega_{peak} \tag{5.4}$$

For regular chains of various M, close coincidence of this $\tau_{\varepsilon,1}$ and the second-moment average relaxation time $<\tau_\varepsilon>_w$ (eq 2.18) has been confirmed.[32]

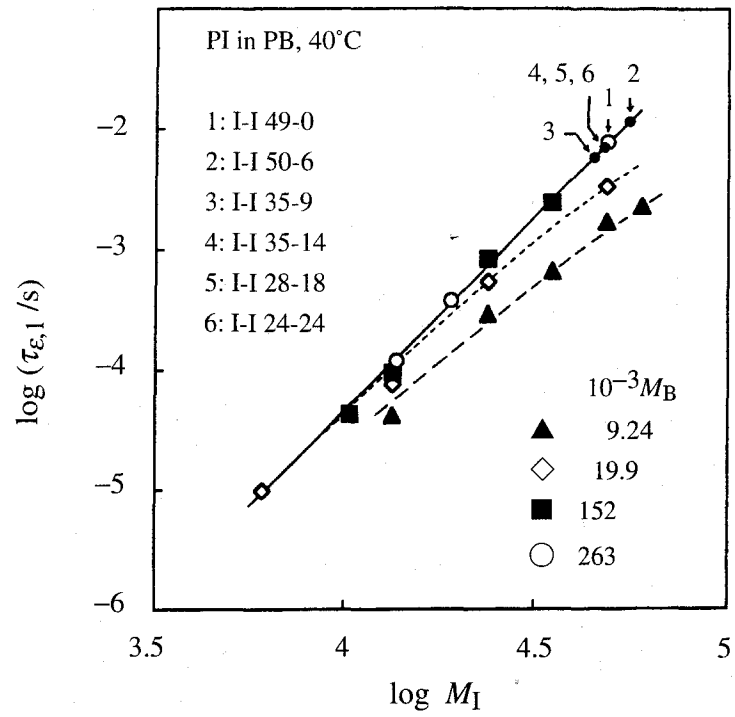

Fig. 5-3 Longest relaxation time $\tau_{\varepsilon,1}$ of dilute PI chains (without dipole inversion) entangled with PB matrices of various molecular weights M_B as indicated (large symbols). The $\tau_{\varepsilon,1}$ data at 40°C are plotted against the PI molecular weight M_I. The $\tau_{\varepsilon,1}$ data for $M_B = 263 \times 10^3$ were obtained in this study, and the other data were from previous work.[13,15,16] Small filled circles indicate the $\tau_{\varepsilon,1}$ of dipole inverted PI chains calculated from an empirical equation (eq 5.5; shown with the solid line).

In Fig. 5-3, these $\tau_{\varepsilon,1}$ data obtained in the B263 matrix are plotted against the PI molecular weight M_I (unfilled circles). For comparison, the $\tau_{\varepsilon,1}$ data are also shown for PI chains ($\phi_{PI} \leq 0.06$) in the other entangling PB matrices examined in previous studies.[13,15]

In PI/PB blends, the PI chains are not entangled among themselves if they satisfy the criterion, $M_I < 2M_{e,I}/\phi_{PI}$, where $M_{e,I}$ is the molecular weight between entanglements for the PI chains placed in the PB matrix ($M_{e,I} \cong 1.7 \times 10^3$ for $\phi_{PI} = 0.05$; see Chapter 6). (Validity of this criterion has been confirmed from the ϕ_{PI}-independence of the reduced loss ε''/ϕ_{PI} of dilute PI chains satisfying the criterion.[13]) All PI chains examined in Fig. 5-3 satisfy the criterion. Thus the $\tau_{\varepsilon,1}$ data shown there characterize the global motion of the *dilute* PI chains entangled *only with* the PB matrices.

Fig. 5-3 demonstrates characteristic features for the constraint release (CR) relaxation of the PI chains: In the matrices of PB chains not much longer than the PI chains, $\tau_{\varepsilon,1}$ decreases, i.e., the global motion of the PI chains is accelerated with decreasing matrix molecular weight M_B. This acceleration is indicative of the enhanced contribution of the CR mechanism to the PI dynamics. This CR contribution becomes smaller with increasing M_B. In particular, for the PI chains with $M_I = 10 \times 10^3$ - 50×10^3, no change of $\tau_{\varepsilon,1}$ is observed upon increasing M_B from 152×10^3 to 263×10^3. Thus the CR mechanism makes negligibly small contributions to the motion of these PI chains in the matrices with $M_B = 152 \times 10^3$ and 263×10^3. In these matrices, the $\tau_{\varepsilon,1}$ data for $M_I = 10 \times 10^3$ - 50×10^3 are well described by an empirical equation (solid line

in Fig. 5-3),

$$\tau_{\varepsilon,1}/\mathrm{s} = 7.2 \times 10^{-18} M_\mathrm{I}^{3.2} \tag{5.5}$$

As explained in the experimental section, $\tau_{\varepsilon,1}$ of the *dipole-inverted* PI chains are not easily determined from their ε'' data, in particular when the inversion point is close to the chain center. Thus, the molecular weight M_I of the dipole-inverted PI chains was utilized in eq 5.5 to evaluate $\tau_{\varepsilon,1}$ of those chains in B263 matrix. The results are shown in Fig. 5-3 (small filled circles).

The above empirical equation is different from the relationship, $\tau_{\varepsilon,1} \propto M_\mathrm{I}^3$, deduced from a conventional molecular picture of *pure* reptation[33] in very long matrices (see section 4-3). For PI chains with M_I in the narrow range between 24×10^3 and 50×10^3, the $\tau_{\varepsilon,1}$ data (Fig. 5-3) can be also cast in this conventional relationship within experimental uncertainties,

$$\tau_{\varepsilon,1}/\mathrm{s} = 6.4 \times 10^{-17} M_\mathrm{I}^3 \tag{5.6}$$

The $\tau_{\varepsilon,1}$ values for the dipole-inverted PI chains evaluated from eqs 5.5 and 5.6 were very close to each other. However, the difference between the power-law indices in eqs 5.5 and 5.6 raises a conceptually important problem about the probe chain dynamics in high-M matrices.[31] This problem is discussed in Chapter 6.

5-3-2. Overview of dielectric behavior of dipole-inverted PI chains

Fig. 5-4 shows the dielectric behavior of the dipole-inverted PI chains ($\phi_\mathrm{PI} = 0.05$) in the B263 matrix at 40°C (circles). The behavior of the same PI chains in a shorter B9 matrix ($\phi_\mathrm{PI} = 0.05$)[15] and in their monodisperse bulk state ($\phi_\mathrm{PI} = 1$)[6] is also shown (triangles and squares, respectively). The B263 and B9 matrices exhibited negligibly small ε'' at the ω examined, and the dispersions seen in Fig. 5-4 are attributed to global motion of the PI chains. (For both PI and PB chains, the segmental motion is too fast to be detected in the ω–range examined.)

In the B263 and B9 matrices, the dipole-inverted PI chains (with $M_\mathrm{I} \cong 50 \times 10^3$) satisfy the criterion for lack of entanglements among themselves, $M_\mathrm{I} < 2M_{\mathrm{e,I}}/\phi_\mathrm{PI}$ ($M_{\mathrm{e,I}} \cong 1.7 \times 10^3$ for $\phi_\mathrm{PI} = 0.05$; see Chapter 6). The $M_\mathrm{I}/M_{\mathrm{e,I}}$ ratio for these PI chains in the PB matrices is $M_\mathrm{I}/M_\mathrm{e} \cong 29$. The ratio for the same PI chains in the monodisperse bulk state is $M_\mathrm{I}/M_{\mathrm{e,I}} \cong 10$ ($M_{\mathrm{e,I}} \cong 5 \times 10^3$ for bulk PI[34,35]).

In Fig. 5-4, the ε'' data are reduced by the total dielectric intensity for the global chain motion $\Delta\varepsilon$ ($= (2/\pi) \int \varepsilon'' \, \mathrm{d}\ln\omega$ with the integral being conducted in the global relaxation regime) and plotted against a reduced frequency $\omega\tau_{\varepsilon,1}$ so that differences of ϕ_PI and the monomeric friction in the three environments are compensated and the dielectric mode distribution is best compared. For the dipole-inverted PI chains in the B263 matrix, the $\tau_{\varepsilon,1}$ values used in these reduced plots were determined from Fig. 5-3. For the same chains in the B9 matrix and in the monodisperse bulk state, the $\tau_{\varepsilon,1}$ values were determined in the previous work.[6,15]

In the reduced plots, small differences in M_I of the dipole-inverted PI chains have been

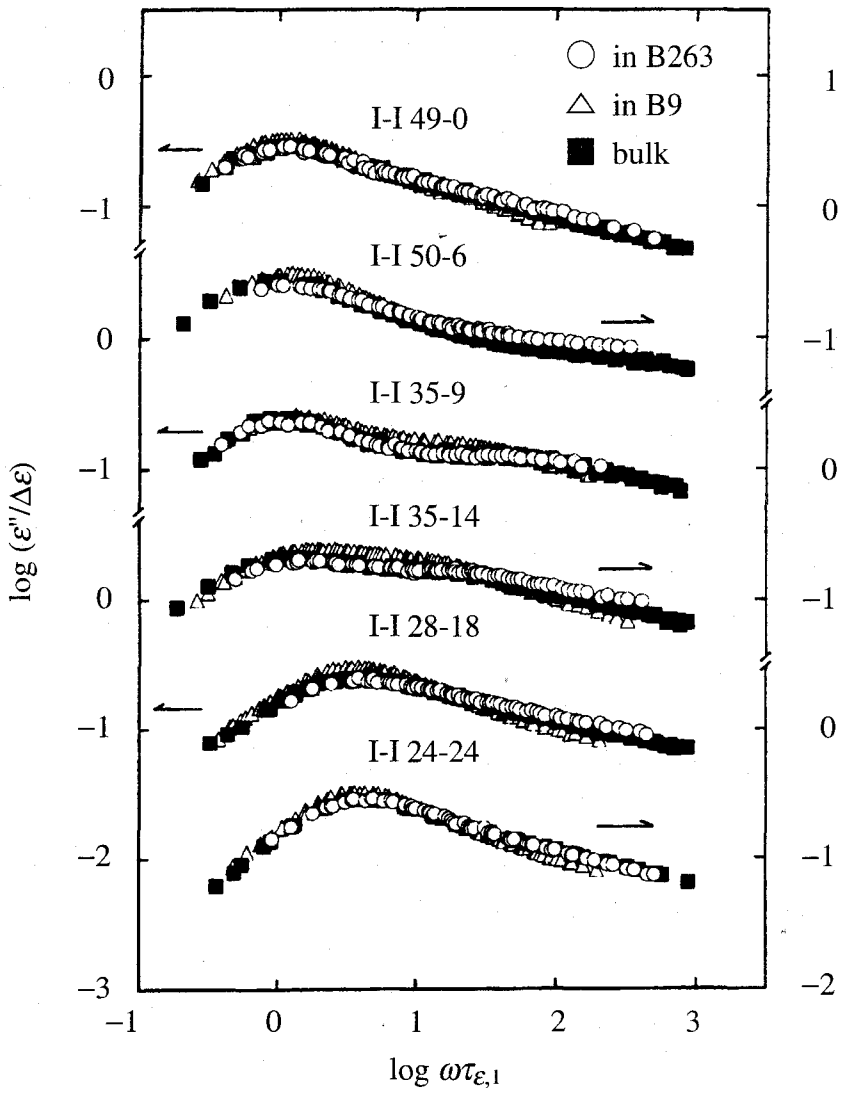

Fig.5-4 Frequency (ω) dependence of dielectric loss ε'' of dilute dipole-inverted PI chains ($\phi_{PI} = 0.05$) entangled with the B263 matrix at 40°C (unfilled circles). For comparison, the ε'' data are shown for the same chains in their monodisperse bulk state[6] (filled squares) and in the B9 matrix[15] ($\phi_{PI} = 0.05$; unfilled triangles). For best comparison of the dielectric mode distribution of the PI chains in the three environments, the ε'' data are reduced by the total dielectric intensity for the global chain motion $\Delta\varepsilon$ and plotted against the reduced frequency $\omega\tau_{\varepsilon,1}$, with $\tau_{\varepsilon,1}$ being the longest relaxation time defined for the local correlation function (cf. eq 5.3).

compensated by the factor $\tau_{\varepsilon,1}$ involved in the reduced frequency. Thus, in respective environments examined in Fig. 5-4, the global motion is regarded to be exactly the same for all six dipole-inverted samples.[36] However, the dielectric behavior is quite different because of the difference in the location of the dipole inversion point, n^*: The ε'' curve becomes broader and then narrower with the shift of n^* from 0 (chain end) to $N/2$ (chain center). The shape of the ε'' curve is almost identical for I-I 49-0 and I-I 24-24 but the ε'' peak is located at higher ω for the latter.

The relative distribution of the slow dielectric modes is reflected in the shape of the ε'' curve at low ω. For PI chains having no dipole inversion, previous studies revealed that the shape is insensitive to the PI content in concentrated solutions,[7-10] to M_I and M_B in entangling

PI/PB blends,[13,14,16] and to M_I in monodisperse bulk systems (cf. Chapter 7).[14,15,32] In Fig. 5-4, a similar result is found for the I-I 49-0 chain: The shape of the ε'' curve of this chain is almost identical in the three environments. In contrast, the dipole-inverted chains having n^* between 0 and $N/2$ display modest differences in the shape of the ε'' curve at intermediate ω in the three environments .

5-3-3. Estimation of CR contribution

In the three environments examined in Fig. 5-4, the CR mechanism due *to the matrix motion* should contribute differently to the relaxation of the PI chains. This difference can be quantitatively examined with the ratio of the characteristic time τ_{CR} for this mechanism to the observed longest relaxation time $\tau_{\varepsilon,1}$ for the I-I 49-0 chain. In matrices of long chains that exhibit very slow diffusion, I-I 49-0 relaxes *via* its own motion irrespective of the matrix diffusion and has $\tau_{\varepsilon,1} << \tau_{CR}$. On the other hand, in entangled matrices of sufficiently short chains, the relaxation is induced by the matrix diffusion and $\tau_{\varepsilon,1}$ coincides with τ_{CR}. Thus the $\tau_{CR}/\tau_{\varepsilon,1}$ ratio (≥ 1) can be utilized as a measure of the CR contribution to the observed relaxation of the I-I 49-0 chain: The larger the ratio, the smaller this contribution.

Extensive viscoelastic studies on binary blends of polystyrenes revealed that the relaxation of dilute probe chains (with molecular weight M_{probe}) entangled with *much shorter* matrix chains (of molecular weight M_{mat}) is governed by the CR mechanism and the τ_{CR} of such probes is proportional to $M_{probe}^2 M_{mat}^3$ (cf. eq 4.24).[14,22-25] For dilute PI probe chains in entangling PB matrices, a previous study[13] gave an empirical equation for $\tau_{CR,\varepsilon}$ including the proportionality constant,

$$\tau_{CR,\varepsilon}/\mathrm{s} = 8.94 \times 10^{-25} M_I^2 M_B^3 \quad (\text{at } 40^\circ\mathrm{C}) \tag{5.7}$$

From this equation and the $\tau_{\varepsilon,1}$ data for the I-I 49-0 chain in the B263 and B9 matrices, the $\tau_{CR,\varepsilon}/\tau_{\varepsilon,1}$ ratio of this chain was evaluated. The results are summarized in Table 5.1.

For *dilute* PI probes in entangling PI matrices, only a limited amount of viscoelastic/dielectric data has been reported and no accurate empirical equation of $\tau_{CR,\varepsilon}$ is found in literature. Here, an attempt is made to estimate the $\tau_{CR,\varepsilon}/\tau_{\varepsilon,1}$ ratio from dielectric data for the entangling PI/PI blends reported by Adachi et al.[12] They compared the $\tau_{\varepsilon,1}$ data of dilute PI probes with the prediction of a modified tube model[20] that incorporates the Rouse-type CR and pure reptation processes. The $\tau_{CR,\varepsilon}/\tau_{\varepsilon,1}$ ratio deduced from this model is written as[20]

$$\tau_{CR,\varepsilon}/\tau_{\varepsilon,1} = 1 + [2(\pi^2/12)^{z_g} N^2 / z_g \pi^2] \tag{5.8}$$

Here, N represents the M/M_e ratio for the probe chain (with $M_e \cong 5 \times 10^3$ for bulk PI systems), and z_g is a parameter representing the number of topological constraints per each entanglement point for the probe chain (cf. section 4-4-1). The $\tau_{\varepsilon,1}$ data of Adachi et al.[12] are reasonably well described by eq 5.8 with $z_g \cong 4$. For the I-I 49-0 chain in its monodisperse bulk state, the $\tau_{CR,\varepsilon}/$

Table 5.1.

Ratio of the CR relaxation time to the observed longest relaxation time for the dilute I-I 49-0 chain in various environments.

matrix	$\tau_{CR,\varepsilon}/\tau_{\varepsilon,1}$
B263	5600
I-I 49-0	3.5 ± 0.3^a
B9	1.1

a: rough estimate for I-I 49-0 in the monodisperse bulk state.

$\tau_{\varepsilon,1}$ ratio evaluated from eq 5.8 with this z_g value is shown in Table 5.1.

The above model predicts the pure reptation behavior for the probe in matrices of very long chains. The I-I 49-0 chain in such a matrix (B263) does not exhibit this behavior (cf. Fig. 5-6 shown later). Because of this difference, the $\tau_{CR,\varepsilon}/\tau_{\varepsilon,1}$ ratio obtained from eq 5.8 should be regarded as a rough estimate. However, this estimate is still useful for the argument below.

As seen in Table 5.1, the $\tau_{CR,\varepsilon}/\tau_{\varepsilon,1}$ ratio for the dilute I-I 49-0 chain is much larger than unity and very close to unity, respectively, in the B263 and B9 matrices. Thus the CR mechanism makes a negligible contribution to the global motion of I-I 49-0 in the B263 matrix while this mechanism dominates the I-I 49-0 motion in the B9 matrix. The CR contribution for bulk I-I 49-0 is between these two extreme cases.

5-3-4. Evaluation of f_p and $\tau_{\varepsilon,p}$

The dielectric loss $\varepsilon''(\omega;n^*)$ of a PI chain having the dipole inversion at the n^*-th segment is given by the imaginary part of Fourier transform of the dielectric relaxation function $\Phi(t;n^*)$ (eq 5.2). Thus, ε'' can be expressed in terms of $f_p(n)$ and $\tau_{\varepsilon,p}$,[6]

$$\varepsilon''(\omega;n^*) = \sum_{p=1}^{N} g_p(n^*) \frac{\omega \tau_{\varepsilon,p}}{1 + \omega^2 \tau_{\varepsilon,p}^2} \tag{5.9}$$

with

$$g_p(n^*) = \Delta\varepsilon [2F_p(n^*) - F_p(N)]^2 \tag{5.10}$$

and

$$F_p(n^*) = \frac{\sqrt{2}}{N} \int_0^{n^*} f_p(n)\, dn \quad (= 0 \text{ for } n^* = 0) \tag{5.11}$$

Here, $\Delta\varepsilon$ is the total dielectric intensity for the global motion of the chain, and $F_p(n^*)$ is an integrated eigenfunction. As seen in eq 5.10, F_p is evaluated from the normalized intensity factor $g_p(n^*)$ for the p-th dielectric mode for the PI chain having the dipole inversion at the n^*-th segment. (The requirement of smooth and continuous n^* dependence of $F_p(n^*)$ as well as symmetric features of $F_p(n^*)$ are utilized in this determination.[6])

The $g_p(n^*)$ values for the lowest three eigenmodes (p = 1-3) can be determined from the ε'' data at low ω where the higher order eigenmodes with $p \geq 4$ have already relaxed.[37] At such low ω well below $1/\tau_{\varepsilon,p}$ for $p \geq 4$, eq 5.9 becomes[6]

$$\varepsilon''(\omega;n^*) = \sum_{p=1}^{3} \varepsilon_p''(\omega;n^*) + \omega\varepsilon^o_{p\geq 4}(n^*) \tag{5.12}$$

with

$$\varepsilon_p''(\omega;n^*) = g_p(n^*)\,\frac{\omega\,\tau_{\varepsilon,p}}{1+\omega^2\,\tau^2_{\varepsilon,p}}, \quad \varepsilon^o_{p\geq 4}(n^*) = \sum_{p\geq 4} g_p(n^*)\,\tau_{\varepsilon,p} \tag{5.13}$$

Here, $\varepsilon_p''(\omega;n^*)$ represents the contribution of the p-th eigenmode to the ε'' data, and the term $\omega\,\varepsilon^o_{p\geq 4}(n^*)$ indicates the low-ω asymptote of the contribution from all higher eigenmodes with $p \geq 4$. If the $\tau_{\varepsilon,1}$ - $\tau_{\varepsilon,3}$ values are known, eq 5.12 becomes a linear function of the unknown quantities, $g_p(n^*)$ (p = 1-3) and $\varepsilon^o_{p\geq 4}(n^*)$. Then, these quantities are best determined from a linear least-square fit[6] of the $\varepsilon''(\omega;n^*)$ data with eq 5.12.

The $\tau_{\varepsilon,1}$ - $\tau_{\varepsilon,3}$ values required in this fit are determined in the following way. Since the two ends of a chain have equivalent effects on the chain motion, the eigenfunctions $f_p(n)$ should be either symmetric or anti-symmetric with respect to the chain center, i.e., $f_p(n) = f_p(N-n)$ for p = *odd* and $f_p(n) = -f_p(N-n)$ for p = *even*.[6] Because of these features of f_p, only odd eigenmodes contribute to ε'' for a chain having no dipole inversion ($g_p(0) = 0$ for p = even) while only even eigenmodes contribute to ε'' for a chain having symmetrical dipole inversion ($g_p(N/2) = 0$ for p = odd);[6] see eqs 5.10 and 5.11. Thus the terminal dielectric mode corresponds to the slowest and second slowest eigenmodes for I-I 49-0 ($n^* = 0$) and I-I 24-24 ($n^* = N/2$), respectively. Since the ε'' peak of these chains is immediately followed by the terminal tail ($\varepsilon'' \propto \omega$) on the low-$\omega$ side (see Fig. 5-4), the peak corresponds to the terminal dielectric mode. Thus $\tau_{\varepsilon,1}$ and $\tau_{\varepsilon,2}$ *for I-I 49-0* are evaluated as the reciprocal of the peak frequencies for I-I 49-0 and I-I 24-24, respectively, with $\tau_{\varepsilon,2}$ being subjected to a minor correction for the small difference in M of these chains. (The correction factor is given by the ratio of the $\tau_{\varepsilon,1}$ values of those chains, where $\tau_{\varepsilon,1}$ of I-I 24-24 is determined from Fig. 5-3.) The $\tau_{\varepsilon,3}$ value for I-I 49-0 is evaluated from a linear least-square analysis[6] of the ε'' data of this chain.

For the dilute I-I 49-0 in the B263 matrix, the above method gave

$$\tau_{\varepsilon,1} = 7.76\times10^{-3}\ \text{s},\ \ \tau_{\varepsilon,2} = 1.95\times10^{-3}\ \text{s},\ \ \tau_{\varepsilon,3} = 0.854\times10^{-3}\ \text{s}\ \ (\text{at } 40^\circ\text{C}) \tag{5.14}$$

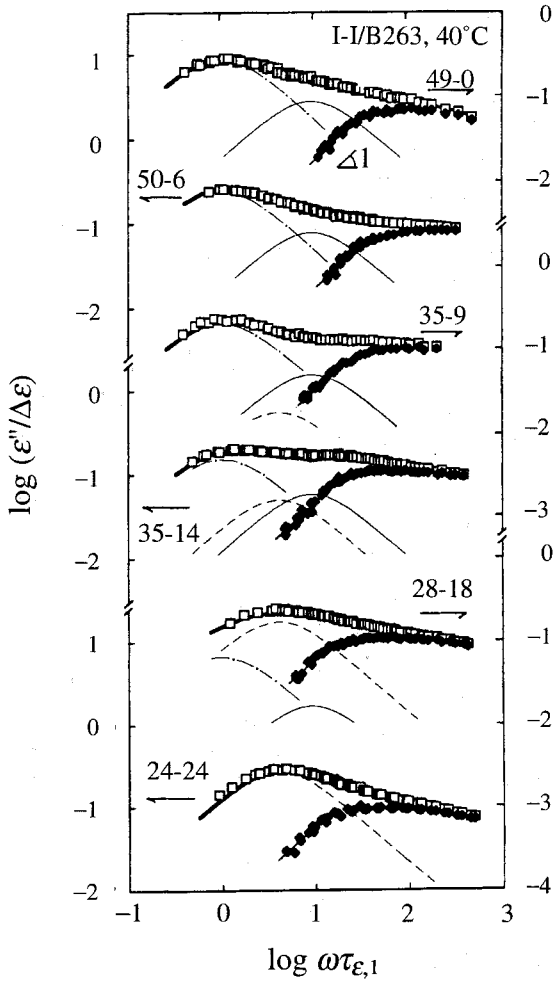

Fig.5-5 Decomposition of the ε'' data (unfilled squares) of dilute dipole-inverted PI chains ($\phi_{PI} = 0.05$) entangled with the B263 matrix at 40°C into contributions from eigenmodes. The contributions from the slowest, second slowest, and third slowest eigenmodes are shown with the thin dash-dot, dashed, and solid curves, respectively, and the contribution from all higher (faster) eigenmodes ($p \geq 4$) is indicated with the filled diamonds. The thick solid curves indicate the sum of all these contributions.

From eqs 5.12 and 5.13 with these $\tau_{\varepsilon,1}$ - $\tau_{\varepsilon,3}$ values, the linear least-square fitting analysis was made for the $\varepsilon''(\omega;n^*)$ data of the dipole-inverted PI chains in the B263 matrix. The results are shown in Fig. 5-5. The contributions of the slowest three eigenmodes,$\varepsilon_p''(\omega;n^*)$ with $p = 1, 2, 3$ (eq 5.13), are shown with the thin dash-dot , dashed, and solid curves, respectively. The filled diamonds indicate the contribution of the higher eigenmodes with $p \geq 4$, $\varepsilon''_{p\geq4}(\omega;n^*) = \Sigma_{p\geq4}$ $\varepsilon_p''(\omega;n^*)$: This $\varepsilon''_{p\geq4}$ was obtained by subtracting ε_p'' with p = 1-3 from the data (squares). Note that $\varepsilon''_{p\geq4}(\omega;n^*)$ satisfies the prerequisite for the fit, $\varepsilon''_{p\geq4}(\omega;n^*) \rightarrow \omega\varepsilon^{o}_{p\geq4}(n^*) \propto \omega$ at sufficiently low ω (cf. eq 5.12).

From the $g_p(n^*)$ factors (p = 1-3) determined from the above fit, the integrated eigenfunctions were obtained for the I-I 49-0 chain (cf. eqs 5.10 and 5.11). In Fig. 5-6, these functions in the B263 matrix (circles) are compared with the integrated eigenfunctions previously determined for the same chain in the B9 matrix (triangles)[15] and in the monodisperse bulk

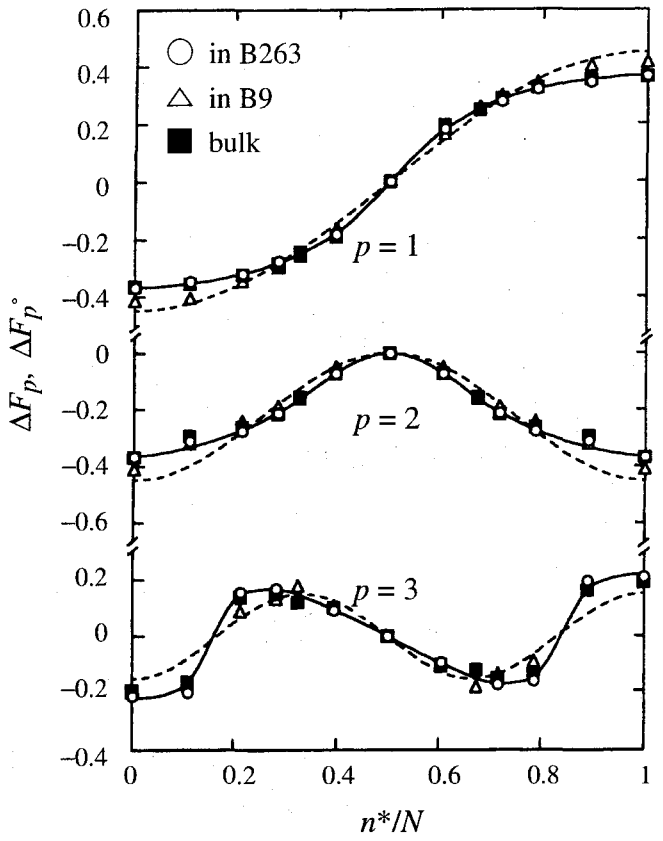

Fig.5-6 Dependence of integrated eigenfunctions $F_p(n^*)$ for the slowest three eigenmodes of the dilute I-I 49-0 chain ($\phi_{PI} = 0.05$) entangled with the B263 matrix on the reduced segment position n^*/N (unfilled circles). For comparison, the eigenfunctions are shown for the same chain in its monodisperse bulk state[6] (filled squares) and in the B9 matrix[15] ($\phi_{PI} = 0.05$; unfilled triangles). For the best comparison of the behavior of I-I 49-0 in the three environments, the plots are shown for the *base-shifted* eigenfunctions $\Delta F_p(n^*) = F_p(n^*) - F_p(N/2)$ that have a value 0 irrespective of the dynamic nature of the environment. The dashed curves indicate the sinusoidal eigenfunctions commonly deduced from the pure reptation and Rouse-type CR models.

state (squares).[6] The normalization and orthogonality of these eigenfunctions are summarized in the Appendix 5A. For the clearest comparison of these eigenfunctions, Fig. 5-6 shows plots of the base-shifted eigenfunctions $\Delta F_p(n^*) \equiv F_p(n^*) - F_p(N/2)$ that have the value of 0 at $n^* = N/2$ irrespective of the environment. The dashed curves indicate the sinusoidal eigenfunctions $\Delta F_p^\circ(n^*)$ commonly deduced from the reptation and Rouse-type CR models (cf. eq 5.17 shown later).

Fig. 5-7 shows dependence of the eigenmode relaxation time on the mode index p (= 1, 2, 3) for the I-I 49-0 chain in the B263 matrix (eq 5.14), in the B9 matrix, and in the monodisperse bulk state. The $\tau_{\varepsilon,p}$ data for the latter two cases were obtained in the previous work.[6,15] The segmental friction ζ of the I-I 49-0 chains is the same in the blends with the B263 and B9 matrices, and the difference of $\tau_{\varepsilon,p}$ in these blends reflects the difference of the CR contribution to the I-I 49-0 dynamics. On the other hand, ζ is different in the I-I 49-0 bulk and blend systems, and this difference also contributes to the difference of $\tau_{\varepsilon,p}$ in these systems. For convenience for later comparison with models, Table 5.2 summarizes the $\tau_{\varepsilon,2}/\tau_{\varepsilon,1}$ and $\tau_{\varepsilon,3}/\tau_{\varepsilon,1}$ ratios that are not

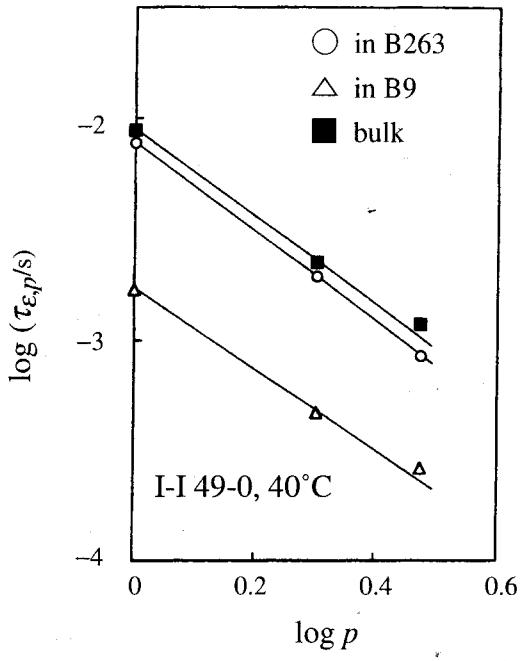

Fig.5-7 Dependence of the relaxation time $\tau_{\varepsilon,p}$ on the eigenmode index p for the dilute I-I 49-0 chain (ϕ_{PI} = 0.05) entangled with the B263 matrix at 40°C (unfilled circles). For comparison, the $\tau_{\varepsilon,p}$ data at 40°C are also shown for the same chain in its monodisperse bulk state[6] (filled squares) and in the B9 matrix[15] (ϕ_{PI} = 0.05; unfilled triangles).

Table 5.2.
$\tau_{\varepsilon,2}/\tau_{\varepsilon,1}$ and $\tau_{\varepsilon,3}/\tau_{\varepsilon,1}$ ratios for the dilute I-I 49-0 chain in various environments.

matrix	$\tau_{\varepsilon,2}/\tau_{\varepsilon,1}$	$\tau_{\varepsilon,3}/\tau_{\varepsilon,1}$
	observed results	
B263	0.251	0.110
I-I 49-0[a]	0.257	0.135
B9	0.277	0.154
	model prediction[b]	
	0.250	0.111

a: I-I 49-0 in the monodisperse bulk state.
b: ratios commonly deduced from pure reptation and Rouse-type CR models.

affected by this difference of ζ.

5-4. Discussion

5-4-1. CR effects on eigenmodes

In Fig. 5-6, good agreement is seen for $\Delta F_p(n^*)$ in the B263 matrix and in the monodisperse bulk state. $\Delta F_p(n^*)$ is nearly the same also in the low-M B9 matrix, although small differences may be noted for $\Delta F_1(n^*)$ at $n^* < 0.2N$. The CR contribution to motion of the I-I 49-0 chain is significantly different in these three environments (Table 5.1). Thus, the CR mechanism hardly affects the eigenfunctions $\Delta F_p(n)$ and $f_p(n)$ (= $\{N/\sqrt{2}\}\{d\Delta F_p(n)/dn\}$; cf. eq 5.11) for the *slowest three* eigenmodes.

In Fig. 5-7, the $\tau_{\varepsilon,p}$ data can be described by a power-law relationship, $\tau_{\varepsilon,p} \propto p^{-\beta}$ (solid lines). The power-law index β slightly decreases with increasing CR contribution, from $\beta = 2.0_1$ in B263 to $\beta = 1.9_8$ in bulk state and further to $\beta = 1.8_5$ in B9 (see also Table 5.2). However, this decrease of β is very mild compared to the huge increase in the CR contribution (Table 5.1). Thus the relaxation time spacing for p= 1 -3 is only slightly affected by the CR contribution.

In Fig. 5-4, modest differences are observed in the shape of the ε'' curve for each dipole-inverted PI chain ($0 < n^* < N/2$) in the three environments. The differences are the most prominent at intermediate ω; see, for example, the data of I-I 35-9. These differences are partly due to the small differences of the slowest three eigenmodes in those environments (e.g., the small differences in the $\tau_{\varepsilon,p}/\tau_{\varepsilon,1}$ ratio). However, the shape of the ε'' curve at intermediate ω is more strongly affected by the higher eigenmodes ($p \geq 4$), and the shape differences are expected to be essentially due to differences in these higher eigenmodes. This expectation is examined below.

In Fig. 5-5, the dielectric loss $\varepsilon''_{p\geq 4}$ due to the higher eigenmodes ($p \geq 4$) is shown with the filled diamonds. The relative contribution of these eigenmodes to the ε'' data is specified by the ratio, $\varepsilon''_{p\geq 4}/\varepsilon''$. At intermediate ω where the ε'' curves exhibit modestly different shapes in the three environments, the $\varepsilon''_{p\geq 4}/\varepsilon''$ ratio was found to increase with increasing CR contribution to the PI dynamics. For example, for the I-I 35-9 and 35-14 chains in the B263 (CR-free) and B9 (CR-dominant) matrices, the $\varepsilon''_{p\geq 4}/\varepsilon''$ ratio at a representative frequency, $\omega = 10/\tau_{\varepsilon,1}$, is

$$\varepsilon''_{p\geq 4}/\varepsilon'' = 0.25 \text{ (I-I 35-9)},\ 0.27 \text{ (I-I 35-14)} \quad \text{in B263} \tag{5.15}$$

$$\varepsilon''_{p\geq 4}/\varepsilon'' = 0.49 \text{ (I-I 35-9)},\ 0.44 \text{ (I-I 35-14)} \quad \text{in B9}^{15)} \tag{5.16}$$

The above results strongly suggest that the functional form of $f_p(n)$ and the relaxation time spacing ($\tau_{\varepsilon,p}/\tau_{\varepsilon,1}$ ratio) for the higher eigenmodes ($p \geq 4$) change with the CR contribution. Nevertheless, the shape of the ε'' curve for I-I 49-0 is almost identical in the three environments and is hardly affected by the changes in the higher eigenmodes (Fig. 5-4). This result is related to the fact that only a half of the eigenmodes (i.e., odd eigenmodes) contribute to the ε'' of I-I 49-0 and the intensities of those modes, $g_p(0)$ (cf. eq 5.10), rapidly decrease with increasing p (because $f_p(n)$ oscillates with n more frequently for larger p). Due to this rapid decrease, the ε'' of I-I 49-0 (Fig. 5-4) is not significantly affected by the changes in the higher eigenmodes. The situation is

similar for I-I 24-24: For this case, only even eigenmodes contribute to ε'' and their intensities ($g_p(N/2)$; cf. eq 5.10) decrease rapidly with increasing p, thereby giving an almost identical shape to the ε'' curve in the three environments(cf. Fig. 5-4).

In summary, the CR mechanism has an only minor effect on the distribution of the slowest three eigenmodes ($\tau_{\varepsilon,p}/\tau_{\varepsilon,1}$ ratio and the functional form of f_p) but the effect is enhanced for higher eigenmodes.

5-4-2. Comparison of ΔF_p and $\tau_{\varepsilon,p}$ data with models

The pure reptation and Rouse-type CR models, frequently used in interpretation of dynamic data for entangled chains, commonly have sinusoidal eigenfunctions, (cf. eqs 4.5 and 4.21) [20,21,33]

$$f_p^\circ(n^*) = \sin(p\pi n^*/N) \tag{5.17a}$$

$$F_p^\circ(n^*) = (\sqrt{2}/p\pi)[1 - \cos(p\pi n^*/N)] \tag{5.17b}$$

The base-shifted eigenfunctions of the models, $\Delta F_p^\circ(n^*) = F_p^\circ(n^*) - F_p^\circ(N/2)$, are shown in Fig. 5-6 with the dashed curves. The observed ΔF_p are non-sinusoidal and deviate from these ΔF_p°.

One might suspect that the non-sinusoidal feature of ΔF_p may be an artifact due to uncertainties in the analysis (eqs 5.9 - 5.11 and 5-12). However, the same analysis yielded sinusoidal ΔF_p for the dipole-inverted PI chains in *dilute solutions* (at $c = 0.8c^*$),[10] as anticipated from coincidence[10] of their ε'' data with the ε'' calculated from the bead-spring model having the sinusoidal ΔF_p°. Thus, the non-sinusoidal feature of ΔF_p found for the PI chains in the blend and bulk systems (Fig. 5-6) reflects the real nature of the chain dynamics in these environments.

This feature can be inferred also from the direct comparison of the normalized loss ($\varepsilon''/\Delta\varepsilon$) of I-I 49-0 with that calculated from the Rouse-CR/reptation models having the sinusoidal F_p°. At ω well above ω_{peak}, the data and calculation commonly exhibit the power-law behavior, $\varepsilon''/\Delta\varepsilon \propto \omega^{-\alpha}$. However, the calculated exponent ($\alpha = 1/2$) is significantly larger than the measured exponent ($\alpha \cong 1/4$; see Fig. 5-4).

The non-sinusoidal feature of F_p indicates that the behavior of the I-I 49-0 chain is not accurately described by the Rouse-type CR and pure reptation models even for the two extreme cases where the CR mechanism makes either a negligible or a dominant contribution to the chain motion (in B263 or in B9). The corresponding failure of the pure reptation model is noted for viscoelastic moduli.[31]

The eigenfunction equation for the sinusoidal $f_p^\circ(n)$ coincides with the Schrödinger equation for a quantum particle in a square well potential (having the boundaries at $n = 0$ and N),

$$\frac{1}{\tau_{\varepsilon,p}} f_p^\circ(n) = -\left(\frac{N^2}{\pi^2 \tau_{\varepsilon,1}}\right) \frac{d^2}{dn^2} f_p^\circ(n) \tag{5.18}$$

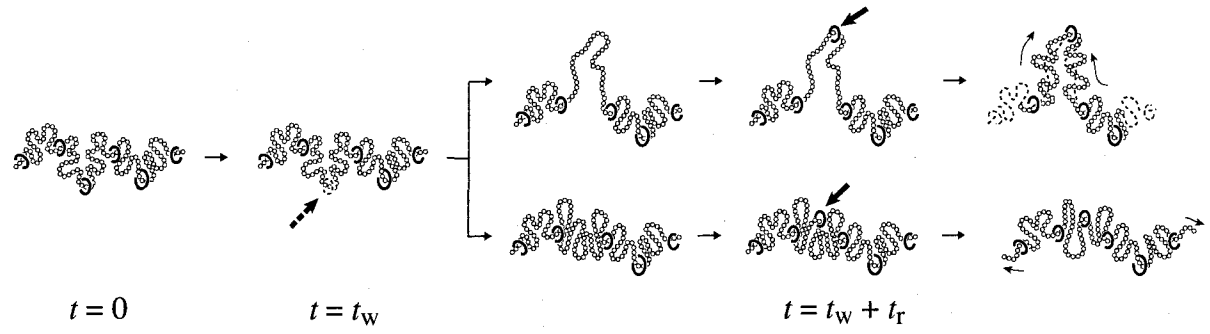

Fig.5-8 Schematic illustration of length-variable local CR jump. The slip-links indicate the entanglement constraints, and the small circles represent the monomers. The slip link removed at $t = t_w$ is reconstructed at $t = t_w+t_r$.

Thus, $[f_p°(n)]^2$ is analogous to the probability density of this particle.[6,15] This analogy can be utilized to attribute the difference between $f_p°(n)$ and $f_p(n)$ (between F_p and $F_p°$) to an additional potential near the well boundaries that decreases the probability density $[f_p(n)]^2$ near the boundaries.[6,15] This potential corresponds to a relaxation mechanism(s) not considered in the Rouse-type CR and reptation models. This extra mechanism enhances the relaxation near the chain ends to provide f_p (and F_p) with the non-sinusoidal feature.

For the non-Rouse type CR relaxation observed for dilute probes entangled with much shorter matrix chains, a previous study[15] suggested one possible mechanism enhancing the relaxation near the chain ends, the contour-length variable local jumps schematically shown in Fig. 5-8. The tension unbalance induced by this jump activates the extra motion at chain ends thereby providing the extra relaxation source.[15]

However, any mechanism enhancing the relaxation near chain ends can yield the non-sinusoidal feature of f_p.[6,15] In other words, the origin of this feature is not necessarily identical for the two cases of CR-free and CR-dominant environments. Further theoretical studies are desirable to clarify this problem.

In contrast to the differences between ΔF_p and $\Delta F_p°$ (Fig. 5-6), the observed $\tau_{\varepsilon,p}/\tau_{\varepsilon,1}$ ratios (Table 5.2) are close to the ratios deduced from the pure reptation and Rouse-type CR models,

$$\tau_{\varepsilon,p}/\tau_{\varepsilon,1} = p^{-2} \tag{5.19}$$

In particular, excellent agreement with the models is noted for I-I 49-0 in the CR-free B263 matrix. Thus the above mechanism enhancing the relaxation near the chain ends hardly affects the relaxation time spacing deduced from the reptation and Rouse-type CR models.

Finally, it is important to note that the CR effect is quite different for dielectric and viscoelastic relaxation: In contrast to the behavior seen in Fig. 5-4, changes in the CR contribution to the chain dynamics result in drastic changes in the viscoelastic mode distribution.[14,23,25,26,31] This reflects an essential difference between the local correlation function and the orientation function[15,17,33] describing the fundamental features of the dielectric and viscoelastic relaxation processes, respectively (cf. section 3-5). Chapter 6 utilizes this difference to examine detailed features (short-time coherence) of the chain motion.

5-5. Concluding Remarks

For the dipole-inverted PI chains in a long entangling matrix, eigenfunctions $f_p(n)$ and relaxation times $\tau_{\varepsilon,p}$ accompanying the local correlation function were dielectrically determined. For the slowest three eigenmodes, $f_p(n)$ and $\tau_{\varepsilon,p}/\tau_{\varepsilon,1}$ ratios are hardly affected by changes in the CR contribution to the chain motion, as revealed from comparison of $f_p(n)$ and $\tau_{\varepsilon,p}$ in the B263 matrix and these in shorter matrices (B9 and I-I 49-0). For higher eigenmodes, some CR effects are noted. In all matrices, $f_p(n)$ (p = 1-3) are non-sinusoidal with respect to the segment position n and deviate from the eigenfunctions deduced from the pure reptation and Rouse-type CR models, although the $\tau_{\varepsilon,p}/\tau_{\varepsilon,1}$ ratios are close to the model prediction. These results provide an important starting point for refining molecular models that describe the dynamics of entangled chains in various environments.

Appendix 5A. Characteristic Relationships for the Eigenfunctions

In general, the fundamental form of eigenfunctions $f_p(n)$ changes with the type of chain dynamics. Specifically, the functional form of $f_p(n)$ is determined by the type of the chain dynamics. Thus, some relationships between the eigenfunctions of different order, $f_p(n)$ with p = 1, 2, 3, ..., are not universal and change with the type of dynamics. However, a universal relationship(s) can be also found, as explained below.

Normalization: In the blends and monodisperse bulk system examined in this study, the PI chains should have the Gaussian conformation. As noted from eqs 3.13 and 5.3, this conformation determines the initial condition of the local correlation function $C(n,t;n')$,

$$C(n,0;n') = \frac{2}{N}\sum_{p=1}^{N} f_p(n) f_p(n') = \delta_{nn'} \tag{5A.1}$$

Equation 5A.1, indicating the equilibrium feature of the chain, specifies a relationship between the eigenfunctions that is valid irrespective of the type of chain dynamics. In particular, eq 5A.1 holds for any set of eigenfunctions that are expanded in a form,

$$f_p(n) = \sum_{\alpha} a_{p\alpha} \sin(\alpha\pi n/N) \tag{5A.2}$$

where $a_{p\alpha}$ are the components of a normalized, orthogonal matrix defined by

$$\sum_{\alpha} a_{p\alpha}\, a_{q\alpha} = \delta_{pq}, \quad \sum_{p} a_{p\alpha}\, a_{p\beta} = \delta_{\alpha\beta} \tag{5A.3}$$

For the integrated eigenfunctions $F_p(n)$ (Fig. 5-6) determined from the ε'' data, eq 5A.1 is rewritten as

$$\sum_{p=1}^{N} F_p(n)\, F_p(n') = n/N \ (\textit{for } n < n'),\ n'/N \ (\textit{for } n > n') \tag{5A.4}$$

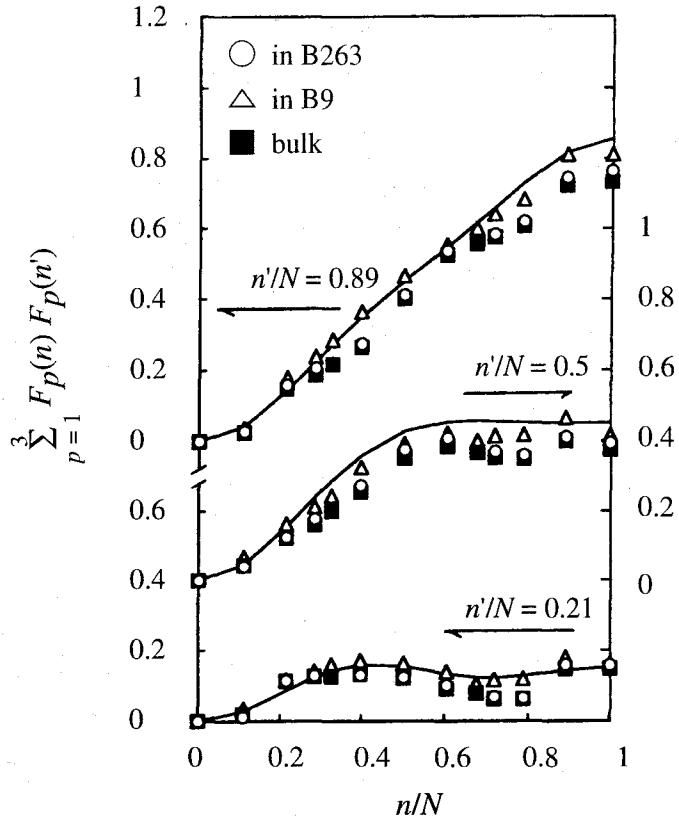

Fig.5-9 Plots of the sum $\sum_{p=1}^{3} F_p(n)\, F_p(n')$ for the I-I 49-0 chain in the three environments against the reduced segment position n/N. The plots are shown for representative n'/N values. The solid curves indicate the sum calculated for the sinusoidal $F_p^{\circ}(n)$ with p = 1-3.

The sum $\sum_{p=1}^{3} F_p(n)\, F_p(n')$ was evaluated for the $F_p(n)$ data (p = 1-3) to examine the validity of eq 5A.4. For some representative n'/N values, the n/N dependence of this sum is shown in Fig. 5-9. The solid curves indicate the sum calculated for the lowest three *sinusoidal* eigenfunctions, $F_p^{\circ}(n) = [\sqrt{2}/p\pi]\{1 - \cos[p\pi n/N]\}$ with p = 1-3.

The plots shown in Fig. 5-9 are based only on the experimentally available set of F_p with p = 1-3. Thus, eq 5A.4 cannot be expected to hold rigorously for the data shown in Fig. 5-9. However, these data qualitatively reproduce the characteristic feature of eq 5A.4, the linear increase of the sum for $n < n'$ and the leveling-off for $n > n'$. In addition, good agreement is noted between the data (in particular for the PI chains in B9) and the solid curves for the sinusoidal F_p° (p = 1-3). These results confirm the Gaussian nature of the PI chains.

Orthogonality: The orthogonality holds for any set of non-sinusoidal f_p given by eqs 5A.2 and 5A.3, i.e.,

$$I_{pq} = \frac{2}{N}\int_0^N f_p(n) f_q(n)\, dn = \delta_{pq} \qquad (5A.5)$$

Table 5-3.
Second-order integrals[a] of eigenfunctions for the I-I 49-0 chain in various environments.

	I_{11}	I_{13}	I_{22}	I_{33}
in B263	0.95	–0.18	0.74	1.29
in B9	1.04	–0.07	0.84	1.22
bulk	0.98	–0.17	0.73	1.08

a: $I_{pq} = (2/N)\int_0^N f_p(n) f_q(n)\, dn$

To test this orthogonality relationship for the empirically determined eigenfunctions, the $\Delta F_p(n)$ data for the I-I 49-0 chain in the blends and monodisperse bulk system (Fig. 5-6) were numerically differentiated to evaluate $f_p(n) = [N/\sqrt{2}][d\Delta F_p(n)/dn]$. This differentiation was carried out for curves smoothly connecting the ΔF_p data points in respective environments.

From the symmetry of f_p, $f_p(n) = f_p(N-n)$ for $p = 1, 3$ and $f_2(n) = -f_2(N-n)$, the integrals I_{pq} (= I_{qp}) automatically vanish for $[p,q]$= [1,2] and [2,3]. The integrals for the other set of $[p,q]$ are summarized in Table 5-3. The $|I13|$ is considerably smaller than I_{11} and I_{33} and the differences between I_{pq} and δ_{pq} are within the estimated uncertainties (less than 40% for the product $f_p f_q$). Thus the orthogonality relationship (eq 5A.5) appears to be valid for the f_p data. This result is consistent with the form of eigenmode expansion for $C(n,t;n')$ (eq 5.3).

Finally, it should be emphasized that the eigenfunctions are orthogonal for many types of chain dynamics. In other words, the orthogonality itself does not specify the type of chain dynamics.

References and Notes

1. Imanishi, Y.; Adachi, K.; Kotaka, T. *J. Chem. Phys.* **89**, 7585 (1988); see the references therein for the earlier work on polydisperse PI chains.
2. Adachi, K.; Yoshida, H.; Fukui, F.; Kotaka, T. *Macromolecules* **23**, 3138 (1990).
3. Yoshida, H.; Watanabe, H.; Adachi, K.; Kotaka, T. *Macromolecules* **24**, 2981 (1991).
4. Adachi, K.; Kotaka, T. *Prog. Polym. Sci.* **18**, 585 (1993).
5. Boese, D.; Kremer, F.; Fetters, L. J. *Macromolecules* **23**, 829 (1990); *ibid.* **23**, 1826 (1990).
6. Watanabe, H.; Urakawa, O.; Kotaka, T. *Macromolecules* **26**, 5073 (1993).
7. Yoshida, H.; Adachi, K.; Watanabe, H.; Kotaka, T. *Polymer J. (Japan)* **21**, 863 (1989).
8. Patel, S. S.; Takahashi, K. M. *Macromolecules* **25**, 4382 (1992).
9. Urakawa, O.; Adachi, K.; Kotaka, T. *Macromolecules* **26**, 2036 (1993); *ibid.* **26**, 2042 (1993).

10. Watanabe, H.; Yamada, H.; Urakawa, O. *Macromolecules* **28**, 6443 (1995).
11. Urakawa, O.; Watanabe, H. *Macromolecules* **30**, 652 (1997).
12. Adachi, K.; Itoh, S.; Nishi, I.; Kotaka, T. *Macromolecules* **23**, 2554 (1990).
13. a) Watanabe, H.; Yamazaki, M.; Yoshida, H.; Adachi, K.; Kotaka, T. *Macromolecules* **24**, 5365 (1991). b) Watanabe, H.; Yamazaki, M.; Yoshida, H.; Kotaka, T. *ibid.* **24**, 5372 (1991).
14. Watanabe, H.; Kotaka, T. *CHEMTRACTS Macromol. Chem.* **2**, 139 (1991); see also the references therein.
15. Watanabe, H.; Urakawa, O.; Kotaka, T. *Macromolecules* **27**, 3525 (1994).
16. Watanabe, H.; Urakawa, O.; Yamada, H.; Yao, M.-L. *Macromolecules* **29**, 755 (1996).
17. Watanabe, H.; Yao, M.-L.; Osaki, K. *Macromolecules* **29**, 97 (1996).
18. Equation 5.3 is derived for a Gaussian chain.[6] For non-Gaussian chains, eq 5.3 remains the same except that the prefactor 2/N is replaced by an appropriate normalization factor.
19. Klein, J. *Macromolecules* **11**, 852 (1978).
20. Graessley, W. W. *Adv. Polym. Sci.* **47**, 67 (1982).
21. Watanabe, H.; Tirrell, M. *Macromolecules* **22**, 927 (1989).
22. Watanabe, H.; Kotaka, T. *Macromolecules* **17**, 2316 (1984).
23. Watanabe, H.; Sakamoto, T.; Kotaka, T. *Macromolecules* **18**, 1008 (1985); *ibid.* **18**, 1436 (1985).
24. Watanabe, H.; Kotaka, T. *Macromolecules* **19**, 2520 (1986).
25. Watanabe, H.; Yoshida, H.; Kotaka, T. *Macromolecules* **21**, 2175 (1988); *ibid.* **25**, 2442 (1992).
26. Watanabe, H.; Yamazaki, M.; Yoshida, H.; Kotaka, T. *Macromolecules* **24**, 5573 (1991).
27. Montfort, J.-P.; Marin, G.; Monge, P. *Macromolecules* **17**, 1551 (1984).
28. Montfort, J.-P.; Marin, G.; Monge, P. *Macromolecules* **19**, 1979 (1986).
29. Struglinski, M. J.; Graessley, W. W. *Macromolecules* **18**, 2630 (1985).
30. Struglinski, M. J.; Graessley, W. W.; Fetters, L. J. *Macromolecules* **21**, 783 (1988).
31. Watanabe, H.; Matsumiya, Y.; Sato, T.; Osaki, K.; Yao, M.-L. *Macromolecules*, **31**, 7538 (1998).
32. Watanabe, H. *Macromol. Rapid Commun.*, **22**, 127 (2001).
33. M. Doi, S. F. Edwards, *The Theory of Polymer Dynamics,* Clarendon: Oxford (1986).
34. Ferry, J. D. *Viscoelastic Properties of Polymers,* 3rd Ed., Wiley: New York, (1980).
35. Graessley, W. W. *Adv. Polym. Sci.* **16**, 55 (1974).
36. The coincidence of the shape of the ε'' curves for I-I 49-0 and I-I 24-24 was confirmed in each environment (B263, B9, and monodisperse bulk system) from excellent superposition of the curves mutually shifted along the frequency axis.
37. In principle, The ε'' data at higher ω can be utilized to determine $g_p(n^*)$ for higher p (≥ 4). However, the $\tau_{\varepsilon,p}$ spacing was too narrow for those p and the higher dielectric modes were not accurately resolved. Thus, as before,[6,10,15] the $g_p(n^*)$ factors were determined only for p = 1-3.

CHAPTER 6

Effects of Constraint Release on the Coherence of the Submolecule Motion in Linear Chain

6-1. Intruduction

In Chapter 5, the eigenfunctions $f_p(n)$ (in an integrated form) and relaxation times $\tau_{\varepsilon,p}$ (eq 5.3) defined for the local correlation function $C(n,t;n')$ (eq 3.13) were experimentally determined for the dipole-inverted PI chains in a *high-M* entangling PB matrix (B263; $M = 263 \times 10^3$). The PI/B263 blends are chemically identical to the previously examined PI/B9 blends,[1] but the dynamics of the dilute PI probes is quite different in these blends. The *constraint release* (CR) mechanism (cf. section 4-4-1)[2-4] has a negligible contribution to the PI relaxation in the B263 matrix while it dominates the relaxation in the B9 matrix. Despite this difference, $f_p(n)$ (p = 1-3) are almost identical and the decay of the $\tau_{\varepsilon,p}/\tau_{\varepsilon,1}$ ratio with p is nearly the same in the two matrices. Furthermore, the observed eigenfunctions are non-sinusoidal, ruling out the pure reptation mechanism even in the CR-free, high-M B263 matrix.

On the basis of the above result, this Chapter compares the dielectric and viscoelastic behavior of the dipole-inverted PI chains. The global motion of the PI chains results in the dielectric as well as viscoelastic relaxation. The local correlation function and orientation function describing the dielectric and viscoelastic relaxation, $C(n,t;n')$ and $S(n,t)$, are related to the first- and second-order moments of the bond vector *at the time t*, $\mathbf{u}(n,t)$ (see eqs 3.4 and 3.13). Thus the motion of the PI chain is differently reflected in these functions. Utilizing this difference, one can examine changes in the bond vectors of two submolecules in a short interval of time.[1,5] These changes are perfectly correlated if the submolecules move *coherently* in this interval, while the changes are uncorrelated for the case of *incoherent* submolecular motion. For these two extreme cases of the submolecule motion, the linear viscoelastic moduli G_{coh}^* and G_{incoh}^* can be explicitly calculated from the dielectrically determined $f_p(n)$ and $\tau_{\varepsilon,p}$.[1,5] Comparison of these moduli with the G^* data specifies the coherence of the submolecular motion.

For PI chains in solutions, this strategy was utilized to reveal that the short-time motion of the submolecules is incoherent in the non-entangled solutions and some degree of coherence emerges in entangled solutions.[5] However, even for the case of well entangled PI in a monodisperse bulk state ($M/M_e \cong 10$ and 28; M_e = entanglement spacing), imperfect coherence was found.[5]

This imperfect coherence could be related to the constraint release (CR) mechanism that has a considerable contribution to the viscoelastic relaxation of chains in monodisperse systems with M/M_e as large as 30.[5-8] Upon removal of the constraint, the submolecules would acquire the freedom to move in a more or less random (uncorrelated) way. Thus the CR mechanism could lead to lack of perfect coherence of the submolecule motion even in these well entangled systems.

To test this hypothesis about the CR effect on the coherence of the submolecule motion,

this Chapter compares the moduli data with G_{coh}^* and G_{incoh}^* calculated from ε'' data for dilute PI chains ($M = 48.8 \times 10^3$) in various environments. Firstly in section 6-2, the theoretical framework and strategy of this test are explained. Then, the remaining part of this Chapter is devoted for comparison of the measured and calculated moduli to elucidate the CR effect on the coherence of submolecular motion.

6-2. Theoretical

6-2-1. General

Relationships between the dielectric and viscoelastic quantities have been derived for the two extreme cases of coherent and incoherent submolecular motion.[1,5] The results for *entangled* linear chains with molecular weight M and concentration c are summarized below.

For description of the global motion of an entangled chain, the entanglement segment is naturally chosen as the submolecule, the modulus-sustaining unit for slow viscoelastic relaxation. For a chain composed of N submolecules ($N = M/M_e$; M_e = entanglement spacing), a change in the submolecular bond vector $\mathbf{u}$ in a short interval of time between t and $t + \Delta t$ is considered here. This change is generally determined by the chain conformation at time t and described by a time-evolution equation of the form,[5]

$$\mathbf{u}(n,t + \Delta t) = L^*(n;\Delta t)\,\mathbf{u}(n,t) + \text{thermal noise term} \tag{6.1}$$

Here, $L^*(n;\Delta t)$ (= 1 for $\Delta t = 0$) is an operator acting on $\mathbf{u}$ at time t: L^* is determined by the nature of the global chain dynamics and the operation $L^*\mathbf{u}$ may involve either local or non-local operations (or both).[1] On the basis of eq 6.1, the time evolution equation can be formulated (in the continuous limit) for the local correlation function and orientation function, and the dielectric and viscoelastic properties are calculated accordingly.

6-2-2. Expression of ε''

For the local correlation function $C(n,t;n')$, the time evolution equation derived from eq 6.1 is given by[5]

$$\frac{\partial}{\partial t}C(n,t;n') = L_C(n)\,C(n,t;n') \tag{6.2}$$

Here, the operator L_C is defined in terms of L^* as

$$L_C(n) = \left[\frac{\partial \langle L^*(n;\Delta t)\rangle}{\partial \Delta t}\right]_{\Delta t \to 0} \tag{6.3}$$

Under a boundary condition representing the random orientation at the chain ends ($C(n,t;n') = 0$ for n, $n' = 0$ and N), the eigenfunctions $f_p(n)$ and the relaxation times $\tau_{\varepsilon,p}$ accompanying eq 6.2 are determined by[5]

$$L_C(n)f_p(n) = -[1/\tau_{\varepsilon,p}]f_p(n) \quad (f_p(0) = f_p(N) = 0) \tag{6.4}$$

From the symmetry of the orientational correlation, $\langle \mathbf{u}(n,t)\bullet\mathbf{u}(n',0)\rangle = \langle \mathbf{u}(n',t)\bullet\mathbf{u}(n,0)\rangle$, the solution of eq 6.2 is written in a form of eigenmode expansion given by eq 5.3.[11] (The $f_p(n)$ used in eq 5.3 are normalized so as to satisfy the initial condition representing the Gaussian conformation of the chain, $C(n,0;n') = \delta_{nn'}$.[9,10])

From the solution of eq 6.2, the dielectric loss $\varepsilon''(\omega)$ of PI chains at angular frequency ω is expressed in terms of $f_p(n)$ and $\tau_{\varepsilon,p}$. (cf. eqs 5.3, 3.12, and 2.15)[1,5,9,11] Specifically, for *regular* PI chains having no dipole-inversion, $\varepsilon''(\omega)$ is given by[5]

$$\varepsilon''(\omega) = 2\Delta\varepsilon \sum_{p=1}^{N} \left[\frac{1}{N}\int_0^N f_p(n)\, dn \right]^2 \frac{\omega\tau_{\varepsilon,p}}{1+\omega^2\tau_{\varepsilon,p}^2} \tag{6.5}$$

Here, $\Delta\varepsilon$ is the dielectric intensity for the global chain motion.

6-2-3. Expression of G^*

For a chain subjected to a small step shear strain at $t = 0$, an orientation function for two (n-th and n'-th) submolecules is defined as,

$$S_2(n,n',t) = (1/a^2)\langle u_x(n,t)u_y(n',t)\rangle \qquad (t > 0) \tag{6.6}$$

For $n = n'$, this S_2 is reduced to the orientation function $S(n,t)$ defined by eq 3.4.

For $S_2(n,n',t)$, the time evolution equation deduced from eq 6.1 is written as[5]

$$\frac{\partial}{\partial t} S_2(n,t;n') = L_S(n;n')\, S_2(n,t;n') \tag{6.7}$$

Here, L_S is an operator defined in terms of L^* (eq 6.1),

$$L_S(n;n') = \left[\frac{\partial \langle L^*(n;\Delta t)L^*(n';\Delta t)\rangle}{\partial \Delta t} \right]_{\Delta t \to 0} \tag{6.8}$$

This L_S is given as the second-order moment of L^* while the operator L_C for C (eq 6.3) includes the first-order moment. Thus, a relationship between L_S and L_C changes with the stochastic nature of the chain dynamics represented by L^*, implying that the solution of eq 6.7 cannot be generally expressed in terms of $f_p(n)$ and $\tau_{\varepsilon,p}$ defined for $C(n,t;n')$. However, for two extreme cases, specific expressions are obtained.

For the case of incoherent submolecular motion where the short time motions of two

submolecules in individual chains are not correlated at all, eq 6.8 is decoupled as $L_S(n;n') = L_C(n) + L_C(n')$. For this case, $S_2(n,n',t)$ can be explicitly expanded with respect to f_p and $\tau_{\varepsilon,p}$ to obtain the relaxation modulus $G(t)$ ($\propto \int_0^N S_2(n,n,t)\,dn$; cf. eq 3.6).[5] The resulting expression for the reduced linear viscoelastic modulus, $G_r^* = G^*M/cRT = G_r' + iG_r''$ (R = gas constant), is[5]

$$G_{r,incoh}^*(\omega) = 2\sum_{p=1}^{N}\left[\frac{1}{N}\int_0^N \{f_p(n)\}^2\,dn\right]\frac{i\omega\tau_{\varepsilon,p}/2}{1+i\omega\tau_{\varepsilon,p}/2} \quad (i=\sqrt{-1}) \qquad (6.9)$$

For the other case of coherent submolecular motion where the submolecule motions are perfectly correlated in individual chains to satisfy a relationship, $[<L^*(n;\Delta t)L^*(n';\Delta t)>S_2(n,n',t)]_{n=n'} = <L^*(n;\Delta t)>S_2(n,n,t) + O(\Delta t^2)$, $S_2(n,n',t)$ is differently expanded with respect to fp and $\tau_{\varepsilon,p}$. For this case, reduced modulus G_r^* is given by[5]

$$G_{r,coh}^*(\omega) = \left(\frac{2G_NM}{cRT}\right)\sum_{p=1}^{N}\left[\frac{1}{N}\int_0^N f_p(n)\,dn\right]^2\frac{i\omega\tau_{\varepsilon,p}}{1+i\omega\tau_{\varepsilon,p}} \qquad (6.10)$$

Here, G_N is the plateau modulus of the chains having the molecular weight M and concentration c (in mass/volume units). (Equations 6.9 and 6.10 are derived on the basis of an expression of G_N for affine deformation, $G_N = cRT/M_e = NcRT/M$. If the Doi-Edwards expression, $G_N = 4cRT/5M_e$, is used, eq 6.9 is slightly modified (the front factor of 2 becomes 8/5)[1] but eq 6.10 remains the same.[5])

The calculated moduli are quite different for the above two cases, and the coherence of the submolecular motion can be examined by comparing these moduli with the G_r^* data. The coherence can be also examined through direct comparison of the ε'' and G'' data: *If the submolecule motion is coherent,* these data of regular PI chains (with no dipole-inversion) obey a simple relationship[5] (cf. eqs 6.5 and 6.10)

$$\varepsilon''(\omega)/\Delta\varepsilon = G''(\omega)/G_N \quad \text{(for regular PI)} \qquad (6.11)$$

Thus, some degree of incoherence can be concluded if a difference is found between the $\varepsilon''(\omega)/\Delta\varepsilon$ and $G''(\omega)/G_N$ data.

6-3. Experimental

A regular PI sample, I-I 49-0 ($M = 48.8 \times 10^3$), and two polybutadiene samples, B263 ($M = 263 \times 10^3$) and B9 ($M = 9.24 \times 10^3$), were used. The molecular characteristics of these samples were summarized in Table 2.1.

Linear viscoelastic measurements were carried out with a laboratory rheometer, RMS 605

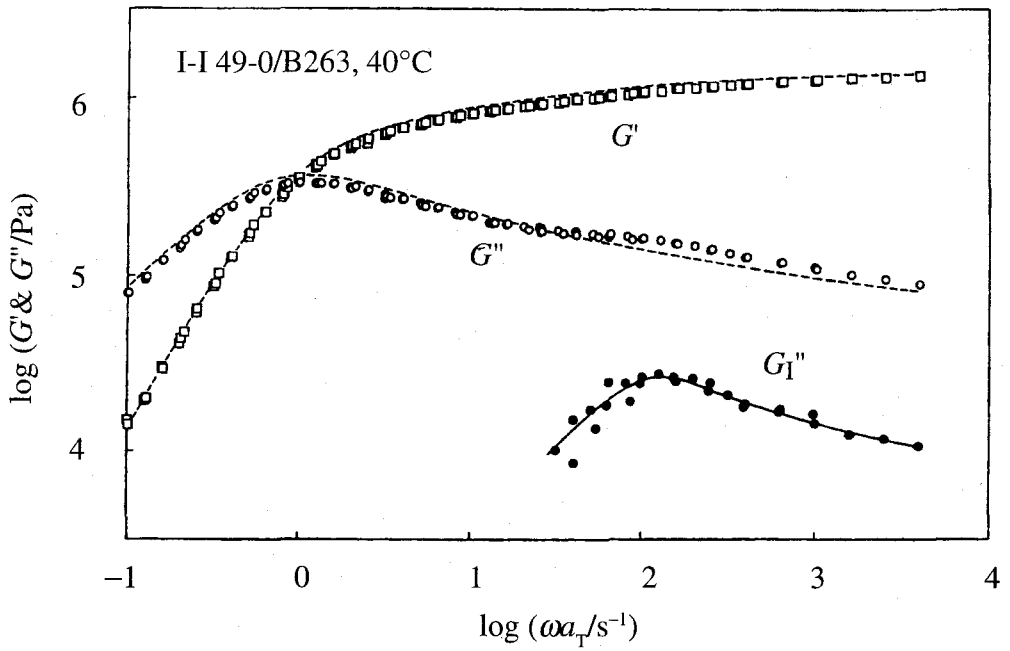

Fig.6-1 Linear viscoelastic moduli of the I-I 49-0/B263 blend (ϕ_{PI} = 0.05) at 40°C (unfilled symbols). The dashed curves indicate the moduli of bulk B 263 matrix. The filled circles indicate the loss moduli G_I" of the dilute I-I 49-0 chains in the blend evaluated from eq 6.12.

(cf. section 2-3-3). Storage and loss moduli, G' and G'', were determined for homogeneous blends of I-I 49-0 (with the volume fraction ϕ_{PI} = 0.05) in the B263 and/or B9 matrices and for bulk B263 and B9 matrices. The moduli were measured also for bulk I-I 49-0 system, and the results were in excellent agreement with the previous data.[5] Time-temperature superposition worked very well for all these G' and G'' data, and the data were reduced to T_r = 40°C and directly compared with the dielectric data of the same systems obtained in Chapter 5 and in previous studies.[1,9]

The shift factors $a_{T,G}$ for G^* was the same for the I-I 49-0/B263 and I-I 49-0/B9 blends as well as for respective matrices in the bulk state. The $a_{T,G}$ data for the I-I 49-0/B263 blend and bulk B263 matrix, shown in Fig. 5-2, coincided with $a_{T,\varepsilon}$ for ε'' of the I-I 49-0 chains in the B263 matrix. This result indicates that the dilute I-I 49-0 chains (ϕ_{PI} = 0.05) were uniformly mixed with the B263 matrix and the segmental motion of the I-I chains is activated by the motion of B matrix segment. Similar results were found for the I-I 49-0/B9 blend[1] and other PI/PB blends containing dilute PI chains.[12]

6-4. Results

6-4-1. Overview of viscoelastic behavior of I-I 49-0/PB blends

Figs. 6-1 and 6-2, respectively, show the master curves of linear viscoelastic moduli for the I-I 49-0/B263 and I-I 49-0/B9 blends at 40°C. The unfilled squares and circles indicate G_b' and G_b'' of the blends. For comparison, the moduli G_m' and G_m'' of respective matrices *in the bulk state* are shown with the dashed curves. The dilute I-I 49-0 chains (ϕ_{PI} = 0.05) are entangled only with the B263 and/or B9 matrices, as explained later in section 6-5-1. The constraint release (CR) mechanism has a negligible contribution to the relaxation of the dilute I-I 49-0

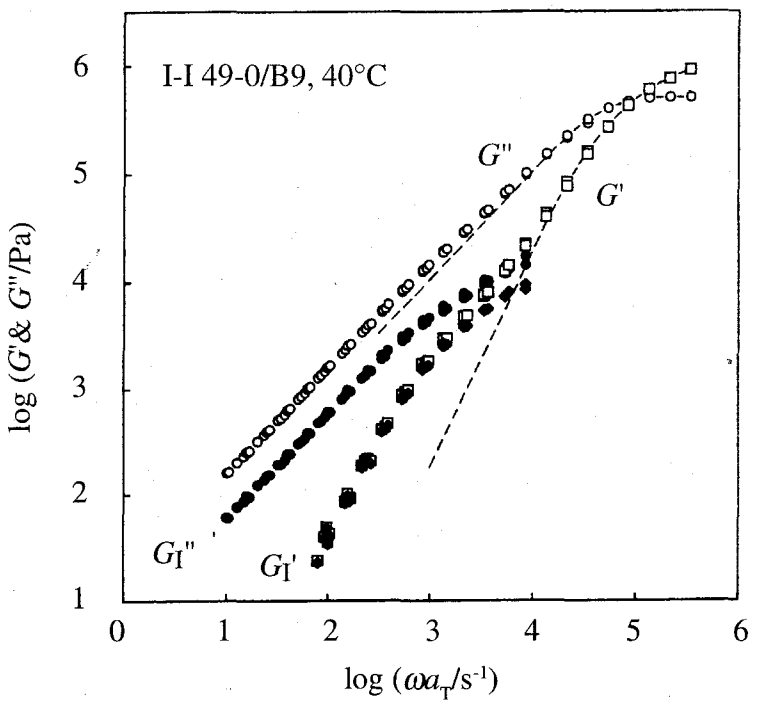

Fig.6-2 Linear viscoelastic moduli of the I-I 49-0/B9 blend (ϕ_{PI} = 0.05) at 40°C (unfilled symbols). The dashed curves indicate the moduli of bulk B9 matrix. The filled symbols indicate the moduli G_I* of the dilute I-I 49-0 chains in the blend evaluated from eq 6.12.

chains in the B263 matrix while it dominates the relaxation in the B9 matrix;[10] cf. Chapter 5.

Fig. 6-1 demonstrates that G_b" is larger than G_m" and exhibits a shoulder at $\omega a_T > 20$ s^{-1} where G_m' shows a well defined rubbery plateau. At lower ωa_T, G_b" becomes smaller than G_m". These results indicate that the blend has a fast relaxation process of small intensity that is absent in the bulk matrix. This relaxation process is also seen for the G' data, though less prominently. (In general, G" has a higher sensitivity to fast and weak relaxation modes than G'; cf. section 2-3-2.)

The fast and weak relaxation process seen above corresponds to the relaxation of the dilute I-I 49-0 chains in the blend: At ωa_T well above 20 s^{-1}, the I-I 49-0 chains hardly relax and effectively contribute to G_b' of the blend. On the other hand, at $\omega a_T < 20$ s^{-1}, these chains completely relax and behave as a "solvent" for the much longer B263 chains. The difference between G_b* and G_m* at low ωa_T reflects this "solvent-like" role of I-I 49-0 for the terminal relaxation of the B263 matrix.

In Fig. 6-2, a different feature is noted for the I-I 49-0/B9 blend. For this case, the I-I 49-0 relaxation is slower than the matrix relaxation. Thus the difference between the blend (unfilled symbols) and bulk matrix (dashed curve) is more prominently observed for G' than for G" (because slow and weak relaxation modes are more sensitively detected in G'). At $\omega a_T < 10^4$ s^{-1}, G_b' is significantly larger than G_m' and exhibits a clear shoulder while G_b" is only moderately larger than G_m". This shoulder corresponds to the terminal relaxation of I-I 49-0 in the B9 matrix. These results indicate that the B9 matrix chains, being much *shorter* than the I-I 49-0 chain, behave as the "solvent" for the terminal relaxation of I-I 49-0. This type of the matrix behavior has been also noted in the other blend systems.[6-8,13-15]

6-4-2. Evaluation of G_I^* for I-I 49-0 in PB matrices

From the G_b^* and G_m^* data shown in Figs. 6-1 and 6-2, the viscoelastic moduli G_I^* of the dilute I-I 49-0 chains in the B263 and B9 matrices are evaluated in the following way.

6-4-2-1. G_I^* in B9 matrix

The coincidence of G_m^* and G_b^* at $\omega a_T > 10^4$ s^{-1} (Fig. 6-2) indicates that the dilute I-I 49-0 chains do not affect the terminal relaxation of the B9 chains. Thus, the contribution of the B9 matrix to the viscoelastic modulus of the blend is given by $\phi_m G_m^*(\omega)$, where ϕ_m (= 0.95) is the matrix volume fraction in the blend and $G_m^*(\omega)$ is the modulus of bulk B9. At $\omega a_T < 10^4$ s^{-1} where the I-I 49-0 chains exhibit their terminal relaxation, the B9 chains have fully relaxed and behave as a "solvent" for the I-I 49-0 chains. In this range of ωa_T, G_I^* is simply evaluated by subtracting the matrix contribution from the G_b^* data,

$$G_I^*(\omega) = G_b^*(\omega) - \phi_m G_m^*(\omega) \tag{6.12}$$

The validity of this subtraction has been confirmed in previous studies for long, dilute probe chains entangled with much shorter matrix chains.[6-8,13-15]

At $\omega a_T < 10^4$ s^{-1}, G_I' and G_I'' thus evaluated are shown in Fig. 6-2 with filled diamonds and filled circles, respectively. Since G_b' (unfilled squares) is significantly larger than G_m' (dashed curve) and G_I' is close to G_b' in this range of ωa_T, uncertainties in the evaluation of G_I' are negligibly small. Although G_b'' (unfilled circles) is not much larger than G_m'' (dashed curve), G_I' and G_I'' obtained from eq 6.12 exhibit the Kramers-Kronig type consistency (that resembles the dependence deduced from bead-spring models)[16] in their a_T dependence. This result strongly suggests that G_I'' is also evaluated satisfactorily. In particular, at sufficiently low ωa_T (< 100 s^{-1}) where the blend and bulk matrix exhibit respective zero-shear viscosities, $\eta_{0,b}$ and $\eta_{0,m}$, G_I'' is accurately evaluated from eq 6.12 as $G_I''(\omega) = \omega[\eta_{0,b} - \phi_m \eta_{0,m}]$.

6-4-2-2. G_I^* in B263 matrix

In the B263 matrix, the I-I 49-0 chains relax at $\omega a_T > 20$ s^{-1}; see Fig. 6-1. The evaluation of G_I^* in this matrix requires some molecular considerations. Specifically, the evaluation is made for two cases.

Case 1: If the dilute I-I 49-0 chains do not affect the relaxation behavior of the B263 matrix at $\omega a_T > 20$ s^{-1}, $G_I^*(\omega)$ is given by eq 6.12 with G_m^* being the modulus of the bulk B263 matrix. The $G_I''(\omega)$ data evaluated in this way are shown in Fig. 6-1 with filled circles. Since G_b' and G_m' are close to each other, the G_I' evaluated from eq 6.12 exhibited a large scatter. Those G_I' data are not shown in Fig. 6-1.

Case 2: If the dilute I-I 49-0 chains behave exactly as a "solvent" for the B263 matrix at $\omega a_T >$ 20 s^{-1}, $G_I^*(\omega)$ is obtained by subtracting the modulus $G_{sol}^*(\omega)$ of a "solution" of B263 (with the

volume fraction $\phi_m = 0.95$) from the $G_b^*(\omega)$ data. Since ϕ_m is close to unity and the "solvent" is the polymeric I-I 49-0 that is chemically similar to B263, the segmental friction of B263 in this "solution" would be close that in bulk B263. For this case, $G_{sol}^*(\omega)$ of the "B263 solution" is given by[13,15,16]

$$G_{sol}^*(\omega) = \phi_m^2 G_m^*(\phi_m^{1.5}\omega) \tag{6.13}$$

where $G_m^*(\omega)$ is the modulus of bulk B263 at the frequency ω. In eq 6.13, the front factor, ϕ_m^2, accounts for the dilution of B263 to the volume fraction ϕ_m and the increase of M_e ($\propto \phi_m^{-1}$) on this "dilution", and the multiplication factor $\phi_m^{1.5}$ for ω accounts for acceleration of the B263 relaxation due to this increase of M_e. In fact, $G_{sol}^*(\omega)$ given by eq 6.13 agreed very well with the G_b^* data at low $\omega a_T < 5\ s^{-1}$ where the I-I 49-0 chains fully relax and actually behave as the "solvent" for the B263 chains (cf. Fig. 6-1). Thus, in the case 2, $G_I^*(\omega)$ is evaluated as

$$G_I^*(\omega) = G_b^*(\omega) - \phi_m^2 G_m^*(\phi_m^{1.5}\omega) \tag{6.14}$$

Validity of eq 6.12: At sufficiently high ω where the dilute I-I 49-0 chains have not relaxed, the behavior of the B263 matrix chains in the blend should be close to the behavior in their bulk system. These B263 chains begin to adjust their M_e in the blend to that in the "solution" after the I-I 49-0 relaxation is completed, and this adjustment requires some time. Thus, during the I-I 49-0 relaxation at $\omega a_T > 20\ s^{-1}$, the behavior of the B263 chains in the blend would be essentially the same as that in their bulk system. This argument suggests that the case 1 is close to the real situation and the G_I^* evaluated from eq 6.12 is to be used as the modulus for the I-I 49-0 chains in the B263 matrix.

Here, an uncertainty is examined for the G_I^* evaluated for the case 1 (eq 6.12) by comparing this G_I^* with the G_I^* for the case 2 (eq 6.14): Among all possibilities for the evaluation of G_I^*, eq 6.12 gives the lower bound for the G_I^* value while eq 6.14 gives the upper bound. Thus, the true modulus of I-I 49-0 is determined from eq 6.12 with no uncertainty if the two G_I^* obtained from eqs 6.12 and 6.14 are indistinguishable. This comparison is made in Fig. 6-3. The G_I'' for the case 1 (eq 6.12) is shown with the filled circles. The G_I'' for the case 2 (eq 6.14) exhibited a peak that was $\cong$ 25% higher than the peak of the G_I'' for the case 1. For the best comparison of the viscoelastic mode distribution (ω dependence of G_I^*) for the cases 1 and 2, the G_I' and G_I'' for the case 2 are *multiplied by a factor of 0.75* and shown with unfilled squares and filled triangles. Good agreement is found for the filled circles and triangles over the entire range of ω examined. This result demonstrates that the true viscoelastic mode distribution of the I-I 49-0 chain is satisfactorily determined by eq 6.12. In addition, the agreement suggests that the G_I'' determined by eq 6.12 includes the uncertainty less than 25%. Thus, this G_I'' can be safely utilized in tests of the coherence of the submolecule motion.

The above argument for the B263 matrix relaxation at $\omega a_T > 20\ s^{-1}$ suggests that the G_I' for the case 1 (eq 6.12) is the true storage modulus of the I-I 49-0 chains in this matrix. How-

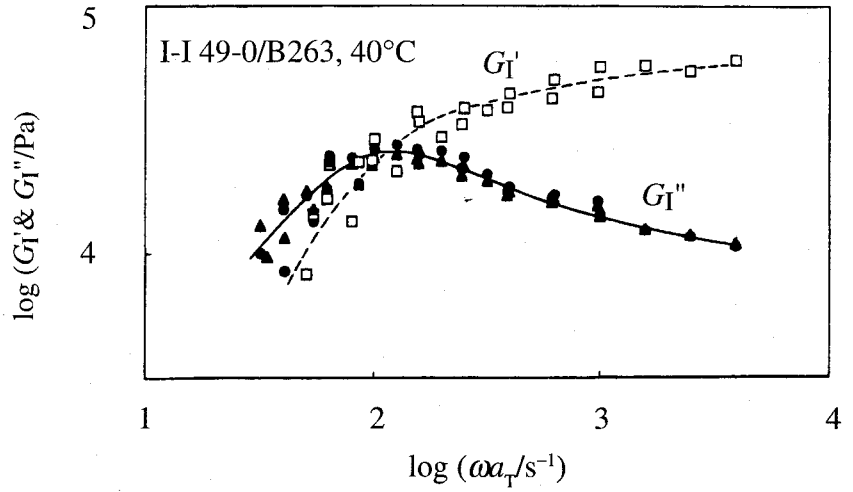

Fig.6-3 Comparison of the linear viscoelastic moduli G_I^* of the I-I 49-0 chains ($\phi_{PI} = 0.05$) in the B263 matrix evaluated from eq 6.12 (filled circles) and eq 6.14 (filled triangles and unfilled squares). The G_I^* evaluated from eq 6.14 are multiplied by a factor 0.75.

ever, direct application of eq 6.12 to the G_b^* and G_m^* data resulted in scattered estimates of G_I'. The results shown in Fig. 6-3 are helpful to avoid this difficulty. The G_I' and G_I'' for the case 2 (eq 6.14) exhibit the Kramers-Kronig type consistency[16] in their ω dependence (cf. unfilled squares and filled triangles), and the latter multiplied by the factor of 0.75 coincides well with the true G_I'' determined by eq 6.12. These results indicate that the true G_I' (for the case 1) can be evaluated as the G_I' for the case 2 multiplied by the same factor. Thus the G_I' and G_I'' for the case 2 multiplied by 0.75 are used later in Fig. 6-4 as the true moduli of the I-I 49-0 chains.

6-5. Discussion

6-5-1. Entanglement spacing for I-I 49-0 in PB matrices

In Fig. 6-1, the G_I'' data for the dilute I-I 49-0 chains in the B263 matrix (determined by eq 6.12) exhibit a sharp peak; see filled circles. Thus, the plateau modulus $G_{N,I}$ of these chains can be evaluated as $G_{N,I} = (2/\pi)\int_{-\infty}^{\infty} G_I''\, d\ln\omega$. From this $G_{N,I}$, the entanglement spacing for the I-I 49-0 chains is obtained as $M_{e,I} = \rho_b \phi_{PI} RT/G_{N,I}$ (ρ_b = density of the blend). For the solid curve smoothly connecting the G_I'' data points in Fig. 6-1, the above integration was numerically carried out to give

$$G_{N,I} \cong 7.0 \times 10^4 \text{ Pa} \quad \text{for dilute I-I 49-0 in PB } (\phi_{PI} = 0.05) \tag{6.15}$$

and

$$M_{e,I} \cong 1700 \quad \text{for dilute I-I 49-0 in PB} \tag{6.16}$$

The G_N and M_e of monodisperse systems are independent of the molecular weight and determined by local topological interactions of the chains.[16] Thus, G_N and M_e of I-I 49-0 in both

B263 and B9 matrices should be given by eqs 6.15 and 6.16.

It should be noted that the $M_{e,I}$ value is close to the $M_{e,B}°$ value (= 1900)[17] for bulk PB. For *dilute* PI chains in entangling PB matrices, a previous study[18] determined a hypothetical monodisperse state as a state where the PI chains and PB matrices have the same relaxation time. This state was found to be realized when the PI and PB chains have the same molecular weight, meaning that the dynamics of the dilute PI chains is equivalent to the dynamics of the PB matrix chains having the same M. This result is in harmony with the above coincidence of $M_{e,I}$ and $M_{e,B}°$.

The $M_{e,I}$ value (eq 6.16) specifies a critical PI molecular weight $M_{c,I}$ that is required for PI chains in the PB matrix to be entangled among themselves. In usual solutions, the chains with a volume faction ϕ are entangled among themselves if their M is larger than $M_c°/\phi \cong 2M_e°/\phi$,[16,17] where $M_c°$ and $M_e°$ are the characteristic molecular weight and entanglement spacing in the bulk state. From this criterion with the above $M_{e,I}$ value, the PI chains of $\phi_{PI} = 0.05$ are concluded to entangle among themselves if their M_I is larger than $2M_{e,I}/\phi_{PI} \cong 68 \times 10^3$. According to this result, the PI chains are entangled among themselves in *none* of the PI/PB blends ($M_I \leq 50 \times 10^3$) used in this Chapter and Chapter 5.

6-5-2. Calculation of $G_{r,coh}^*$ and $G_{r,incoh}^*$

For the I-I 49-0 chains in the B9 matrix ($\phi_{PI} = 0.05$) as well as in their monodisperse bulk system, the eigenfunctions $f_p(n)$ and the relaxation times $\tau_{\varepsilon,p}$ (p = 1-3) of the local correlation function (eq 5.3) have been determined in previous studies.[1,5,9] In these studies, the integrated eigenfunctions $F_p(n^*)$ were obtained from analyses of ε'' data of the dipole-inverted PI chains, and $f_p(n)$ were evaluated from numerically differentiation of $F_p(n^*)$,

$$F_p(n^*) = \frac{\sqrt{2}}{N}\int_0^{n^*} f_p(n)\,\mathrm{d}n,\quad f_p(n) = \frac{1}{\sqrt{2}}\left(\frac{\mathrm{d}F_p(n)}{\mathrm{d}(n/N)}\right) \tag{6.17}$$

For the I-I 49-0 chains in the B263 matrix ($\phi_{PI} = 0.05$), $\Delta F_p(n^*) = F_p(n^*) - F_p(N/2)$ and $\tau_{\varepsilon,p}$ for the lowest three eigenmodes (p = 1-3) were obtained in Chapter 5. As done before,[1,5] the numerical differentiation (eq 6.17) was made for the solid curves shown in Fig. 5-6 that smoothly connect the $\Delta F_p(n^*)$ data points to evaluate $f_p(n)$.

For the I-I 49-0 chains in the above three environments, the $f_p(n)$ and $\tau_{\varepsilon,p}$ data for p= 1-3 were utilized to calculate the reduced moduli for the two extreme cases of incoherent and coherent submolecule motion, $G_{r,incoh}^*$ (eq 6.9) and $G_{r,coh}^*$ (eq 6.10). The $G_{r,incoh}^*$ and $G_{r,coh}^*$ thus obtained are different from (smaller than) the moduli contributed form all eigenmodes (p = 1-N). For the storage modulus $G_{r,incoh}'(\omega)$ being insensitive to fast eigenmodes, this difference is negligibly small at $\omega < 6/\tau_{G,1}$ where $\tau_{G,1}$ is the longest relaxation time of $G_{r,incoh}^*$.[5,19] Since the intensity factor for $G_{r,coh}'$ ($\propto [(1/N)\int_0^N f_p(n)\,\mathrm{d}n]^2$; eq 6.10) decays with increasing p more

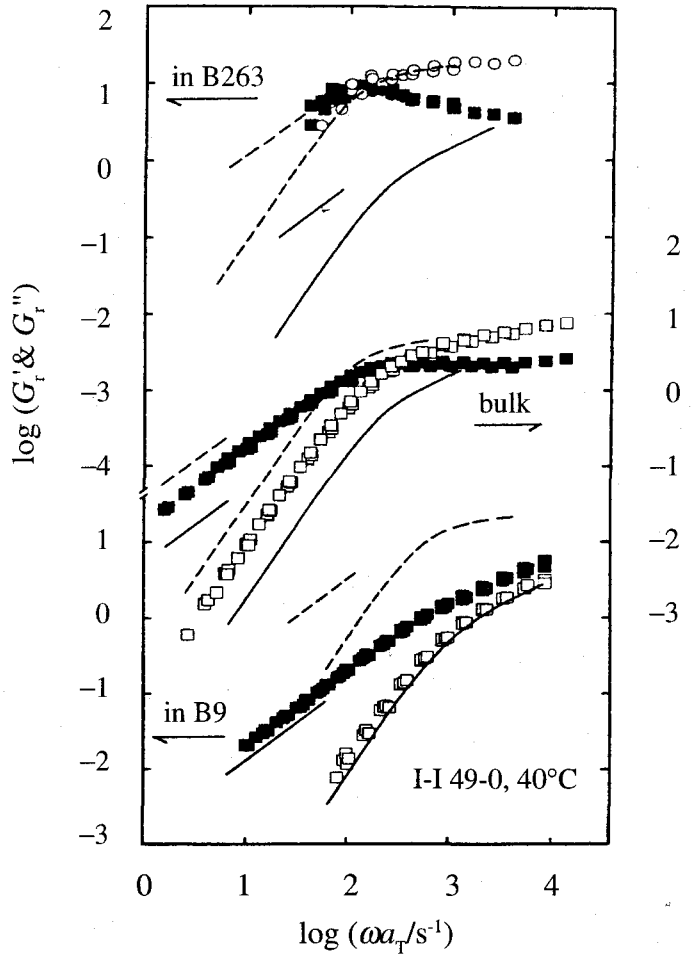

Fig.6-4 Comparison of $G_{r,incoh}$* (solid curves; eq 6.9) and $G_{r,coh}$* (dashed curves; eq 6.10) evaluated from the dielectrically determined $f_p(n)$ and $\tau_{\varepsilon,p}$ (p = 1-3) with the G_r* data of the I-I 49-0 chain. The comparison is made in the three environments at 40°C.

strongly than the factor for $G_{r,incoh}$' ($\propto (1/N)\int_0^N \{f_p(n)\}^2 dn$; eq 6.9) the difference between the moduli calculated for p = 1-3 and p = 1-N is smaller for $G_{r,coh}$' than for $G_{r,incoh}$' . Thus, at $\omega < 6/\tau_{G,1}$, these storage moduli calculated for p = 1-3 can be safely utilized in comparison with the G_r' data.

The situation is somewhat different for the loss modulus being more significantly contributed from fast eigenmodes than the storage modulus. In the zero-shear regime at $\omega < 1/\tau_{G,1}$, the difference between the loss moduli calculated for p = 1-3 and p = 1-N is estimated to be $\cong$ 20%[19] for $G_{r,incoh}$" and $\cong$ 10%[20] for $G_{r,coh}$". This difference specifies an error in the G_r" calculated for p = 1-3. For both $G_{r,incoh}$" and $G_{r,coh}$", the error becomes larger at higher ω. Thus, the $G_{r,incoh}$" and $G_{r,coh}$" calculated for p = 1-3 can be compared with the G_r" data only in the zero-shear regime, and the uncertainties in this comparison are 10% ~ 20%.

6-5-3. CR effects on coherence of submolecule motion

Fig. 6-4 compares the calculated moduli, $G_{r,incoh}$* (solid curves) and $G_{r,coh}$* (dashed curves), with the G_r* data at 40°C for the I-I 49-0 chains in the B263 and B9 matrices and in the monodisperse bulk system. The $G_{r,incoh}$' and $G_{r,coh}$' are shown at $\omega < 6/\tau_{G,1}$ while the $G_{r,incoh}$" and

$G_{r,coh}$" (the short straight lines with slope of unity) are shown only in the zero-shear regime for the reasons explained above. The unfilled and filled squares indicate the G_r' and G_r" data: For the bulk I-I 49-0 system, the G^* data are straightforwardly converted to the reduced modulus G_r^* = $G^*M_I/\rho_I^\circ RT$ (ρ_I° = bulk PI density). For the I-I 49-0 chain in the B263 and B9 matrices (cf. Figs. 6-1 and 6-2), the G_I^* data determined from eq 6.12 were used to evaluate $G_r^* = G_I^* M_I / \rho_b \phi_{PI} RT$ (ρ_b = blend density).

For the I-I 49-0 chain in the B263 matrix, the true G_I" values are determined by eq 6.12; see section 6-4-2. However, the ω dependence of this G_I" is almost identical to that of the G_I" determined by eq 6.14 and the magnitude is larger for the latter by a factor of 25%; see Fig. 6-3. Thus, Gr' and G_r" are also evaluated from the G_I' and G_I" determined by eq 6.14 and multiplied by 0.75: These G_r' and G_r" are shown in Fig. 6-4 with the unfilled circles and filled circles, the latter almost indistinguishable from the filled squares.

Fig. 6-4 demonstrates the following features of the I-I 49-0 chain in the three environments. In the B9 matrix, $G_{r,incoh}$' is in excellent agreement with the G_r' data. The agreement of $G_{r,incoh}$" and the G_r" data is also satisfactory if the small error ($\cong$ 20%) in the calculated $G_{r,incoh}$" is considered. In contrast, significant differences are found between $G_{r,coh}^*$ and the G_r^* data. Thus, the incoherence of the short-time motion of the submolecules is concluded for the dilute I-I 49-0 chains entangled with highly mobile, low-M B9 matrix.

For the monodisperse bulk I-I 49-0 system, some degree of coherence of the submolecule motion is noted from the deviation of $G_{r,incoh}^*$ from the G_r^* data. However, $G_{r,coh}^*$ is also different from the G_r^* data, indicating that the coherence is not perfect in this system.

For the I-I 49-0 chain in the B263 matrix, the G_r^* data may include the small uncertainty explained earlier (less than 25%). The calculated $G_{r,coh}^*$ agrees with the G_r^* data within this uncertainty, while $G_{r,incoh}^*$ exhibits significant deviation. Thus, the submolecule motion is highly coherent for the I-I 49-0 chain in the B263 matrix.

Fig. 6-5 compares the G_I" and ε" data of the I-I 49-0 chain. According to eq 6.11, G_I" is reduced by the plateau modulus, $G_N = 4.8 \times 10^5$ Pa for bulk I-I 49-0 and $G_{N,I} = 7.0 \times 10^4$ Pa (eq 6.15) for the I-I 49-0 chains in the B263 and B9 matrices ($\phi_{PI} = 0.05$), while ε" is reduced by the dielectric intensity $\Delta\varepsilon$ in respective environments. Since $G_{N,I}$ was evaluated from the G_I" data, the small uncertainty (< 25 %) of G_I" in the B263 matrix is canceled in the comparison of the normalized losses, $G_I''/G_{N,I}$ and $\varepsilon''/\Delta\varepsilon$. Thus, Fig. 6-5 clearly tests whether the submolecule motion is perfectly coherent or not by comparing these losses over a wide range of ω.

For the I-I 49-0 chain in the B263 matrix, the $G_I''/G_{N,I}$ and $\varepsilon''/\Delta\varepsilon$ data agree with each other within experimental scatter and eq 6.11 is valid. This result confirms that the submolecule motion is highly coherent for the dilute I-I 49-0 chains in the B263 matrix. The coherence is incomplete in the bulk I-I 49-0 system and in the B9 matrix, as noted from the differences between the $G_I''/G_{N,I}$ and $\varepsilon''/\Delta\varepsilon$ data. In fact, Fig. 6-4 demonstrates that the submolecular motion is perfectly incoherent in the B9 matrix. (Note that the comparison in Fig. 6-5 specifies whether the coherence is complete or not. In contrast, the comparison of $G_{r,incoh}^*$ and $G_{r,coh}^*$ with the G_r^* data (Fig. 6-4) specifies whether the submolecule motion is perfectly coherent or perfectly inco-

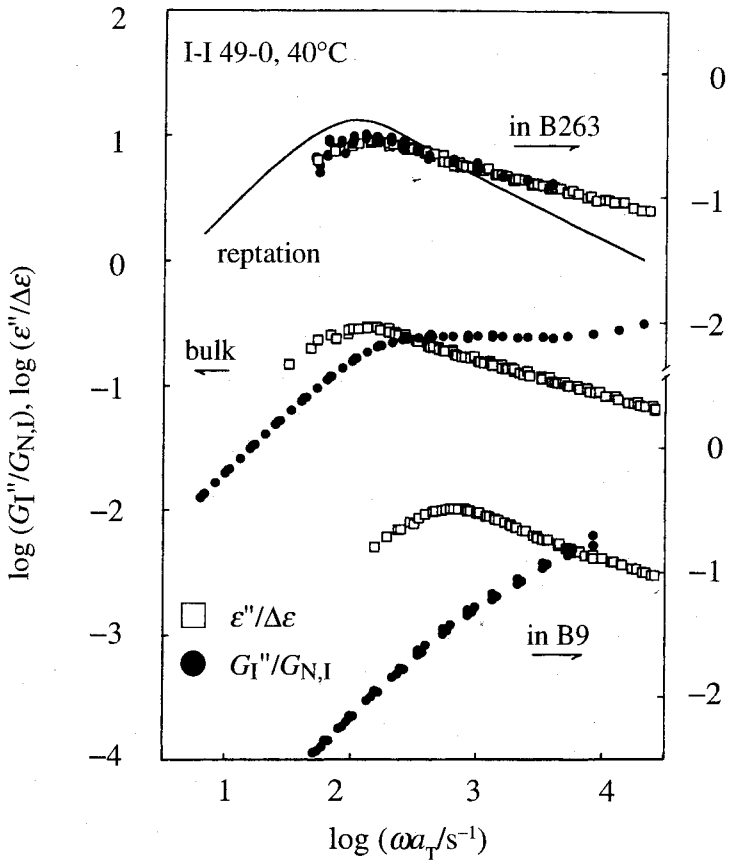

Fig.6-5 Comparison of the $G_I''/G_{N,I}$ and $\varepsilon''/\Delta\varepsilon$ data at 40°C for the I-I 49-0 chain in the three environments as indicated. The solid curve shown for the I-I 49-0 chain in the B263 matrix indicates $G_I''/G_{N,I}$ and $\varepsilon''/\Delta\varepsilon$ calculated from the pure reptation model. (The frequency scale of this curve is adjusted so that the curve has the maximum at the same frequency as the $G_I''/G_{N,I}$ and $\varepsilon''/\Delta\varepsilon$ data.)

herent.)

The constraint release (CR) contribution to the PI dynamics, measured by the ratio of the CR relaxation time $\tau_{CR,\varepsilon}$ to the observed longest relaxation time $\tau_{\varepsilon,1}$, is quite different in the three environments: As explained in Chapter 5, the CR mechanism dominates the PI dynamics in the B9 matrix ($\tau_{CR,\varepsilon}/\tau_{\varepsilon,1}$ = 1.1) while it has negligible effects in the B263 matrix ($\tau_{CR,\varepsilon}/\tau_{\varepsilon,1}$ = 5600) and modest effects in the monodisperse bulk I-I 49-0 system ($\tau_{CR,\varepsilon}/\tau_{\varepsilon,1} \cong 3.5$); see Table 5.1. From this result and those found in Figs. 6-4 and 6-5, the CR contribution to the probe chain dynamics is concluded to be the dominant factor that determines the short-time coherence of the submolecule motion in the probe: The larger this contribution, the smaller the degree of coherence.

Here, it should be emphasized that the magnitude of entanglements measured by the M_I/M_e ratio is not a factor determining the degree of the coherence: This ratio is ≅ 29 for the dilute I-I 49-0 chains in both B263 and B9 matrices ($M_{e,I} \cong 1.7 \times 10^3$ for ϕ_{PI} = 0.05; eq 6.16) and ≅ 10 in the bulk I-I 49-0 system ($M_{e,I}^\circ \cong 5 \times 10^3$ for bulk PI[16,17]). Despite the coincidence of the $M_I/M_{e,I}$ ratio in the B263 and B9 matrices, the submolecular motion is much more coherent in the former.

6-5-4. Comparison with tube model

Here, the reptation model is examined for the I-I 49-0 probe in the high-M B 263 matrix (Fig. 6-5). The solid curve shown there is the normalized losses, $G_I''/G_{N,I}$ and $\varepsilon''/\Delta\varepsilon$, for a chain relaxing by the perfectly coherent, pure reptation mechanism; cf. section 4-3. (The frequency scale for this curve is adjusted so that the curve has the maximum at the same frequency as the $G_I''/G_{N,I}$ and $\varepsilon''/\Delta\varepsilon$ data.) Despite the high coherence of the submolecular motion experimentally found in the B263 matrix, the $G_I''/G_{N,I}$ and $\varepsilon''/\Delta\varepsilon$ data are significantly different from the pure reptation curve. This difference, found for the *normalized* losses, indicates that the highly coherent motion of the I-I 49-0 chains in the B263 matrix results from a mechanism other than pure reptation. This conclusion is in harmony with that of Chapter 5.

One may argue that the $M/M_{e,I}$ ratio ($\cong 29$) of the I-I 49-0 chain in the B263 matrix is not large enough to allow the purely reptative motion of this chain and that the contour length fluctuation mechanism[3,21,22] has a significant contribution to the dynamics of the chain. In fact, a power-law exponent for the data of the I-I 49-0 chain in the B263 matrix at high ω, $G_I''/G_{N,I} = \varepsilon''/\Delta\varepsilon \propto \omega^{-\alpha}$ with $\alpha \cong 1/4$ (see Fig. 6-5), is in close agreement with the exponent theoretically deduced for the combined mechanism of reptation plus contour length fluctuation.[21] In addition, the M_I dependence of $\tau_{\varepsilon,I}$ for the PI chains in matrices of much longer chains (eq 5.5) is not far from the dependence deduced for this combined mechanism.[21,22]

However, the eigenfunctions $f_p(n)$ for the local correlation function (eq 5.3) have not been calculated for the combined mechanism of reptation plus contour length fluctuation. Thus, it is still uncertain whether the experimentally obtained non-sinusoidal $f_p(n)$ can be explained by this mechanism. Further theoretical studies are desirable to clarify this problem.

6-6. Concluding Remarks

The short-time coherence of the submolecule motion in individual chains was examined by comparing viscoelastic and dielectric data of dilute PI chains in various environments. The comparison unequivocally indicated that the constraint release (CR) mechanism determines this coherence: The larger the CR contribution to the PI dynamics, the smaller the degree of the coherence. None of available molecular models seems to explain these experimental findings. Specifically, it is still unclear whether the results can be explained within the framework of the generalized tube model considering the CR, contour length fluctuation, and reptation mechanisms. Further tests for the dynamics in monodisperse systems and blends are conducted in Chapter 7.

References and Notes

1. Watanabe, H.; Urakawa, O.; Kotaka, T. *Macromolecules* **27**, 3525 (1994).
2. Klein, J. Macromolecules **11**, *852* (1978).
3. Graessley, W. W. *Adv. Polym. Sci.* **47**, 67 (1982).
4. Watanabe, H.; Tirrell, M. *Macromolecules* **22**, 927 (1989).
5. Watanabe, H.; Yao, M.-L.; Osaki, K. *Macromolecules* **29**, 97 (1996).

6. Watanabe, H. *Prog. Polym. Sci., 24, 1253 (1999).*
7. Watanabe, H.; Sakamoto, T.; Kotaka, T. *Macromolecules* **18**, 1436 (1985).
8. Watanabe, H.; Yoshida, H.; Kotaka, T. *Macromolecules* **21**, 2175 (1988); *ibid.* **25**, 2442 (1992).
9. Watanabe, H.; Urakawa, O.; Kotaka, T. *Macromolecules* **26**, 5073 (1993).
10. Matsumiya, Y.; Watanabe, H.; Sato, T.; Osaki, K.; Yao, M.-L. *Macromolecules*, **31**, 7528 (1998).
11. Watanabe, H.; Yamada, H.; Urakawa, O. *Macromolecules* **28**, 6443 (1995).
12. a) Watanabe, H.; Yamazaki, M.; Yoshida, H.; Adachi, K.; Kotaka, T. *Macromolecules* **24**, 5365 (1991). b) Watanabe, H.; Yamazaki, M.; Yoshida, H.; Kotaka, T. *ibid.* **24**, 5372(1991).
13. Watanabe, H.; Kotaka, T. *Macromolecules* **17**, 2316 (1984).
14. Watanabe, H.; Kotaka, T. *Macromolecules* **19**, 2520 (1986).
15. Watanabe, H.; Yamazaki, M.; Yoshida, H.; Kotaka, T. *Macromolecules* **24**, 5573 (1991).
16. Ferry, J. D. *Viscoelastic Properties of Polymers,* 3rd Ed.,Wiley: New York, (1980).
17. Graessley, W. W. *Adv. Polym. Sci.* **16**, 55 (1974).
18. Watanabe, H.; Urakawa, O.; Yamada, H.; Yao, M.-L. *Macromolecules* **29**, 755 (1996).
19. The estimate of the difference between $G_{r,incoh}$* calculated for p = 1-3 and p = 1-N was obtained for the Rouse-type CR model.[5] Although this model does not accurately describe the detailed feature (non-sinusoidal f_p[1,10]) of actual CR relaxation, G_r* of the model is close to the G_r* data in the CR regime.[1] Thus, the above estimate can be applied to $G_{r,incoh}$* of the PI chains.
20. The difference between $G_{r,coh}$* calculated for p = 1-3 and p = 1-N was estimated for the reptation model. For any type of coherent submolecule motion, the viscoelastic intensity factor ($\propto [(1/N)\int_0^N f_p(n)\,dn]^2$; eq 6.10) rapidly decays with increasing p because $f_p(n)$ oscillates with n more frequently for larger p, meaning that the $G_{r,coh}$* at low ω is dominated by a few slow eigenmodes. Thus the estimate obtained for the reptation model may be applied to $G_{r,coh}$* of the PI chains exhibiting the coherent submolecule motion.
21. Doi, M. J. Polym. Sci. Polym. Lett. E*d.* **19**, 265 (1981).
22. Doi, M. *J. Polym. Sci. Polym. Phys. Ed.* **21**, 667 (1983).

CHAPTER 7
Test of Tube Dilation Molecular Picture for Linear Chains

7-1. Introduction

This chapter focuses on the dynamic tube dilation (DTD) mechanism for entangled linear chains at equilibrium (in the linear response regime): cf. section 4-5. The stress partially relaxes when the chain explores all local configurations in the dilated tube, and the terminal relaxation is accelerated if the chain reptates along the dilated and shortened tube with its intrinsic curvilinear diffusion coefficient.

The validity of DTD for linear chains combined with reptation is sometimes questioned.[1,2] However, the tube dilation process itself has been neither verified nor disproved from experiments for systems in which the tube can, in principle, dilate in time scales of the chain relaxation.

For this problem, an interesting possibility of testing the DTD molecular picture is noted through comparison of the viscoelastic and dielectric properties. For a chain having the type-A dipoles[3] that are parallel along its backbone, the global motion is differently reflected in these properties and the comparison provides some detailed information for this motion,[4] see Chapter 3. In fact, the comparison on the basis of the eigenmode analysis (Chapter 6) revealed that the entanglement in monodisperse systems provides the chain with some degree of coherence in its submolecule motion and that the CR mechanism tends to decrease this coherence.

For the experimental examination of the DTD picture, a specific relationship was derived between the viscoelastic and dielectric properties that should hold if the tube dilates in time scales of the chain relaxation; see section 4-5. Furthermore, this relationship was tested for linear *cis*-polyisoprene (PI) chains having the non-inverted type-A dipoles and the tube was found to actually dilate in monodisperse systems. The results are summarized in this chapter.

7-2. Theoretical Background

7-2-1. Monodisperse systems

For the viscoelastic and dielectric relaxation functions $\mu(t)$ and $\Phi(t)$ of a monodisperse system of linear, Gaussian type-A chains, the DTD relationship, $\mu(t) = [\Phi(t)]^{1+\alpha} \cong [\Phi(t)]^2$ (eq 4.36), was derived in section 4-5.

In presence of the viscoelastic and dielectric mode distributions of the chain, eq 4.36 can be further rewritten for the dielectric loss $\varepsilon''(\omega)$ and complex modulus $G^*(\omega) = G'(\omega) + iG''(\omega)$ ($i = \sqrt{-1}$) at the angular frequency ω. (ε'' and G^* are given as the Fourier transformation of Φ and μ.) For the case of $\alpha = 1$, the result is simply written as

$$\frac{\varepsilon''(\omega)}{\Delta\varepsilon} = \sum_{p} g_p \frac{\omega\tau_{\varepsilon,p}}{1 + \omega^2\tau_{\varepsilon,p}^2} \tag{7.1}$$

and

$$\frac{G'(\omega) + iG''(\omega)}{G_N} = \sum_{p,p'} h_{pp'} \frac{\omega^2\tau_{pp'}^2 + i\omega\tau_{pp'}}{1 + \omega^2\tau_{pp'}^2} \tag{7.2}$$

with

$$h_{pp'} = g_p g_{p'} \text{ and } \tau_{pp'} = \left[\tau_{\varepsilon,p}^{-1} + \tau_{\varepsilon,p'}^{-1}\right]^{-1} \tag{7.3}$$

Here, $\{g_p, \tau_p\}$ is the dielectric spectrum, $\Delta\varepsilon$ is the dielectric relaxation intensity due to the global motion of the chain, and G_N is the entanglement plateau modulus. The $\varepsilon''(\omega)$ and $G^*(\omega)$ should satisfy the relationship specified by eqs 7.1-7.3 when the tube actually dilates in the time scale of the chain relaxation.

7-2-2. Blends

For binary blends, the DTD relationship between $\mu(t)$ and $\Phi(t)$ was also derived in section 4-5. For the blend composed of monodisperse, dilute probe chains having non-inverted type-A dipoles (hereafter referred to as component 2) and dielectrically ineat matrix chains (component 1), the DTD relationship is given by $\mu_2(t) \cong [\mu_{1,m}(t)]^{1/2}\Phi_2(t)$ (eq 4.39). Here, $\mu_2(t)$ and $\Phi_2(t)$ are the dielectric and viscoelastic relaxation functions of the probe, respectively, and $\mu_{1,m}(t)$ is the viscoelastic relaxation function of the matrix chains in their monodisperse bulk state.

This result can be rewritten for ε_2'' and G_2^* of the probe: If the dielectric modes of the probe have the relaxation times and intensities $\tau_{\varepsilon,p}$ and g_p (cf. eq 7.1), the modulus G_2^* of the probe in the dilated tube should be written as

$$\frac{G_2'(\omega) + iG_2''(\omega)}{G_{N2}} = \sum_{p,p'} \tilde{h}_{pp'} \frac{\omega^2\tilde{\tau}_{pp'}^2 + i\omega\tilde{\tau}_{pp'}}{1 + \omega^2\tilde{\tau}_{pp'}^2} \tag{7.4}$$

with

$$\tilde{h}_{pp'} = g_p r_{p'} \text{ and } \tilde{\tau}_{pp'} = \left[\tau_{\varepsilon,p}^{-1} + \tau_{r,p'}^{-1}\right]^{-1} \tag{7.5}$$

Here, G_{N2} (= $\upsilon_2 G_N$ with υ_2 being the probe volume fraction) is the probe contribution to the plateau modulus, and $\tau_{r,p'}$ and $r_{p'}$ are the characteristic times and intensities for the relaxation modes of $[\mu_{1,m}(t)]^{1/2}$.

7-3. Experimental

A linear *cis*-polyisoprene (PI) was synthesized/characterized *via* anionic polymerization, as

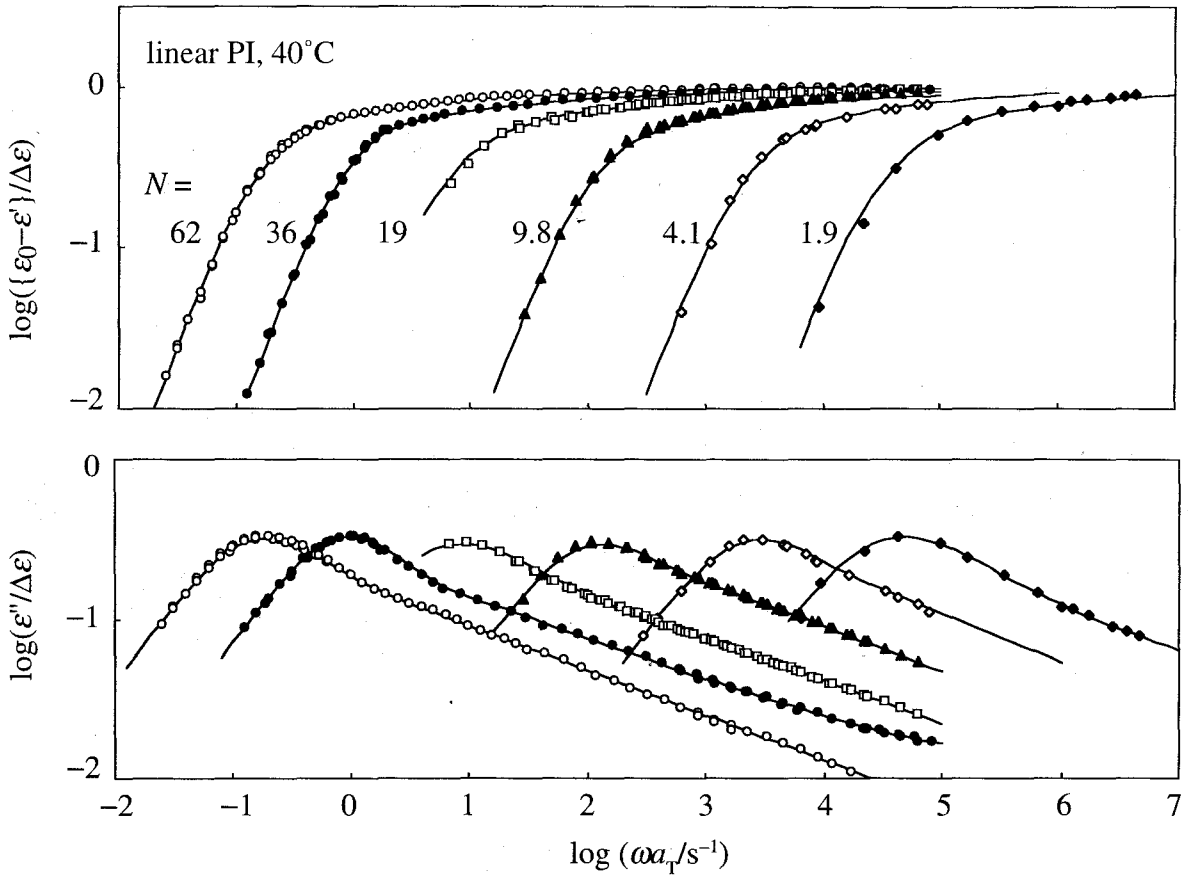

Fig. 7-1 Normalized dielectric constant $\{\varepsilon_0-\varepsilon'\}/\Delta\varepsilon$ and dielectric loss $\varepsilon''/\Delta\varepsilon$ at 40°C measured for entangled linear PI chains with N ($=M/M_e$) ≥ 1.9. These linear PI chains have the non-inverted type-A dipoles.

explained in section 2-2. Characteristics of all PI samples examined in this chapter are summeized in Table 2.2. For these samples, linear viscoelastic and dielectric measurements were conducted with the methods explained in sections 2-3 and 2-4. The time-temperature superposition[5] worked very well for the dielectric and viscoelastic data (with the same shift factor a_T). These data are reduced and compared at 40°C.

7-4. Results and Discussion

As explained in section 4-3-1, the numerical prefactor in the expression of G_N in terms of M_e changes a little according to the choice of the initial condition for the orientation function $S(n,t)$, $G_N = [4/5]cRT/M_e$ for the Doi-Edwards condition and $G_N = cRT/M_e$ for the affine-deformation condition. However, this change does not affect eqs 7.1-7.5 deduced for the *normalized* viscoelastic and dielectric quantities of the chains in the dilated tube. Hereafter, the affine deformation is adopted to specify the entanglement density in the system as $N = M/M_e = G_N/\nu k_B T$ (ν = chain number density).

7-4-1. Monodisperse systems

Fig. 7-1 shows the normalized dielectric constant $\{\varepsilon_0-\varepsilon'\}/\Delta\varepsilon$ and dielectric loss $\varepsilon''/\Delta\varepsilon$ of monodisperse PI chains with the entanglement densities N as indicated. The dielectric test

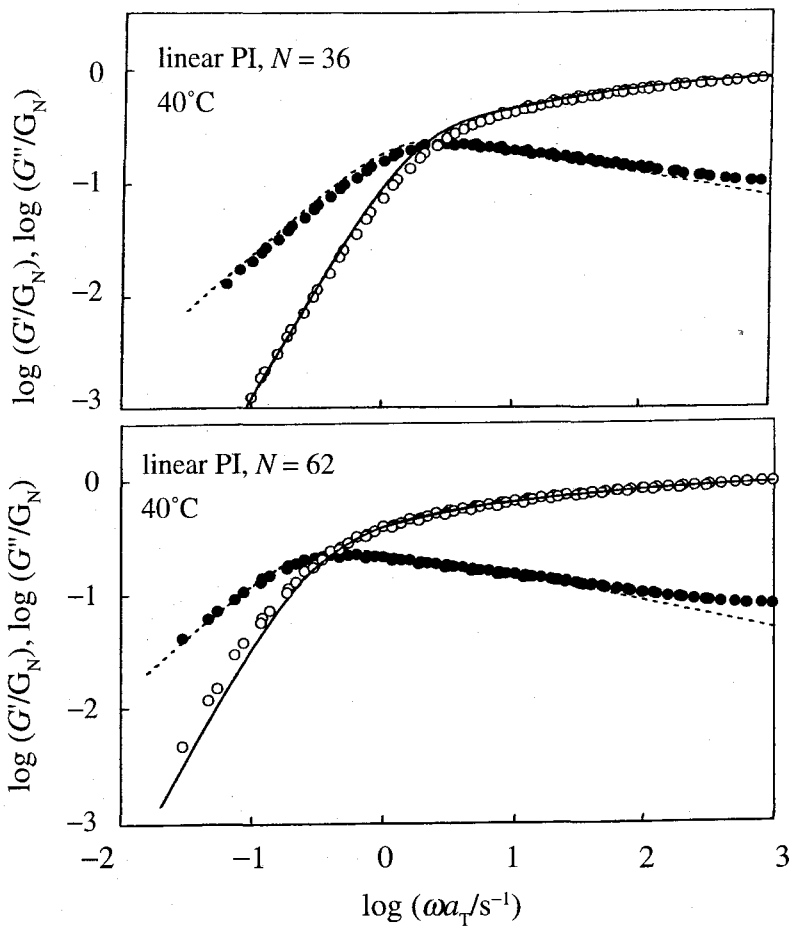

Fig. 7-2 Test of the DTD relationship (eq 4.36) for highly entangled linear PI chains ($N = 36$ and 62) at 40°C. Normalized moduli data, G'/G_N (unfilled circles) and G''/G_N (filled circles), are compared with the moduli calculated from dielectric data through this relationship (curves).

covers a low-ω range comparable to that examined in typical viscoelastic tests. The adsorption current method (section 2-4-3) was very helpful to cover such low ω where the highly entangled PI chains exhibited the terminal dielectric relaxation.

At the reference tempareture, $T_r = 40°C$, the local (or segmental) relaxation of PI emerges at $\omega > 10^7$ s^{-1}.[6] Thus, the dielectric relaxation observed in Fig. 7-1 is exclusively attributed to the global motion of the PI chain.

The mode distribution of this global dielectric relaxation is insensitive to N, as noted from the N-insensitive shape of the $\{\varepsilon_0-\varepsilon'\}/\Delta\varepsilon$ and $\varepsilon''/\Delta\varepsilon$ curves (Fig. 7-1). This N-insensitivity is similar to that known for the viscoelastic distribution in the well entangled regime.[5,7]

These dielectric data were utilized to evaluate the dielectric spectrum of each linear PI chain with an iteration method explained in Appendix 7A. The G'/G_N and G''/G_N for the DTD process were calculated from these dielectric spectrum (through eqs 7.2 and 7.3), and compared with the G'/G_N and G''/G_N data. Fig. 7-2 shows typical results (obtained for linear PI with $N =$ 36 and 62). The DTD predictions (curves) are close to the measured moduli (circles), meaning that the DTD picture holds (as a very good approximation) for the highly entangled linear PI chain. This success of the DTD picture was found also for less entangled linear PI chains shown

in Fig. 7-1. (The validity of the DTD picture seen for the linear PI chains is further discussed later in section 8-4-5 in relation to the behavior of the star chains.)

It should be emphasized that the above validity of eqs 7.1-7.3 just suggests that the tube dilates in the time scale of the chain relaxation. In other words, this validity does not necessarily mean that the chain reptates along the dilated tube with its intrinsic curvi-linear diffusion coefficient, D_c (= $N\zeta/k_BT$). The non-reptative motion in the dilated tube (that satisfies eqs 7.1-7.3) is found, for example, in the model by Viovy et al:[2] In the chain reptation regime in their model, the chain reptates with D_c along the thin (non-diluted) tube of diameter a and this thin tube fluctuate in the dilated tube (supertube in their terminology). Viscoelastic relaxation attributable to this type of chain motion was observed by Struglinski and Graessley for polybutadiene (PB) blends.[8]

For examination of the chain motion in the dilated tube, useful information can be found in the ratio of the global constraint release (CR) relaxation time τ_{CR} ($\propto N^5$ in the monodisperse systems)[9,10] to the observed terminal relaxation time τ_1 ($\propto N^{3.5}$). For the PI chain with M = 48.8×10^3, the ratio was estimated (from PI/PI blends data[11]) to be $\tau_{CR,\varepsilon}/\tau_{\varepsilon,1} \cong 3.5$. (Table 5.1 in Chapter 5) From this $\tau_{CR,\varepsilon}/\tau_{\varepsilon,1}$ value, the $\tau_{CR,\varepsilon}/\tau_{\varepsilon,1}$ ratio for the other linear PI samples examined in this study were evaluated. For example, $\tau_{CR,\varepsilon}/\tau_{\varepsilon,1} \cong 55$ for PI with the highest M (= 308 $\times 10^3$). These results suggest that the terminal relaxation of the well-entangled linear PI chains is faster than the global CR relaxation. The reptation in the dilated tube would occur only after the chain contour length measured along this tube is equilibrated *via* the global CR mode, i.e., at $t > \tau_{CR}$, as suggested from the viscoelastic data of blends.[12] Thus the motion of the PI chains examined in Fig. 7-2 may be more or less similar to that considered in the model by Viovy et al[2] (although their model does not incorporate the contour length fluctuation (CLF) mechanism and its prediction for $\tau_{\varepsilon,1}$ is quantitatively different from experiments.[12])

Since the tube dilates as a result of mutual equilibration of successive entanglement segments through their CR motion,[7,13,14] the DTD picture is valid only at times longer than the CR-equilibration time τ^{**}. A test of this DTD criterion ($t > \tau^{**}$) is postponed to Chapter 8 where the behavior of linear and star PI chains is compared.

7-4-2. Dilute PI probe in blends

In Chapters 5 and 6, the ε_2" and G_2* data were obtained for the dilute PI probe (M_2 = 48.8 $\times 10^3$, $\upsilon_2 = 0.05$) in high-M and low-M linear polybutadiene (PB) matrices with $10^{-3}M_1$ = 9.24 and 263 (M/M_e = 5.0 and 142; $M_e = 1.85 \times 10^3$ for bulk PB[8]). The matrix PB chains have no type-A dipoles. Thus the G_2* data are expected to be described by eqs 7.4 and 7.5 *if* the tube dilates in the time scale of the probe relaxation. This expectation is examined below.

As done for the monodisperse PI systems, the ε_2" data[7,15] were utilized to determine the dielectric spectrum $\{g_p, \tau_{\varepsilon,p}\}$ of the PI probe; see Appendix 7A. For evaluation of the relaxation times and intensities $\tau_{r,p}$ and r_p for $[\mu_{1,m}(t)]^{1/2}$ of the pure PB matrices, the G* data (Chapter 6) of these matrices were converted into $G(t)$ with the method of Ninomiya and Ferry,[5]

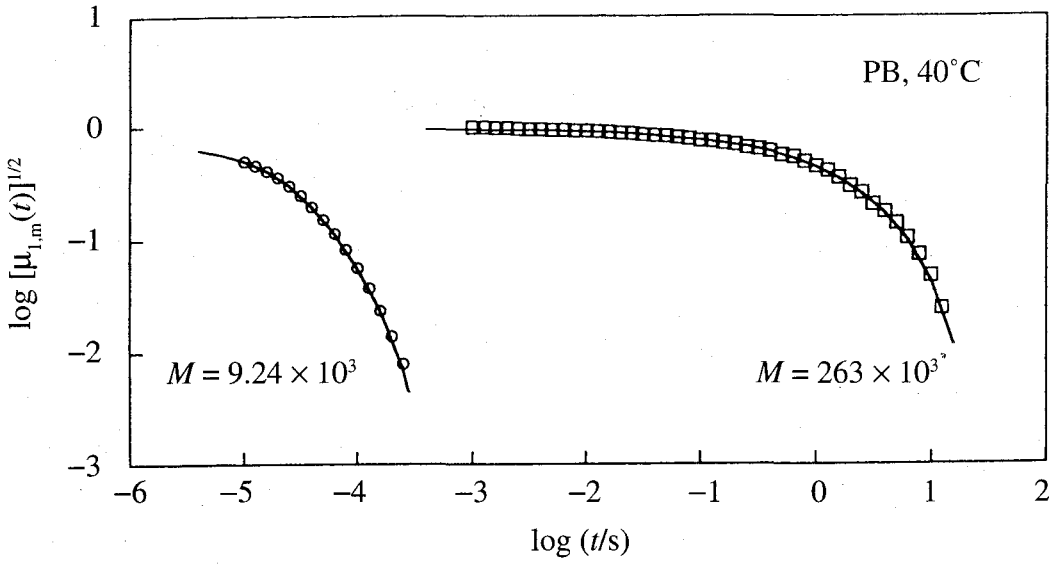

Fig. 7-3 Square-root of the normalized relaxation moduli, $[\mu_{1,m}(t)]^{1/2} = [G(t)/G_N]^{1/2}$, of two monodisperse polybutadienes (PB) at 40°C. These PB were utilized as the matrices of the blends examined in Fig. 7-4.

$$G(t) \cong [\, G'(\omega) - 0.40G''(0.40\omega) + 0.014G''(10\omega)\,]_{\omega = 1/t} \qquad (7.6)$$

Fig. 7-3 shows the $[\mu_{1,m}(t)]^{1/2} = [G(t)/G_N]^{1/2}$ thus obtained (symbols). From fit of these $[\mu_{1,m}(t)]^{1/2}$ data with a sum of exponentially decaying terms, $\tau_{r,p'}$ and $r_{p'}$ were determined. The solid curves, indicating the $[\mu_{1,m}(t)]^{1/2}$ re-calculated from these $\tau_{r,p'}$ and $r_{p'}$, demonstrate that $\tau_{r,p'}$ and $r_{p'}$ were evaluated accurately.

In Fig. 7-4, the G_2^*/G_{N2} data (Chapers 5 and 6) for the dilute PI probe are compared with the G_2^*/G_{N2} calculated from the g_p, $\tau_{\varepsilon,p}$, $r_{p'}$, and $\tau_{r,p'}$ determined above. The data (symbols), obtained by subtracting the matrix PB contribution from G^* of the PI/PB blends, are shown only at low ω where the uncertainties due to the subtraction is acceptably small (cf. Chapter 6). At such low ω, the glass-to-rubber transition modes have negligible contributions to the G_2^*/G_{N2} data. Thus, the data exclusively reflect the global motion of the dilute PI probe in the PB matrices.

In the PB matrices, the entanglement spacing for the dilute PI probe was found to be $M_{e,2} \cong 1.7 \times 10^3$ (Chapter 6). Thus, the PI probe examined in Fig. 7-3 has $N_2 = M_2/M_{e,2} \cong 28.7$ and is in a well entangled state. Nevertheless, the G_2^*/G_{N2} data are quite different in the two matrices. This difference reflects a different contribution of the constraint release (CR) mechanism in these matrices: ratio of the CR relaxation time τ_{CR} and the observed terminal relaxation time τ_1, τ_{CR}/τ_1, is a good measure of this CR contribution. The $\tau_{CR,\varepsilon}/\tau_{\varepsilon,1}$ value is 5600 for the PI probe in the high-M PB matrix (Table 5.1) and thus the probe relaxation is much faster than the CR relaxation; namely, the CR mechanism has a negligible contribution to the probe relaxation in this matrix (cf. Chapter 6). In contrast, the PI probe in the low-M matrix has $\tau_{CR\varepsilon}/\tau_{\varepsilon,1} = 1.1$ (Table 5.1) and its relaxation is dominated by the CR mechanism.

As noted in Fig. 7-4a, the G_2^*/G_{N2} data (symbols) in the high-M matrix coincide with the G_2^*/G_{N2} calculated from eqs 7.4 and 7.5 (curves). In this matrix, $[\mu_{1,m}(t)]^{1/2}$ hardly decays and

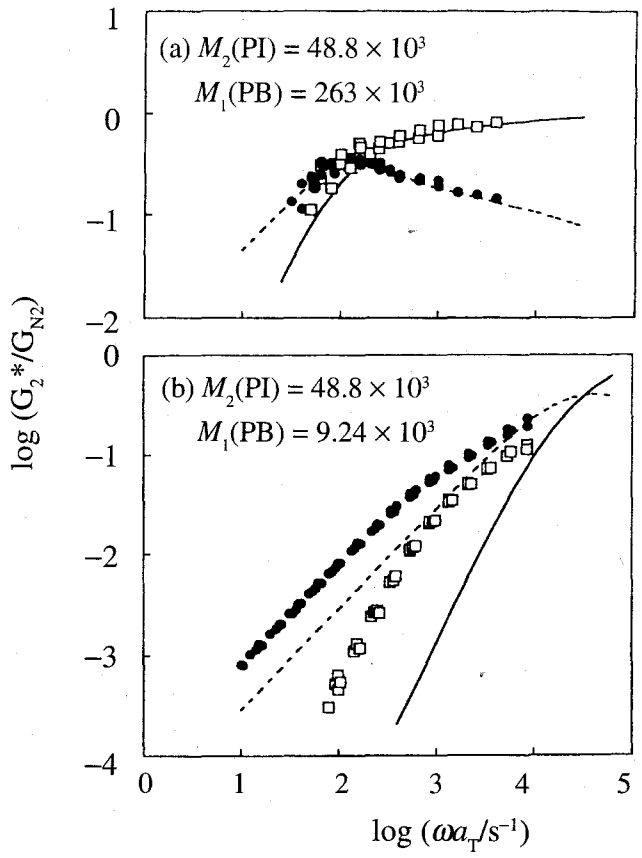

Fig. 7-4 Comparison of normalized viscoelastic moduli G_2^*/G_{N2} of dilute PI probe ($M_2 = 48.8 \times 10^3$, volume fraction $\upsilon_2 = 0.05$) in entangling matrices of high-M and low-M linear PB chains ($10^{-3}M_1 = 9.24$ and 263) at 40°C with the moduli calculated from the dielectric spectra for the case of tube dilation (eqs 7.2 and 7.4). The G_2'/G_{N2} and G_2''/G_{N2} data are shown with the unfilled squares and filled circles, respectively, and the calculated G_2'/G_{N2} and G_2''/G_{N2} are denoted with the solid and dotted curves. (The normalized relaxation moduli of the matrices, utilized in the calculation, are shown in Fig. 7-3.)

the tube diameter (determined by this $\mu_{1,m}$) does not increase in the time scale of the probe relaxation ($t \leq 10^{-2}$ s, or, $\omega \geq 10^2$ s^{-1}); see Fig. 7-3. The above coincidence of the observed and calculated G_2^*/G_{N2} reflects this lack of tube dilation. In fact, the relationship $G_2''/G_{N2} = \varepsilon_2''/\Delta\varepsilon$ (eq 6.11) derived from eq 4.39 with $[\mu_{1,m}(t)]^{1/2} = 1$ (no dilation) was confirmed to be valid for the viscoelastic and dielectric data of the probe in the high-M matrix; see Fig. 6-5. All these results are consistent with the CR-free nature of the probe relaxation in this matrix ($\tau_{CR,\varepsilon}/\tau_{\varepsilon,1} = 5600 >> 1$): Since the tube dilates as a result of the CR motion of the probe, no dilation occurs in the CR-free environment.

In the low-M matrix (Fig. 7-4b), the CR mechanism dominates the probe relaxation (Chapters 5 and 6) and the tube can dilate *in principle*. Nevertheless, the G_2^*/G_{N2} calculated for the tube dilation process (eqs 7.4 and 7.5) is significantly different from the data. Specifically, the calculated probe relaxation is considerably faster than the data: The terminal relaxation time $<\tau_2>_w = [G_2'/\omega G_2'']_{\omega\to 0}$ is 5×10^{-5} s for the calculation and 7×10^{-4} s for the data . These results demonstrate the importance of the mutual equilibration of the entanglement segments of the probe,[15] as explained below.

The tube dilation process includes two steps, the removal of the constraints due to diffusion of the matrix chains and the CR motion of the probe chain activated by this removal. This CR motion results in the above equilibration of the probe segments and allows the tube to dilate. The DTD relationship (eq 4.39) assumes that the CR equilibration completes immediately on the removal of the constraints to allow the tube to dilate instantaneously. (The factor $[\mu_{1,m}(t)]^{1/2}$ in eq 4.39 reflects this assumption.) However, the actual CR motion requires a characteristic time $\tau^{**} \sim \beta^2 t_w$, where t_w is the entanglement lifetime determined by the matrix diffusion and β is the number of the probe entanglement segments involved in this motion.[12] Thus the tube diameter increases to $a' = \beta^{1/2}a$ only at $t \geq \beta^2 t_w$. This difference between the model assumption and the behavior of the actual probe leads to the difference between the observed and calculated G_2^* (Fig. 7-4b). In fact, Chapters 5 and 6 demonstrated that the dilute probe in the low-M matrix relaxes completely *via* the CR mechanism during the equilibration process, i.e., before the expected tube dilation is completed.

7-5. Concluding Remarks

For entangled monodisperse linear PI chains (N = 1.9 - 62) having non-inverted type-A dipoles, the DTD relationship between viscoelastic and dielectric properties was found to hold as a good approximation. This result suggests the importance of tube dilation for the terminal relaxation of these PI chains, although the chains do not necessarily reptate along the dilated tube with their intrinsic curvi-linear diffusion coefficient.

In contrast, for dilute probe PI chain in the low-M entangling PB matrix, the relationship completely failed at long t. This result indicates that the probe fully relaxes *via* the CR mechanism during the mutual equilibration of its entanglement segments, demonstrating the importance of the CR motion of the probe in the tube dilation process. The lack of the tube dilation was also confirmed for the probe in the high-M PB matrix where the CR mechanism negligibly contributed to the probe relaxation.

Appendix 7A. Iteration Method for Evaluation of Dielectric Spectrum

7A-1. Iteration Method

In calculation of the dielectric spectrum with the iteration method,[16] a constant logarithmic interval of the dielectric relaxation times, $\log [\tau_{\varepsilon,p}/\tau_{\varepsilon,p+1}] = \Delta$ (p = 1, 2, ...), was assumed and a corresponding set of the dielectric intensities g_p that reproduced the normalized $\varepsilon''/\Delta\varepsilon$ data (written in terms of $\tau_{\varepsilon,p}$ and g_p; cf. eq 2.17) was determined. The Δ value was chosen to be sufficiently small ($\Delta \leq 0.2$), meaning that the spectrum was determined in a semi-continuous sense.

As a first estimate of g_p, $g_p^{(1)} = 0.5\pi\{\varepsilon''(\omega=1/\tau_p)/\Delta\varepsilon\}_{obs}$ being suggested from the crudest approximation for the spectrum[7] was chosen. (Hereafter, the superscript enclosed in parenthesis

denotes the number of iterated calculation cycles.) The $\{\varepsilon''/\Delta\varepsilon\}_{\rm calc}^{(1)}$ calculated from the first set of $g_p^{(1)}$ and $\tau_{\varepsilon,p}$ were obviously different from the $\varepsilon''/\Delta\varepsilon$ data. Thus, the convergence factor for $C_p^{(1)}$ was introduced:

$$C_p^{(1)} = \left(\frac{\{\varepsilon''(\omega=1/\tau_p)/\Delta\varepsilon\}_{\rm obs}}{\{\varepsilon''(\omega=1/\tau_p)/\Delta\varepsilon\}_{\rm calc}^{(1)}} \right)^{\delta} \qquad (7A.1)$$

Here, the exponent δ adjusts the rate of convergence and magnitude of oscillation in the calculation. The δ value was chosen to be 0.4-0.7. Utilizing this $C_p^{(1)}$ factor, the intensity in the second cycle of iteration was evaluated as $g_p^{(2)} = C_p^{(1)} g_p^{(1)}$.

The calculation cycles were iterated in this way, with the convergence factor $C_p^{(n)}$ being re-evaluated at the end of each cycle. After the iteration over 30 cycles, the difference between the calculated and measured $\varepsilon''/\Delta\varepsilon$ became less than 0.01 %, which was much smaller than the experimental uncertainties in the $\varepsilon''/\Delta\varepsilon$ data. Thus, the $g_p^{(30)}$ values were utilized as the dielectric intensities to calculate G^*/G_N for the DTD process (cf. eqs 7.1-7.5).

For different Δ values (≤ 0.2), different dielectric spectra $\{g_p^{(30)}, \tau_{\varepsilon,p}\}$ that equally reproduced the $\varepsilon''/\Delta\varepsilon$ and $\{\varepsilon_0-\varepsilon'\}/\Delta\varepsilon$ data were obtained. This non-uniqueness is a well known problem in empirical determination of semi-continuous spectra. However, the non-uniqueness did not disturb the test of the DTD relationship because the dielectric spectra for different Δ values (≤ 0.2) gave indistinguishable G^*/G_N. Thus, the G^*/G_N calculated $\Delta = 0.1$ was utilized in Figs. 7-2 and 7-4 (as well as in Figs. 8-3 and 8-6).

7A-2. meaning of the use of dielectric spectrum in the test of DTD picture

In principle, the test of the DTD relationship (eqs 4.36 and/or 4.39) does not require the explicit evaluation of the dielectric spectrum: The $\Phi(t)$ and/or $\Phi_2(t)$ values can be directly obtained as a function of t *via* the numerical, inverse Fourier transformation of the $\varepsilon''/\Delta\varepsilon$ data (cf. 2.15). Then, the moduli for the DTD process can be numerically calculated as the Fourier transformation of $[\Phi(t)]^2$ (eq 4.36) and/or $[\mu_{1,m}(t)]^{1/2}\Phi_2(t)$ (eq 4.39). However, this straightforward method required a long calculation time (for the numerical transformation in two steps). Thus, in Chapter 7, the dielectric spectrum was utilized to calculate the moduli in a semi-analytic way (cf. eqs 7.2 and 7.4). In this sense, the use of the spectrum in the test of the DTD relationship is just for convenience of calculation.

A further comment needs to be added for the dielectric spectrum itself. In description of the slow entanglement dynamics, the entanglement segment are naturally chosen as the motional unit; see Chapter 6. Then, in a discretized expression, $\Phi(t)$ of a chain composed of N entanglement segments is contributed from N modes. In contrast, in Chapters 7 and 8, the semi-continuous spectrum contributed from more than N modes was evaluated with the method explained in Appendix 7A-1.

Since the test of the DTD relationship just requires the $\Phi(t)$ value, the test can be safely made by the use of this semi-continuous spectrum (instead of the discretized N-mode spectrum)

as long as the former spectrum reproduces the $\varepsilon''(\omega)$ and $\Phi(t)$ data with a high accuracy, e.g., with a difference less than 0.01 %. This was the case for the spectra utilized in Chapters 7 and 8.

References

1. Ball, R. C.; McLeish, T. C. B. *Macromolecules* **22**,1911 1989),.
2. Viovy, J. L.; Rubinstein, M.; Colby, R. H. *Macromolecules* **24**, 3587 (1991).
3. Stockmayer, W. H. *Pure Appl. Chem.* **15**, 539 (1967).
4. Watanabe, H.; Yao, M.-L.; Osaki, K. *Macromolecules* **29**, 97 (1996).
5. Ferry, J. D. *Viscoelastic Properties of Polymers*, 3rd ed.; Wiley: New York (1980).
6. Milner, S. T.; McLeish, T. C. B. *Macromolecules* **30**, 2159 (1997).
7. Graessley, W. W. *Adv. Polym. Sci. 16*, 1 (1974).
8. Struglinski, M. J.; Graessley, W. W. *Macromolecules* **18**, 2630 (1985).
9. Watanabe, H.; Urakawa, O.; Kotaka, T. *Macromolecules 26*, 5073 (1993).
10. Watanabe, H.; Urakawa, O.; Kotaka, T. *Macromolecules* **27**, 3525 (1994).
11. Adachi, K.; Itoh, S.; Nishi, I.; Kotaka, T. *Macromolecules* **23**, 2554 (1990).
12. Watanabe, H. *Prog. Polym. Sci.*, **24**, 1253 (1999).
13. Graessley, W. W. *Adv. Polym. Sci.* **47**, 68 (1982).
14. Marrucci, G. *J. Polym. Sci., Polym. Phys. Ed.* **23**, 159 (1985).
15. Matsumiya, Y.; Watanabe, H.; Osaki, K.; Yao, M.-L. *Macromolecules 31*, 7528 (1998).
16. Yoshida, H.; Adachi, K.; Watanabe, H.; Kotaka, T. *Polymer J. 21*, 863 (1989).

CHAPTER 8
Tube Dilation Process in Star-Branched *cis*-Polyisoprenes

8-1. Introduction

In the previous chapter, comparison of the normalized viscoelastic and dielectric relaxation functions $\mu(t)$ and $\Phi(t)$ was made to experimentally test the validity of the DTD molecular picture for a typical type-A polymer, *cis*-polyisoprene (PI): For monodisperse *linear* PI chains having non-inverted type-A dipoles, $\mu(t)$ and $\Phi(t)$ satisfy the relationship $\mu(t) \cong [\Phi(t)]^2$ (eq 4.36) *if* the tube dilates in the time scale of the chain relaxation. For the PI chains examined ($M \leq 62M_e$ with M_e being the entanglement spacing), this relationship was valid and the DTD picture gave a good approximation for the behavior of those chains. In addition, the analyses of the CR time suggested that no simple reptation occurs along the dilated tube: The chain appeared to move with its intrinsic (Rouse) diffusivity D_c along an *undilated* tube that fluctuated in the dilated tube (the supertube considered by Viovy et al.[1]).

A DTD relationship between $\mu(t)$ and $\Phi(t)$ in blends was also derived (Chapter 4). This relationship did not hold for dilute PI probes entangled with *much shorter* matrix chains (cf. Chapter 7), indicating the importance of the CR motion of the probe. This CR motion, enabling the probe to explore all local configurations and equilibrate itself in the dilated tube, is required for the tube to effectively dilate. Those dilute PI probes fully relaxed *via* the CR mechanism during this equilibration process (before the tube dilation was completed) to violate the DTD relationship.

In relation to this CR equilibration, it has been argued that the tube dilates more easily for star chains than for the linear chains because the star chains have broad relaxation mode distribution and their intensive fast modes may help rapid equilibration in the dilated tube.[2-4] This argument might sound plausible for stars having large arm molecular weight M_a. In fact, the viscoelastic behavior of entangled star chains is well described by the Ball-McLeish (section 4-6-1)[2] and Milner-McLeish (section 4-6-2)[3,4] models considering the arm retraction in the dilating tube (under an assumption of very rapid CR equilibration).

However, for the star chains, the DTD process *itself* has been neither verified nor disproved from experiments. In attempt to test the validity of the DTD picture, this chapter compares the viscoelastic and dielectric behavior of monodisperse star PI. The results are discussed is relation to the DTD criterion, and the DTD model is modified accordingly.

8-2. Theory

For the normalized dielectric and viscoelastic relaxation functions $\Phi(t)$ and $\mu(t)$ of well-entangled type-A star chain, the simplest DTD relationship in absence of tube-edge effect, $\mu(t) \cong [\Phi(t)]^2$ (eq 4.60), was derived in section 4-6-3-2. In addition, viscoelastic and dielectric properties of the Ball-McLeish (BM) and Milner-McLeish (MM) models were calculated (in section

4-6). These models were utilized in the detailed test of the DTD picture with/without the tube-edge effect.

8-3. Experimental

8-3-1. Materials

A series of 6-arm star PI samples having various M_a (= 30.6×10^3 - 80.1×10^3) and the other series of star PI samples having the same M_a (= 35.5×10^3) but different arm numbers q were anionically synthesized/characterized; cf. section 2-2. These star PI samples were subjected to the dielectric and viscoelastic measurements explained below.

In addition, 6-arm star PI synthesized by Yoshida et al[5] were also utilized. For these star PI samples ($M_a = 9.49 \times 10^3$ and 20.5×10^3), the data were available for both the dynamic dielectric constant ε' and dielectric loss ε''. Those samples, containing an anti-oxidant, butyl-hydroxytoluene (BHT), had been sealed in Ar atmosphere and stored in a deep freezer. In this study, no degradation of these stored PI samples was confirmed through GPC measurements. In fact, the ε' and ε'' data were reproduced in this study. Characteristics of all these PI samples are summerized in Tables 2.3 and 2.4.

8-3-2. Measurements

For the star-PI samples explained above, linear viscoelastic and dielectric measurements were conducted with the methods explained in sections 2-3 and 2-4. The time-temperature superposition[6] worked very well for the dielectric and viscoelastic data with the *same* shift factor a_T. These data were reduced at 40°C and compared with each other.

8-4. Results and Discussion

8-4-1. Overview of dielectric data

Fig. 8-1 shows the dielectric data of the monodisperse 6-arm star PI chains with the number of entanglement segments per each arm N_a (= M_a/M_e; $M_e \cong 5 \times 10^3$)[6] as indicated. The data cover barely-to-highly entangled regimes. These data were normalized by the dielectric intensity $\Delta\varepsilon$. ($\Delta\varepsilon$ was evaluated from the ε'' data as $\Delta\varepsilon = (2/\pi)\int\varepsilon''$ dln ω, where the integration was conducted in the ω range for the global relaxation.)

As noted from Fig. 8-1, the dielectric tests cover a low-ω range comparable to that examined in typical viscoelastic tests. The adsorption current method was very useful to detect dielectric responses at such low ω where the highly entangled star PI chains exhibited the terminal relaxation.

At the reference temperature, 40°C, the local (or segmental) relaxation of PI chains emerges at $\omega > 10^7$ $s^{-1.5}$,[7] Thus, the dielectric relaxation observed in Fig. 8-1 is exclusively attributed to the global motion of the star PI chains. At sufficiently low ω, these chains exhibit the terminal tails $\{\varepsilon_0 - \varepsilon'\} \propto \omega^2$ and $\varepsilon'' \propto \omega$ characterizing the completion of the global dielectric

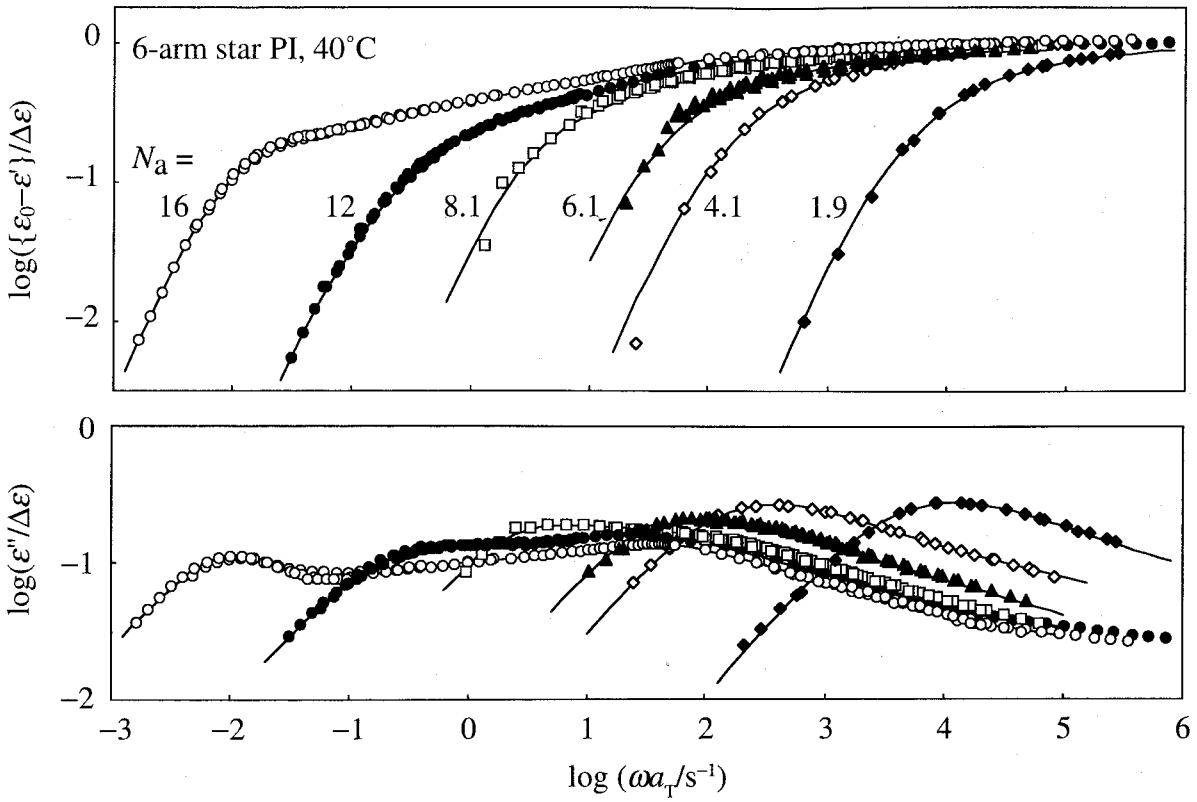

Fig. 8-1 Dielectric data of monodisperse 6-arm star PI chains with N_a as indicated. These PI stars have the type-A dipoles inverted at the branching point.

relaxation. From these tails, the second-moment average relaxation time $<\tau_\varepsilon>_w$ (eq 2.18) is evaluated. This $<\tau_\varepsilon>_w$ is related to the dielectric spectrum $\{g_p,\tau_p\}$ in a well-defined way (eq 2.18) and close to the longest dielectric relaxation time.[8,9] In fact, $<\tau_\varepsilon>_w$ is analogous to the viscoelastic terminal relaxation time $<\tau_G>_w = J_e\eta_0$ (eq 2.9).

For the linear and star PI chains examined in Figs. 7-1 and 8-1, Fig. 8-2 shows plots of $<\tau_\varepsilon>_w$ (unfilled symbols) and $<\tau_G>_w$ (filled symbols) against the span molecular weight $2M_a$ (for the star PI) and/or the total molecular weight M (for the linear PI). For comparison, the terminal relaxation times are shown also for lightly entangled/unentangled PI chains examined in the previous studies.[7,8,10-12] For both star and linear PI chains, $<\tau_\varepsilon>_w$ and $<\tau_G>_w$ are close to each other. This result confirms that the viscoelastic and dielectric relaxation processes detect the same global motion of the chains.

Figs. 7-1, 8-1 and 8-2 clearly demonstrate differences in the dielectric behavior of the star and linear chains. As seen in Fig. 8-2, $<\tau_\varepsilon>_w$ of the entangled linear chains increases in proportion to $M^{3.5\pm0.1}$ while the entangled stars exhibit much stronger, exponential M_a dependence of $<\tau_\varepsilon>_w$. (This difference has been well known for the viscoelastic $<\tau_G>_w$.[2-4,6,13-16] This study confirms the same difference for the dielectric $<\tau_\varepsilon>_w$ in the well-entangled regime.)

A more important difference between the linear and star chains is noted for the dielectric mode distribution reflected in the ω dependence of $\{\varepsilon_0-\varepsilon'\}/\Delta\varepsilon$ and $\varepsilon''/\Delta\varepsilon$. For the linear PI chains, this distribution is insensitive to N; see Fig. 7-1.

In contrast, the dielectric mode distribution of the star PI chains broadens significantly with

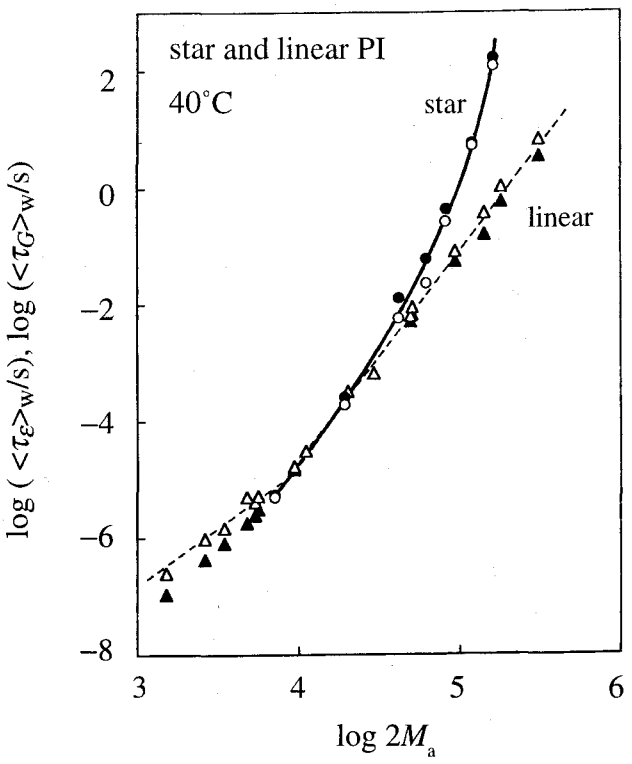

Fig.8-2 Dielectric and viscoelastic terminal relaxation times, $<\tau_\varepsilon>_w$ (unfilled symbols) and $<\tau_G>_w$ (filled symbols) at 40°C, plotted against the span molecular weight $2M_a$ (for PI stars) and/or the total molecular weight M (for linear PI chains).

increasing N_a; see Fig. 8-2. In particular, the stars with $N_a \geq 12$ exhibit two broad peaks of ε''. This result indicates the existence of a dielectric relaxation process much faster than the terminal relaxation process. Viscoelastic G'' of highly entangled stars exhibit a similar high-ω peak[13,16] (with an example seen later in Fig. 8-3), and this peak has been assigned to the Rouse-type thermal fluctuation of the arm length. Thus, the fast dielectric process reflected in the ε''-peak at ωa_T = 50-100 s^{-1} (for N_a = 12 and 16; cf. Fig. 8-1) can be also attributed to this fluctuation. With decreasing N_a , the terminal relaxation process is significantly accelerated to reduce the separation between the fast and terminal relaxation processes. Thus, for the star PI with N_a = 8.1, the fast fluctuation process does not give a well-resolved ε''-peak but is observed as a shoulder of the ε'' curve at $\omega a_T \cong 200\ s^{-1}$; cf. Fig. 8-1. For the shorter stars with $N_a \leq 4.1$, the two processes merge with each other to give a single broad ε''-peak at $\omega a_T \geq 400\ s^{-1}$.

The ε''-peak/shoulder assigned to the arm length fluctuation shifts to lower ω with increasing N_a ; see Fig. 8-1. This shift is quantitatively consistent with the $N_a^{-2.6}$ dependence reported for the G''-peak frequency.[16]

Differing from this fluctuation process, the terminal viscoelastic/dielectric relaxation of the entangled stars is exponentially retarded with increasing N_a ; cf. Fig. 8-2. On the basis of the excellent agreement of the tube model prediction and viscoelastic data,[3,4] one may assign the retarded terminal relaxation to the full retraction of the star arm along the dilated tube. However, the test of the DTD picture utilizing both viscoelastic and dielectric data poses a question for this assignment. The results of this test are summarized below.

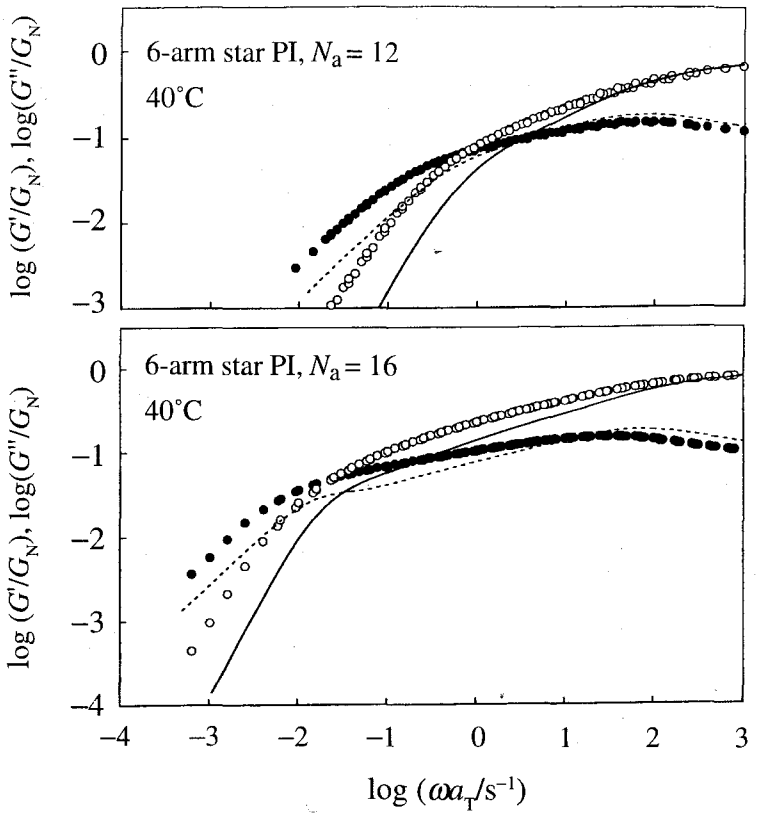

Fig.8-3 Test of the simplest DTD relationship (eq 4.60; derived in absence of the tube edge effect) for highly entangled PI stars at 40°C. Normalized moduli data, G'/G_N (unfilled circles) and G''/G_N (filled circles), are compared with the moduli calculated from dielectric data through this relationship (curves).

8-4-2. Test of DTD relationship in absence of tube-edge effect

The DTD relationship derived for the star PI chains in absence of the tube-edge effect, eq 4.60, can be easily tested. If these chains satisfy eq 4.60 with the smallest possible dilation exponent $\alpha = 1$, their normalized moduli should be related to the dielectric spectrum $\{g_p, \tau_{\varepsilon,p}\}$ as

$$\frac{G'(\omega)}{G_N} = \omega^2 \sum_{p,p'\geq 1} \frac{h_{pp'}\tau_{pp'}^2}{1+\omega^2\tau_{pp'}^2}, \quad \frac{G''(\omega)}{G_N} = \omega \sum_{p,p'\geq 1} \frac{h_{pp'}\tau_{pp'}}{1+\omega^2\tau_{pp'}^2} \tag{8.1}$$

with

$$h_{pp'} = g_p g_{p'} \text{ and } \tau_{pp'} = \left[\tau_{\varepsilon,p}^{-1} + \tau_{\varepsilon,p'}^{-1}\right]^{-1} \tag{8.2}$$

For a given dielectric $\Phi(t)$, eqs 8.1 and 8.2 specify the slowest possible viscoelastic DTD relaxation. (For the general cases of $\alpha > 1$, the viscoelastic relaxation is faster than that for $\alpha = 1$; cf. eq 4.60.)

The dielectric data shown in Fig. 8-1 were utilized to evaluate the dielectric spectrum of the highly entangled star PI with the iteration method[5] explained in Appendix 7A. In Fig. 8-3, the G'/G_N and G''/G_N calculated from this spectrum for the star PI with $N_a = 12$ and 16 are

shown with the solid and dotted curves. These calculated moduli are close to the G'/G_N and G''/G_N data (unfilled and filled circles) at high $\omega a_T > 10\ s^{-1}$ where the G''-peak attributable to the arm length fluctuation is observed. However, at lower ω, considerable differences are noted for the measured and calculated moduli. Specifically, the viscoelastic DTD relaxation calculated from the dielectric data is *faster* than observed. Since the dilation exponent utilized in the calculation ($\alpha = 1$) gives the slowest possible DTD relaxation, the result seen in Fig. 8-3 unequivocally indicates the failure of the DTD picture (in absence of the tube-edge effect) at long times where the highly entangled PI stars exhibit the terminal relaxation. This failure was observed also for less entangled star PI.

8-4-3. Effect of branching-point fluctuation in dilated tube

The above failure of the DTD molecular picture for the star chains suggests that the relaxation of the portion of the star arm near the branching point (BP), occurs before the CR-equilibration (pre-requisite of DTD) for this portion is completed: Since the portion near BP is mostly entangled with quickly relaxing portions near the free ends of the arms, the dynamic situation for the former portion is similar to the situation for long, dilute probe chains entangled with much shorter matrix chains (Chapter 7). Extensive experiments indicated that such probes relax with the CR mechanism.[13] This seems to be the case also for the portion of the star arm near BP. For this point, further discussion is made later in section 8-4-3-4.

However, the DTD relationship ($\mu(t) \cong [\Phi(t)]^2$; eq 4.60) for the star chains was derived under the assumption of short-ranged BP fluctuation in the dilated tube. Although this assumption sounds reasonable within the context of the DTD model, there still remains a non-negligible possibility that the failure of this relationship observed for the 6-arm star PI is due to breakdown of this assumption.

In relation to this problem, the viscoelastic and dielectric properties were examined for a series of star PI chains having the same arm molecular weight M_a ($= 35.5 \times 10^3$) but different arm number q (= 4 - 15). Since the entropic penalty for large-amplitude BP fluctuation increases with increasing q, the DTD relationship should become valid for large q *if* the breakdown of the above assumption was the main reason for the failure observed for $q = 6$. Thus, this relationship was tested for the series of star PI chains having different q. The results are summerized below.

8-4-3-1. Test of DTD relationship for star chains with various q

Fig. 8-4 shows the dielectric behavior for the series of well entangled star PI chains having identical M_a ($\cong 7M_e$) and different q (= 4, 6, 9 and 15). For convenience of later comparison with viscoelastic data, the dielectric data are presented in a normalized form, $\{\varepsilon_0-\varepsilon'\}/\Delta\varepsilon$ and $\varepsilon''/\Delta\varepsilon$ plotted against ωa_T; cf. eq 2.17.

The dielectric relaxation seen in Fig. 8-4 is exclusively attributed to the global motion of the star PI chains. (The relaxation due to local segmental motion occurs at high ω not covered here.) The ω dependence of $\{\varepsilon_0-\varepsilon'\}/\Delta\varepsilon$ and $\varepsilon''/\Delta\varepsilon$ is nearly the same for the star PI chains of

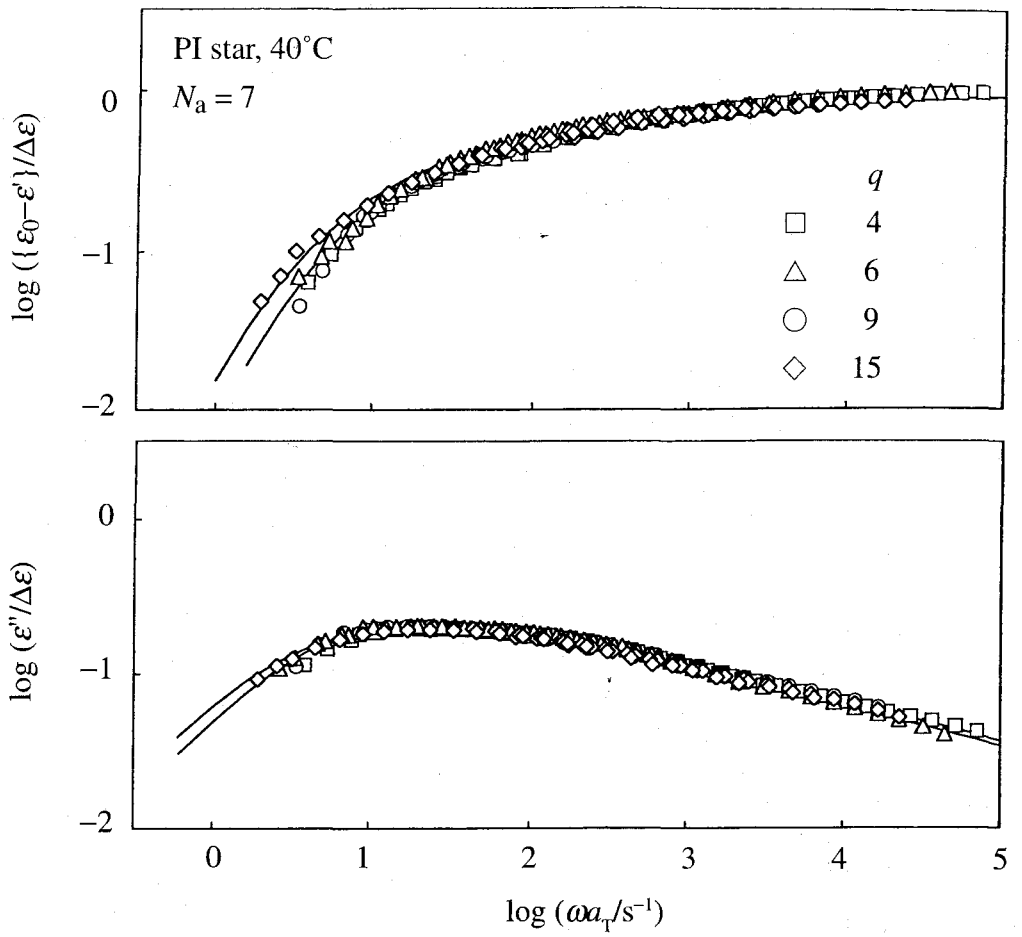

Fig. 8-4 Normalized dielectric data at 40°C obtained for the star PI chains having identical M_a ($\equiv 7M_e$) and various q (= 4, 6, 9, and 15). The solid curves indicate the {ε_0–ε'}/$\Delta\varepsilon$ and $\varepsilon''/\Delta\varepsilon$ of the chains with q = 6 and 15 re-calculated from the dielectric spectra.

various q. In particular, the dependence is indistinguishable for q = 4 and 6. The dielectric mode distribution of the well entangled star PI chains, reflected in this dependence, is broader than that of linear PI chains. The dielectric relaxation spectrum {g_p, $\tau_{\varepsilon,p}$} (eq 2.17) was determined from the $\varepsilon''/\Delta\varepsilon$ data with the method described in Appendix 7A.

For the star PI chains with q = 4, 6, 9, and 15, the normalized viscoelastic moduli G'/G_N and G''/G_N are shown in Fig. 8-5. The dominant part of the viscoelastic relaxation, seen at $\omega < 10^3$ s^{-1}, is hardly contributed from the fast rubber-to-glass transition and reflects the global chain motion.

Extensive experiments indicated that the viscoelastic mode distribution for well entangled star chains is much broader than the distribution for linear chains.[9,13] This is the case also for the star PI examined here, for which the mode distribution is observed through the ω dependence of the moduli (Fig. 8-5). This distribution is almost identical for the star PI with q = 4 and 6 and becomes a little broader at low ω for the star PI with larger q (= 9 and 15). Similar broadening is noted also for the viscoelastic data of star polybutadienes reported by Adams et al.[17] This moderate broadening of the mode distribution may be partly related to suppression of the branching-point fluctuation for large q.

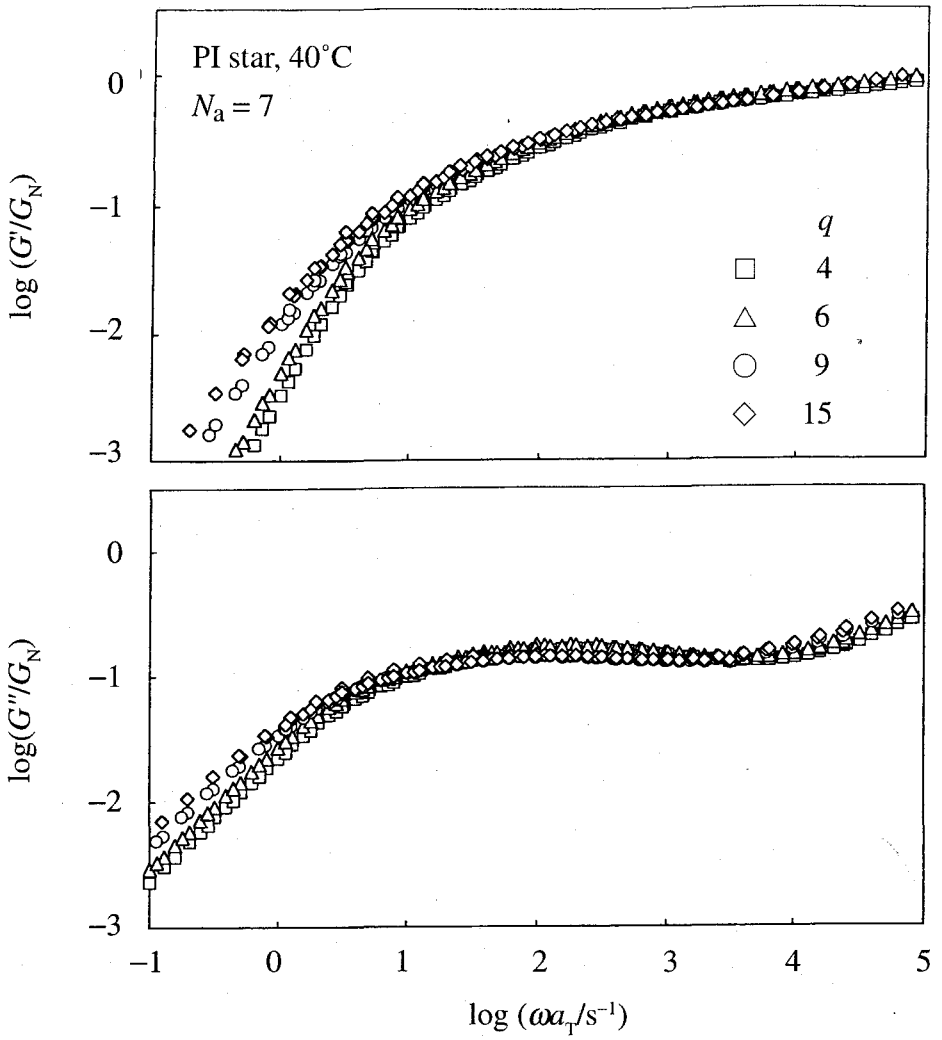

Fig. 8-5 Normalized viscoelastic moduli at 40°C obtained for the star PI chains having identical M_a ($\cong 7M_e$) and various q (= 4, 6, 9, and 15).

The dielectric mode distribution (Fig. 8-4) changes with q less prominently compared to the viscoelastic mode distribution. This difference may reflect the intrinsic difference of the viscoelastic and dielectric properties, the former representing the isochronal orientational anisotropy while the latter detecting the orientational correlation at two separate times (cf. Chapter 3).

For the star PI chains with q = 4, 6, 9, and 15, Fig. 8-6 compares the G'/G_N and G''/G_N data (unfilled squares and circles) with those calculated from the dielectric spectra (dashed curves). The small filled circles indicate the $\varepsilon''/\Delta\varepsilon$ data, and the thin dotted curve is the $\varepsilon''/\Delta\varepsilon$ re-calculated from the spectra. Differences observed between the $\varepsilon''/\Delta\varepsilon$ and G''/G_N data unequivocally indicate that the tube is not fixed in space. (In the fixed tube, the chains have $\mu(t) = \Phi(t)$ and their normalized dielectric and viscoelastic losses coincide with each other.[8])

More importantly, Fig. 8-6 demonstrates that the moduli calculated for the case of DTD are different from the data to *nearly the same extent* for the star PI chains of various q. For all PI chains, the observed viscoelastic relaxation is slower than that expected for the case of DTD with α = 1. Since this expected relaxation represents the slowest possible viscoelastic DTD relaxation for a given dielectric spectrum, the difference between the observed and calculated moduli seen

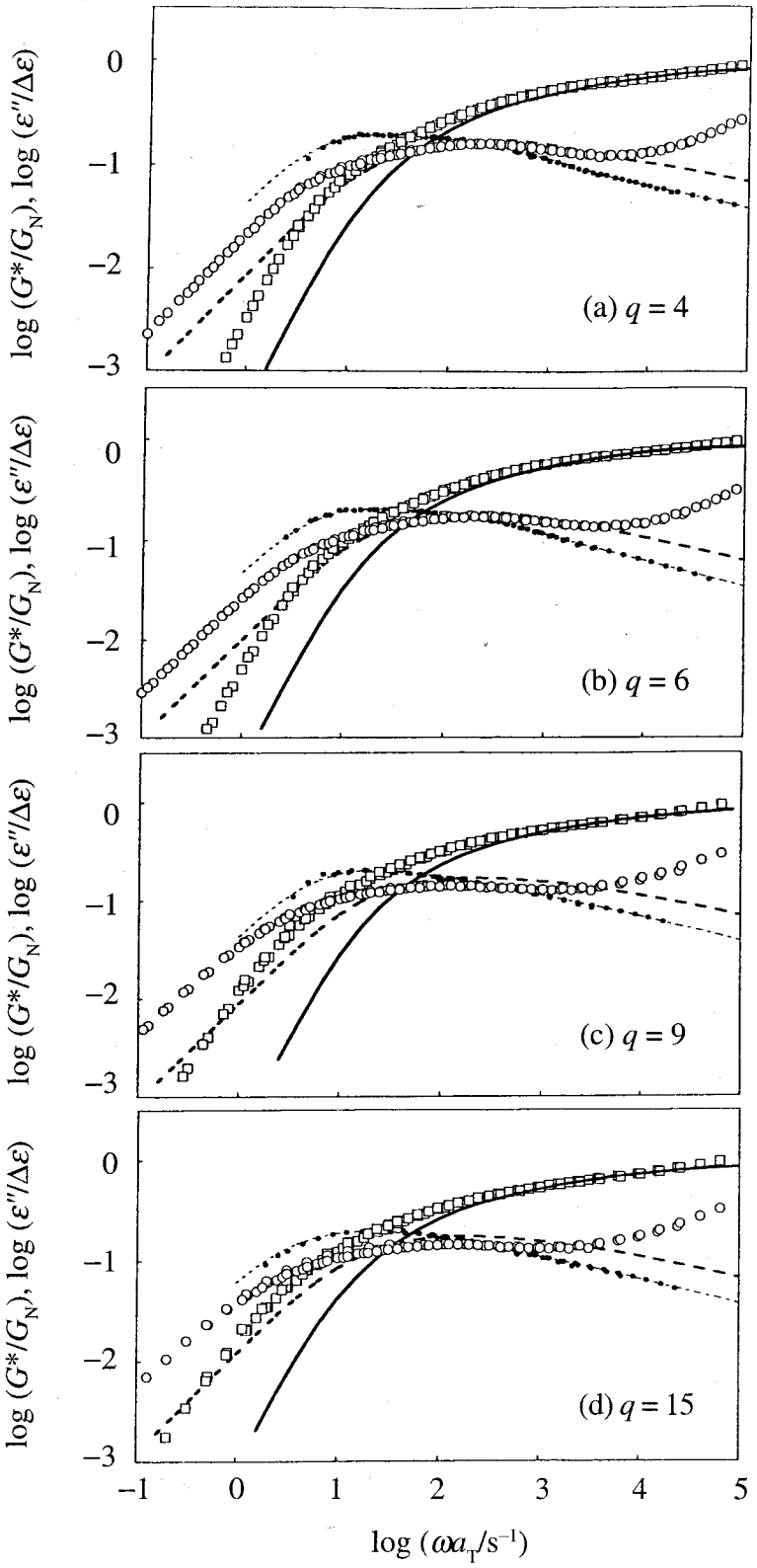

Fig. 8-6 Comparison of normalized viscoelastic moduli G'/G_N (unfilled squares) and G''/G_N (unfilled circles) of the star PI chains with the moduli calculated from the dielectric spectra through the DTD relationship with $\alpha = 1$ (eq 4.60 derived in absence of the tube edge effect; thick solid and dashed curves for G'/G_N and G''/G_N). Small filled circles indicate the normalized dielectric loss $\varepsilon''/\Delta\varepsilon$ of respective PI chains, and the thin dotted curves represents the $\varepsilon''/\Delta\varepsilon$ re-calculated from the dielectric spectra.

here indicates that the failure of the DTD relationship is not due to breakdown of the assumption of the short-ranged BP fluctuation but is intrinsically related to the star chain dynamics.

8-4-3-2. DTD criteria in absence of tube-edge effect

The DTD process occurs as a result of mutual CR-equilibration of entanglement segments. For the tube diameter to dilate from a to a', successive $(a'/a)^2$ segments need to be equilibrated.[8,21] This CR-equilibration requires a time,[8,13] $\tau^{**} = f(a'/a)^4 t_w$, where t_w is an average lifetime[22] of the entanglement point and f is a numerical prefactor. The entanglement lifetime has some distribution, and t_w is an effective CR time-unit that determines the rate of CR-equilibration over $(a'/a)^2$ segments. This lifetime distribution is further discussed in the next section.

The tube can dilate up to a' only in a time scale longer than τ^{**}, meaning that the coarse-graining of the spatial scale (the DTD molecular picture) is intrinsically associated with the coarse-graining of the time scale.[13] This DTD criterion corresponds to that discussed by Milner et al. for star/linear blends.[23] In addition, the DTD picture loses its sound meaning when a' becomes comparable to/larger than the chain dimension R ($= N^{1/2}a$ and $N_a^{1/2}a$ for the linear chain and star arm composed of N and N_a entanglement segments, respectively).

These DTD criteria can be summarized as,

$$t \geq f\left[\frac{a'(t)}{a}\right]^4 t_w \; (> t_w) \tag{8.3}$$

$$\left[\frac{a'(t)}{a}\right]^2 \leq N \text{ (for linear chains)}, \; N_a \text{ (for star chains)} \tag{8.4}$$

The prefactor f is estimated in the next section.

The DTD picture is valid only in the time scale where eqs 8.3 and 8.4 are satisfied. In this time scale, the dielectric $\Phi(t)$ coincides with the survival fraction of the dilated tube (cf. eq 4.59) in absence of the tube-edge effect, and the diameter of this tube is given by $a'(t) \cong a[\Phi(t)]^{-1/2}$.[8,10] Then, eqs 8.3 and 8.4 can be rewritten, in terms of experimentally measured/estimated quantities, as

$$\Phi(t) \geq \left[\frac{f t_w}{t}\right]^{1/2} \tag{8.5}$$

$$\Phi(t) \geq \frac{1}{N} \text{ (for linear chains)}, \; \frac{1}{N_a} \text{ (for star chains)} \tag{8.6}$$

For representative highly entangled linear PI ($N = 62$) and 6-arm star PI ($N_a = 12$) having almost identical relaxation times, the validity of eqs 8.5 and 8.6 are examined later in Fig. 8-7. The f and t_w values utilized in this test are estimated below.

8-4-3-3. Estimation of f and t_w

For linear chains compared of entanglement segments, the prefactor f and effective entanglement lifetime t_w can be estimated on the basis of the Graessley model[22] considering the Rouse-like CR process. The global, dielectric CR relaxation time deduced from this model is expressed as (cf. section 4-4-1)[13,22]

$$\tau_{CR,\varepsilon} = \frac{4t_w}{\pi^2} N^2 \text{ (for linear chain)} \qquad (8.7)$$

The factor $[a'/a]^4$ appearing in eq 8.3 is the squared number of CR-equilibrated entanglement segments and corresponds to the factor N^2 in eq 8.7. Thus, the f for linear chains is estimated to be $4/\pi^2$.

For dilute linear probe in linear matrices, the Graessley model relates t_w to the matrix reptation time $\tau_{m,rep}$ as $t_w = (\pi^2/12)^{z_g}\tau_{m,rep}/z_g$, where z_g represents a number of constraints per entanglement (cf. eq 4.23). Adachi et al.[24] examined the dielectric behavior of blends of linear PI and reported that the terminal dielectric relaxation time τ_ε of the probe PI is close to the model prediction with $z_g \cong 4$. The probe and matrix are identical in monodisperse systems. Thus, the t_w of the monodisperse linear PI ($N = 62$) can be estimated from this z value as $t_w = (\pi^2/12)^{z_g}\tau_\varepsilon/z_g = 0.11\tau_\varepsilon$.[25]

For the star chains, no explicit expression of f is available. In addition, no dielectric data are available for blends of star PI chains, and the t_w of the monodisperse star PI cannot be estimated with the above method. However, viscoelastic experiments for polystyrene blends indicated that the relaxation time of monodisperse star chains with $N_a \leq 6$ is close to the global CR relaxation time.[13,26] This would be the case also for the monodisperse star PI ($N_a = 12$), and the measured τ_ε ($\cong \tau_{CR,\varepsilon}$) may be expressed in terms of f and t_w as

$$\tau_\varepsilon \cong \tau_{CR,\varepsilon} = f t_w N_a^2 \qquad (8.8)$$

Thus the product ft_w for the star PI is estimated to be τ_ε/N_a^2.

Here, a few comments should be added for the entanglement lifetime for a linear probe chain. This lifetime, being determined by the first passage of surrounding chains, should have a distribution. The DTD criterion using the single, effective lifetime t_w (eq 8.5) is approximate in this sense. However, for the dilute linear probe (having the lifetime distribution as suggested by Rubinstein and Colby[27]), the CR model with the single t_w well describes the relaxation data at long times:[13] The slow (global) CR relaxation of the probe results from cooperative motion of many entanglement segments therein, and smearing/averaging of the lifetimes of those segments possibly leads to this validity of the single-t_w model. Correspondingly, the single-t_w criterion (eq 8.5) can be safely utilized to test the DTD picture for the monodisperse linear chains in long time scales.

The situation would be different for monodisperse star chains. Since the monodisperse star chains have much more widely distributed motional modes compared to the linear chains, the distribution of the entanglement lifetime would be broader for the former. This suggests a limitation of the single-t_w DTD criterion for the star chains.[28] However, the smearing/averaging of the lifetimes explained above is expected also for the star chains *in the long time end of the relaxation*. Thus, in the following section, this criterion is utilized at long times.

8-4-3-4. Origin of failure/validity of DTD picture

On the basis of the DTD criteria (eqs 8.5 and 8.6), the reason why the DTD picture is valid for the monodisperse linear PI in the terminal regime (Fig. 7-2) but not for star PI (Figs. 8-3 and 8-6) can be specified. For the representative linear PI ($N = 62$) and 6-arm star PI ($N_a = 12$), respectively, Fig. 8-7 shows plots of the dielectric $\Phi(t)$ data, the $\{ft_w/t\}^{1/2}$ factor, and N or N_a against a reduced time t/τ_ε. The f and t_w utilized in the plots were estimated in the previous section ($f = 4/\pi^2$ and $t_w = 0.11\tau_\varepsilon$ for the linear PI and $ft_w = \tau_\varepsilon/N_a^2$ for the star PI), and the terminal dielectric relaxation time τ_ε was evaluated from the ε' and ε'' data as the second-moment average dielectric relaxation time through eq 2.18.

In Fig. 8-7, a range of t where the DTD criteria are satisfied can be specified: For the linear PI, $\Phi(t)$ (circles) is comparable with and/or larger than both $\{ft_w/t\}^{1/2}$ (solid line) and $1/N$ (dotted line) in a considerably wide range in the terminal regime, $\tau_\varepsilon/8 \le t$ ($\le \tau_\varepsilon$). Similar results were found for the other linear PI chains (with $N < 36$) examined in the previous chapter. This wide validity of the DTD picture reflects a fact that $\Phi(t)$ of well-entangled linear PI chains has a M-insensitive, narrow mode distribution and relaxes just moderately at $t < \tau_\varepsilon$: Since $\Phi(t)$ remains considerably large at $t \le \tau_\varepsilon$ (because of this distribution), the tube diameter can increase only up to $a'(\tau_\varepsilon) = a[\Phi(\tau_\varepsilon)]^{-1/2} \cong 2.2a$. In this rather thin tube, the chain can equilibrate itself (through the CR motion) within the given time scale t and thus the tube actually dilates at $t \ge \tau_\varepsilon/10$.[29] This result is consistent with the validity of the DTD relationship (eq 4.36) observed for the viscoelastic G^* and dielectric ε'' of linear PI in a wide range of ω (Fig. 7-2).

In contrast, the DTD criterion fails for the star PI; see left pannel of Fig. 8-7. Similar results were found for the other star PI examined in this chapter. This failure of the DTD picture in the dominant part of the terminal relaxation, being consistent with the violation of eq 4.60 for G^* at low ω (Figs. 8-3 and 8-6), is related to the broad dielectric mode distribution of the star: Because of this broadness, $\Phi(t)$ significantly decays at short t and the tube diameter expected from the DTD picture at long t ($a' \cong a\Phi^{-1/2} \cong 3.6a$ at $t = \tau_\varepsilon$) becomes too large to allow the CR-equilibration to occur in time.

Concerning this result, it should be emphasized that the $[ft_w/t]^{1/2}$ factor at a given t/τ_ε is considerably larger for the linear PI than for star PI (cf. Fig. 8-7). Nevertheless, the DTD criterion (eq 8.5) at long t is more easily satisfied for the linear PI because of its narrow distribution of motional modes (reflected in the dielectric and viscoelastic spectra). Thus, the difference between the linear and star PI chains (success and failure of the DTD picture at long t) is related to the difference in the dynamics of these chains. The star dynamics intrinsically results in the

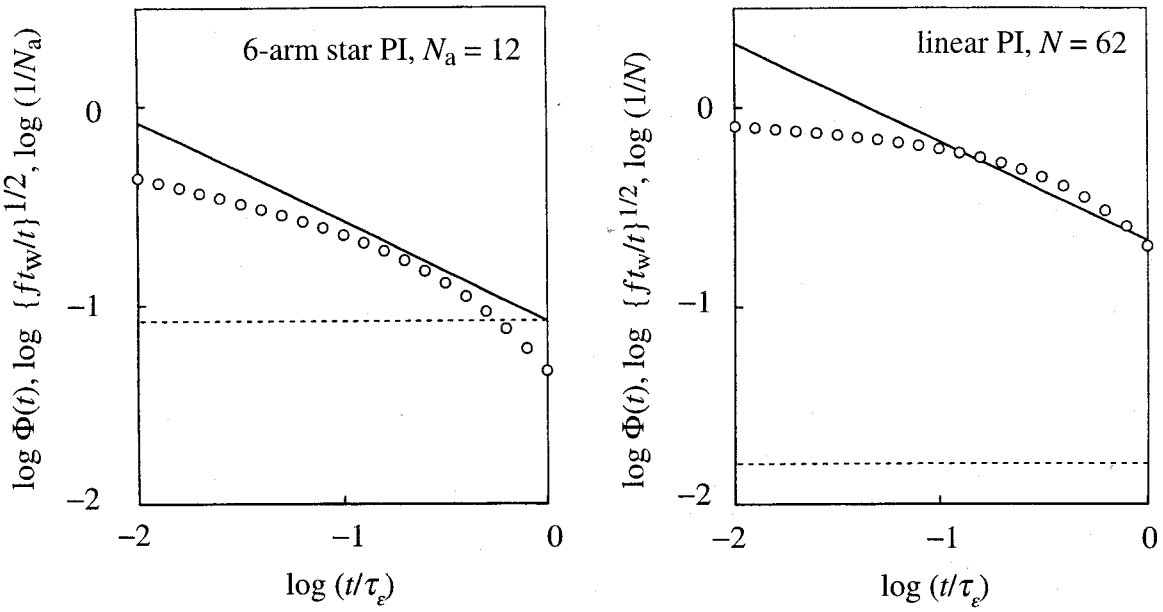

Fig.8-7 Test of DTD criteria (in absence of the tube-edge effect) for highly entangled star and linear PI chains having nearly the same longest dielectric relaxation time τ_ε. The criteria are satisfied if $\Phi(t)$ (circles) is larger than $\{ft_w/t\}^{1/2}$ (solid line) and $1/N_a$ or $1/N$ (dotted line).

broad motional modes that lead to this failure.

This broadness reflects large differences in the relaxation rates of the portions of arm near the branching point (BP) and free end (FE). In this sense, the monodisperse star chains may be regarded as a blend of slowly relaxing, dilute species (the portion near BP) entangled with quickly relaxing matrix (the portion near FE). This situation is analogous to that for dilute linear probe chains in much shorter matrix chains (Chapter 7). Such probe PI fully relaxes *via* the CR mechanism, and the DTD picture fails. Thus, the relaxation of the portion of the star arm near BP, observed as the terminal relaxation of the monodisperse star PI, is possibly dominated by the CR mechanism due to fast motion of the portions near FE. This result is consistent with the coincidence of the terminal relaxation time and the global CR time found for monodisperse stars with $N_a \leq 6$.[13,26)]

8-4-4. Comparison of data with DTD model in absence of tube-edge effect

The above test revealed the failure of the simplest DTD picture (eq 4.60) for the highly entangled star PI. Here, the models considering the DTD relaxation (BM and MM models in absence of the tube-edge effect) are utilized to test the DTD picture in a more quantitative sense.

For these models, the normalized moduli G'/G_N and G''/G_N are calculated as the Fourier transformation of $\mu(t)$ (= $G(t)/G_N$) given by eq 4.46 (BM) and eq 4.51(MM). For the highly entangled PI stars with N_a = 12 and 16, respectively, the top panels of Figs. 8-8 and 8-9 compare the moduli data (circles) with the MM prediction (solid curves). For the star with N_a = 12, the data are also compared with the BM prediction in the top panel of Fig. 8-10. In the calculation, the N_a value was allowed to be adjusted a little ($N_{a,cal}$ = 15 and 20 instead of N_a = 12 and 16) to achieve the best agreement of the calculated and measured moduli. This adjustment (~ 20%) is

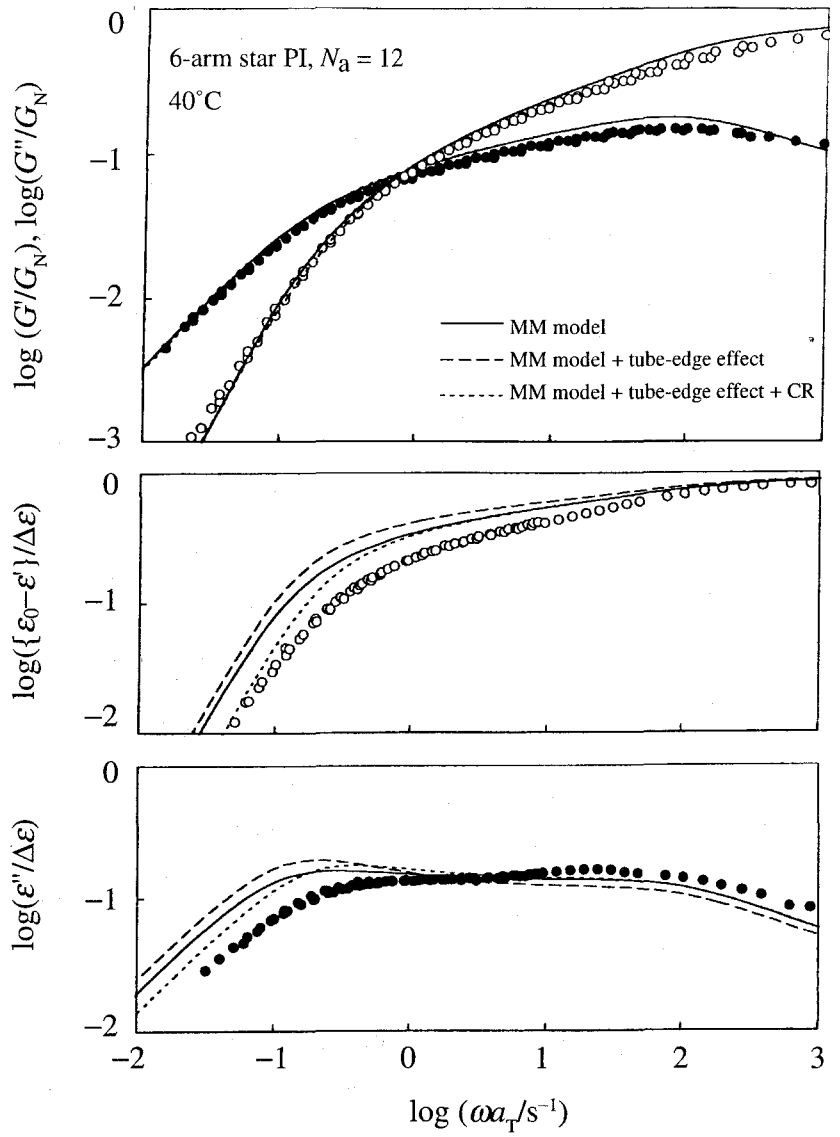

Fig.8-8 Comparison of viscoelastic/dielectric data (circles) of a PI star (N_a = 12) with predictions of MM model without the tube-edge effect (solid curves). Dashed curves indicate the prediction of the model combined with the tube-edge effect on the dielectric behavior. Dotted curves represent the prediction of the DTD-CR model (= MM model modified through incorporation of the CR process).

comparable in magnitude to uncertainties in the experimental M_a and G_N values utilized in calculation of $N_a = M_a G_N/\rho RT$ (ρ = density). In fact, the adjustment of similar magnitude was made in previous studies.[2-4)]

The remaining model parameter, the Rouse relaxation time within one entanglement segment τ^* (cf. eqs 4.44, 4.47, and 4.49), was determined in a way that the BM/MM models (with the above $N_{a,cal}$ values) reproduced the viscosity η_0 of the PI stars. As noted in the top panels of Figs. 8-8, 8-9 and 8-10, the models with this choice of τ^* excellently describe the moduli data in the dominant part of the terminal relaxation ($\omega a_T < 100\ s^{-1}$); compare the solid curves and circles. In particular, the MM model excellently reproduces the G'' peak (at ωa_T = 10-100 s^{-1}) attributable to the Rouse fluctuation of the star arm length. Similar agreement between the viscoelastic data and models was demonstrated previously.[2-4)]

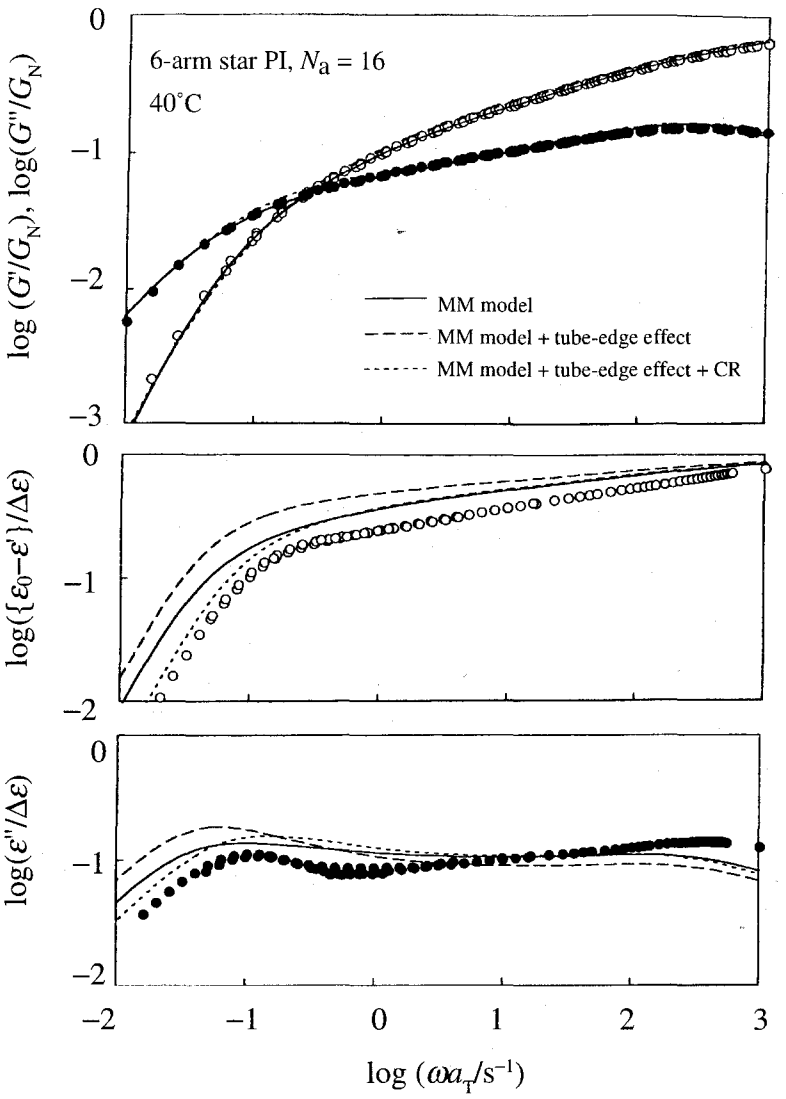

Fig.8-9 Comparison of viscoelastic/dielectric data (circles) of a PI star (N_a = 16) with predictions of MM model without the tube-edge effect (solid curves). Dashed curves indicate the prediction of the model combined with the tube-edge effect on the dielectric behavior. Dotted curves represent the prediction of the DTD-CR model (= MM model modified through incorporation of the CR process).

The dielectric $\Phi(t)$ formulated for the MM model in absence of the tube-edge effect is given by eq 4.71 with $\alpha = 4/3$, $z_c = L_{eq}$, $K_n = 1$, and the pre-exponential factor in the integral being replaced by unity. The model predictions for $\{\varepsilon_0-\varepsilon'\}/\Delta\varepsilon$ and $\varepsilon''/\Delta\varepsilon$ of the PI stars, calculated as the Fourier transformation of this $\Phi(t)$, are shown with the solid curves in the middle and bottom panels of Figs. 8-8 and 8-9. The values of the model parameters ($N_{a,cal}$ and τ^*) are the same as those giving the excellent agreement between the calculated and measured moduli (top panels). Nevertheless, the calculated $\{\varepsilon_0-\varepsilon'\}/\Delta\varepsilon$ and $\varepsilon''/\Delta\varepsilon$ are considerably different from the data in the terminal regime, although the model fairly well describes the high-ω ε'' peak attributable to the Rouse fluctuation.

The BM predictions for $\{\varepsilon_0-\varepsilon'\}/\Delta\varepsilon$ and $\varepsilon''/\Delta\varepsilon$, calculated in a similar way (except that α is set to be unity in eq 4.71), is shown with the solid curves in the bottom panel of Fig. 8-10. Differences between the model and experiments are noted not only in the terminal regime but also

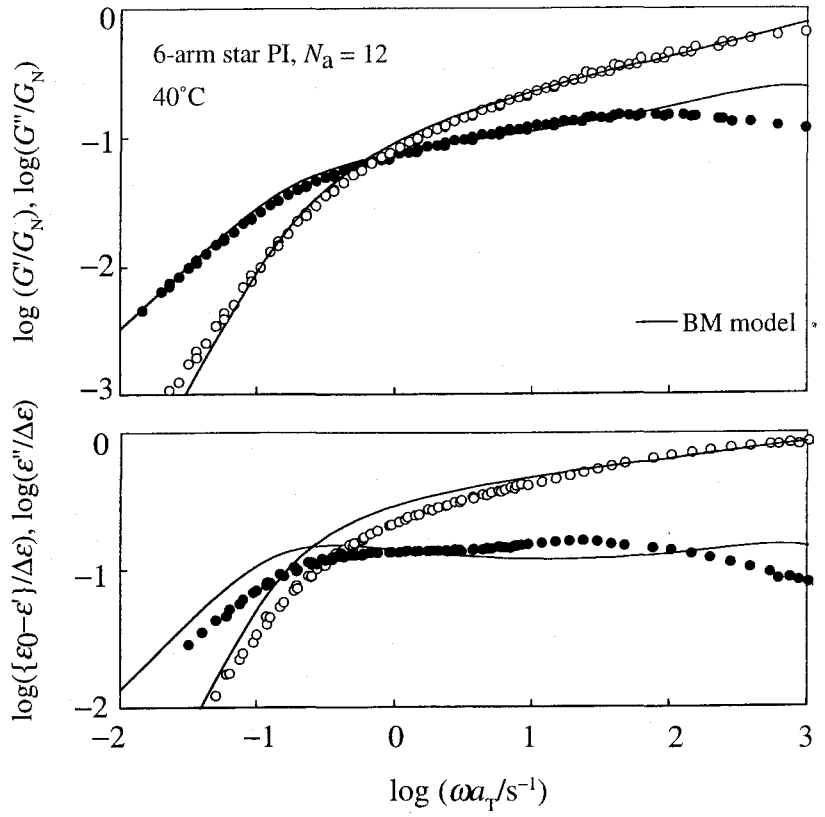

Fig.8-10 Comparison of viscoelastic and dielectric data (circles) of a PI star (N_a = 12) with the predictions of BM model (solid curves).

in the Rouse-fluctuation regime. The high-ω ε'' peak, reproduced by the MM model, is not predicted from the BM model. Correspondingly, the BM model does not describe the G'' peak at ωa_T = 50-100 s^{-1}; see the top panel of Fig. 8-10. The BM model focuses on the terminal relaxation and does not incorporate the Rouse fluctuation mechanism, thereby exhibiting this disagreement at these ω.

As noted in Fig. 8-8, 8-9 and 8-10, the BM and the MM models (with slightly adjusted N_a values) commonly predict the dielectric terminal relaxation slower than observed if the model parameters are chosen to excellently reproduce the moduli data. The models with non-adjusted N_a was found to give no better agreement with the dielectric data. Thus, the deviation between the dielectric data and model prediction is not due to the minor adjustment of N_a.

As shown in Fig. 8-3, the viscoelastic DTD relaxation calculated from the dielectric data (in absence of the tube-edge effect) is faster than observed. Consequently, the dielectric relaxation calculated from the viscoelastic data through the DTD relationship (eq 4.60) is slower than observed. This result is in harmony with that seen in Figs. 8-8, 8-9 and 8-10. In particular, the $\mu(t)$ of the MM model is numerically close to $[\Phi(t)]^2$ in the entire range of t (although the rigorous DTD relationship for this model is given by $\mu(t) = [\Phi(t)]^{1+\alpha} = [\Phi(t)]^{7/3}$ at short t); see Appendix 8A. Thus, the result seen in Fig. 8-3 (failure of the simplest DTD relationship) is almost equivalent to those observed in Figs. 8-8 and 8-9.

8-4-5. Comparison of data with DTD model in presence of tube-edge effect

For the highly entangled PI stars, the previous sections confirmed the failure of the DTD picture in absence of the tube-edge effect. However, the DTD relationship (eq 4.60) is modified if the tube-edge effect on the dielectric $\Phi(t)$ is considered. Thus, the validity of the DTD picture needs to be also tested in presence of this effect. Here, this test is made through comparison of the data of the PI stars and the MM model combined with the tube-edge effect. (The MM model is utilized in this test because this model can describe the Rouse-fluctuation of the arm length.)

For the largest possible displacement of the segment in the tube-edge, the $\Phi(t)$ formulated for the MM model is given by to eq 4.71 (with $\alpha = 4/3$). This displacement induces no significant change in the expression of $\mu(t)$ (eq 4.51). Thus, in the calculation of $\{\varepsilon_0-\varepsilon'\}/\Delta\varepsilon$ and $\varepsilon''/\Delta\varepsilon$ in presence of the tube-edge effect, the parameters ($N_{a,cal}$ and τ^*) giving the best agreement between the moduli data and the MM prediction without this effect (cf. top panels of Figs. 8-8 and 8-9) were chosen. The dielectric behavior thus calculated is shown with the dashed curves in the middle and bottom panels of Figs. 8-8 and 8-9. Since eq 4.71 is formulated for the maximum tube-edge effect, these dashed curves overestimate this effect for the PI chains. (Thus, the dielectric curves calculated for a realistic magnitude of the tube-edge effect should be between the dashed and solid curves.)

As noted in Figs. 8-8 and 8-9, the tube-edge effect moderately increases the terminal dielectric intensity of the DTD process because the displacement of the edge segment is larger in a more dilated tube at longer t; cf. dashed and solid curves. However, the calculated terminal relaxation time does not change with this effect, and the calculated dielectric relaxation is still slower than observed.

From this result as well as those demonstrated in the pervious sections, it can be concluded that the PI star arm does not retract along the fully dilated tube (with the diameter $a' = a\{\varphi'(t)\}^{-\alpha/2}$) at long t. This failure of the DTD picture (either with or without the tube-edge effect) suggests an important contribution of the constraint release (CR) mechanism to the terminal dynamics of the star chains, as pointed out also in the previous sections. From this point of view, the MM model is to be modified by incorporating the CR process (though in a crude way. The method of this modification is described in the next section.

Here, a comment should be added for the DTD relationship for linear chains modified for the tube-edge effect. This modified relationship is cast in a form similar to that shown in eq 4.68 (with $1/8N_a$ factor being replaced by $1/4N$; N = the total number of entanglement segments).[36] Thus, in principle, the tube-edge effect changes the viscoelastic moduli of the linear chains relaxing through the DTD mechanism. However, for the linear chains with $N >> 1$, the terminal viscoelastic modes have a considerably narrow distribution and $\mu(t)$ remains considerebly close to unity up to $t = <\tau_G>_w$. For this case, the correction term due to the tube-edge effect, having the order of $\mu(t)^{-\alpha/(1+\alpha)}/N$ (cf. second term in eq 4.68), can be neglected in the entire range of t up to $<\tau_G>_w$. For this reason, the DTD relationship without this effect is valid for the highly entangled linear chains, as observed in Fig. 7-2.

8-4-6. Effect of terminal CR relaxation

The DTD molecular picture is valid in a time scale $t > \tau^{**}$, where τ^{**} is a time required for CR-equilibration of the successive $(a'/a)^2$ entanglement segments in the dilated tube. In the MM model, every segment has the relaxation time $\tau_{MM}(z)$ determined by its curvilinear coordinate z; cf. eq 4.50. Thus, the DTD formulation in this model may be valid for the segments having $\tau_{MM}(z) > \tau^{**}(z)$ but a modification (explicit incorporation of the CR process) is required for those having $\tau_{MM}(z) < \tau^{**}(z)$, where $\tau^{**}(z)$ is the CR-equilibration time over the $(1-z/L_{eq})^{-4/3}$ segments. Here, L_{eq} $(= N_a a)$ is equilibrated arm length. (Note that the dilation to the diameter a' $= a(1-z/L_{eq})^{-2/3}$ is equivalent to the equilibration over $(1-z/L_{eq})^{-4/3}$ segments.)

Following this molecular picture, the segment coordinate z^{**} specifying the crossover from the DTD picture ($z < z^{**}$ and $\tau_{MM} > \tau^{**}$) to the CR picture ($z > z^{**}$ and $\tau_{MM} < \tau^{**}$) was estimated and the MM model was modified by incorporating the CR process for the segments at $z > z^{**}$. Features of this modified model and results of comparison with experiments are summarized below.

8-4-6-1. Estimation of z^{**} and t_w

Graessley formulated the entanglement lifetime t_w for a linear chain as a mean waiting time for the first removal of local constraint due to motion of surrounding linear chains:[22] $t_w = \int_0^\infty \{F(t)\}^{z_g} dt$ with $F(t)$ being an appropriate relaxation function (that coincide with the tube survival fraction in the Graessley model) and z_g representing the number of constraints per each entanglement point; see section 4-4.

In the above DTD-CR crossover molecular picture for the star arm, the first removal of constraint for an entanglement segment in a given arm can occur through two modes: If the entangling partner (a segment in the other arm) has the curvilinear coordinate $z < z^{**}$, the removal would be dominated by the MM-type arm retraction. On the other hand, if the partner has $z > z^{**}$, the removal can occur at the time t_w through the CR motion of this partner. Applying the Graessley formulation to this dual-mode removal, the t_w for the star arm may be estimated as

$$t_w = \int_0^\infty \{F(t)\}^{z_g} dt$$

$$\text{with } F(t) = \frac{1}{L_{eq}} \int_0^{z^{**}} \exp\left(-\frac{t}{\tau_{MM}(z')}\right) dz' + \left(1 - \frac{z^{**}}{L_{eq}}\right) \exp\left(-\frac{t}{t_w}\right) \qquad (8.9)$$

From the t_w obtained by numerically solving eq 8.9, the CR-equilibration time τ^{**} can be estimated in the following way.

Characteristic times of the actual CR process are close to those predicted by the Rouse-CR model.[13,22] In this model, an effective friction coefficient for the CR motion of the entanglement segment is given by $12 k_B T t_w / a^2$. Thus, for a given retraction distance z (that leads to $a' = (1-z/$

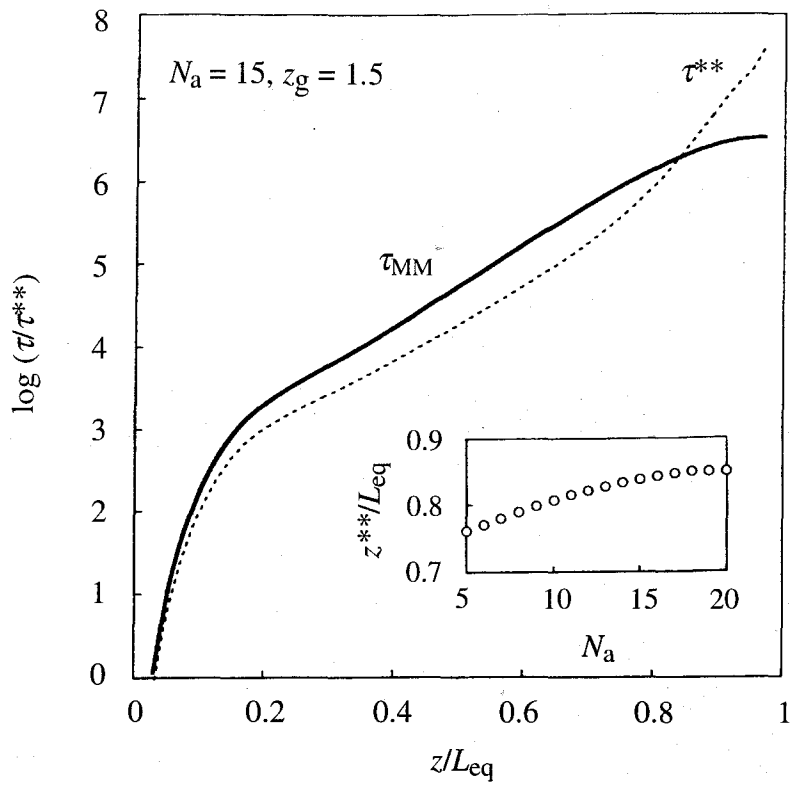

Fig.8-11 Comparison of the relaxation time $\tau_{MM}(z)$ for an entanglement segment at curvilinear coordinate z deduced from the MM model (solid curve) with the time $\tau^{**}(z)$ required for CR-equilibration over $(1-z/L_{eq})^{-4/3}$ segments (dashed curve). This CR equilibration is necessary for the tube to dilate in a way assumed in the model; the assumed full dilation occurs if $\tau_{MM}(z) > \tau^{**}(z)$, and CR process dominates the relaxation if $\tau_{MM}(z) < \tau^{**}(z)$. The N_a dependence of the curvilinear coordinate z^{**} specifying this DTD-CR crossover is shown in the inserted panel.

$L_{eq})^{-2/3}$ if the DTD picture is valid), τ^{**} can be estimated as an orientational Rouse-equilibration time for successive β entanglement segments:

$$\tau^{**}(z) = \frac{t_w}{2} \sin^{-2}\left(\frac{\pi}{2\beta}\right) \tag{8.10}$$

with

$$\beta = \frac{1}{(1 - z/L_{eq})^{4/3}} \tag{8.11}$$

Here, the discretized Rouse dynamics[6,13] is uitilized so that the resulting expression of τ^{**} (eq 8.10) is applicable in the entire range of β (≥ 1). For large β, eq 8.10 is reduced to the continuous Rouse-CR expression, $\tau^{**} = f(a'/a)^4 t_w$ (utilized in section 8-4-3-2).

For the stars of various N_a, $\tau^{**}(z)$ was calculated from eqs 8.9 and 8.10 (with z^{**} in eq 8.9 being replaced by z) and the DTD-CR threshold z^{**} was estimated by comparing this $\tau^{**}(z)$ with $\tau_{MM}(z)$ (eq 4.50). The results for $N_a = 15$ and $z_g = 1.5$ are shown in Fig. 8-11, where $\tau^{**}(z)$ and $\tau_{MM}(z)$ reduced by the Rouse relaxation time in one entanglement segment τ^{**} are plotted against

the *reduced coordinate* z/L_{eq}. The threshold, $z^{**} = 0.84L_{eq}$, is evaluated as the coordinate where the $\tau^{**}(z)$ and $\tau_{MM}(z)$ curves cross each other. For $z > z^{**}$, τ^{**} is larger than τ_{MM} and the CR-equilibration (pre-requisite for DTD) does not occur in time.

The DTD-CR threshold z^{**} evaluated in this way increases gradually with N_a; see the insert in Fig. 8-11. However, for $N_a \leq 20$ (a practically accessible range of N_a), z^{**} remains considerably smaller than L_{eq}. Thus, a non-negligible number of segments near the branching point should relax at long t through the CR motion, not through the full arm retraction along the dilated tube.

Of course, the z^{**} value changes with the choice of z_g and the method of estimating t_w. In addition, the distribution of the entanglement lifetime, having a delicate effect on the CR dynamics, may also change the $\tau^{**}(z)$. However, irrespective of these details, the insufficient CR equilibration (= failure of the DTD picture) seems to be concluded for large z (for slow relaxation). Thus, in this study, the z^{**} determined in Fig. 8-11 is utilized to modify the MM model by explicitly incorporating the CR process (though in a crude way). The aim of this modification is to examine the importance of the CR mechanism and explore a direction of the model refinement, not to obtain numerical agreement with the data through incorporation of many adjustable model parameters.

8-4-6-2. CR-relaxation process

During the CR process for the segments at $z > z^{**}$, the branching point is allowed to move with the characteristic time t_w. Thus, the Rouse-Ham model[13,30,31] (allowing this motion; section 4-4-2) is utilized to formulate the viscoelastic and dielectric relaxation functions $\mu_{CR}(t)$ and $\Phi_{CR}(t)$ for the CR process of these segments. These $\mu_{CR}(t)$ and $\Phi_{CR}(t)$ are defined as the normalized functions satisfying $\mu_{CR}(0) = \Phi_{CR}(0) = 1$.

The Rouse-Ham model describes the stochastic motion of a star-branched bead-spring chain having a frictionless branching point; cf. Fig. 4-2a. The arm is composed of N_{CR} beads each having an effective friction coefficient ζ_{eff}. For the CR process at long t, the bead (motional unit) is equivalent to the entanglement segment of the size a. Thus, the bead number (=spring number) and the spring constant κ are chosen to be

$$N_{CR} = N_a\left(1 - \frac{z^{**}}{L_{eq}}\right) \quad \text{and} \quad \kappa = \frac{3k_BT}{a^2} \tag{8.12}$$

Here, z^{**} is the DTD-CR threshod (evaluated in Fig. 8-11). Since this N_{CR} is not very large (< 4 for the PI stars examined in Figs. 8-8 and 8-9), the $\mu_{CR}(t)$ and $\Phi_{CR}(t)$ are to be calculated from the discretized Rouse-Ham equation.

In the Rouse-Ham model for monodisperse q-arm star chains, the eigenmodes of the chain motion are classified into two series; see Fig. 4-2b. The odd eigenmodes activate the synchronized motion of a particular pair of arms (chosen from the q arms). Thus, the odd modes for a given relaxation time has a degeneracy of $q-1$.[30,31] In contrast, the even eigenmodes activate the

synchronized motion of all q arms. These even modes are not degenerated.

These Rouse-Ham eigenmodes (calculated from the discreteized RH equation) were utilized to obtain $\mu_{CR}(t)$ and $\Phi_{CR}(t)$:

$$\mu_{CR}(t) = \frac{1}{qN_{CR}}\left[\sum_{p=1}^{N_{CR}} (q-1)\exp\left(-\frac{2t}{\tau_{2p-1}^{(CR)}}\right) + \sum_{p=1}^{N_{CR}} \exp\left(-\frac{2t}{\tau_{2p}^{(CR)}}\right)\right] \tag{8.13}$$

and

$$\Phi_{CR}(t) = \frac{1}{K_{CR}} \sum_{p=\text{odd} \le N_{CR}} \sin^{-2}\left(\frac{p\pi}{2N_{CR}}\right)\exp\left(-\frac{t}{\tau_{2p}^{(CR)}}\right) \tag{8.14}$$

with

$$K_{CR} = \sum_{p=\text{odd} \le N_{CR}} \sin^{-2}\left(\frac{p\pi}{2N_{CR}}\right) \tag{8.15}$$

The eigenmode relaxation times $\tau_{2p-1}^{(CR)}$ and $\tau_{2p}^{(CR)}$ appearing in eqs 8.13 and 8.14 are given by

$$\tau_{2p-1}^{(CR)} = \frac{\zeta_{eff}}{4\kappa}\sin^{-2}\left(\frac{\{2p-1\}\pi}{2\{2N_{CR}+1\}}\right) \text{ for odd modes } (p = 1, 2, ..,N_{CR}) \tag{8.16}$$

$$\tau_{2p}^{(CR)} = \frac{\zeta_{eff}}{4\kappa}\sin^{-2}\left(\frac{p\pi}{2N_{CR}}\right) \text{ for even modes } (p = 1, 2, ...,N_{CR}) \tag{8.17}$$

The coefficient ζ_{eff} included in these relaxation times is specified later in relation to the arm motion during the terminal CR process at long t.

Here, a few comments should be added for the above expression of μ_{CR} and Φ_{CR}. First of all, the dielectric mode relaxation times are identical to the eigenmode relaxation times $\tau_\alpha^{(CR)}$ ($1 \le \alpha \le 2N_{CR}$) while the viscoelastic mode relaxation times are half of $\tau_\alpha^{(CR)}$, as noted from the decaying terms $\exp\{-t/\tau_\alpha^{(CR)}\}$ and $\exp\{-2t/\tau_\alpha^{(CR)}\}$ included in eqs 8.13 and 8.14. This difference reflects a difference between the dielectric and viscoelastic properties, the former detecting the orientational correlation at two times t and 0 (cf. eq 3.14) while the latter representing the isochronal orientational anisotropy (cf. eq 3.7). Because of this difference, the Φ_{CR} and μ_{CR} for the incoherent CR process include the first-order and second-order moments of the eigenmode amplitudes that decay as $\exp\{-t/\tau_\alpha^{(CR)}\}$ and $\exp\{-2t/\tau_\alpha^{(CR)}\}$, respectively (cf. Chapter 6).

It should be also noted that $\Phi_{CR}(t)$ is contributed only from a subset of even eigenmodes having the mode indices equal to twice of odd integers; see eq 8.14. This dielectric extinction of the other eigenmodes reflects the inversion of the type-A dipoles at the branching point.[31] Because of this inversion, the odd eigenmodes do not change the total polarization of the chain and are dielectrically inert; see Fig. 4-2b. The even eigenmodes with the mode indices equal to twice of even integers are also inert because these modes activate the same displacements for the arm

end and branching point to induce no change in the polarization in each arm. (Of course, all eigenmodes contribute to the viscoelastic μ_{CR} (eq 8.13) irrespective of the dipole inversion.)

Even with the inverted dipoles, this extinction does not occur if the motion of the q arms is not synchronized and not described as a sum of eigenmodes. From this point of view, the dielectric extinction can be regarded as a characteristic feature of the (Rouse-Ham type) CR process.

8-4-6-3. Effective friction for terminal CR relaxation

The motional unit considered in the CR process (eqs 8.13 and 8.14) is the entanglement segment of the size a, not the coarse-grained (dilated) segment considered in the DTD process. The effective friction coefficient ζ_{eff} specifies an average hopping rate of this unit during the terminal CR process.

The friction coefficient defined for the *local* CR-hopping over the distance a is written as $\zeta^{(local)} = 4\kappa t_w$ $(= 12k_BTt_w/a^2)$,[13,22] where t_w is the local entanglement lifetime (cf. eq 8.9). The corresponding longest relaxation time τ_1 is calculated from eq 8.16 with $p = 1$ and $\zeta_{eff} = \zeta^{(local)}$:

$$\tau_1\{\zeta^{(local)}\} = t_w \sin^{-2}\left(\frac{\pi}{2\{2N_{CR}+1\}}\right) \tag{8.18}$$

However, for the terminal CR relaxation to occur, the N_{CR}-th segments located at z^{**} (shown with the filled circles in Fig. 4-2a) need to hop over a distance $N_{CR}^{1/2}a^2$. This hopping is allowed only after the arm retracts over the distance z^{**} to release these segments, namely, only at $t > \tau_{MM}(z^{**})$. The τ_1 for this retraction-determined CR hopping process can be calculated by re-modeling the RH arm (Fig. 4-2a) as an arm composed of only one end-segment that is bound to the branching point through a spring of the strength $\kappa' = \kappa/N_{CR}$: The friction coefficient $\zeta^{(ret)}$ for that hopping process is given by $4\kappa'\tau_{MM}(z^{**})$, and the corresponding τ_1 is obtained from eq 8.16 with $N_{CR} = 1$, $p = 1$, and κ and ζ_{eff} being replaced by κ' and $\zeta^{(ret)}$:

$$\tau_1\{\zeta^{(ret)}\} = 4\tau_{MM}(z^{**}) \tag{8.19}$$

The prefactor of 4 appearing in eq 8.19 reflects a fact that the terminal CR relaxation requires the anti-symmetric motion of *two* end-segments.

The difference between $\tau_1\{\zeta^{(ret)}\}$ and $\tau_1\{\zeta^{(local)}\}$ suggests that the entanglement lifetime has a distribution determined by the length scale (and direction) of the CR hopping. The lifetime for the local hopping over the distance a is given by t_w (cf. eq 8.9), and the tube should dilate as a result of accumulation of such local hopping (in both radial and axial directions of the tube). However, the terminal CR process requires a larger scale hopping (predominantly in the axial direction of the dilated tube at $t = \tau_{MM}(z^{**})$), and the entanglement lifetime assigned to each segment *during this process* should be different from t_w.

The effective friction coefficient ζ_{eff} (included in eqs 8.16 and 8.17) is determined according to this distribution of the lifetime. Accumulation of the local CR hopping leads to the termi-

nal CR relaxation, and this accumulation requires the time $\tau_1\{\zeta^{(local)}\}$. Thus, if $\tau_1\{\zeta^{(local)}\} > \tau_1\{\zeta^{(ret)}\}$, this relaxation should occur at $\tau_1\{\zeta^{(local)}\}$. For this case, $\tau_1\{\zeta^{(local)}\}$ and $\tau_1^{(CR)}$ (eq 8.16) can be equated to obtain $\zeta_{eff} = 4\kappa\tau_W$.

On the other hand, if $\tau_1\{\zeta^{(ret)}\} > \tau_1\{\zeta^{(local)}\}$, the terminal CR relaxation rate should be determined by the arm retraction over the distance z^{**}. For this case, $\tau_1\{\zeta^{(ret)}\}$ and $\tau_1^{(CR)}$ can be equated to evaluate ζ_{eff} as

$$\zeta_{eff} = 16\kappa\tau_{MM}(z^{**}) \sin^2\left(\frac{\pi}{2\{2N_{CR}+1\}}\right) \tag{8.20}$$

(This situation is similar to that for a pom-pom chains:[32] The trunk of this chain relaxes only after the relaxation of the arms attached to the trunk ends is completed, and the friction factor for the trunk is determined by the arms.)

For the highly entangled PI stars with N_a = 12 and 16 (cf. Figs. 8-8 and 8-9), the DTD-CR threshold z^{**} shown in Fig. 8-11 was utilized to calculate $\tau_1\{\zeta^{(local)}\}$ and $\tau_1\{\zeta^{(ret)}\}$ (cf. eqs 4.50, 8.9, 8.18, and 8.19). For these stars, $\tau_1\{\zeta^{(ret)}\}$ was found to be longer than $\tau_1\{\zeta^{(local)}\}$. Thus, the viscoelastic and dielectric properties for the combined DTD-CR process were calculated from eqs 8.13-8.17 together with eq 8.20. Comparison of these calculated properties and data is presented below.

8-4-6-4. Comparison of DTD-CR model with experiments

Combining the CR relaxation functions for the entanglement segments at $z > z^{**}$ (eqs 8.13-8.17 and 8.20) and the DTD relaxation functions for those at $z < z^{**}$ (cf. eqs 4.51 and 4.71 with α = 4/3), the CR process can be incorporated in the MM model (with the tube edge effect) to formulate the viscoelastic $\mu(t)$ and dielectric $\Phi(t)$ as

$$\mu(t) = \frac{7}{3L_{eq}}\int_0^{z^{**}} \left[1 - \frac{z}{L_{eq}}\right]^{4/3} \exp\left(-\frac{t}{\tau_{MM}(z)}\right) dz + I_{CR,G}\,\mu_{CR}(t) \tag{8.21}$$

$$\Phi(t) = \frac{1}{L_{eq}}\int_0^{z^{**}} \left[1 + \frac{1}{6N_a}\left\{\left(1-\frac{z}{L_{eq}}\right)^{-7/3} - \left(1-\frac{z}{L_{eq}}\right)^{-5/3}\right\}\right] \exp\left(-\frac{t}{\tau_{MM}(z)}\right) dz + I_{CR,\varepsilon}\,\Phi_{CR}(t) \tag{8.22}$$

with

$$I_{CR,G} = \left(1 - \frac{z^{**}}{L_{eq}}\right)^{7/3}, \quad I_{CR,\varepsilon} = 1 - \frac{z^{**}}{L_{eq}} - \frac{1}{8N_a}\left\{1 - \left(1 - \frac{z^{**}}{L_{eq}}\right)^{-2/3}\right\}^2 \tag{8.23}$$

Here, z^{**} is the DTD-CR crossover coordinate (Fig. 8-11). This modified MM model is hereafter referred to as the DTD-CR model. The fundamental parameters included in this model are

N_a, z^{**}, and τ^{**} (the Rouse relaxation time in one entanglement segment). All other parameters are uniquely calculated from these fundamental parameters.

In eqs 8.21 and 8.22, the first integration terms indicate the DTD contribution, and the second terms represent the CR contribution with the *relative* relaxation intensities $I_{CR,G}$ and $I_{CR,\varepsilon}$ given by eq 8.23. These intensities were evaluated by subtracting the intensities for the DTD process (the integration terms at $t = 0$) from unity. It should be noted that these intensities are smaller than the initial memory ($= 1-z^{**}/L_{eq}$) sustained by the segments at $z_s > z^{**}$. Thus, in the DTD-CR model, these segments partially relax during the DTD process and fully relaxes during the CR process.

For the highly entangled PI stars with $N_a = 12$ and 16, the viscoelastic and dielectric properties calculated from the above DTD-CR model are shown with the dotted curves in Figs. 8-8 and 8-9. The μ_{CR} and Φ_{CR} terms included in eqs 8.21 and 8.22 require N_{CR} to be integer (cf. eqs 8.13 and 8.14), but the N_{CR}(eq 8.12) obtained from z^{**} (Fig. 8-11) was not an integer number. Thus, in the calculation, the N_{CR} was replaced by the closest integer n_{CR} (= 2 and 3 for $N_a = 12$ and 16), and the z^{**} value was adjusted accordingly ($z^{**} = L_{eq}(1-n_{CR}/N_a)$). The $N_{a,cal}$ values utilized in the calculation were the same as those for the original MM model ($N_{a,cal} = 15$ and/or 20), and the only remaining parameter τ^* was chosen in a way that the calculated η_0 coincided with the η_0 data.

As noted in the top panels in Figs. 8-8 and 8-9, the incorporation of the CR process in the MM model hardly changes the model prediction for the viscoelastic moduli; compare solid and dotted curves. This result reflects a fact that a large fraction of the initial modulus sustained by the entanglement segments at $z > z^{**}$ has relaxed during the DTD process and only a small intensity $I_{CR,G}$ (eq 8.23) remains for the CR process of these segments. In other words, the CR process is hardly detected through the viscoelastic moduli.

In contrast, the dielectric behavior is significantly affected by the CR process (because a considerably large dielectric intensity $I_{CR,\varepsilon}$ remains for this process); see the middle and bottom panels of Figs. 8-8 and 8-9. The terminal dielectric relaxation calculated from the DTD-CR model is considerably faster than that deduced from the MM model (with/without tube-edge effect) and appears to be in better agreement with the data; compare the dotted and dashed/solid curves.

For further comparison of the DTD-CR and MM models, Fig. 8-12 shows N_a dependence of the experimentally detectable longest relaxation time τ_{max} predicted from these models. In the original MM model, the terminal relaxation is achieved through full retraction of the arm along the dilated tube, and the viscoelastically and dielectrically detectable τ_{max}'s coincide with $\tau_{MM}(L_{eq})$.

In the DTD-CR model, the rigorously defined *viscoelastic* τ_{max} is given by a half of the slowest CR eigenmode relaxation time, $\tau_G(CR) = \tau_1^{(CR)}/2$; see eq 8.13. However, the terminal CR mode has a very small viscoelastic intensity $I_{CR,G}$. Thus, the experimentally detectable viscoelastic τ_{max}, that should be close to the measured $<\tau_G>_w$ (Fig. 8-2), is decreased to the time $\tau_{MM}(z^{**})$ required for the retraction over the curvilinear distance z^{**}.

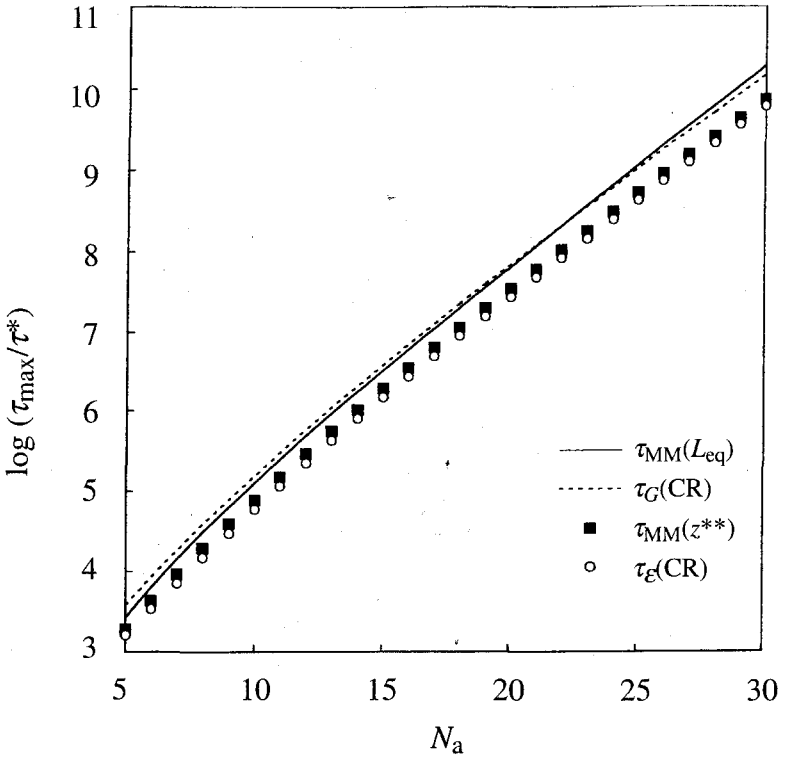

Fig.8-12 N_a dependence of the experimentally detectable longest relaxation time τ_{max} predicted from the MM and DTD-CR models.

The situation is different for the dielectric behavior of the DTD-CR model. Because of the dipole inversion of the PI stars, the slowest CR eigenmode is dielectrically inert. Thus, the dielectrically detectable τ_{max} (that should be close to the measured $<\tau_\varepsilon>_w$; Fig. 8-2) coincides with the relaxation time of the second-slowest CR eigenmode, $\tau_\varepsilon(CR) = \tau_2^{(CR)}$. This $\tau_\varepsilon(CR)$ is close to the viscoelastic τ_{max} (= $\tau_{MM}(z^{**})$) but is considerably smaller than $\tau_{MM}(L_{eq})$. This difference between $\tau_\varepsilon(CR)$ and $\tau_{MM}(L_{eq})$ is reflected in the acceleration of the terminal dielectric relaxation due to the CR mechanism (cf. solid and dotted curves in the middle/bottom panels in Figs. 8-8 and 8-9).

As noted in Fig. 8-12, the incorporation of the CR process in the MM model decreases the viscoelastic and dielectric τ_{max} values but hardly changes the exponential N_a dependence of τ_{max}. (Note that the semi-logarithmic plots of $\tau_{MM}(z^{**})$, $\tau_\varepsilon(CR)$, and $\tau_{MM}(L_{eq})$ have an almost identical slope). Thus, the DTD-CR model can describe the experimentally observed N_a dependence of $<\tau_\varepsilon>_w$ and $<\tau_G>_w$ (Fig. 8-2) with the accuracy similar to that for the MM model. From this result as well as the moderate improvement of the prediction for the dielectric behavior by incorporation of the CR process (Figs. 8-8 and 8-9), the combination of the DTD and CR processes appears to be essential for accurate description of the star chain dynamics.

8-5. Concluding Remarks

For highly entangled PI stars having the type-A dipoles in each arm, the viscoelastic and dielectric relaxation behavior was examined within the context of the tube model considering the DTD and CR processes. Comparison of the viscoelastic and dielectric data indicates that the

simplest DTD picture, the arm retraction in the fully dilated tube (having $a' = a\{\varphi(t)\}^{-\alpha/2}$), fails in the dominant part of the terminal relaxation. This result, found irrespective of the tube-edge effect on the dielectric $\Phi(t)$, suggests that the CR mechanism has a significant contribution to the terminal relaxation of the star chains.

On the basis of this result, the MM model was refined by explicitly incorporating the CR process. This modification was made by introducing the DTD-CR crossover coordinate z^{**} and simply adding the DTD and CR relaxation functions (the latter being defined only for the entanglement segments at $z > z^{**}$). This crude modification, separately treating the relaxation of the segments at $z > z^{**}$ and $z < z^{**}$, moderately improved the model prediction for the dielectric behavior. This improvement is related to the extinction of some CR eigenmodes in the dielectric $\Phi(t)$ due to the dipole inversion at the branching point.

Of course, the real DTD-CR crossover would be gradual (not occurring sharply at z^{**}), and the real CR dynamics is not necessarily identical to the Rouse-Ham dynamics assumed in the above DTD-CR model. In addition, a self-consistent treatment would be necessary for the effect of the relaxed segments at $z < z^{**}$ on the terminal CR relaxation of the segments at $z > z^{**}$. (In the DTD-CR model, this effect was considered in a crude way explained for eqs 8.18-8.20) Furthermore, the experimentally observed failure of the simplest DTD picture may be also related to the other possible relaxation route, the arm retraction in a partially dilated tube (having $a' < a\{\varphi(t)\}^{-\alpha/2}$), as suggested by McLeish.[28] Refinement for these points would improve the model prediction.

The DTD model (MM model) excellently describe the *viscoelastic* behavior of PI stars. However, the results presented in this chapter unequivocally demonstrate the importance of the CR mechanism in accurate description of the arm *motion* (that determines all kinds of relaxation phenomena including the viscoelastic relaxation).

Appendix 8A. Viscoelastic and Dielectric Features of BM and MM Models

For convenience of the detailed test of the DTD picture within the context of the tube model, this appendix summarizes viscoelastic and dielectric features of the BM and MM models in absence of the tube edge effect.

The $\mu(t)$ $(=G(t)/G_N)$ of the BM and MM models is given by eqs 4.46 and 4.51. The $\Phi(t)$ formulated for these models is given by eq 4.71 with $z_c = L_{eq}$, $K_n = 1$, and the pre-exponential factor in the integral being replaced by unity. For a star with $N_a = 15$, Fig. 8-13 shows plots of these $\mu(t)$ and $\Phi(t)$ against a reduced time t/τ_{arm}. Here, τ_{arm} denotes the longest relaxation time deduced from the models; $\tau_{arm} = \tau_{BM}(L_{eq})$ and/or $\tau_{MM}(L_{eq})$ (cf. eqs 4.44 and 4.50).

For these models, validity of the simplest DTD relationship, $\mu(t) = [\Phi(t)]^{1+\alpha}$ (eq 4.60) is tested in Fig. 8-13. The $\mu(t)$ calculated from the $\Phi_{BM}(t)$ and $\Phi_{MM}(t)$ through this relationship are shown with the solid curve (in top panel; $\alpha = 1$ for the BM model) and dashed curve (in bottom panel; $\alpha = 4/3$ for the BM model). At short t, these curves agree with the $\mu_{BM}(t)$ and $\mu_{MM}(t)$ of the models directly calculated from eqs 4.46 and 4.51 (unfilled circles). However, a deviation is

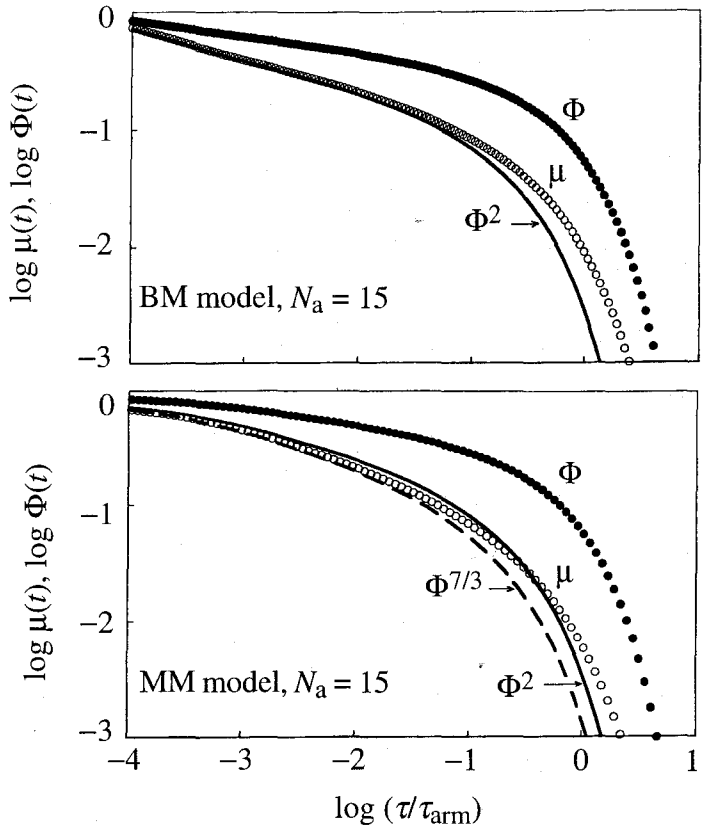

Fig. 8-13 Plots of $\mu(t)$ and $\Phi(t)$ of BM model (top panel) and MM model (bottom panel) against a reduced time τ/τ_{arm} (τ_{arm} = longest relaxation time deduced from the models). The solid and dashed curves indicate plots of $[\Phi(t)]^2$ and $[\Phi(t)]^{7/3}$, respectively.

observed at long t (in a vicinity of τ_{arm}), meaning that the simplest DTD relationship does not hold for the BM/MM models at long t. This deviation reflects a fact that the simplest DTD relationship is derived from the analysis of *average* tube survival fraction φ' (section 4-6-3-3) while the BM/MM models are formulated on the basis of the *conditional* tube survival fraction $\tilde{\varphi}' = 1-z/L_{eq}$ defined for a given retraction distance z (section 4-6-3-3).

From the above result, one might argue that the observed failure of the simplest DTD relationship (Fig. 8-3) does not indicate the failure of the BM/MM models. However, Figs. 8-8, 8-9 and 8-10 clearly demonstrate that the models (with/without the tube-edge effect on Φ) excellently describe the viscoelastic data but fail for the dielectric data; cf. dashed/solid curves and circles. This result indicates a necessity of modification of the models (through explicit incorporation of the CR process).

In addition, the $\mu_{MM}(t)$ of the MM model (unfilled circles in the bottom panel of Fig. 8-13) is numerically close to $[\Phi_{MM}(t)]^2$ (solid curves) in the entire range of $t \leq \tau_{arm}$. Thus, the simplest DTD relationship with $\alpha = 1$ holds for the MM model as a good approximation (although the intrinsic α value of this model is 4/3). This approximate validity of the DTD relationship with $\alpha = 1$ was confirmed for the MM model in a wide range of N_a between 5 and 30. Thus the failure of this relationship (Fig. 8-3) is almost equivalent to the deviation of the MM prediction from the dielectric data (Figs. 8-8 and 8-9).

References and Notes

1. Viovy, J. L.; Rubinstein, M.; Colby, R. H. *Macromolecules* **1991**, *24*, 3587.
2. Ball, R. C.; McLeish, T. C. B. *Macromolecules* **1989**, *22*, 1911.
3. Milner, S. T.; McLeish, T. C. B. *Macromolecules* **1997**, *30*, 2159.
4. Milner, S. T.; McLeish, T. C. B. *Macromolecules* **1998**, *31*, 7479.
5. Yoshida, H.; Adachi, K.; Watanabe, H.; Kotaka, T. *Polymer J.* **1989**, *21*, 863.
6. Ferry, J. D. *Viscoelastic Properties of Polymers*, 3rd ed.; Wiley: New York, 1980.
7. Imanishi, Y.; Adachi. K.; Kotaka, T. *J. Chem. Phys.* **1988**, *21*, 157.
8. Watanabe, H.; Matsumiya, Y.; Osaki, K. *J. Polym. Sci. B Polym. Phys.* **2000**, *38*, 1024.
9. Watanabe, H. *Macromol. Rapid Commun.* **2001**, *22*, 127.
10. Matsumiya, Y.; Watanabe, H.; Osaki, K. *Macromolecules* **2000**, *33*, 499.
11. Adachi, K.; Yoshida, H.; Fukui, F.; Kotaka, T. *Macromolecules* **1990**, *23*, 3138.
12. Some of the $<\tau>$ data for the low-M linear PI (with $M \leq 10^4$) shown in Fig. 8-2 were the data reported by Adachi et al.7,[11] Their definition of $<\tau>$ was different from eqs 2.9 and 2.18, but the $<\tau>$ values for those low-M linear PI were not significantly affected by this difference.
13. Watanabe, H. *Prog. Polym. Sci.* **1999**, *24*, 1253.
14. Doi, M.; Kuzuu, N. *J. Polym. Sci. Polym. Lett. Ed.* **1980**, *18*, 775.
15. Pearson, D. S.; Helfand, E. *Macromolecules* **1984**, *17*, 888.
16. Fetters, L. J; Kiss, A. D.; Pearson, D. S.; Quack, G. F.; Vitus, F. J. *Macromolecules* **1993**, *26*, 1647.
17. Adams, C. H.; Hutchings, L. R.; Klein, P. G.; McLeish, T. C. B.; Richards, R. W. *Macromolecules* **1996**, *29*, 5717.
18. Vlassopoulos, D.; Pakula, T.; Fytas, G.; Roovers, J.; Karatasos, K.; Hadjichristidis, N. *Europhys. Lett.* **1997**, *39*, 617.
19. Pakula, T.; Vlassopoulos, D.; Fytas, G.; Roovers, J. *Macromolecules* **1998**, *31*, 8931.
20. Vlassopoulos, D.; Fytas, G.; Roovers, J.; Pakula, T.; Fleischer, G. *Faraday Discuss.* **1999**, *112*, 225.
21. Marrucci, G. *J. Polym. Sci. Polym. Phys. Ed.* **1985**, *23*, 159.
22. Graessley, W. W. *Adv. Polym. Sci.* **1982**, *47*, 68.
23. Milner, S. T.; McLeish, T. C. B.; Young, R. N.; Hakiki, A.; Johnson, J. M.; *Macromolecules* **1998**, *31*, 9345.
24. Adachi, K.; Itoh, S.; Nishi, I.; Kotaka, T. *Macromolecules* **1990**, *23*, 2554.
25. Within the generalized tube picture, the CLF model[33,34] may be utilized to relate τ_ε of the well-entangled PI to its pure reptation time τ_{rep}; $\tau_\varepsilon \cong [1 - N_{DE}^{-1/2}]^2 \tau_{rep} \cong 0.9\tau_{rep}$ where, to be consistent, the entanglement segment number N_{DE} (= 78) corresponding to the Doi-Edwards expression of G_N (= $4\rho RT/5M_e$)[35] is utilized. Thus, τ_ε of the PI is not significantly different from τ_{rep} and $t_w = 0.11\tau_\varepsilon$ can be utilized as a reasonable estimate of the entanglement lifetime for the linear PI: The uncertainty in the $t_w^{1/2}$ factor included in eq

8.5 due to the use of τ_ε instead of τ_{rep} is less than 10% for the linear PI with N_{DE}= 78.
26. Watanabe, H.; Yoshida, H.; Kotaka, T. *Macromolecules* **1992**, *25*, 2442.
27. Rubinstein, M.; Colby, R. H. *J. Chem. Phys.* **1988**, *89*, 5291.
28. private communication with T. C. B. McLeish.
29. Note, however, that the monodisperse linear PI chain does not necessarily reptate with its intrinsic diffusivity along the dilated tube:[13] This type of reptation requires the equilibration of the chain contour length measured along the dilatedtube.[13] This equilibration, involving all entanglement segments in the chain, occurs at $t \geq fN^2 t_w \cong 0.05\, N^2 \tau_\varepsilon$, i.e., not at $t \leq \tau_\varepsilon$ for $N >> 1$.
30. Ham, J. S. *J. Chem. Phys.* **1957**, *26*, 625.
31. Watanabe, H.; Yoshida, H.; Kotaka, T. *Polymer J.* **1990**, *22,* 153.
32. McLeish, T. C. B.; Larson, R. G. *J. Rheol.* **1998**, 42, 81.
33. Doi, M. *J. Polym. Sci. Polym. Lett. Ed.* **1981**, *19*, 265.
34. Doi, M. *J. Polym. Sci. Polym. Phys. Ed.* **1983**, *21*, 667.
35. Doi M.; Edwards, S. F. *The Theory of Polymer Dynamics*, Clarendon: Oxford, 1986.
36. Watanabe, H. *Korea-Australia Rheol. J.*, Submitted.

CHAPTER 9
Summary

In this thesis, the viscoelastic and dielectric properties of *cis*-polyisoprene (PI) have been investigated to elucidate the molecular dynamics of entangled chains. In the linear response regime, these properties detect the same molecular motion in different ways: The viscoelastic properties reflect decay of isochronal orientational anisotropy of the chain, and the dielectric properties detect decay of orientational correlation at two times (t and 0). Comparison of these properties provides detailed information of the chain dynamics.

The results and discussions of the viscoelastic and dielectric tests are described in Chapters 5-8, with the general introduction in Chapter 1, the explanation for preparation of materials and the methods and principles of measurements in Chapter 2, the relationship between the (macroscopic) dynamic properties and the (microscopic) chain motion in Chapter 3, and the summary of the various version of the tube models for entangled chains in Chapter 4. The contents in Chapters 5-8 are summarized as follows:

In Chapter 5, eigenfunctions $f_p(n)$ and relaxation times $\tau_{\varepsilon,p}$ accompanying the local correlation function for the dipole-inverted PI chains (dilute probe) in a long, entangling matrix were dielectrically determined. For the slowest three eigenmodes, $f_p(n)$ and $\tau_{\varepsilon,p}/\tau_{\varepsilon,1}$ ratios are hardly affected by changes in the constraint release (CR) contribution to the chain motion, as revealed from comparison of $f_p(n)$ and $\tau_{\varepsilon,p}$ in the entangling polybutadiene (PB) matrices of different molecular weights M. For higher-order eigenmodes, some CR effects are noted. In all matrices examined, $f_p(n)$ (p = 1-3) of the dilute probe PI are non-sinusoidal with respect to the segment position n and deviate from the eigenfunctions deduced from the pure reptation and Rouse-type CR models, although the $\tau_{\varepsilon,p}/\tau_{\varepsilon,1}$ ratios are close to the model prediction. These results provide an important starting point for refining molecular models that describe the dynamics of entangled chains in various environments.

In Chapter 6, the short-time coherence of the submolecule motion in individual chains was examined by comparing the viscoelastic and dielectric data for dilute PI probe chains in various environments. The comparison unequivocally indicated that the constraint release (CR) mechanism determines this coherence: The larger the CR contribution to the PI dynamics, the smaller the degree of the coherence.

In Chapter 7, the viscoelastic and dielectric properties of linear PI chains having non-inverted type-A dipoles were tested within the context of the current tube model. A specific relationship derived in Chapter 4, that should be valid when the tube dilates in the time scale of the chain relaxation, was utilized in this test. This relationship was found to be valid for the monodisperse PI chains with M/M_e = 1.9 - 62. This result suggests the importance of the dynamic tube dilation (DTD) for the terminal relaxation of these PI chains, although the chains do not necessarily reptate along the dilated tube with their intrinsic curvilinear diffusion coefficient.

In contrast, for the dilute probe PI chain in the low-M entangling PB matrix, the relation-

ship was not valid. This result indicates that the probe fully relaxes *via* the CR mechanism during the mutual equilibration of its entanglement segments (before the expected tube dilation is completed), demonstrating the importance of the CR motion of the probe in the tube dilation process.

In Chapter 8, the viscoelastic and dielectric relaxation behavior of the entangled star-branched PI chains having the type-A dipoles in each arm was examined within the context of the tube model considering the DTD and CR processes. Comparison of the viscoelastic and dielectric data indicated that the simplest DTD picture, the arm retraction in the fully dilated tube, fails in the dominant part of the terminal relaxation. The same comparison, made for a series of star PI with different arm numbers, confirmed that this failure of the DTD picture is not attributed to the assumption of small branching point fluctuation in the dilated tube (underlaying the DTD relationship). This result, found irrespective of the tube-edge effect on the dielectric $\Phi(t)$, suggests that the CR mechanism has a significant contribution to the terminal relaxation of the star chains.

On the basis of this result, Milner-McLeish (MM) model was refined by explicitly incorporating the CR process. This modification was made by introducing the DTD-CR crossover coordinate z^{**} and simply adding the DTD and CR relaxation functions (the latter being defined only for the entanglement segments at $z > z^{**}$). This crude modification, separately treating the relaxation of the segments at $z > z^{**}$ and $z < z^{**}$, moderately improved the model prediction for the dielectric behavior. This improvement is related to the extinction of some CR eigenmodes in the dielectric $\Phi(t)$ due to the dipole inversion at the branching point.

The DTD model (MM model) excellently describe the *viscoelastic* behavior of PI stars. However, the results presented in this chapter unequivocally demonstrate the importance of the CR mechanism in accurate description of the arm motion.

List of Publications

I. *Publications Included in This Thesis*

1. Dynamics of Dipole-Inverted *cis*-Polyisoprene Chains in a Matrix of Long, Entangling Chains. 1. Effects of Constraint Release on the Eigenmodes of the Local Correlation Function
   Yumi Matsumiya, Hiroshi Watanabe, Kunihiro Osaki, and Ming-Long Yao
   Macromolecules, **1998**, *31*, 7528-7537.

2. Dynamics of Dipole-Inverted *cis*-Polyisoprene Chains in a Matrix of Long, Entangling Chains. 2. Effects of Constraint Release on the Coherence of the Subchain motion
   Hiroshi Watanabe, Yumi Matsumiya, Kunihiro Osaki, and Ming-Long Yao
   Macromolecules, **1998**, *31*, 7538-7545.

3. Comparison of Dielectric and Viscoelastic Relaxation Functions of *cis*-Polyisoprenes: Test of Tube Dilation Molecular Picture
   Yumi Matsumiya, Hiroshi Watanabe, and Kunihiro Osaki
   Macromolecules, **2000**, *33*, 499-506.

4. Tube Dilation Process in Star-Branched *cis*-Polyisoprenes
   Hiroshi Watanabe, Yumi Matsumiya, and Kunihiro Osaki
   J. Polym. Sci.: Part B: Polym. Phys. **2000**, *38*, 1024-1036.

5. Entanglement Relaxation of Branched Polymers: Constraint Release and Dynamic Tube Dilation
   Yumi Matsumiya and Hiroshi Watanabe
   Kobunshi Ronbunshu, **2000**, *57*, 618-628.

6. Further Test of the Tube Dilation Process in Star-Branched *cis*-Polyisoprene: Role of Branching-Point Fluctuation
   Yumi Matsumiya and Hiroshi Watanabe
   Macromolecules, **2001**, *34*, 5702-5710.

7. Dielectric and Viscoelastic Relaxation of Highly Entangled Star Polyisoprene: Quantitative Test of Tube Dilation Model.
   Hiroshi Watanabe, Yumi Matsumiya, and Tadashi Inoue
   Macromolecules, in press.

II. *Other Publications*

1. Rheo-Dielectric Behavior of Oligostyrene and Polyisoprene
   Yumi Matsumiya, Hiroshi Watanabe, Tadashi Inoue, Kunihiro Osaki, and Ming-Long Yao
   Macromolecules, **1998**, *31*, 7973-7975.

2. Rheo-Dielectrics: Its Applicability
   Hiroshi Watanabe, Tomohiro Sato, Yumi Matsumiya, Tadashi Inoue, and Kunihiro Osaki
   J. Soc. Rheol. Jpn, **1999**, *27*, 121-125.

3. Synthesis and Linear Viscoelasticity of Model Comb Polymers
   Yumi Matsumiya, Hiroshi Watanabe, Tomohiro Sato, and Kunihiro Osaki
   J. Soc. Rheol. Jpn, ,**1999**, *27*, 127-128.

4. Effects of Spatial Confinement on Dielectric Relaxation of Block Copolymers having Tail, Loop, and Bridge Conformations
   Hiroshi Watanabe, Tomohiro Sato, Kunihiro Osaki, Yumi Matsumiya, and Spiros H. Anastasiadis
   J. Soc. Rheol. Jpn, **1999**, *27*, 173-182.

5. Rheo-Dielectric Behavior of Carbon Black Suspensions
   Hiroshi Watanabe, Yumi Matsumiya, Munetaka Kakiuchi and Yuji Aoki
   J. Soc. Rheol. Jpn, **2001**, *29*, 77-80.

6. Rheology and Structure of a Butadiene-Styrene Diblock Copolymer in Dibutyl Phthalate: Role of Concentration Fluctuation in Disruption and Reformation of Micellar Lattice
   Hiroshi Watanabe, Yumi Matsumiya, Toshiji Kanaya, and Yoshiaki Takahashi
   Macromolecules, **2001**, *34*, 6742-6755.

Acknowledgements

This thesis is based on the study which has been carried out under the direction of Professor Kunihiro Osaki, Institute for Chemical Research, Kyoto University, from 1997 to 2002.

The author wishes to express her sincere gratitude to Professor Kunihiro Osaki, for his continual guidance, advice, and encouragement throughout the course of this work.

The author also wishes to express her thanks to Professor Hiroshi Watanabe, Institute for Chemical Research, Kyoto University, for his instructive discussion, helpful advice, and collaborations in this study.

The author is sincerely grateful to Dr. Tadashi Inoue, Institute for Chemical Research, Kyoto University, for his helpful and valuable discussions and comments during this study.

Special thanks are due to Professor Fumihiko Tanaka, Department of Polymer Chemistry, Kyoto University, and Professor Takenao Yoshizaki, Department of Polymer Chemistry, Kyoto University, for their valuable comments and detailed criticisms on the manuscript of this thesis.

This study has been carried out with experimental help of Dr. Ming-Long Yao, Rheometric Scientific, Inc., for rheological measurements. The author wishes to express her thanks for his kind help.

The author is grateful for the financial support from Hayashi Memorial Foundation for Female Natural Scientists for fiscal year 2000 and from Research Fellowship of the Japan Society for the Promotion of Science for Young Scientists since fiscal year 2001.

Finally, the author expresses her heartfelt thanks to her parents, brother and sister for their care and constant encouragement during the study.

January, 2002

Yumi Matsumiya